# Wave transformation in the surf-zone

Kévin Martins

A thesis presented to the Faculty of Engineering & Design of the University of Bath
in partial fulfilment of the requirements for the degree of Doctor of Philosophy

Bath, November 2017

Water Engineering and Infrastructure Resilience (WEIR)
Faculty of Engineering & Design
University of Bath, UK

# Wave transformation in the surf-zone

**Supervisors:**

| | |
|---|---|
| Dr. Chris Blenkinsopp | Senior Lecturer at University of Bath, UK |
| Dr. Jun Zang | Reader at University of Bath, UK |

**Examination committee:**

| | |
|---|---|
| Dr. Philippe Blondel | Senior Lecturer at University of Bath, UK |
| Dr. Hervé Michallet | CNRS Researcher at LEGI, Grenoble, France |

**Author declarations:**

This thesis is composed of my original work and contains no material previously published or written by another person except where due reference has been made in the text. The contributions by others to the Journal articles used in this thesis is clearly stated in my thesis. The work published in the thesis was carried out since the commencement of my Research degree at the University of Bath and do not include any other work submitted to qualify for another degree or diploma at any other institution.

This work was financially supported by the University of Bath, through a University Research Scholarship.

**Copyright:**

# Acknowledgements

Writing this page comes at exciting and busy times. Finishing this manuscript after three full and intense years might be the principle reason behind this excitement, but thinking not only into the close future, but also of these past three years is likely to be responsible as well. Many persons have contributed to the present work either directly or indirectly; I will try not to forget anyone!

For having betted on a franco-portuguese guy during a single blinded Skype interview, I can only thank you Chris for giving me this fantastic opportunity to work with you and these amazing toys that are LiDARs. You gave me the freedom, the trust, the possibility to meet many researchers in the field and the chance to develop my own skills. That was invaluable to me, and I will always be grateful to you for that. I learned a lot from you, and I hope that we will keep learning together in the future! That might have to pass through some cooking lessons though, we can't survive on jacket potatoes (sorry it's already been a year and a half but I do remember my meals!).

My thanks go to Philippe Blondel and Hervé Michallet for accepting to be my internal and external examiners respectively. Besides the 'three French guys speaking English in a room' that was worth it on its own, we've had some really nice discussions that I hope will bring future collaborations and discoveries!

Thanks Natalie for introducing me to this magnificent world of nearshore processes, I will always be grateful. Although now, I can't walk into a beach without thinking of what is happening around... Nicholas, Rolf, this work was also made possible thanks to you. I learned a huge amount from you and your beautiful country; this motivated me to pursue my ambition of producing such work. I will always be grateful to you and the chance that you gave me!

Thanks to Jun and all the WEIRD'os, that was great.

To every one that I met on the way, by order (?) Pedro, Damien, Fred' et toute la team Rousty, Erwin, Rafael, Thuan, Guillaume, France, Charles et toute la team Vietnam, Jack, Brittany, Hannah (thanks guys for helping us surviving Saltburn...), Philippe, José, Patrício, Roberto, Anne and Harold, such amazing times spent in the field!

Pedro, era um prazer encontrarte. Aprendi muito contigo, e espero o melhor para ti e a tua família no Brazil.

Damien et toute la team Rousty, merci pour m'avoir aussi bien accueilli pendant les deux semaines. Quelque part, cette manip' et toutes les discussions qu'on a eues m'ont mis sur les rails de ma thèse. Sans vous, ça ne se serait sûrement pas passer de cette manière !

Erwin, even if you talk too much about video cameras, it was great to have both Andreia and you home, até ja meu! Ou devrais-je dire à bientôt maintenant ? ;) Sorry for the squash by the way...

Weooonnn! It was great to meet you and Coni, we had some great times really and I can't wait for the next ones! I hope very soon and these will be in French!

Mon Paulo, ça a été court mais bien bon, merci mec! Tu as été la ressource dont j'avais besoin pendant cette dernière année. Bonne route dans ton aventure à Bath, et j'espère qu'au final tu auras la même sensation que j'ai après ces 3 années !

Romain, Jojo, Steven merci d'être venu! Et merci les Toulousains pour avoir toujours été là quand je venais. La thèse est un exercice solitaire, et quand c'est en plus en Angleterre, et bien c'est pas toujours facile !

À ma famille, qui n'a pas toujours compris ce que je foutais ici pendant 3 ans, je ne suis pas sûr que vous lirez ces quelques lignes, mais je ne vous remercierai jamais assez de tout l'amour et le support que vous m'avez toujours donné. Mention spéciale à mamie et à son garage en ces temps uncertains.

Grazie alla familia Vellei e Di Benedetto ! Sono sempre stato benissimo ad Ascoli, anche alla fine fine del nostro lavoro. Non vedo l'ora del nostro prossimo viaggino, magari nel piu bello paese al mondo, chi sa qual'è?!

Eva, Manolis, bonne chance pour la suite de vos aventures où qu'elles soient ! Daniel, all the good luck for finishing your amazing work, and thanks for being Mari's work psychic at times where it was hard! Mariano, in bocca al lupo, e ci vediamo presto in Bordeaux! Elisabetta, ci vediamo in Cataaaania, non vedo l'ora di provare tutto quello che avete di buono. In boca al' luppo per il dottorato sei una persona bellissima! Mirella, ti ho gia scritto quello che penso e non c'ho le parole per esprimere la mia gratitudine.

Mia flora, grazie per tutto. Questa è anche la tua! Ed il futuro è nostro.

# Summary

In recent years, remote-sensing technology has become an essential tool for improving our understanding of nearshore processes. Although LiDAR (Light Detection And Ranging) scanners have been traditionally used for mapping nearshore or land areas, the application of terrestrial laser scanners to study swash zone hydrodynamics and morphodynamics was recently made possible thanks to the initiatives of few researchers. In this thesis, we explore the use of 2D LiDAR scanners to monitor the time-varying surface elevation of breaking waves in the surf zone. The surf zone constitutes one of the most challenging environments in which to deploy instruments, due to the energetic wave conditions often found there. Hence, obtaining complete wave profile measurements at a high sampling rate represents a huge potential for better understanding wave transformation in the surf zone.

In the present study, we first use data obtained from a tower-mounted LiDAR scanner deployed close to the shoreline to develop a new approach for studying inner surf zone waves at the wave-by-wave temporal scale. Waves are individually defined by extracting their crest and are then tracked until the shoreline. In combination with the Radon transform, we then apply this methodology to a numerical dataset of waves propagating and breaking in a prototype scale wave flume. This dataset illustrates the mechanism responsible for wave reflection in the nearshore: the reflected wave energy originates from the potential energy of the preceding swash event. The influence of these reflected waves on surf zone hydrodynamics is investigated at various temporal scales: the interactions between individual waves as well as the impact of the reflected wave field on the mean circulation in the surf zone are analysed and quantified.

The most innovative dataset used in this work was collected from a nearshore pier at Saltburn-by-the-Sea, UK, where an array of three LiDAR scanners was deployed above shoaling and breaking waves. A methodology to match the three LiDAR individual datasets into a unique dataset is proposed and a technique to detect the break point from the scanner measurements is also developed. The LiDAR scanners cover a maximum distance of about 100 meters in the cross-shore direction. This allows for an accurate description of the wave transformation at various stages: from the shoaling area, to the break point and through the inner surf zone until the runup in the swash zone. We finally present the first direct measurements of surface roller geometry in field conditions. These measurements in combination with a surface roller model shed light on the parameterization of energy dissipation in the inner surf zone, where waves propagate as fully developed bores.

# Contents

# List of Figures

# List of Tables

# Chapter 1

# Introduction

## 1.1 The surf-zone

In the nearshore region, waves break due to the decreasing depth and dissipate their energy through many physical processes such as the generation of turbulence and the entrainment of air into the water column. After the break point, waves propagate towards the shoreline in what is referred to as the surf zone. In this dynamic region where both broken and non-broken waves can be present, the breaking process greatly contributes, together with the tides and the wind, to the mean circulation of the nearshore. From their generation by the wind in deep water to the propagation and transformation into shallower regions, the mechanics of oceanic waves are very complex; as such, this problem has kept and will continue to keep scientists busy for many years. This is certainly the case for breaking waves, which are characterized by complex, rotational and highly turbulent flows. The collection of in situ measurements in the surf zone is also made very difficult due to the presence of bubbles generated from entrained air at breaking and the presence of suspended sediment in the water column.

Wave-induced hydrodynamics directly affect the beach, which is effectively the boundary between land and ocean. The multiple spatial and temporal scales at which the wave-induced hydrodynamics interact with the beach explain the complexity of nearshore morphological processes. An individual wave can pick up or deposit material on a beach face in a matter of seconds while the succession of storms in a region can change the shoreline over hundreds of kilometres for years. It is therefore vital to choose and define the temporal and spatial boundaries of the problem when studying the surf zone. Here, we are interested in the cross-shore transformation of individual waves, the geometrical changes that they experience and their influence on surf zone hydrodynamics at a temporal scale ranging from a second to a few wave periods.

The energetic conditions that are generally found in the surf zone (see Figure 1.1) and the lack of adapted in situ instrumentation have previously limited field investigations of nearshore waves. Hence, the understanding of coastal processes mainly originates from laboratory experiments (Svendsen et al., 1978) and visual observations in the field (e.g. Dyhr-Nielson and Sørensen, 1970; Cowell, 1982). With the improvements in infrastructure and instrumentation, a number of field deployments allowed for the collection of field data

Figure 1.1: Photograph of energetic conditions in the surf zone during a storm event: example from Rousty beach, France (Field experiments of Chapter 3).

that the entire coastal research community considerably benefited from; major field experiments include for example DUCK (Ebersole and Hughes, 1987), DELILAH (Birkemeier et al., 1990) and SUPERDUCK (Rosati et al., 1990) in the USA and more recently in Europe with the ECORS experiments (Sénéchal et al., 2011).

In field conditions, the sensors used to study the cross-shore transformation of surf zone waves generally consist of pressure transducers deployed near the sea bed and combined with current velocity meters. Depending on the relative cross-shore position on the beach, the traditional approach to retrieve the surface elevation assumes hydrostatic conditions (Stive, 1980; Sénéchal et al., 2001) or uses linear wave theory to correct for the depth attenuation of the signal (e.g. Guza and Thornton, 1980; Bishop and Donelan, 1987). However, the results reported in this thesis show that at the wave-by-wave scale considerable discrepancies in the wave profile (wave height and skewness) can be introduced when retrieving the surface elevation from a pressure signal in highly non-linear conditions such as those found around the break point. Alternative approaches to directly measure the time-varying surface elevation in the surf zone are therefore required. Using photopoles combined with video imagery, Suhayda and Pettigrew (1977) performed a step in this direction with the first visual measurements of individual wave properties in field conditions. Nonetheless, a large number of in situ sensors are required for measuring wave transformation over a long distance, meaning that the amount of information that can be obtained in the surf zone is generally restricted when using the traditional field instrumentation. This is especially true around the break point, where rapid changes occur over very short distances. A new methodology is therefore needed for obtaining high-resolution field measurements of breaking waves surface elevation.


Figure 1.2: Photographs of the macrotidal site of Saltburn-by-the-Sea, UK: a) aerial view of the pier and the beach and b) view from the beach, with close-up on the LiDAR scanner deployment (Courtesy of Brittany Bruder).

## 1.2 LiDAR technology to measure breaking waves

Irish et al. (2006) first investigated the use of LiDAR technology to monitor the time-varying surface elevation from the pier of the Field Research Facility (FRF) in North Carolina, US. Despite the good agreement obtained in the comparison of wave spectra with in situ sensors, field monitoring of nearshore waves using LiDAR technology was not pursued. Indeed, except until very recently, little attention has been given to this type of measurements (note that the experiments were performed in 1999). Blenkinsopp et al. (2010) explored further the capacity of a 2D commercial LiDAR scanner to monitor swash zone hydrodynamics, and from this study, the interest in this approach has continued to grow (Harry et al., 2010; Blenkinsopp et al., 2012; Brodie et al., 2012, 2015; Vousdoukas et al., 2014; Almeida et al., 2015; this thesis).

The strength of this innovative technology for wave monitoring first lies in its remote-sensing character: the scanner can be safely deployed and cover large distances at a better spatial resolution that can be achieved with in situ sensors. Secondly, its strength resides in its working principle itself: using the time of flight of a transmitted laser beam, it estimates the distance between any reflective surface and the scanner. By scanning hundreds of points in a 2D vertical plane, LiDAR scanners are capable of directly measuring wave geometry and its evolution in the cross-shore direction: no hypothesis/correction are required on the measurements, as is the case when pressure transducers are used. LiDAR technology therefore represents a great opportunity to obtain comprehensive surface elevation datasets of breaking and broken waves in the surf zone.

## 1.3 Research objectives and thesis outline

In the present work, we investigate and use the capacities of a 2D commercial LiDAR scanner (LMS511, SICK) to measure and study surf zone waves. In particular, we focus on the wave-by-wave temporal scale, as the scanner offers a unique possibility to directly

measure the geometrical characteristics of individual waves.

In the studies previously mentioned that used LiDAR technology, the scanners were deployed either from a dune or mounted atop a tower, see example in Figure 1.1 showing the deployment at Rousty beach (Chapter 3). Such deployment is limited by the tidal range experienced by the beach and the typical swash zone width. In macrotidal environments for example, the shoreline position is constantly and rapidly moving, hence posing serious safety issues and limitations for the cross-shore extent of the hydrodynamics data. In the primary experiment reported in this PhD, we overcome this limitation by deploying an array of LiDAR scanners from a nearshore pier in Saltburn-by-the-Sea, UK (see Figure 1.2). By carefully choosing the scanner locations, we demonstrate the possibility to study the cross-shore transformation of shoaling, breaking and broken waves throughout the whole surf zone. The innovative nearshore LiDAR deployment enabled the collection of a novel type of surface elevation dataset, hence requiring the extension of previous or the development of new methodologies to extract and study surf zone wave properties. To achieve these aims, the following research objectives and questions were formulated:

**Objective 1. Develop a new methodology to study individual surf zone wave properties in the high spatial and temporal resolution LiDAR datasets**

- How can we define individual waves in a surface elevation timeseries, and how do we determine their properties?
- Can we develop a new methodology to track the changes of individual wave properties across the surf zone, using high-resolution LiDAR datasets?
- What are the limitations or possible improvements of such an approach, i.e. are we sure incident wave properties are correctly measured independently of other processes? Can we develop an approach to accurately study incident wave properties?

**Objective 2. Obtain a new LiDAR field dataset of breaking and broken waves using the pier from Saltburn-by-the-Sea, UK (Figure 1.2)**

- How can we merge the datasets of three separate LiDAR scanners into a unique dataset?
- Can we quantitatively identify the break point using wave geometric properties as a proxy?
- How do these wave geometric properties relate at various temporal scales?

**Objective 3. Study the energy dissipation in the inner surf zone**

- How fast does a wave dissipate its energy in the inner surf zone?
- Can remotely-sensed breaking wave properties help us to model wave energy within the surf zone?

# Chapter 1.

The outline of this thesis follows the chronology of this PhD, which was mainly based on field experiments. **Chapter 2** introduces the reader to the concepts associated with surf zone wave processes and the methodology to measure these waves in field conditions. The working principle and the innovative aspects of LiDAR technology for wave monitoring are identified. The methodology to analyse the LiDAR dataset from the inner surf zone to the dry part of the beach is presented in **Chapter 3**; the scanner was deployed atop a tower at the microtidal site of Rousty, France. The temporal framework used for defining individual waves is also introduced. The scatter obtained in the different wave properties at the wave-by-wave scale illustrates the complex nature of the surf zone but also the limitations of the tracking algorithms in the presence of multiple physical processes (incident waves, reflected waves and low-frequency waves). In **Chapter 4**, we apply an improvement of the wave tracking methodology on the results from an OpenFOAM® CFD numerical model validated with an innovative LiDAR dataset of breaking waves. Using the Radon Transform (Radon, 1917), the influence of swash-based reflection on incident wave properties and surf zone hydrodynamics at the time-averaged scale is studied. **Chapter 5** describes the field experiment performed at Saltburn-by-the-Sea, UK, at which an array of three LiDAR scanners was deployed from the nearshore pier. The methodology to match the three individual scanner datasets is presented and a new method to detect the break point is developed. Using the previous wave tracking methodology, the geometrical properties of waves (skewness and asymmetry) are studied at several temporal scales. A link between surface and current velocity third-order moments is found. In **Chapter 6**, we present the first direct field measurements to date of surface roller length and angle. This data is used to investigate the energy dissipation rates in inner surf zone waves using the roller model of Svendsen (1984b). We show that in this part of the beach, waves generally dissipate less than hydraulic jumps of the same height. Finally, we conclude this study and propose a range of opportunities to solve some unanswered surf zone problems using these valuable datasets.

# Chapter 2

# Literature review

## 2.1 Introduction to nearshore waves

For more than a century, ocean waves have been studied by engineers, physicists, mathematicians, and yet, many mechanisms associated with their generation, growth, propagation or decay are still not fully understood. At most temporal and spatial scales, the complexity of the physical processes associated with waves limits progress in our understanding and hence capacity to predict or model them. After being generated in deep water under wind action, waves undergo a number of transformations that will affect their shape, the direction in which they propagate and the amount of energy that they transport. As water depth typically decreases closer to shore, waves break and dissipate most of their energy while propagating in the surf zone. In this dynamic region of the nearshore where both broken and unbroken waves can be present, in situ monitoring can be very problematic and hazardous (Puleo et al., 2016). This partly explains the scarcity of field-based datasets of breaking waves until improvement in nearshore infrastructure and instrumentation was made (e.g. Sallenger et al., 1983). Along with the development of innovative monitoring techniques such as remote sensing (e.g. Holman and Haller, 2013), a few comprehensive field experiments allowed for the collection of datasets that shed light on many aspects of wave transformation in the surf zone and the mean circulation that they induce.

Because of the rotational flows associated with breaking waves, the strong turbulence that they generate and the presence of air at various scales (from microscopic bubbles to air cavities), the fluid motions can only be described by the full Navier-Stokes equations. However, there exists no analytical solutions to these equations and despite the consistent improvements in computational resources, resolving these equations numerically (Direct Numerical Simulation, DNS) is a very demanding exercise that remains limited to very specific and idealized cases (e.g., see Deike et al., 2016). The description and understanding of surf zone waves hence necessitate parameterizations that simplify the complex physical processes and their interactions. Despite being only valid in deep water, some properties of linear wave theory (Airy, 1845; Stokes, 1847) are used in these surf zone parameterizations. It is therefore useful to review some of the concepts of linear waves, especially because some of the framework (whether in time or space) used to describe them are similar to those used for surf zone waves. It is worth mentioning that linear wave theory derives

from the Navier-Stokes equations, with some appropriate assumptions made on the flow and the wave characteristics. The derivation from the full Navier-Stokes equations of linear wave theory is considered beyond the scope of this study as extensive literature already exists. For more information on the derivation of linear wave theory, the reader is referred to more comprehensive texts such as Newman (1977), Dean and Dalrymple (1991), White (2003), Svendsen (2006) and Holthuijsen (2007).

### 2.1.1 General form and properties of cosine water waves

The linear solution to the water wave problem is the periodic (in both space and time) cosine function with the radian frequency $\omega$, the wavenumber $k$ and the amplitude noted $H/2$ for convenience:

$$\eta(x,t) = \frac{H}{2}\cos(kx - \omega t) \tag{2.1}$$

where $x$ and $t$ are the horizontal space and time coordinates respectively (see Figure 2.1). The water waves considered in the scope of this study are water motions of the form given in Equation 2.1, generated by the wind in the deep ocean. They are mainly characterized by the following parameters (see also Figure 2.1):

- the wave height $H$
- the wavelength $L$, related to the wavenumber through $k = \dfrac{2\pi}{L}$
- the wave period $T$, related to the radian frequency through $\omega = \dfrac{2\pi}{T}$
- the wave celerity $c$, expressed as follows $c = \dfrac{\omega}{k} = \dfrac{L}{T}$

An important relation between the wave period and wavelength exists and derives from the velocity potential at the free surface (see e.g. Newman, 1977; Dean and Dalrymple, 1991). Generally referred to as the dispersion relation, it relates the wave period, the wavelength and the water depth $h$ as follows:

$$\omega^2 = kg\tanh kh \tag{2.2}$$

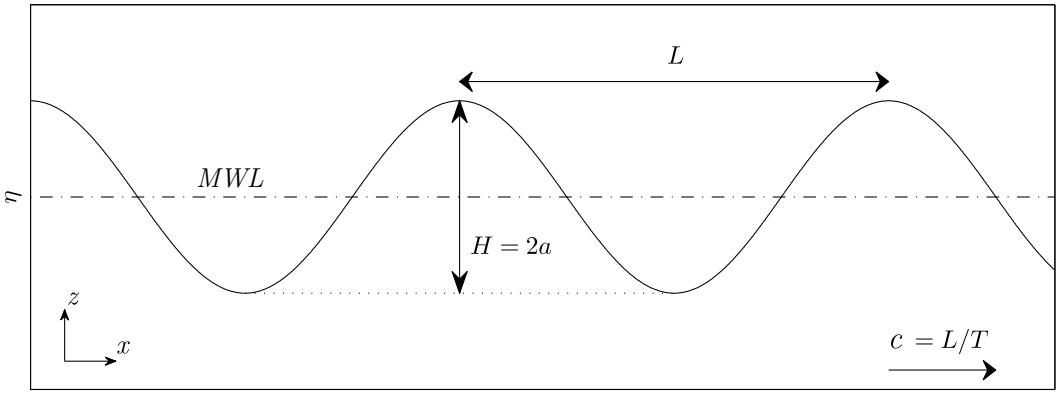


Figure 2.1: Spatial nomenclature of the cosine solution to the water wave problem: $L$ is the wavelength (distance between two crests), $H$ is the wave height (two times the wave amplitude) and $T$ the wave period (time elapsed between the passage of two crest at a certain location). *MWL* is a time Mean Water Level.

Some of the most relevant wave properties from linear wave theory are summarized in Table 2.1. For linear waves it is worth noting that both kinetic and potential energy are equal and take the value $\rho g H^2/16$, where $\rho$ is the water density and $g$ is the gravity constant. Equation 2.2 in particular explains the wave deformation for decreasing depth: $L$ decreases (the wave shortens) and $H$ increases since the energy is mostly conserved, although a fraction of it is dissipated through bottom friction.

Although the derivation of the solutions to the water wave problem is not described here, it is important to note the main hypothesis: the deep water condition is assumed, with the wave height very small against the wavelength $H/L \ll 1$. The monochromatic form of the considered wave (Equation 2.1) can appear unsuitable to describe the actual sea state, which is more complex, with steeper crested waves propagating in every direction. Nevertheless, the surface elevation at a single point can be decomposed into a multitude of these monochromatic motions (Holthuijsen, 2007; Ardhuin, 2012). A commonly used approach to decompose this irregular wave field is Fourier analysis, through the Fast-Fourier Transform (FFT). Spectral analysis leads to the wave Power Spectral Density spectrum (PSD), which provides the amount of energy contained at a given frequency (see example in Figure 2.2). Although some buoys in deep water are capable of estimating the direction of wave propagation, most PSD in nearshore applications are calculated only from the

Table 2.1: Summary of linear wave properties and their approximation to the first order.

| Parameter | Expression | Approximation (1st order) |
|---|---|---|
| Free surface elevation (m) | $\eta(x,t) = \frac{H}{2}\cos(kx - \omega t)$ | |
| Wave celerity (m/s) | $c = \frac{gT}{2\pi}\tanh kh$ | $\begin{cases} \text{Deep water:} & c = \frac{gT}{2\pi} \\ \text{Shallow water:} & c = \sqrt{gh} \end{cases}$ |
| Wavelength (m) | $L = \frac{gT^2}{2\pi}\tanh kh$ | $\begin{cases} \text{Deep water:} & L = \frac{gT^2}{2\pi} \\ \text{Shallow water:} & L = T\sqrt{gh} \end{cases}$ |
| Horizontal orbital velocity (m/s) | $u = \frac{\pi H}{T}\frac{\cosh(k(z+h))}{\sinh(kh)}\cos(kx - \omega t)$ | |
| Vertical orbital velocity (m/s) | $w = \frac{\pi H}{T}\frac{\cosh(k(z+h))}{\sinh(kh)}\sin(kx - \omega t)$ | |
| Energy per unit area | $E = \frac{\rho g H^2}{8}$ | |
| Energy flux | $E_f = \frac{1}{2}\left(1 + \frac{2kh}{\sinh(2kh)}\right)Ec$ | $\begin{cases} \text{Deep water:} & E_f = \frac{1}{2}Ec \\ \text{Shallow water:} & E_f = Ec \end{cases}$ |
| Pressure (Pa) | $p = -\rho g z + \rho g \frac{H}{2}\frac{\cosh(k(z+h))}{\cosh(kh)}\cos(kx - \omega t)$ | |

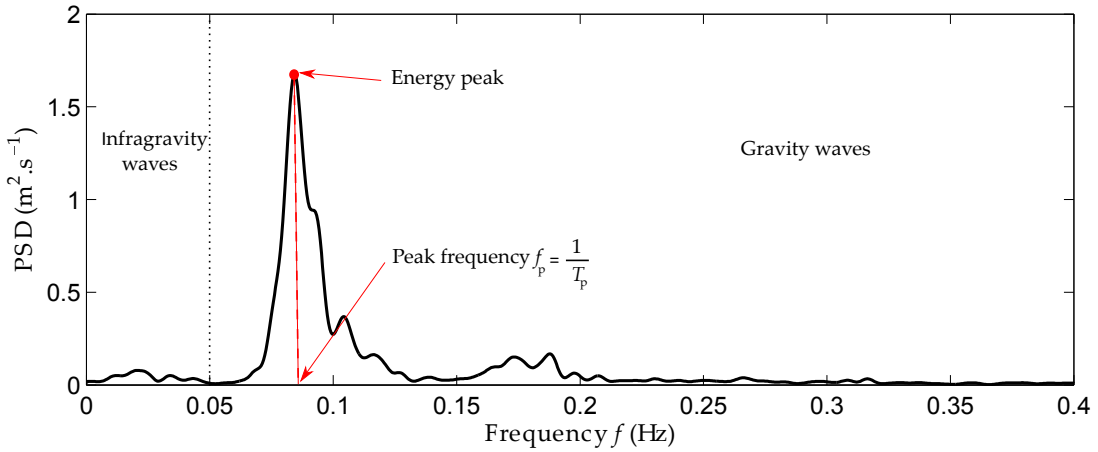


Figure 2.2: Example of Power Spectral Density (PSD) calculated from a surface elevation timeseries. The peak frequency $f_p$ (inverse of the peak period $T_p$) corresponds to the energy peak of the spectrum (shown in red). The boundary between infragravity and gravity energy (typically 0.05 Hz) is shown as dotted black line.

vertical displacements of the water column (e.g. from a pressure transducer), hence not giving any information about wave directionality. Ardhuin (2012) presents a methodology to calculate the PSD, and further details on the different wave spectra and related concepts can be found in Holthuijsen (2007) and Ardhuin (2012).

### 2.1.2 Gravity waves in real sea state conditions

While the representation of the sea state by a spectrum of cosine waves is adequate and can be well-modelled in deep water, the shape of individual waves in shallow water can considerably differ from a cosine wave. Typically, waves travelling in intermediate to shallow waters ($d/L < 0.5$) exhibit a sharper, steeper crest and a flatter trough (e.g., see Svendsen and Buhr Hansen, 1976; and example in Figure 2.3). When propagating over varying bathymetry, ocean waves are influenced by two principal processes: refraction and shoaling. Wave refraction is observed when a changing water depth exists along the wave crest (wave propagating in non-normal isobaths compared to the direction of propagation). The section of the wave in deeper water travels faster, which has the effect to make the wave propagate more shore-normal, dissipating a considerable amount of its energy at the same time. The decrease of wave celerity with decreasing depths (Equation 2.2) also makes the wavelength decrease and hence the wave height increase, since the wave energy flux is mostly conserved (Table 2.1). This phenomenon is referred to as wave shoaling and is responsible for the increase of the wave height up to the break point (Figure 2.3).

To describe the wave propagation in intermediate to shallow water, several theories were developed to overcome the limitations of linear wave theory (Hamm et al., 1993). Most derive from the Euler equations (e.g., see White, 2003), but use different assumptions depending on the local conditions. These wave theories comprise the non-linear Stokes theory, the cnoidal theory or the long wave theory with high amplitude (using the non-linear shallow water equations). Two parameters $\mu$ and $\gamma$ can be introduced to quantify the wave non-linearities and their range defines the validity region for these wave theories. Note that sometimes $\gamma$ is denoted as $\epsilon$ (e.g. in Tissier et al., 2011), after the extension in

shallow water of the non-linear parameter first introduced by Beji (1995). Although non-linear wave theories will not be further explored (extensive literature exists in reference such as Svendsen, 2006), it is worth defining the parameters here:

$$\mu = h/L \tag{2.3}$$

$$\gamma = H/h \tag{2.4}$$

One of the difficulties that arises when describing wave propagation at any depth resides in the hypothesis that waves do not change form. An example of wave propagation in the surf zone is presented in Figure 2.3 (data from Chapter 5) and show the wave shoaling until the break point: the wave height increases and the wave crest becomes sharper (Figure 2.3a). The skewed shape observed indicates the non-linear nature of waves up to the break point: the region of the wave around the crest travels quicker than the lower part meaning that the crest gets closer to the preceding wave trough than the one following. Right after the break point, the wave still exhibits an asymmetric profile with a sharp crest (Figure 2.3c),

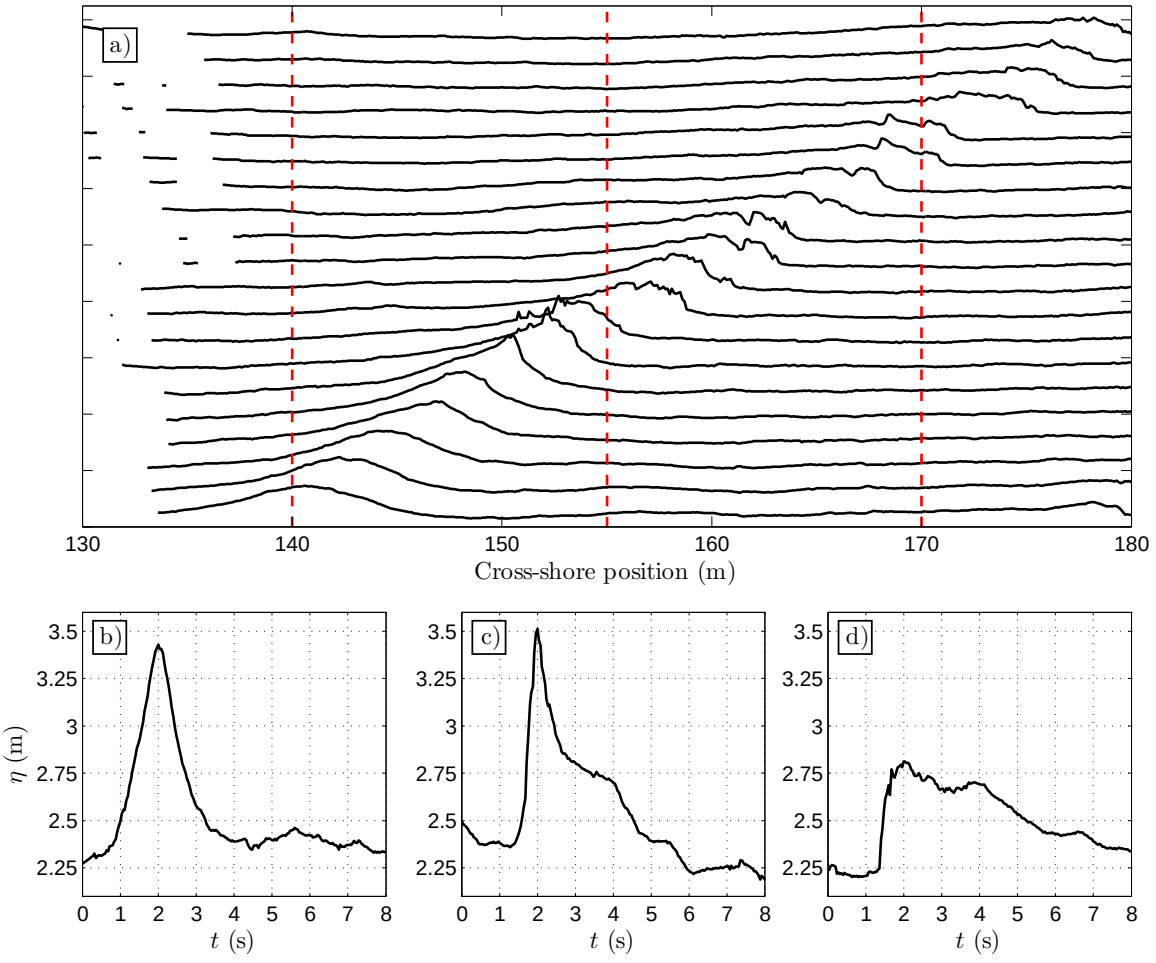


Figure 2.3: Example of shoaling and breaking wave profiles in the surf zone. Panel a) shows the evolution of the wave profile captured by a LiDAR scanner (the wave propagates from left to right). Panels b-d) show the surface elevation timeseries at three cross-shore locations: $x$ = 140, 155, and 170 m (shown as vertical red dashed lines in panel a), and illustrate the asymmetrical development of the wave profile.

with a steeper wave front but a flatter back. When the wave becomes a fully-developed bore (Le Méhauté, 1962; Svendsen et al., 1978), the commonly-assumed saw-tooth shape is clearly observed (Figure 2.3d): the wave front is steep and the back of the wave exhibits a negative gradient. The latter point is of importance as it is the main difference with the shape of a hydraulic jump, which is a concept often used to model the wave hydrodynamics in this region (Le Méhauté, 1962; Battjes and Janssen, 1978; Svendsen, 1984b).

### 2.1.3 Time-domain analysis of waves in deep and shallow water

Three principal methods have been used in the literature to define individual waves from surface elevation timeseries. These timeseries are generally obtained by wave buoys in deep water, and by in situ sensors such as pressure transducers in shallow water. The two traditional methods are the zero-up and zero-down crossing methods: individual waves are defined from the moment where the surface elevation crosses (either up or down) a certain mean water level (*MWL*; see Figure 2.4). The wave crest and trough are then defined as the maximum and minimum values respectively reached by the surface elevation. The two methods yield similar wave statistics if the surface elevation is a Gaussian process, however the zero down-crossing method is generally preferred as the wave height is visually estimated to be the distance between the crest and the precedent trough (e.g., see Holthuijsen, 2007, pp. 25-27).

The definition of a *MWL* in deep or intermediate water is not problematic as the low-frequency motions of the water column are either small relative to the wave height (infragravity waves) or occurring over a too long period of time for affecting the wave statistics (tides). It is however problematic in the shallowest part of the surf zone, where infragravity energy can be important (Power et al., 2010; Inch, 2014; Martins et al., 2016). A third approach was hence used in this study, and is based on local extrema analysis to extract individual wave crests from a timeseries (Power et al., 2010; Postacchini and Brocchini, 2014; Power et al., 2015). As illustrated in Figure 2.4, waves are defined from consecutive troughs.

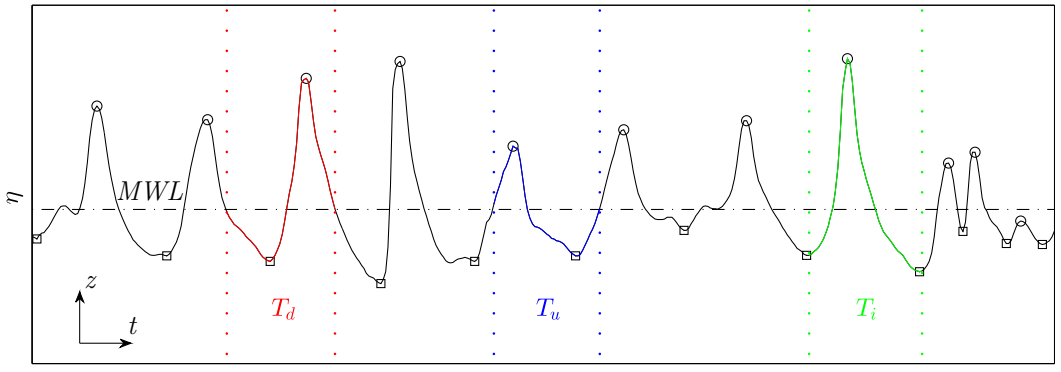


Figure 2.4: Illustration of the methods to define individual waves from a surface elevation timeseries. Two waves extracted with the down and up-crossing methods are shown in red and blue, respectively. A wave defined from the extrema analysis is shown in green, while the wave crest and trough are shown as black circles and squares respectively.

## 2.2 The surf zone

### 2.2.1 Generalities

The surf zone is defined as the part of the nearshore zone ranging from the break point to the shoreline. If we exclude tidal-dominated environments, surf zone processes are the primary driver of nearshore dynamics, both hydro- and morphodynamics, through the generation of currents and turbulence (e.g. Basco, 1983; Battjes, 1988; Deigaard, 1993; Longo et al., 2002). Prior to entering the surf zone, waves first travel in the shoaling area where they steepen and non-linearities in the wave profile become increasingly important. This is well-described by Sénéchal (2003) in terms of non-linear interactions between wave harmonics. These interactions are responsible for the changes observed in the wave profile: from a cosine wave in deep water to the wave shape observed in Figure 2.3b, with a steeper crest and flatter trough. This type of interactions is also visible at the passage of a wave above a submerged sand bar, even in the absence of breaking (Beji and Battjes, 1993; Sénéchal, 2003; Kuznetsov and Saprykina, 2012). This has direct implications on the mean wave period in the surf zone, and on wave energy dissipation modelling (Sénéchal et al., 2002; Hofland et al., 2017).

The surf zone initiates at the break point, where the wave height reaches its maximum, and is generally separated into two regions characterized by distinct wave transformation patterns and wave-breaking-induced hydrodynamics. The outer surf zone (see Figure 2.5) or transition zone (Basco and Yamashita, 1986; Nairn et al., 1990) extends from the break point to the so-called transition point, which is located five to ten times the wave height further landward (Basco, 1985; Svendsen, 2006). Breaking waves in the outer surf zone exhibit very rapid changes and are characterized by rotational and turbulent flows, with the presence of large vortices (Peregrine, 1983; Battjes, 1988; Svendsen, 2006). In contrast, broken waves (or quasi-steady bores, Svendsen, 1984b; Stive, 1984) propagating in the inner surf zone are associated to very slow geometric changes. The wide spectrum

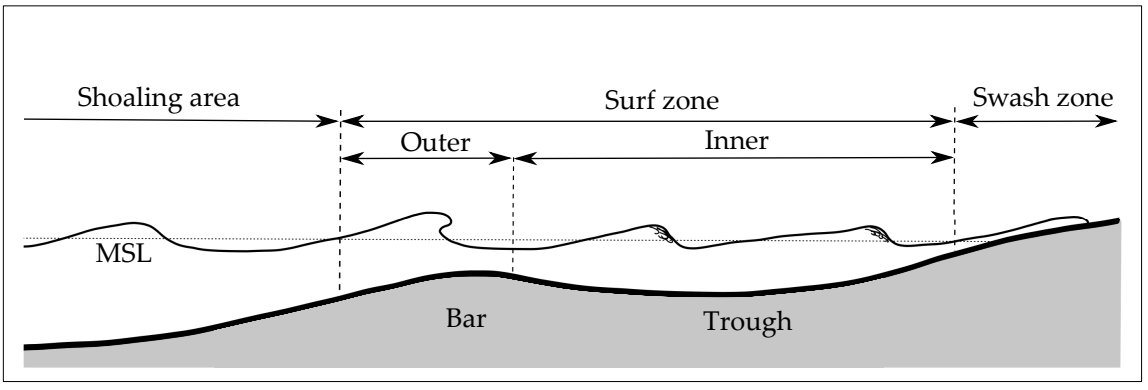


Figure 2.5: Terminology of the nearshore area according to Svendsen et al. (1978). The surf zone generally includes an outer region, where waves break and undergo rapid changes before developing into quasi-steady bores propagating in the inner surf zone, where their shape experience slow changes. The swash zone consists of the alternatively dry and wet area, where waves finish their uprush at the runup limit. Note that the simple bar/trough system chosen here only represents a fraction of the beach types observed in nature (Wright and Short, 1984).

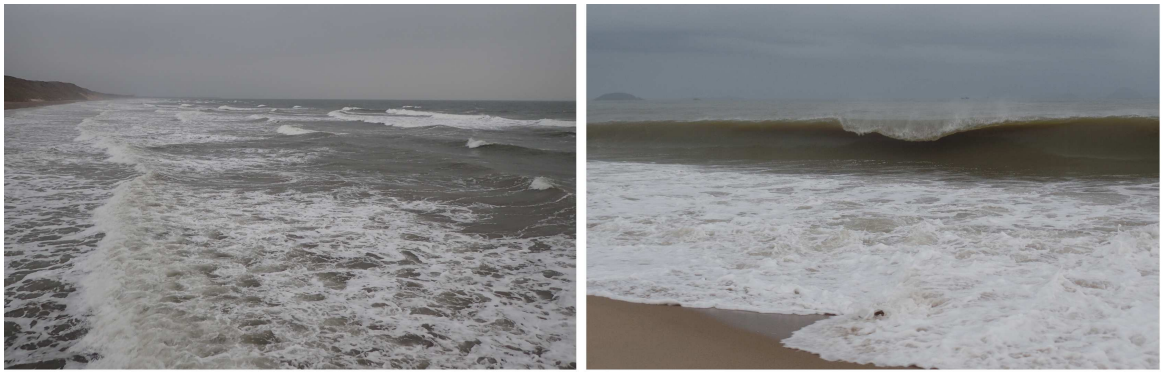

Figure 2.6: Photographs of spilling waves during the experiments at Saltburn, UK (left, taken by the author) and a plunging breaking wave during the experiments at Nha Trang, Vietnam (right, taken by the author). The height of the breakers were about 0.4-0.5 m and 1.2 m respectively.

of breaking types that exists between strongly plunging and spilling breakers make the identification of the transition point difficult. Theoretically, it is defined as the location where the surface roller - the turbulent mass of mixed water and air advected by broken waves - is fully-developed (e.g., Basco, 1985). The following sections aim at introducing the hydrodynamics and physical processes associated with the breaking of waves and their propagation as quasi-steady bores in the inner surf zone. The wave characteristics in the outer and inner parts of the surf zone are described, as well as the different energy dissipation regimes.

### 2.2.2 Outer surf zone: Break point and the transition zone

#### 2.2.2.1 Breaker types

If we exclude the collapse at the shoreline (e.g. for long waves or the bore collapse), three types of breakers are generally observed: spilling, plunging and surging. These are a function of the offshore wave conditions ($H_o$, $L_o$, $T$, where the 'o' subscript refers to offshore) and the beach slope $\tan\beta$ through the surf similarity parameter: $\xi = \tan\beta / \sqrt{H_o/L_o}$ (Battjes, 1974). This parameter is sometimes referred to as the Iribarren number, in recognition of the work done by the Spanish engineers (Iribarren and Nogales, 1949). In this study, we are more concerned about the plunging and spilling types of breaking, which are characterized by two distinctive mechanisms (see examples in Figure 2.6).

The plunging type of breaking occurs for $0.5 < \xi < 3.3$ (Battjes, 1974) and is probably the most spectacular of all breaking types as it involves the forward projection of the upper part of the crest when the wave initiates to overturn (see Figure 2.6), and the generation of large splashes. Between the break point and the moment at which the jet impacts the water surface in front of the wave, the wave travels the plunge distance (e.g., see Cowell, 1982; Grilli et al., 1997; Blenkinsopp and Chaplin, 2008; Peregrine, 1983 and the references therein). This is an important aspect of plunging breakers, especially for parametric models of breaking waves, as it means that there is a temporal and a spatial delay between the initiation of the overturning of the wave and the interaction between the jet and the free surface elevation in front of the wave (e.g., see Nairn et al., 1990). Depending on the plunger

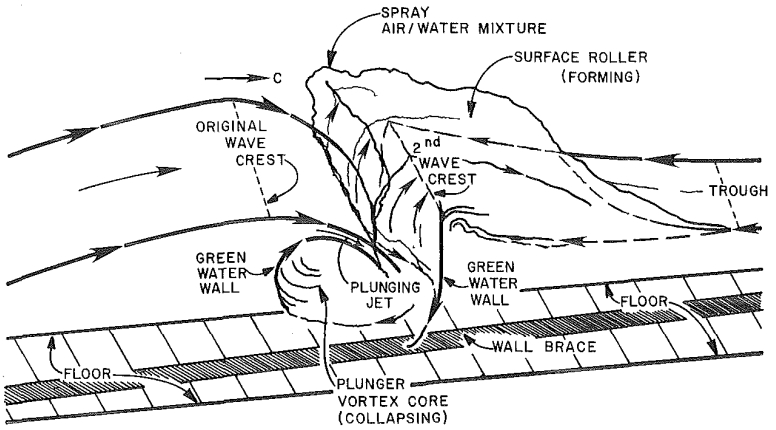


Figure 2.7: Schematic of strongly plunging wave, reproduced from Basco (1985). The rotational region of the wave (plunger vortex) and the region where the roller develops are of particular interest and labelled.

geometry, the jet impacts the free surface to form the splash: observations of this complex phenomenon show interactions ranging from an almost complete reflection of the jet to the complete penetration into the water column (Peregrine, 1983). The generation of this splash is accompanied by the generation of large vortices in the overturning region (Basco, 1985; Miller, 1986; Sakai et al., 1986; Lin and Hwung, 1992) which cause the entrainment of considerable quantities of air (see also Figure 2.7). Along with the energy losses due to viscous effects and the generation of turbulence (e.g., see Svendsen, 1987; Ting and Kirby, 1995; Grasso et al., 2012), the entrainment of air and the burst of air bubbles greatly contribute to the energy dissipation during wave breaking (Führboter, 1970; Nadaoka, 1982; Chanson and Jaw-Fang, 1997; Hoque and Aoki, 2005; Lubin et al., 2006; Blenkinsopp and Chaplin, 2007; Iafrati, 2011). To a minor extent, the generation of sound (Carey and Fitzgerald, 1993; Deane, 1997) and spray (see Wang et al., 2016 and the references therein) are also responsible for the energy decay of the breaking wave. After one or potentially several jet-splash cycles (e.g. Lubin et al., 2006), the surface roller forms from the impact point and gradually increases in size; its kinetic energy originates from the breaking wave potential and kinetic energy.

The spilling type of breaking occurs for $\xi < 0.5$ and is much more gradual than its plunging counterpart (Battjes, 1974). Originally thought of as a small-scale plunging breaker, it has been demonstrated that the spilling type of breaking is linked to the generation of ripples at the top of the crest, due to capillary effects (Lin and Rockwell, 1995; Duncan et al., 1999; Qiao and Duncan, 2001; Liu and Duncan, 2003). The breaking process initiates at the wave crest where masses of water slide downslope, entraining air bubbles, and generating turbulence spreading down into the water column (Duncan, 2001). As the overturning part of the wave keeps growing with the breaking intensity, this turbulence can potentially reach the bed in the surf zone (Peregrine and Svendsen, 1978). Spilling breakers at the initiation of breaking are not yet considered quasi-steady bores since, as stated before, the surface roller is not fully developed. This phenomenon is a function of the local water depth, and spilling breakers can be referred to as saturated or non-saturated (Le Méhauté,

1962; Divoky et al., 1970). In non-saturated breakers, the surface roller (active part of the breaker) occupies only a fraction of the wave face. Hence, they are expected to dissipate less energy than saturated - or fully-developed - breakers. This has direct implications for the energetic state of the surf zone and its description.

#### 2.2.2.2 Other characteristics of the outer surf zone

Despite their distinctive breaking patterns, both spilling and plunging waves evolve into similar quasi-steady bore-like shapes at the landward limit of the outer surf zone, with a steep active front and a flatter back in the inner surf zone (Svendsen et al., 1978, and see also Figure 2.3). However, Ting and Kirby (1995) and Ting and Kirby (1996) noted differences in some wave breaking-induced hydrodynamic features (Svendsen, 2006). These can be inferred to the different scales of the vortices generated by the overturning part of the breaking wave (Figure 2.7), which hence affects the quantity of turbulence which is transmitted down into the water column.

The notion of energy dissipation is thoroughly discussed in Svendsen (2006); he argues that it should be seen as a transfer to 'heat' energy through friction and the production of turbulent energy. The amount of energy released during the breaking process was found dependent on the breaking type, and considering the variety of processes associated with plunging waves (see previous section), more energy dissipation is expected for plunging and strongly plunging waves than for spilling waves. For instance, Blenkinsopp and Chaplin (2007) estimated that the air entrainment and splash generation accounted for at least 6.5-14% of the total energy dissipation, and the largest percentages were for plunging cases. Our understanding of this critical wave transformation phase is still quite limited; this can be explained by the difficulty in accurately measuring the different fluid phases (air, water and air/water interface) or the complex hydrodynamics in the breaking region. Despite the great efforts made in trying to simulate this complex process at all scales through DNS (e.g., Deike et al., 2016) or with the Reynolds-Averaged Navier-Stokes equations (RANS, e.g., Lin and Liu, 1998; Jacobsen et al., 2012; Higuera et al., 2013), these attempts are still limited to very idealized cases. The region where the surface roller develops is a highly turbulent and aerated region of the flow, which makes hydrodynamic measurements difficult. Efforts have been made to model the transition zone in a simpler manner; we can cite the efforts of Basco and Yamashita (1986), Nairn et al. (1990) and Kweon and Goda (1996). Although Nairn et al. (1990) proposed an empirical formulation based on the breaking surf similarity parameter (using monochromatic wave tests), the width of this zone remains one of the parameters that needs to be better quantified for a better description of the wave transformation and energy dissipation in this region.

### 2.2.3 Inner surf zone: Quasi steady broken waves

#### 2.2.3.1 Terminology

Landward of the transition point, waves continue their propagation in the inner surf zone as fully developed bores (Svendsen et al., 1978; Battjes and Janssen, 1978; Stive, 1984).

The changes in this region of the surf zone are typically slow as broken waves gradually dissipate their energy and only small changes in the global wave shape are expected (see example in Figure 2.8). However, it is sometimes observed that the wave stops breaking and 'reforms' when the local beach conditions suit it (e.g. in bar/trough system, Svendsen, 2006).

During his seminal experiments, Duncan (1981) studied the geometry of steady spilling breakers generated by a towed hydrofoil. To describe the surface roller geometry, he introduced a specific terminology that is slightly changed here so that it is consistent with the wave nomenclature introduced earlier. This surface roller terminology is presented in Figure 2.9, and is used throughout the thesis. The wave height is $H$ and corresponds to the vertical distance between the preceding trough and the bore head (equivalent to the wave crest in an unbroken wave). The roller angle $\theta$ is estimated from the wave profile around the breaking region. The roller length $L_r$ is defined as the horizontal distance between the breaker toe (lower limit of the surface roller) and the bore head. The roller region is a turbulent and rotational mix of air and water with an area $A$, contrasting with the irrotational motion of the wave. The wave has a local wavelength denoted as $L$, and defined as the distance between the two troughs surrounding the wave crest.

#### 2.2.3.2 Self-similarity in broken waves geometry

By adjusting the displacement speed and attack angle of the hydrofoil, Duncan (1981) generated a dataset with different values of wave celerity $c$, $H$, $L$ and $\theta$ (Figure 2.9). Two major results that are of interest for the present study were obtained from this dataset:

- Several relations linking the imposed wave celerity $c$ to different roller and wave geometric properties were found. Interestingly, only $c$ and the roller angle $\theta$ were independent parameters.
- The energy dissipation in the breaker is linked to the roller and wave geometries

Figure 2.8: Photograph taken in December 2016 of a propagating broken wave in the inner surf of the Quintero beach, Chile (taken by the author). The height of the broken wave is about 0.8 m.

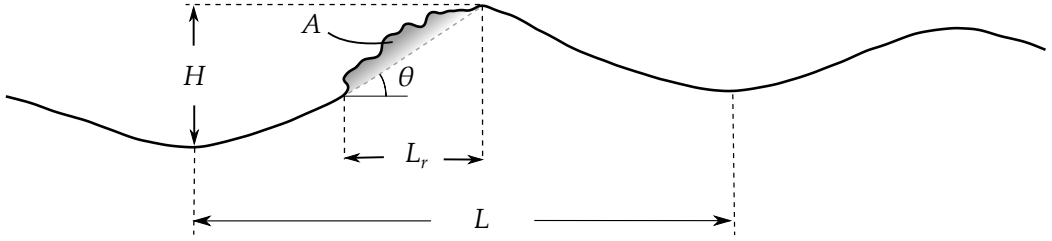


Figure 2.9: Sketch describing the terminology of surface roller properties, after Duncan (1981).

Duncan (1981) described the energy dissipation through shear stresses acting at the boundary between the roller and the underlying flow:

$$\tau = \frac{\rho_r g A \sin\theta \cos\theta}{L_r} \tag{2.5}$$

where $\rho_r$ is the roller density and $g$ is the acceleration due to gravity. The time-averaged energy dissipation rate is then given by:

$$D = \overline{\tau c} \tag{2.6}$$

where $\overline{(\,.\,)}$ is the time-averaging operator. This has important consequences as Equation 2.6 means that we can estimate the energy dissipation in a breaking wave from the geometrical properties of surface rollers. An important relation that Duncan (1981) found in this regard links the roller length to the roller area through:

$$A = 0.11 L_r^2 \pm 0.01 \tag{2.7}$$

Haller and Catalán (2009) used pixel intensity thresholds on processed timestacks from an ARGUS video camera system to estimate $L_r$ by separating the active part of the roller from the remnant foam. Additionally, the authors set up a roller model with the dissipation given by Equation 2.6 yielding relatively good agreement between measured and modelled roller lengths. However their model was hindered by a lack of measurements of other parts of the wave geometry: $H$ was measured at only 6 locations along the 90 m-long wave flume, and $\theta$ was taken as constant. There is also an uncertainty in the accurate detection of the breaking region: the use of pixel intensity thresholds to separate the back of the wave from the surface roller is very challenging (e.g., see Figure 2.8).

Carini et al. (2015) also used Equations 2.6 and 2.7 to estimate energy dissipation rates in the surf zone. The approach to estimate $L_r$ was similar to that used by Haller and Catalán (2009). However, they also tried to estimate $\theta$ using a single surface elevation timeseries through the following relation:

$$\theta = \arctan\left(\frac{H}{c t_w}\right) \tag{2.8}$$

where $t_w$ is the time elapsed between the passage of the preceding trough and the wave crest at the in situ sensor location (see also Zhang et al., 2014, 2017). $c$ was taken from linear wave theory as $\sqrt{gh}$ (Table 2.1), with $h$ the mean water depth. This assumes that

the wave does not change form over the duration $t_w$, which is a sensible approximation. However, it also assumes that the roller initiates at the preceding trough, which is much more questionable. Similarly amplitude dispersion is known to play an important role in the surf zone, meaning that waves travel quicker than linear wave theory predicts (Schäffer et al., 1993; Tissier et al., 2011; Martins et al., 2016). Zhang et al. (2014) presented cross-shore varying estimates of $\theta$ by re-analysing the dataset from Haller and Catalán (2009). They initiated $t_w$ at the up-crossing instant and used the celerity of a solitary wave instead, which is much more likely to yield accurate estimates. Zhang et al. (2014) found $\theta$ values at least twice that usually taken in the surf zone ($\tan\theta = 0.1$, $\theta \sim 5.7°$, Dally and Brown, 1995; Reniers and Battjes, 1997; Ruessink et al., 2001). Nonetheless, the applicability of Equations 2.5 and 2.6 still needs to be assessed for unsteady breakers in a natural surf zone and this is the subject of Chapter 6 of this thesis.

#### 2.2.3.3 Energy dissipation in the inner surf zone

Despite being applied in a few recent studies (Duncan, 1981; Haller and Catalán, 2009; Carini et al., 2015), Equations 2.5 and 2.6 are not the most common approach to predict energy dissipation in broken waves. This is mainly explained by the difficulty in measuring roller properties, and the lack of parameterizations for these parameters. In the most common approach to model energy dissipation in the surf zone, the resemblance between broken waves and bores is used: broken waves are assimilated to moving hydraulic jumps of the same height $H$ (Le Méhauté, 1962; Hwang and Divoky, 1970; Battjes and Janssen, 1978; Svendsen et al., 1978). The period-averaged energy dissipation per unit area has the following form:

$$D = \frac{B}{4}\rho g \frac{H^3}{hT} \tag{2.9}$$

The parameter $B$ can be regarded as a data-derived tuning coefficient that should be around 1 in the inner surf zone (Battjes and Janssen, 1978; Thornton and Guza, 1983 and other studies that are based on these models). $B$ can also be seen as an extension to irregular wave probabilistic models of the non-saturated breaker concept introduced by Le Méhauté (1962). The many successful attempts based on this approach showed that the energy dissipation in a surf zone breaking wave is close, but a-priori smaller than that of a bore of the same height (e.g., see Hwang and Divoky, 1970; Battjes and Janssen, 1978; Thornton and Guza, 1983; Svendsen, 1984b; Stive, 1984; Apotsos et al., 2008).

It is worth noting that this contradicts conclusions obtained by Svendsen et al. (1978) and Svendsen (1984b) that inner surf zone bores dissipate more energy than hydraulic jumps of the same height. Svendsen (1984b) suggests that the disagreement with previous studies can be attributed to the use of cnoidal or solitary wave theory for describing the wave energy flux in the surf zone. In a modelling attempt, if the initial energy flux is underestimated, energy can be dissipated at a lower rate to match the data than if the initial energy flux was correctly estimated. However, Svendsen et al. (2003) later demonstrated that the use of cnoidal theory accurately predicted the wave energy flux from the shoaling

region to the inner surf zone, for a given energy dissipation. This raises an important question that needs to be addressed and will also be looked further into in Chapter 6: how can the wave energy flux be modelled in the surf zone? In models of wave transformation, it is essential to accurately describe the wave energy flux in every region of the nearshore. Indeed, incorrect formulations of the wave energy flux in the surf zone for instance lead to the use of incorrect energy dissipation rates to match data, or the use of non-physical tuning factors.

Another approach to estimate energy dissipation in the inner surf relies on the fact that waves are often found to be depth-controlled (Thornton and Guza, 1982), i.e. waves are only a function of water depth (saturated conditions). Raubenheimer et al. (1996), Sénéchal et al. (2001), and Martins et al. (2016) also observed a strong dependency of the significant wave height $H_{m0}$ ($H_{m0} = 4\sqrt{m_0}$, where $m_0$ is the zeroth wave spectrum, e.g. see Martins et al., 2016) on the quantity $\tan\beta/kh$, which is a measure of the fractional change in water depth $h$ over a wavelength. However, these studies found different coefficients in the linear relationship between $H_{m0}$ and $\tan\beta/kh$, revealing the difficulties associated with the choice of frequency cutoffs for defining $H_{m0}$ (see also Sénéchal et al., 2001, and Salmon et al., 2015).

### 2.2.4 The swash zone

Except for very steep beaches where shore breaks can occur, waves dissipate the majority of their energy in the surf zone. The remaining fraction of the incident energy arrives on the shoreface and runs up the beach in what is referred to as the swash zone (see Figure 2.5, and Svendsen et al., 1978; Cowell, 1982; Svendsen, 2006). This region of the beach, where oscillations of the surface elevation can no longer be described as waves (Svendsen, 2006), exhibits complex, rapid and turbulent flows (e.g. Puleo et al., 2003; Butt et al., 2004) promoting high sediment transport rates both in the cross-shore and alongshore directions (Elfrink and Baldock, 2002; Masselink and Puleo, 2006). This makes it one of the most dynamic zone of the nearshore region.

The complexity of the processes in the swash zone and the multiple temporal scales at which they occur forced for a long time the research community to study this region of the beach in an isolated manner, although it is known to be intrinsically linked and coupled to the inner surf zone and potentially to the dune system (e.g. Puleo and Butt, 2006; Brocchini and Baldock, 2008). For instance, strong interactions between incident waves and backwashes are characterized by more important energy dissipation rates that lead to reduced runup for the incident waves (Pujara et al., 2015; García-Medina et al., 2017), but also to more suspended sediment in the water column, which affect the amount of suspended sediment entering the swash zone (e.g., see Alsina et al., 2009; Alsina and Cáceres, 2011). The difficulty in measuring and quantifying the hydrodynamic features of wave-wave interactions at the inner surf/swash zone boundary means that defining the correct boundary conditions to the swash zone remain one of the most challenging problems in the modelling of nearshore hydro- and morphodynamics (Brocchini, 2006; Guard and Baldock, 2007; Alsina et al., 2009). For more recent reviews of swash hydro-

and morphodynamics processes and their numerical modelling, the reader is referred to Chardón-Maldonado et al. (2016) and Briganti et al. (2016).

Further than the complex interactions occurring at the boundary between the inner surf and swash zones, wave reflection is another hydrodynamic process that has been quite overlooked in natural swash zones. Incident broken waves continue to dissipate their energy during the uprush phase, mainly by generating turbulence and through friction (e.g., see Puleo and Holland, 2001; Longo et al., 2002; Elfrink and Baldock, 2002). However, only a fraction of it is dissipated, and the masses of water end up running down the beach face during the backwash. Similarly, part of the backwash energy might dissipate, e.g. through wave-backwash interactions (Erikson et al., 2005; Alsina et al., 2012; Pujara et al., 2015), but the remaining part of the energy travels back into the surf zone, which explains the presence of reflected energy at the incident wave frequency (Elgar et al., 1994; Almar et al., 2014b). Very early, engineers have studied wave reflection from structures (e.g. breakwaters and sea walls) as it is an essential aspect of harbour and ports designs (Iribarren and Nogales, 1949; Miche, 1951; Battjes, 1974; Goda and Suzuki, 1976). Wave reflection processes in the low-frequency ($f < 0.05$ Hz) part of the spectrum have also been investigated on natural beaches (e.g. Suhayda, 1974; Guza and Bowen, 1976; Huntley, 1976, and many other studies). Many studies suggested an influence of the presence of reflected waves on beach morphodynamics at various spatial scales, from the generation and spacing of sand bars (Short, 1975; O'Hare and Davies, 1993; Sánchez-Badorrey et al., 2008) to the generation and migration of ripples (Cobos et al., 2017, and the references therein). However, only few studies on wave reflection processes in the sea-swell part of the spectrum are reported (e.g., see Elgar et al., 1994; Baquerizo et al., 1997). Although the role of the beach slope on wave reflection has been studied, e.g. via its signature in swash spectra (Miche, 1951; Huntley et al., 1977; Mizuguchi, 1984; Hughes et al., 2014), reflection processes at the wave-by-wave scales are still not well understood. This will be further looked at in Chapter 4 of this thesis.

### 2.2.5 Measuring waves in the surf zone

Although this might be an over-simplification of the concept, the problem of measuring waves can be reduced to our capacity in detecting the air/water interface. In this regard, a wide range of techniques exists for both field and laboratory environments; these techniques can be intrusive with sensors deployed either under the water or at the surface, or can employ remote sensing technology. Here, we review the principal methods that have been used in field conditions for nearshore wave monitoring.

The most common technique for measuring nearshore waves in the field consists of deploying pressure transducers (PT) in the lower part of the water column (see example of the deployment of a PT in Figure 2.10a). The first use of PTs for wave monitoring dates from the 1940's (Folsom, 1947; Seiwell, 1947); after these two seminal studies, this type of sensors have been increasingly used to study wave propagation in the nearshore (Homma et al., 1966; Esteva and Harris, 1970; Grace, 1978; Cavaleri, 1980, and many others).


Figure 2.10: Photographs of one in situ and one remote sensing instruments: a) example of pressure transducer deployed close to the sea bed in the macrotidal environment of Saltburn; and b) example of camera deployement for coastal monitoring (Photos taken by the author during the field experiment presented in Chapter 5).

To retrieve the surface elevation signal, a correction to the dynamic pressure is generally applied using linear wave theory to account for depth attenuation of the signal (second term in the pressure field, see Table 2.1). While various factors (e.g. $n$ in Esteva and Harris, 1970) have been proposed to correct for errors associated with this method, Bishop and Donelan (1987) suggests that differences as low as 5% of the wave height could be expected. After the break point, the hydrostatic condition is generally applied (e.g. Stive, 1980; Sénéchal, 2003, and the references therein).

As part of the Nearshore Sediment Transport Study (NSTS), extensive field experiments were conducted to study wave transformation from the shoaling area to the swash zone by deploying PTs and current meters along with wave staffs, used to visually estimate wave heights (Seymour and Duane, 1978; see also e.g. Thornton and Guza, 1986). Similarly, the DUCK85 study (Ebersole and Hughes, 1987) included an experiment in which 14 photopoles (round poles with marked dimensions) were deployed every 6 m across a beach and videoed using six synchronised cameras, following Hotta et al. (1982). Despite the presence of poles in the water, the wave measurement is based on remote sensing from the camera. Because of their footprint (limited by their resolution) and the spatial extent of the zone that they cover, video camera systems are traditionally used for large spatial scale and long term monitoring applications (see example of the deployment in Figure 2.10b) such as mapping nearshore bar morphology (e.g. Lippmann and Holman, 1989) or to retrieve bathymetric information (e.g. Catálan and Haller, 2008; Holman et al., 2013). However, they have been recently applied to indirectly measure breaking wave properties using assumptions on the wave geometry (Almar et al., 2012; Shand et al., 2012; Carini et al., 2015). Using complex image geo-localisation procedures, a combination of two cameras were also used to reconstruct in 3D the surface elevation field offshore (Bergamasco et al., 2017), and in the surf (Vries et al., 2011) and swash zones (Astier et al., 2012). These indirect reconstructions of the surface elevation in 3D have great potential for surf zone waves

studies as the longshore variations in energy dissipation rates are often overlooked.

Although more appropriate for controlled environments such as in laboratories, techniques based on capacitance and resistance type of wave probes have been used in field conditions to measure wave runup (e.g. Guza and Thornton, 1982). Ultrasonic acoustic sensors have also been used with success to study swash zone dynamics (Turner et al., 2008; Blenkinsopp et al., 2016). These sensors are capable of accurately measuring (accuracy of $O$(mm)) swash event depths and bed level changes at the wave-by-wave scale (see also Blenkinsopp et al., 2011). However, a large number of them is required to cover the whole beach face. The first deployments of 2D LiDAR scanners for swash zone monitoring (Blenkinsopp et al., 2010; Brodie et al., 2012) demonstrated the possibility to obtain high spatial resolution measurements of both wave and beach profiles with a single instrument. As hundreds of points per wave or beach profile are measured at a high sampling rate, they have to potential to be used to investigate hydro- and morphodynamic processes in the swash zone at a much finer scale than before.

LiDAR scanners constitute a relatively new technology for monitoring waves in the nearshore, which opens up the possibility to look at field data in a novel way. This remark can be generalized to the instrumentation used nowadays for studying nearshore processes, especially regarding remote sensors. Since the very first field studies, in situ instrumentation and remote sensors generally improved, meaning that more comprehensive and more accurate measurements of waves can be performed. Thanks to the ever-increasing computational capacities, new and more robust post-processing techniques are also developed and can be applied to the collected datasets. To conclude this part and prior to focus on LiDAR scanners, we refer the reader to more comprehensive texts on the monitoring of nearshore processes such as Holman and Haller (2013) and Inch (2014); note that LiDAR scanners are not treated in these studies.

## 2.3 LiDAR scanners in nearshore waves studies

### 2.3.1 Introduction to LiDAR technology

LiDAR scanners (see Table 2.2 for a list of abbreviations used hereafter) are remote sensors that use a pulsed laser beam and its reflection from an object (surface, substance or material) to estimate the distance between the two. It uses the time of flight technique: knowing the speed of light, the distance between the scanner and the object is calculated using the time required for the pulsed laser to be backscattered to the scanner. Depending on the application, the wavelength $\lambda$ varies from the ultra-violet to the infra-red spectra.

LiDAR technology was initially developed to detect particles in the atmosphere (National Oceanic and Atmospheric Administration (NOAA) Coastal Services Center, 2012), it was also used to measure the distance between the Earth to the Moon (Smullin and Fiocco, 1962) and to map the Moon's surface (Abshire, 2010). Nowadays, its application range has widened to much more diverse fields: from industrial use and morphology studies (*e.g.* cliff erosion monitoring) to benthic species mapping and vegetation detection (see for example Brock and Purkis, 2009; Reineman et al., 2009). Hence, in the following, we only

aim at presenting the evolution of LiDAR technology for nearshore wave measurement.

### 2.3.2 Airborne LiDAR

Following the invention of GPS in the late 1970's, mobile remote sensing systems comprising LiDAR and GPS have been used for a range of applications. Airborne LiDAR for example started to be used as a surveying system for coastal topography and for nearshore bathymetry (Allis et al., 2011). For this application in particular, wavelength in the green spectrum was used ($\lambda$ = 532 nm) as it corresponds to one of the least absorbed wavelength by water. This choice naturally enhances the penetration potential of the LiDAR, and thus the extent where this surveying method can be used.

A new field of investigation was opened when Hwang et al. (1998) used both LiDAR and RaDAR scanning devices to study wave propagation over the continental shelf off Duck, NC. In the study by Hwang et al. (1998) the method used for the LiDAR mapping was originally designed by the NASA and EG&G Technical Services and consists of a conically scanning LiDAR (Reineman et al., 2009). Due to the shape of the scanned profile and the sampling rate, gaps up to 2 seconds can exist between the LiDAR profile edges and its centres (phenomenon known as Doppler effect). After their first attempt, Hwang et al. (2000a,b) used another LiDAR dataset that was corrected for the previously mentioned Doppler effect, to retrieve the wavenumber spectra and study the distribution of wave directions. In particular, comparison of the wavenumber spectra from the LiDAR with that of an offshore buoy showed very good agreement. The main advantages of the LiDAR are the high spatial resolution; this allows for a much better description of the directional energy spreading compared to classic wave buoys, and similar vertical accuracy (Root-Mean Square Error, *RMSE* of 0.08 m, obtained with GPS comparisons). Similarly, Sun et al. (2005) investigated the potential of a wavelet analysis on data obtained with the same type of system. Vrbancich et al. (2011) measured waves with a 10 cm-accuracy in the surf zone of a beach located on Kangaroo Island, Australia. Although this method just provides a snapshot of the local conditions and is therefore not adapted for long term monitoring, it demonstrated the potential for using a LiDAR to measure waves in the surf zone.

In summary, airborne LiDAR is a powerful remote-sensing tool, which can be used for a wide range of applications (e.g. Brock and Purkis, 2009): coastal morphodynamics and hazards, vegetation detection but also for benthic topography. However, for long-term monitoring and temporal evolution of local wave conditions, this is not an ideal system as

Table 2.2: List of abbreviations used for the remote-sensing and mapping technology in this thesis

| Abbreviation | Meaning |
|---|---|
| GPS | Global Position System |
| LASER | Light Amplification by Stimulated Emission Radiation |
| LiDAR | Light Detection And Ranging |
| RaDAR | Radio Detecting And Ranging |
| TLS | Terrestrial Laser Scanner |

the plane is in constant movement. Instead, a fixed terrestrial laser scanner seems more adequate.

### 2.3.3 LiDAR scanners used for nearshore wave monitoring

As previously mentioned, local and ground-based deployments of LiDAR scanners in nearshore areas seem more adequate in order to obtain comprehensive measurements of surf zone waves. In this regard, Irish et al. (2006) performed what is thought to be the first-ever nearshore wave measurements from a tower-mounted LiDAR scanner. A 4-rangefinder LiDAR was mounted atop a tower on the Field Research Facility pier (FRF), NC, to investigate the potential of this instrument for measuring nearshore waves. A directional wave spectrum was calculated using the slope array method (Borgman, 1979 and Longuet-Higgins et al., 1963 in Carvalho and Parente, 2000), and the wave parameters compared favourably with in situ data (pressure transducer). Since the experiments of Irish et al. (2006), performed in 1999, the use of nearshore deployment of LiDAR scanner remained scarce until the study of Blenkinsopp et al. (2010) in a natural swash zone. Deploying three different models of 2D scanners, Blenkinsopp et al. (2010), Brodie et al. (2012) and Almeida et al. (2015) all demonstrated the capacity of LiDAR technology to accurately measure swash zone hydrodynamics and morphodynamics at high spatial resolution. In contrast to traditional instrumentation (pressure transducers or ultrasonic sensors), the strength of LiDAR scanners reside in their capacity to capture highly detailed 2D profiles of the waves, at a high sampling rate (Blenkinsopp et al., 2010).

A few attempts to capture the surface of breaking waves and estimate their height in natural surf zones were also performed with 3D LiDAR scanners (e.g. Harry et al., 2010). Despite successfully capturing the wave geometry, the time spent by the scanner to scan in the alongshore direction was a major drawback as it introduced a time shift in the wave crest location in the alongshore direction, similar to the Doppler effect previously mentioned for airborne LiDAR. Their conclusion was that a 2D LiDAR scanner might be a better alternative to measure the wave profile in the cross-shore direction. Park et al. (2011) also used a 3D LiDAR scanner to measure breaker heights. They compared the scanner data with visual measurements performed with a vertical staff; a relatively good agreement over the 26 measured waves was obtained, with a Root Mean Square Error (RMSE) of 5 cm. Combined with a video camera, a mobile 3D scanner fixed on an automated robot could be used by Wübbold et al. (2012) to measure broken wave heights and propagation speed. A similar video and 2D LiDAR system was carefully calibrated in laboratory conditions by Vousdoukas et al. (2014). Besides being able to monitor individual waves propagating in the inner surf zone, the combination of the two remote sensors allow for a better calibration of the video imagery geo-rectification. Overall, the precision of 2D LiDAR scanners for wave monitoring in the inner surf and swash zone was found lower than that of ultrasonic altimeters, but their ability to capture small scale features thanks to the high spatial resolution and small footprint compared to other remote sensors make this instrument a powerful tool for obtaining detailed measurements of wave transformation.

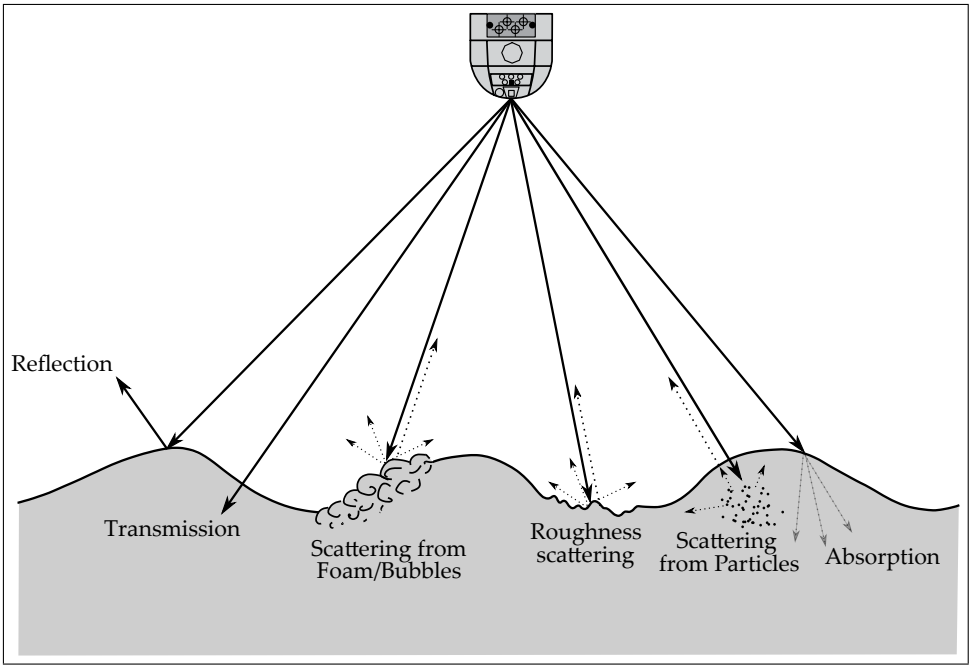


Figure 2.11: Variety of laser interaction with the water environment (inspired from Howe, 2016).

### 2.3.4 Working principle of the LiDAR scanner for wave measurements

For the LiDAR scanner, the surf zone represents a diverse environment as in a single profile, the pulse laser potentially interacts with wave-generated foam, clear water, turbid water due to high sediment concentration and the dry beach. Figure 2.11 shows the nature of the different interactions that the laser beam can have with the water. If we exclude the specular reflection at the nadir, the three types of interaction where a signal is actually returned to the scanner are: 1) scattering from foam or air bubbles at the surface produced by a source of aeration; 2) scattering from the free surface roughness (presence of ripples at the interface between air and water or on a solid surface); 3) scattering due to the presence of particles in the water column, known as the Tyndall effect (Tamari et al., 2016). The level of absorption depends on the wavelength employed: it is minimum for the lower part of the visible spectrum (blue/violet) and increases with increasing wavelength.

Previous studies (Blenkinsopp et al., 2010; Evans, 2010) have shown that an aerated and turbulent water surface is required for the laser to be sufficiently scattered to enable detection by the instrument. The type of scattering in most of the studies previously cited naturally corresponds to a mix between scattering from foam and bubbles present at the sea surface due to breaking waves and scattering from the surface roughness (Blenkinsopp et al., 2010; Evans, 2010; Harry et al., 2010; Wübbold et al., 2012; Brodie et al., 2012; Vousdoukas et al., 2014; Almeida et al., 2015). In laboratory conditions however, the surface is generally much smoother, and even with wave breaking events, air bubbles persist much less in freshwater than in saltwater conditions (Blenkinsopp and Chaplin, 2011). In the absence of bubbles and in clear water conditions, the laser signal can be absorbed or penetrate through the water to some depth and be scattered by suspended particles, as it was the case in Streicher et al. (2013) (see the explanation in Martins et al., 2017a). To avoid this issue, the

water turbidity can be locally increased so that the laser signal does not penetrate the water column. Allis et al. (2011) and Blenkinsopp et al. (2012) achieved this by adding kaolinite particles; a turbidity level of 40 NTU was found necessary to ensure sufficient accuracy in the surface elevation measurement.

Environmental conditions (luminosity, air humidity, wind) also have a direct or indirect impact on the scanner measurement quality (e.g. Soudarissanane et al., 2009). Hence, they have to be accounted for during field deployments. While the influence of humidity or water drops on the screen - represented by noise or spikes in the data - can be corrected, under strong wind conditions the scanner system (e.g. deployed on a tower or a scaffolding structure) can become too unstable for the data to be used. Indeed, while the error made by the instrument used in this study is typically of the order of millimetres, small oscillations of the mounting system lead to larger errors that increase with distance from the instrument and can be of the order of dozens of centimetres at the edges of the measured profile.

# Chapter 3

## Monitoring individual wave characteristics in the inner surf with a 2-Dimensional laser scanner (LiDAR)

Kévin Martins, Chris E. Blenkinsopp*, and Jun Zang, "Monitoring Individual Wave Characteristics in the Inner Surf with a 2-Dimensional Laser Scanner (LiDAR)", Journal of Sensors, vol. 2016, Article ID 7965431, 11 pages, 2016. DOI: 10.1155/2016/7965431

## Abstract

This paper presents an investigation into the use of a 2-dimensional laser scanner (LiDAR) to obtain measurements of wave processes in the inner surf and swash zones of a microtidal beach (Rousty, Camargue, France). The bed is extracted at the wave-by-wave timescale using a variance threshold method on the time series. Individual wave properties were then retrieved from a local extrema analysis. Finally, individual and averaged wave celerities, are obtained using a crest-tracking method and cross-correlation technique respectively, and compared with common wave celerity predictors. Very good agreement was found between the individual wave properties and the wave spectrum analysis, showing the great potential of the scanner to be used in the surf and swash zone for studies of nearshore waves at the wave-by-wave timescale.

# Chapter 3.

## Declaration concerning the article used for this Chapter:

| | |
|---|---|
| Title | Monitoring individual wave characteristics in the inner surf with a 2-Dimensional laser scanner (LiDAR) |
| Status | Published and available in Open Access in Journal of Sensors (Hindawi): Special Issue (2016) "Sensors for Coastal Monitoring" |
| Details | Kévin Martins, Chris E. Blenkinsopp*, and Jun Zang, "Monitoring Individual Wave Characteristics in the Inner Surf with a 2-Dimensional Laser Scanner (LiDAR)", Journal of Sensors, vol. 2016, Article ID 7965431, pp. 1-11, 2016.<br>DOI: 10.1155/2016/7965431 |
| Contribution from the authors | K. Martins: Collection/Processing/Analysis of data; Manuscript (75%)<br>C.E. Blenkinsopp: Assistance with analysis of data; Edited drafts of manuscript (20%)<br>J. Zang: Edited drafts of manuscript (5%) |
| Statement | This paper reports on original research I conducted during the period of my Higher Degree by Research candidature. |
| Date and Signature | |

## Preamble

The data presented in this chapter were collected during the major nearshore experiments performed at the Rousty beach (Camargue, France) and led by a collaboration of three French research institutions: MIO (Institut Méditerranéen d'Océanologie), CEREGE and Géosciences Montpellier. The principal objectives were to study the role of groundwater dynamics on swash and surf zone hydrodynamics and morphodynamics, at various temporal scales (Sous et al., 2016).

This field campaign was undertaken at an early stage of my PhD studies and hence provided an ideal opportunity to develop new methodologies related to the measurement and study inner surf zone waves at various temporal scales using a LiDAR scanner. The model used here is a SICK LMS511 commercial 2D LiDAR (see Figure 3.P1); a common application for this type of scanner is the detection of objects or volumes such as containers in ports, for automated processes (SICK, 2015). The instrument contains an internal mirror which rotates at high frequency (25 to 37.5 Hz were used in the studies reported in this thesis) to achieve laser range measurement over a 190° scan angle with an angular resolution of 0.1667°. Thus several hundred measurements of elevation along a water surface/exposed beach profile can be measured at high frequency with a theoretical accuracy of ±5 mm.

As the main focus of this thesis is on surf zone waves, the lack of infrastructure at the microtidal site of the Rousty beach raises a critical question for the remainder of the project to be answered: how and where can the scanner be efficiently deployed for the duration of a storm event on a beach lacking infrastructure? The approach adopted here was to deploy the LiDAR scanner atop a tower buried in the sand. Due to the effective range of the scanner, both the swash and the inner surf zone could be captured. Methods to study the swash zone, in particular the separation of dry beach and swash measurements, were already in development and reported in the literature (e.g., Almeida et al., 2013; Almeida

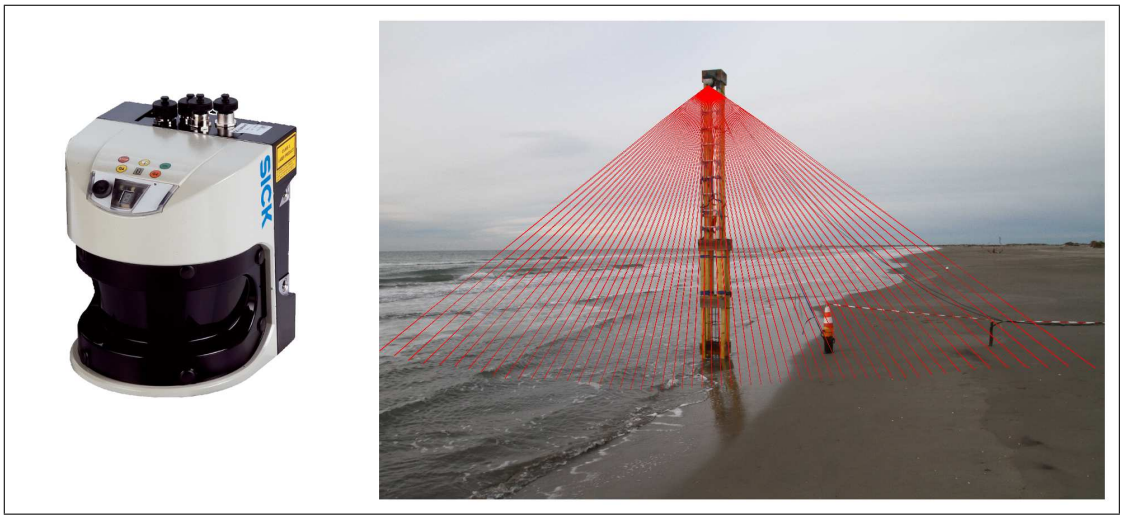


Figure 3.P1: Photographs of the SICK LMS511 used in the studies reported in this thesis: left, a close view reproduced from Howe, 2016 and right, the deployment atop a tower from the Rousty experiments (this Chapter). The red lines were added to illustrate the working principle of the scanner (scanning in a 2-dimensional vertical plane).

et al., 2015). However, new approaches had to be developed to extend these methods to inner surf waves. In the present Chapter, the following research objectives/questions were addressed:

- Development of a new methodology to enable wave-by-wave analysis of the properties of surf zone waves and the corresponding beach evolution.
- Validation of the wave-by-wave analysis with classic spectral methodology
- Discussion of the newly acquired understanding of inner surf zone waves in the context of previous work.

Brodie et al. (2012) presented the first time-averaged wave measurements from the inner surf zone of a sandy beach using a dune-mounted LiDAR. No validation with in situ sensors was presented, hence the quality of the data at the wave-by-wave scale is uncertain considering the low sampling rate used (2 Hz) and the gaps present in their dataset due to the high incidence angle (e.g. their Figure 2). Here, we present a more detailed dataset of waves from the inner surf and measurements of swash hydrodynamics and morphodynamics. The methodology relies on wave crest detection: they are detected as peaks in the surface elevation timeseries and are then followed in the inner surf zone by neighbour-looking techniques, taking advantage of the high spatial resolution provided by the LiDAR scanner.

## 3.1 Introduction

### 3.1.1 LiDAR in coastal engineering

The use of remote sensing techniques in coastal engineering has become increasingly popular during the past 3 decades. These instruments can provide measurements at temporal and spatial scales that are not reached by common in situ instruments. As an example, video imagery has been used for a wide range of applications: from bathymetric inversion (Stockdon and Holman, 2000) to alongshore swash motion variability (Guedes et al., 2012).

Since remote sensors are non-intrusive instruments, they have the advantage of being easily and safely deployed on existing beachfront structures or specifically installed towers. Furthermore, instruments like the terrestrial LiDAR scanner (TLS) directly measure the wave profile and the wave properties (e.g. wave height and period) can subsequently be extracted. This represents an important advantage over other remote sensing techniques (e.g. video or radar) which are able to cover large domains but cannot directly obtain wave properties. Additionally, the ability of a single TLS to obtain data at multiple locations provides significant advantages over in situ sensors like pressure transducers, which are commonly used in surf zone studies but provide only point measurements.

The first reported experiment using a TLS to study wave processes is that of Irish et al. (2006), who mounted a 4-rangefinder laser on a pier. A directional wave spectrum obtained with the scanner was compared to that from a submerged wave gauge, showing good agreement.

Recently, a few attempts were made to study the wave propagation or measure wave breaker heights. Harry et al. (2010) investigated the potential of a 3D TLS to capture the water surface of a surf zone. Despite capturing the wave profile successfully, the time spent by the scanner to scan on the three dimensions was a major drawback since it introduced an alongshore time shift on the wave crest propagation. Their conclusion was that a 2D TLS might be a better alternative. Park et al. (2011) also used a 3D TLS to measure breaker heights. They compared the scanner data with visual measurements against a vertical staff, and obtained a relatively good agreement over the 26 measured waves, with a Root Mean Square Error (*RMSE*) of 5 cm. Individual wave height and celerity measurement was also made possible by combining the use of video camera and a 3D TLS, fixed on an automated robot, in Wübbold et al. (2012). Interestingly, this technique enabled the measurement of several alongshore points of the wave crest, allowing a 2-dimensional description of the wave propagation.

Swash zone data have been obtained using fixed 2D TLS instruments by Blenkinsopp et al. (2010), Brodie et al. (2012) and Almeida et al. (2015), who demonstrated the ability of the instrument to measure swash hydro and morphodynamics with high accuracy. The approach of Wübbold et al. (2012) was also used by Vousdoukas et al. (2014) in laboratory conditions to measure wave-by-wave events in the swash zone. Overall, it was found that the precision of such instruments was lower than that of ultrasonic altimeters which had previously been used to make such swash measurements, however the ability to capture

Figure 3.1: Photograph showing the experimental setup and their location on the upper part of Rousty beach. The TLS was fixed on the 4.8 meters-high tower standing on the left part of the picture while the scaffold is on the right. The buried sensors can be observed in between.

small scale features due to the high spatial resolution and small measurement footprint compared to other remote sensors make this instrument a powerful tool for coastal studies.

### 3.1.2 Known drawbacks of the 2D-LiDAR for wave processes studies

Previous studies (Blenkinsopp et al., 2010; Evans, 2010) have shown that an aerated and turbulent water surface is required for the laser to be sufficiently scattered to enable detection by the instrument. While in the laboratory, this can be achieved by adding particulates to increase the water turbidity (Allis et al., 2011), this is not feasible in the field.

Fortunately, when the wave conditions are sufficiently energetic (wave breaking occurring), the surf and swash zones are very dynamic and are characterised by high levels of turbulence and aeration, which cause sufficient scattering for the consistent detection of the free surface elevation.

Environmental conditions (luminosity, air humidity, wind) also have an impact on the scanner measurements. While the influence of humidity or water drops, characterized by noise or spikes in data can be corrected, under high wind conditions the TLS can become too unstable for the data to be used. Indeed, while instrument accuracies are typically of the order of millimetres, the error induced by small oscillations of the instrument increases with distance from the instrument and can lead to measurement errors of the order of centimetres.

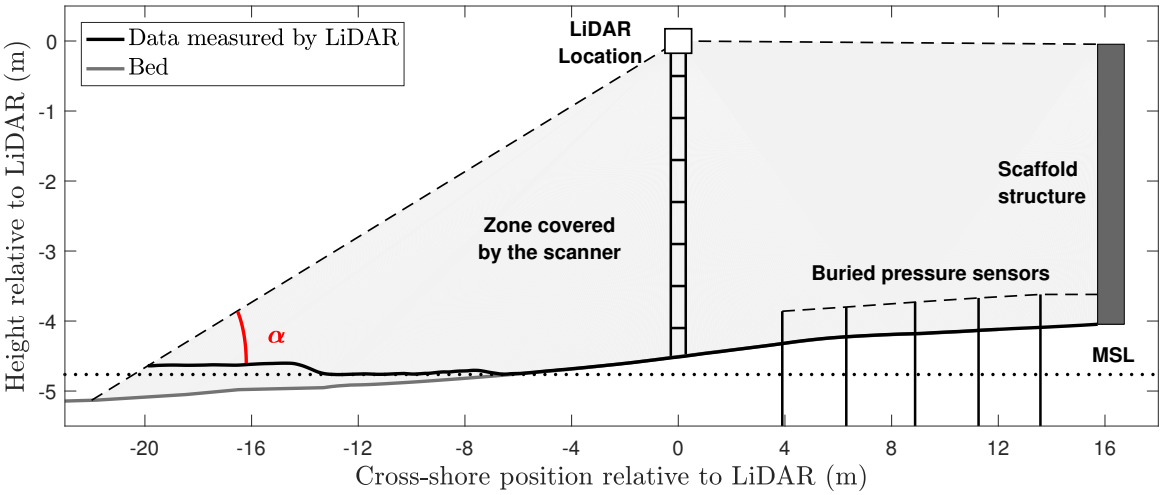


Figure 3.2: Schematic of the experimental setup at the Rousty experiments, for the 18 December 2014. The TLS, erected on top of a tower, covered a 35m-long zone from the scaffold structure where it was logged, to the point where the incident angle with the water surface ($\alpha$) becomes too small for a sufficiently strong return signal. The cross-shore locations of the 15 buried pressure sensors are also shown (3 sensors were fixed to each buried pole, at different depth).

## 3.2 Experimental Setup

### 3.2.1 Site Location - Rousty

The experiment described in this paper was completed at Rousty beach, Camargue, which is located in the South of France on the Mediterranean Sea, from November 2014 until February 2015. The overall aim of the experiment was to study the coupling between the wave field, groundwater table dynamics and the beach morphodynamics. It was organised in two different phases: a 10-day short-term and high-frequency phase within a 3-month long period of low-frequency measurements.

The site presents morphodynamic characteristics typical of the beaches in the National park of Camargue (Sabatier, 2008; Sabatier et al., 2009b). Despite the microtidal environment (tidal range ~0.4 m), this part of the coastline presents very dynamic beach/dune morphologies. This region is subject to seasonal storms accompanied by storm surges that flood the low-lying area of the Camargue beaches (Sabatier, 2008). This region is also exposed to very strong onshore wind episodes (mistral), which cause huge losses of sand due to aeolian transport (Sabatier et al., 2009a).

The high-frequency part of the experiments took place from the $8^{th}$ to the $18^{th}$ of December 2014 (10 days). During this period, 15 buried pressure sensors were deployed on the berm located at approximately 60 m from the dune system in addition to a laser scanner fixed on top of a 4.8 m-high tower erected at the shoreline, see Figure 3.1. Both sets of instruments were logged by a computer placed on a scaffold structure, 16 m landward of the scanner.

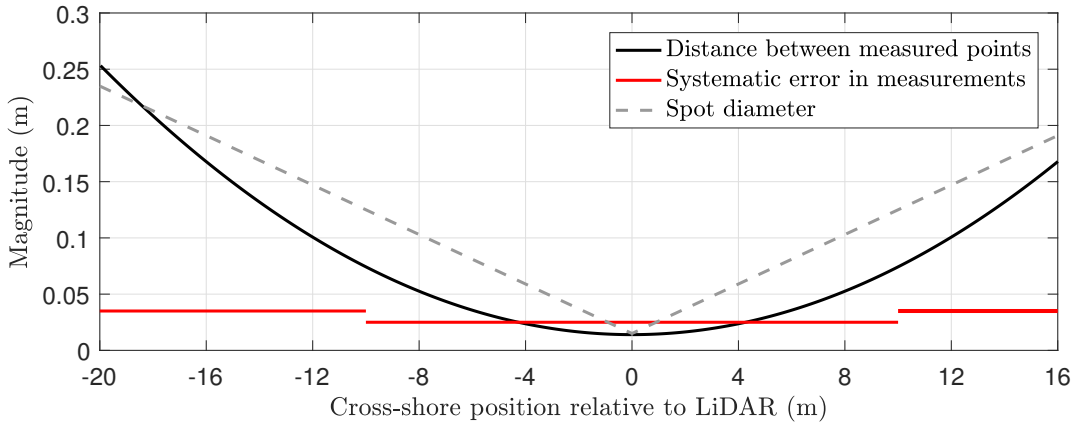


Figure 3.3: Distance between the points measured by the TLS (black line), for this experimental setup described in this paper. This value evolves from 0.014 m at the Nadir to 0.25 m at the most seaward captured location. The systematic error and the spot diameter provided by the manufacturer are also plotted (red continuous and grey dashed lines respectively).

### 3.2.2 Instrumentation

In this section, only the scanner instrumentation will be described since this paper focusses on the capacity of a commercial 2D scanner for inner surf and swash zones studies. During the Rousty experiments, the TLS used was a commercial LMS511 Laser Measurement System manufactured by SICK. This ranging device uses the time of flight method: the distance between two objects is calculated using the time required for an eye-safe pulsed beam ($\lambda$ = 905 nm) to be detected after reflection from the target. This instrument is similar to that used by Blenkinsopp et al. (2010) in terms of its function and specification.

The TLS has a range of 65 m, a 190° field-of-view with an angular resolution of 0.1667°, and can be sampled at the sample rate of 25 Hz (SICK, 2015). With this sampling rate, each spatial measurement location is measured 25 times per second; the instrument thus providing a total of 28500 measured points per second. During the experiment, a 4.8m-high tower was erected around the shoreline position for mounting the scanner and from this position it was possible to obtain measurements across the whole beach profile and into the inner surf zone (approximately 30% of the surf zone was covered in the present dataset). A schematic of the high-frequency experimental setup can be observed in Figure 3.2.

For the experimental setup at Rousty and using an angular resolution of 0.1667°, the distance between measurement points varied from 0.014 m at the Nadir point (zero grazing angle) to 0.25 m at the most seaward valid measurement location (Figure 3.3). This spatial resolution allows the detection of the instantaneous shape of small wave features, something that most conventional, point-measurement instruments such as pressure transducers or wave gauges are unable to do. The systematic error and spot diameter provided by the manufacturer (SICK, 2015) are also shown in the same figure. The systematic error naturally increases with increasing spot diameter and evolves from ±0.025 m from 1 to 10 m from the scanner to ±0.035 m between 10 and 20 m.

As the grazing angle between the laser beam and the target decreases ($\alpha$, Figure 3.2), the signal reflected by the water surface and returning to the scanner gets weaker. While bore

fronts can still be captured due to a more normal-oriented surface relative to the instrument, a signal is not always returned from a more horizontal surface (e.g. wave troughs), resulting in increasing gaps in the dataset as we move offshore. As a result, a cross-shore position of -20 m relative to the TLS was set as the seaward extent of the dataset for the extraction of wave properties. If we consider a plane surface, the minimum incident angle allowing good quality data with this specific scanner model was found to be around 13.5°. It is noted however that, since wave crests could still be followed from further offshore, the bore celerities were calculated from -22 m relative to the TLS, as discussed in Section 3.3.4.

## 3.3 Methodology

### 3.3.1 Pre-processing

Before analysing the dataset to study wave characteristics in the inner surf and swash zones, pre-processing is required. As in Almeida et al. (2015), a beach survey carried out the same day as the dataset presented in this study (18 December 2014) was used to find the instrument orientation relative to the cross-shore profile. Data transformation from the scanner-centroid coordinate system to the cross-shore coordinate system is then possible from this analysis. This results in two arrays X and Z containing the cross-shore position and height relative to the scanner.

The dataset was de-spiked to reduce noise in the measurements and environmental effects such as splashes or people passing within the TLS field-of-view. De-spiking the time series was achieved using gradient thresholds between two consecutive points. Then to reduce random noise, the dataset was time-averaged using a moving averaging method (window of 0.2 s), and spatially interpolated onto a regular cross-shore grid ($\delta x$ = 0.1 m).

### 3.3.2 Bed extraction

Since the instrument simply measures the distance to the closest target, no distinction on the medium is made, e.g. water or sand. Due to the scanner's location in the swash zone which is alternatively dry and submerged, an important step in the data processing is to separate the water signal from the bed. The methodology used in this study to extract the bed follows the work of Almeida et al. (2015).

Almeida et al. (2015) calculated the time series variance over 4-second windows at every point on the regular grid. This methodology relies on the fact that the time series variance when the target is the exposed bed is much smaller than that from a moving water surface. Therefore, by defining empirical thresholds at every cross-shore location, one can extract data corresponding to stationary, dry bed. By defining a water-depth criterion (0.015 m in this study) one can separate the original time series into separate 'bed' and 'wet' time series. This water-depth criterion ensures that the noise in the measurements (of the order $O$(mm)) is not interpreted as 'wet' data.

By interpolating in time the extracted bed points, a beach profile can be obtained at each time step. This enables the monitoring of bed morphology at several hundred points and at the time scale of individual waves. An example of the result from this extraction is

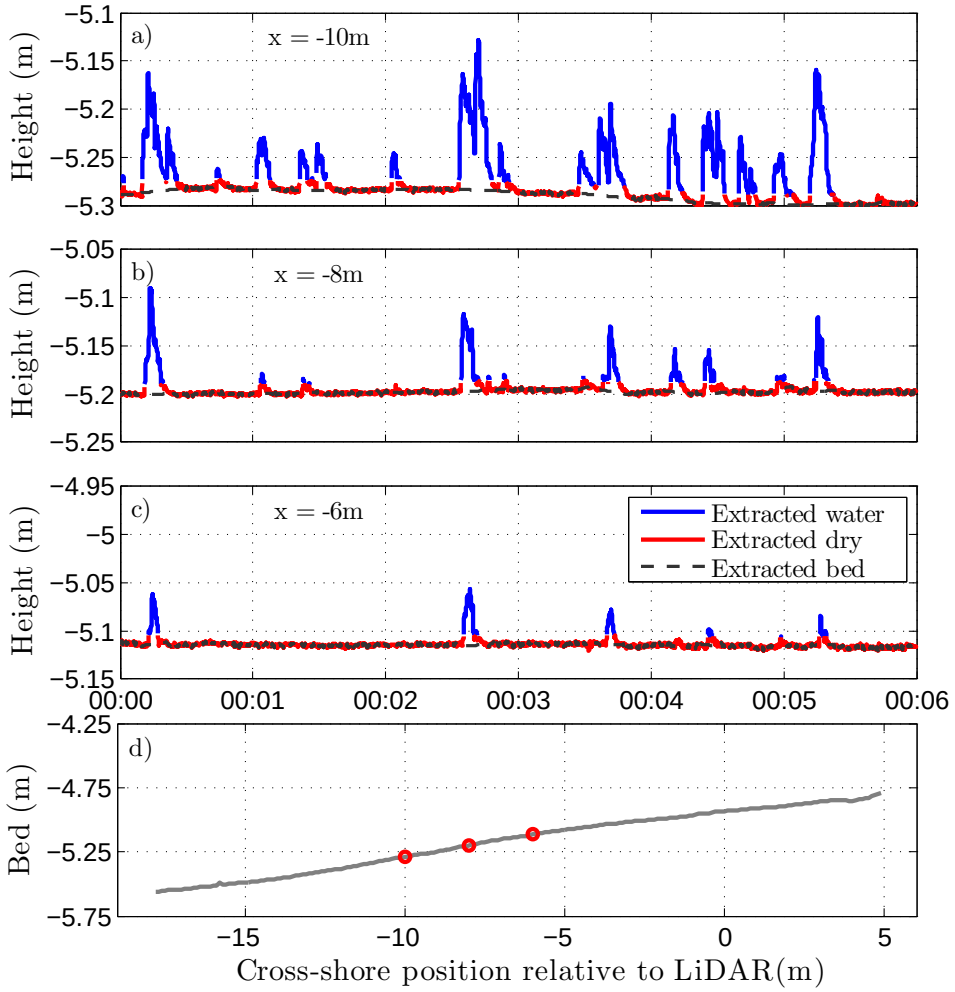


Figure 3.4: Example of bed extraction for the 14th of December. 3 cross-shore positions are shown in the panels (a), (b) and (c), and are represented by a red circle on the bed profile, in the panel (d). In blue is represented the 'wet' timeseries, in red the 'bed' one and in grey the time-interpolated bed. Interestingly, we can observe accretive and erosional patterns at the event time scale at the cross-shore position $x = -10$ m.

shown in Figure 3.4, where both accretionary and erosive swash events can be observed at $x = -10$ m.

### 3.3.3 Wave properties extraction

In order to obtain the individual wave characteristics at each point on the grid, a local maxima analysis was carried out on the surface elevation time series to detect the wave crests. This technique has been used in previous surf zone studies by Power et al. (2010) or Postacchini and Brocchini (2014) because it is insensitive to low-frequency motions, unlike most common methods such as zero-down crossing which define waves relative to intersection between the instantaneous free-surface elevation and mean sea level. When studying the surf zone, and especially the inner surf where low-frequency motions can be predominant, this aspect becomes critical since both the wave crest and trough can be under/above the defined mean water level. This is illustrated in Figure 3.5.

The wave troughs were defined as the minima reached between two crests and the wave

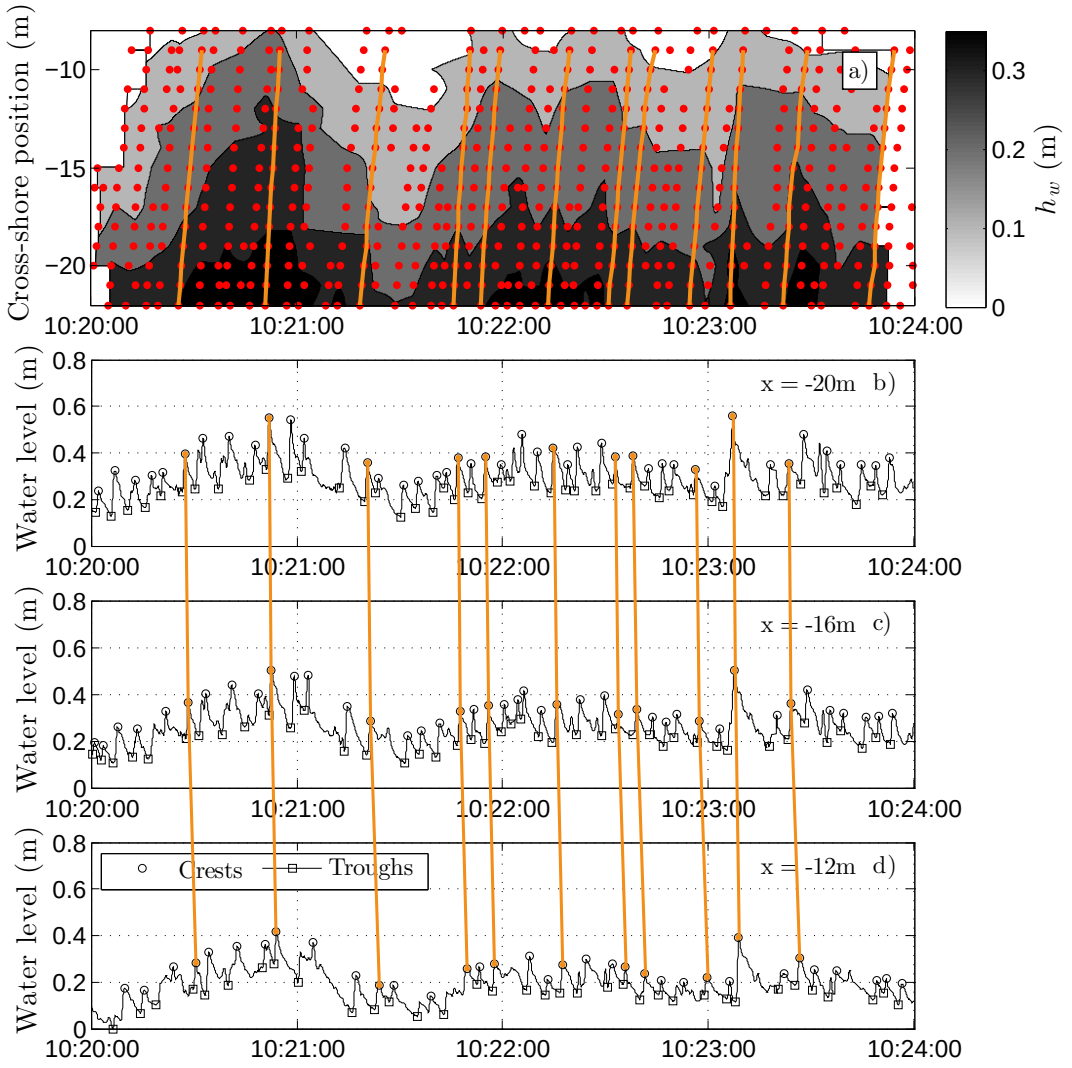


Figure 3.5: Example showing the wave extraction method in the inner surf zone. The wave period-averaged water depth $h_w$ contours are shown in (a), where red dots represent the detected wave crests. The orange lines are the waves selected in this time window for the celerity calculations. The panels (b), (c), (d) represent the water surface elevations at three cross-shore locations, with the chosen waves tracked across them. Extracted wave crests and troughs are represented by black circles and squares respectively.

period as the time elapsed between the passage of the troughs preceding and following a wave crest at the same location. A filter was applied to delete incorrect detections by limiting the time between 2 crests (2 s for this study). The wave height was defined as the elevation difference between the wave crest and trough elevations. Two other parameters were extracted, following the notation of Power et al. (2010): $h_w$ the wave-period-averaged mean water depth (mean surface elevation between the two troughs immediately before and after a crest), and $h_{tr}$ the trough depth. These are used for the analysis of individual wave celerities and the wave height to water depth ratio, $\gamma$.

### 3.3.4 Wave celerities

To calculate the wave celerities, two different approaches have been used. The first one was developed in the scope of this study and is based on a simple crest-tracking technique,

allowing the estimation of individual wave celerities. The second uses a cross-correlation between two time series to calculate the averaged wave celerities over the time series length, following Tissier et al. (2011).

Individual wave celerities were calculated every 1 m between the cross-shore locations $x = -21$ and $-10$ m using a tracking algorithm. This algorithm is initiated by manually choosing waves at the cross-shore position $x = -22$ m and storing the corresponding time-index. At the next position ($x = -21$ m), the first detected crest after this time index is assumed to be the same wave. The same methodology is used to track the wave until $x = -9$ m and every time-index is stored. The wave celerity at a cross-shore position $x_i$ is then defined as the ratio of the distance between the two adjacent measurement points $x_{i-1}$ and $x_{i+1}$ (2 m) and the time elapsed between the passage of the wave crest at these two positions.

Due to the simplicity of the tracking algorithm and the difficulties caused by superposition of multiple waves within the inner surf, a careful visual inspection was carried out on all of the detected crests. Only waves not presenting obvious visual wave-wave interactions with other crests were selected. For the current study, this still enabled the detection of 275 waves and thus more than 3000 individual wave celerities. The process described above is illustrated for a 4-minute-period in Figure 3.5a, where the selected waves for this time window are shown in orange.

Averaged wave celerities were calculated following the method of Tissier et al. (2011). The cross-correlation was calculated between two 10-minute time series from two cross-shore locations (separated by 2 m). The maximum correlation found between the two time series is the averaged time delay between the surface elevation features. Physically, it represents an estimation of the averaged wave celerity over the time series.

Using these two different methods to estimate the wave celerity is interesting in several aspects. The TLS data opens up the possibility to detect wave celerity and geometry in shallow water right up to the shoreline without any mathematical transformation on the measurements (e.g. Radon transform in Almar et al., 2013). The present dataset corresponds to shallower water than investigated by Tissier et al. (2011), thus the relationship between wave properties and celerity can be studied closer to the shoreline. Furthermore, the estimation of individual celerities will provide more insight into the dispersion of these values.

## 3.4 Results

### 3.4.1 Bed Monitoring

Following the methodology presented in Section 3.3.2, the bed morphology has been monitored using the bed time series. By subtracting the initial beach face profile from the measured profile at each time step, erosion/accretion patterns over the measurement period can be observed. An example is presented in Figure 3.6 where the erosion/accretion patterns are shown every minute, after window-averaging the extracted bed (15-second window), for the period of the 13$^{th}$ to the 14$^{th}$ of December (30 continuous hours). This

corresponded to the most energetic period of the 10-day experiments (energy peak around 13pm on the 13$^{th}$ of December).

Offshore wave conditions were measured by a buoy[1] located 40 km west of Rousty beach, moored in a water depth of 30 m. Measured significant wave height and peak and mean spectral periods are shown in Figure 3.6a and 3.6b respectively. Mean water levels were obtained by a tidal gauge located at Fos-sur-Mer port[2] (20 km east of Rousty). Interestingly, we can observe the influence of the tide even in this microtidal environment (high tides at 12:55pm on the 13$^{th}$, 1:25am and 1:35pm on the 14$^{th}$). In addition to the direct influence on the mean sea level, a significant reason for these oscillations is thought to be the weaker energy dissipation during high tides on this low-sloping barred beach (Guedes et al., 2011). During the first part of this storm event (9am to 6pm on the 13$^{th}$ of December), the swash zone profile flattened and experienced the strongest erosion (~0.15 m) between $x = -10$ and $-5$ m. When the conditions became milder, there is evidence of berm building centred around $x = -10$ m at a rate of approximately 10 mm/hr. This berm remained present until the end of the experiment, with evolving steepness depending on the offshore conditions.

### 3.4.2 Validation of the extracted wave-by-wave properties

The methodology to extract wave properties based on the extrema analysis was compared to a classic spectral analysis (Figure 3.7). Significant wave height $H_s$ was calculated by means of a Fast-Fourier Transform on a 15-minute time series, between cutoff frequencies of 0.05 Hz and 0.5 Hz. $H_s$ was compared to the averaged extracted wave height of the 1/3 highest waves $H_{1/3}$ from the wave-by-wave analysis described in Section 3.3.3, over the same period. The mean extracted individual wave period $T_{i,m}$ was compared to the mean wave period $T_{01} = m_0/m_1$, which is the inverse of the centroidal frequency, where $m_n$ is the n$^{th}$ spectral moment is defined as:

$$m_n = \int_0^\infty f^n E(f) df \tag{3.1}$$

with $E(f)$ the power density spectrum.

Plotted against the mean water depth over the same time period $\bar{h}$, $H_s$ and $H_{1/3}$ show very good agreement at all water depths (Figure 3.7a), validating the extraction method based on the local extrema analysis. Both statistical ($H_{1/3}$) and spectral ($H_s$) significant wave height were found to show little scatter and to linearly decrease with averaged water depth ($r^2 = 0.86$). Though such depth-dependence is generally observed when saturated conditions are found in the inner surf (Sallenger and Holman, 1985), the relatively short dataset (2h30) and the consistent offshore conditions do not allow for such statement. Furthermore, waves were found to stop breaking and reform between the two beach bars, consistent with unsaturated conditions (Thornton and Guza, 1982).

[1] Data provided by CEREMA/DREAL Languedoc Roussillon
[2] Data provided by REFMAR/SHOM

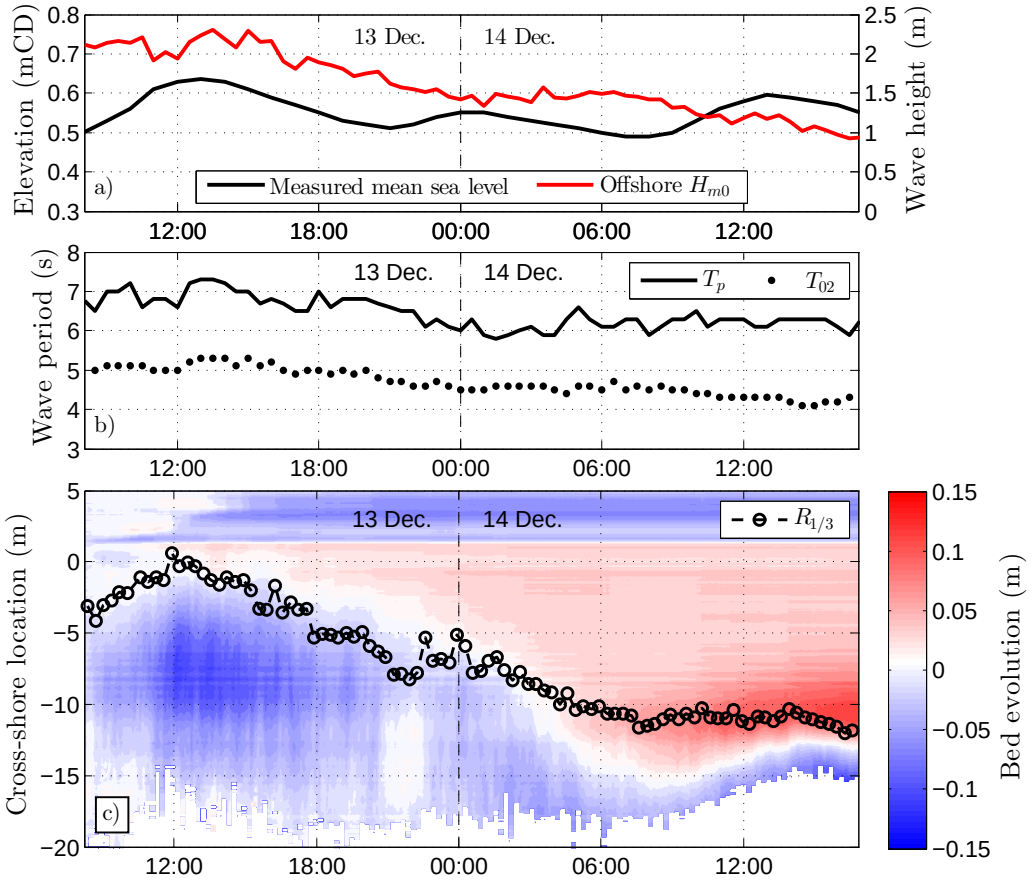


Figure 3.6: Bed extraction results: a) Measured mean water levels above Chart Datum at Fos-sur-Mer port and offshore significant wave height measured by a buoy close to Sete; b) Measured wave periods ($T_p$ and $T_{02}$) by the same buoy; c) Beach morphological evolution for the 13$^{th}$ and 14$^{th}$ of December (30 continuous hours of measurement). Erosion and accretion patterns were calculated by subtracting the initial beach profile to that of the actual moment. Red color corresponds to accretion while blue corresponds to erosion. The significant runup limit $R_{1/3}$ is shown as a circled black line.

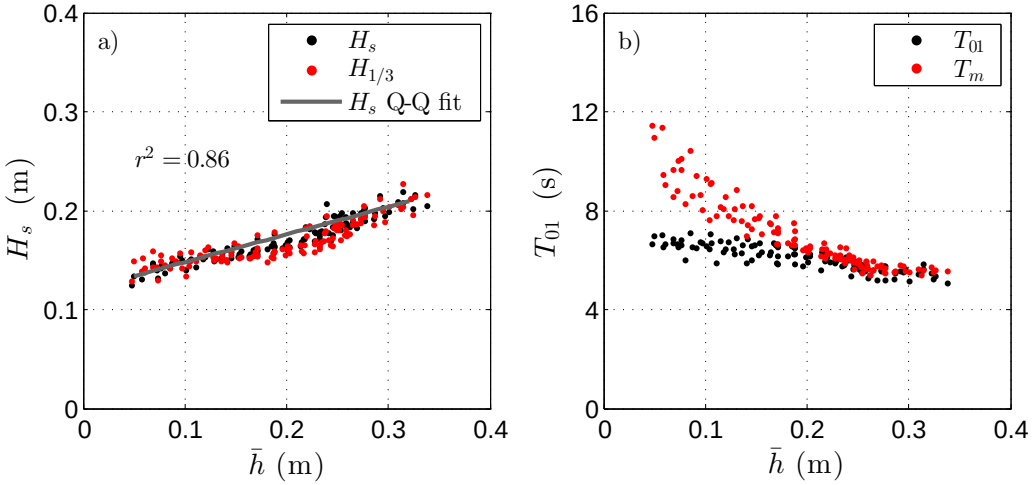


Figure 3.7: Comparison of a) significant wave heights and b) mean wave period calculated with two different methods: using the centroidal frequency inverse from spectral analysis (black dots) and averaged values over the same period of time, from an extrema analysis (red dots).

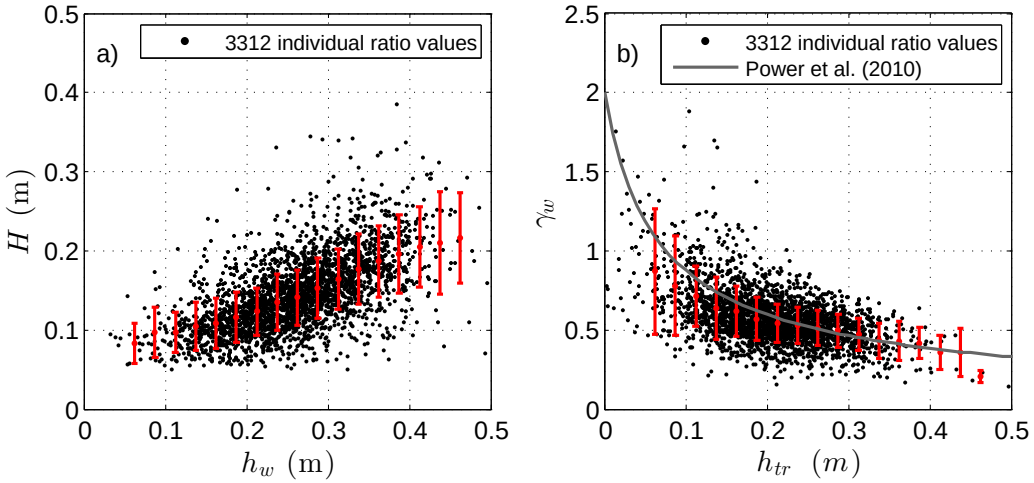


Figure 3.8: Individual wave properties: a) Wave height as a function of the wave-period-averaged water depth and b) wave height to water depth ratio as a function of the depth under the trough. Standard deviations are shown by the red bars and are calculated for 0.025m-wide bins. In b), the empirical fit equation obtained by Power et al. (2010) using averaged $\gamma_w$ values is shown as the gray line.

In contrast to averaged values, measured individual wave heights showed considerably more scatter, see Figure 3.8a. This scatter is explained by two main factors: the influence of infra-gravity motions and the presence of high-frequency waves increasing or lowering the wave trough height. Naturally, it is also visible in the individual wave height to water depth ratio $\gamma_w = H/h_w$ (Figure 3.8b), which shows increasing values as waves approach the shoreline, something previously observed by Sénéchal et al. (2004) and Power et al. (2010). In particular, the wide range of observed individual $\gamma_w$ values show the inappropriateness of choosing constant values for this parameter in numerical models. Finally, the individual $\gamma_w$ values, obtained closer to the shoreline than these two previous studies, seem to be in agreement with the line fit obtained with averaged $\gamma_w$ values by Power et al. (2010).

The comparison between $T_{i,m}$ and $T_{01}$ (Figure 3.7b) also shows interesting results. While for the deepest waters considered ($h \geq 0.2$ m), the mean extracted individual wave periods are consistent with $T_{01}$, as we get closer to the shoreline, the difference between the two values increases with decreasing water depth. This analysis gives some support to the idea of using the centroidal frequency to define a characteristic period in the inner surf, as suggested by Raubenheimer et al. (1996) and Sénéchal et al. (2004).

### 3.4.3 Influence of the characteristic period on the $\gamma$ parametrization

To further compare the characteristic wave periods, the ratio between averaged significant wave height and water depths noted $\bar{\gamma}_s$ has been plotted against $\beta/\bar{k}\bar{h}$, which represents the fractional change in water depth over a wavelength. In this expression, $\beta$ represents the bed slope, $\bar{k}$ the wave number calculated from the averaged estimated celerities and a characteristic period and $\bar{h}$ the averaged water depth over the same period.

Two different comparisons were made (using the same typology as in Section 3.4.2):

1. Comparison shown in Figure 3.9a using $H_{1/3}$ for $\bar{\gamma}_s$ and $T_{i,m}$ to derive $\bar{k}$.
2. Comparison shown in Figure 3.9b using $H_s$ for $\bar{\gamma}_s$ and $T_{01}$ to derive $\bar{k}$.

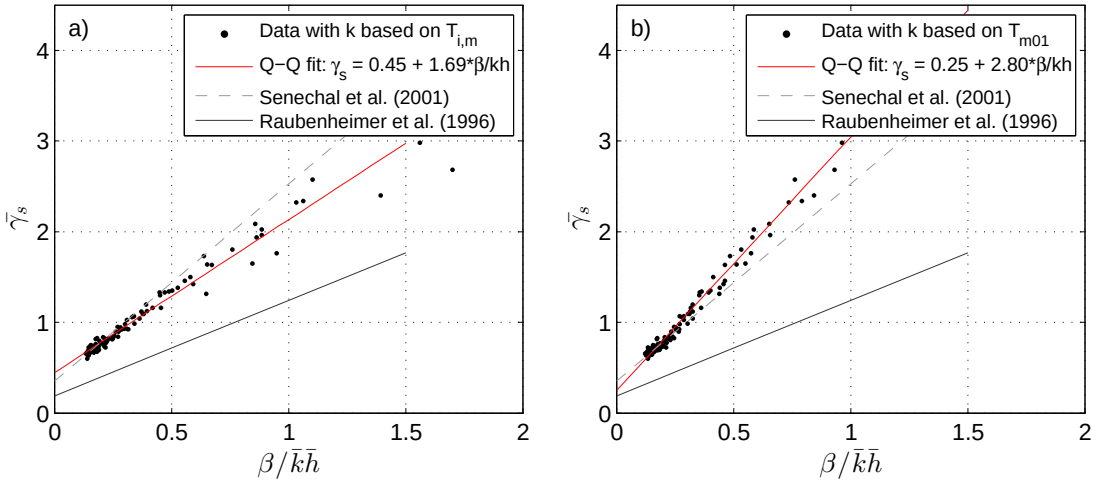


Figure 3.9: Averaged significant wave height to averaged water depth ratio plotted against $\beta/\bar{k}\bar{h}$: a) Ratio calculated with $\bar{k}$ based on the mean extracted individual wave period $T_{i,m}$; b) Ratio calculated with $\bar{k}$ based on the mean spectral wave period $T_{01} = m_0/m_1$, inverse of the centroidal frequency. The present dataset (black dots, and its Q-Q fit shown as red line) is compared to the fit obtained in two previous studies: dashed gray lines for Sénéchal et al. (2001) and gray continuous line for Raubenheimer et al. (1996).

For both comparisons, a strong linear dependence was found between $\bar{\gamma_s}$ and $\beta/\bar{k}\bar{h}$. For deeper water and using two different frequency cutoffs, Raubenheimer et al. (1996) and Sénéchal et al. (2001) found similar linear relationship, but with different coefficients. For the present dataset and for both derived $\bar{\gamma_s}$, a good match is found with the linear fit obtained by Sénéchal et al. (2001) when $0 \geq \beta/\bar{k}\bar{h} \geq 0.5$. For greater values of $\beta/\bar{k}\bar{h}$, lower values compared to Sénéchal et al. (2001) are obtained when using the mean extracted wave period $T_m$, while that using $T_{01}$ still match the linear fit. This limit value of $\beta/\bar{k}\bar{h}$ corresponds to the critical depth where $T_{01}$ does not match to $T_{i,m}$ any more (Figure 3.7b).

It is noted that the three compared datasets use different frequency cutoffs ($0.05\,\text{Hz} \leq f \leq 0.18\,\text{Hz}$ for Raubenheimer et al. (1996), $0.09\,\text{Hz} \leq f \leq 0.3\,\text{Hz}$ for Sénéchal et al. (2001) and $0.05\,\text{Hz} \leq f \leq 0.5\,\text{Hz}$ for the present study). Except for the influence of the much lower high frequency cutoff used by Raubenheimer et al. (1996), it is unclear why the present dataset shows higher values than in Raubenheimer et al. (1996) but matches that of Sénéchal et al. (2001). Finally, it has to be noted that the dataset presented in this study contains much shallower depths than that considered in the two previous studies. For instance, the highest value of $\beta/\bar{k}\bar{h}$ considered by the previous studies was 0.25 while it is approximately 1.75 in the current work.

### 3.4.4 Wave celerities

Individual wave celerities were compared to a range of previously developed predictors summarized in Table 3.1. In the different formulations, $h$, $h_c$, $h_t$ are respectively the mean water depths, the crest height and the trough height. A more complete introduction to these predictors is given by Catálan and Haller (2008) who compared a wider range of celerity predictors against measurements obtained using video imagery from laboratory experiments.

Prior to this work, only a few studies have been published on the measurement of individual broken-wave celerities in the surf zone. Radon transform on video camera data have been used by Yoo et al. (2011) and Almar et al. (2014a) to track wave crests, while Tissier et al. (2013) used a large array of wave gauges for this purpose. Additionally, Postacchini and Brocchini (2014) calculated individual broken-wave celerities by correcting the averaged celerities obtained by a cross-correlation method (Tissier et al., 2011) for each detected wave. While Tissier et al. (2011) found better agreement with Bonneton (2004) predictor using averaged celerities, individual celerities from Postacchini and Brocchini (2014) and this study were found to better match the solitary wave theory celerity, see Figure 3.10a.

In contrast to the study of Tissier et al. (2011) whose data was concentrated in the outer and mid-surf zone, the present study uses data from the inner surf to the swash zone. In particular, this enables one to look more closely at the boundary between the two zones in terms of wave celerities using the cross-correlation method. This is illustrated in Figure 3.10b, where the 10-minute averaged celerities are plotted against the corresponding averaged water-depth.

Between water depth of 0.2 and 0.4 m, the averaged celerities show good agreement with the modified shallow water wave predictor, though they are slightly underestimated. This is in agreement with the results found in Figure 3.10a. Indeed, the modified shallow water wave predictor corresponds to the solitary wave predictor with a constant wave height to water depth ratio of 0.78. Hence, despite a not-insignificant scatter when using the individual celerities (shown by Postacchini and Brocchini (2014), not shown in this study), the modified shallow water predictor provides good estimates of the averaged wave celerities seaward of $h \geq 0.2$ m, corresponding to $\gamma = 0.5$ in this study, see Figure 3.8b. Interestingly landward of this depth, averaged celerities remain quite constant, slightly decreasing, to finally present a much broader value range at the shoreline position ($1.3\,\mathrm{m.s^{-1}} < c_b < 2.2\,\mathrm{m.s^{-1}}$). This scatter of averaged values implies a wider range of individual celerities at the surf-swash boundary, which could be explained by the interaction between

Table 3.1: List of the different tested wave celerity predictors. For individual wave celerities, the mean water depth $h$, becomes the wave-period-averaged mean water depth $h_w$.

| Predictor | Formulation of $c$ |
|---|---|
| Linear theory (shallow water assumption) | $c = \sqrt{gh}$ |
| Modified shallow water formulation (Schäffer et al., 1993) | $c = 1.3\sqrt{gh}$ |
| Solitary wave theory | $c = \sqrt{gh(1+\frac{H}{h})}$ |
| Bore model (Svendsen et al., 1978) | $c = \sqrt{gh_c h_t \frac{(h_t+h_c)}{2h^2}}$ |
| Shock model (Bonneton, 2004) | $c = -2\sqrt{gh} + 2\sqrt{gh_t} + \sqrt{gh_c \frac{(h_t+h_c)}{2h_t}}$ |

surf and swash processes.

## 3.5 Conclusion

In this study, a methodology for monitoring the beach morphology and individual wave characteristics using a shore-mounted 2-dimensional commercial laser scanner has been presented. The conclusions of this investigation can be summarized with the following points:

- The laser scanner can be used to measure time-varying water surface profiles in the inner surf and swash zones, enabling the study of wave propagation on a wave-by-wave as well as time-averaged basis.
- Individual wave properties ($H$, $T$) can be extracted using an extrema analysis on the measured time series. The extracted wave height was found to compare well with that from spectral analysis. It was also shown that for these conditions, the wave period derived from the centroidal frequency could be chosen as a characteristic wave period for water depths down to 0.2 m. Further investigation is needed on the reason why this changes at the swash/inner surf boundary.
- $\gamma_s$ was found to be linearly dependent on $\beta/\bar{k}\bar{h}$. Furthermore, the present dataset seem to match well that of Sénéchal et al. (2001), for values of $\beta/\bar{k}\bar{h}$ lower than 0.5. For higher values, discrepancies are observed and are due to the differences observed between $T_m$ and $T_{01}$.
- Individual wave celerities were estimated using a simple crest-tracking method. Comparisons with various predictors showed that the solitary wave theory gave

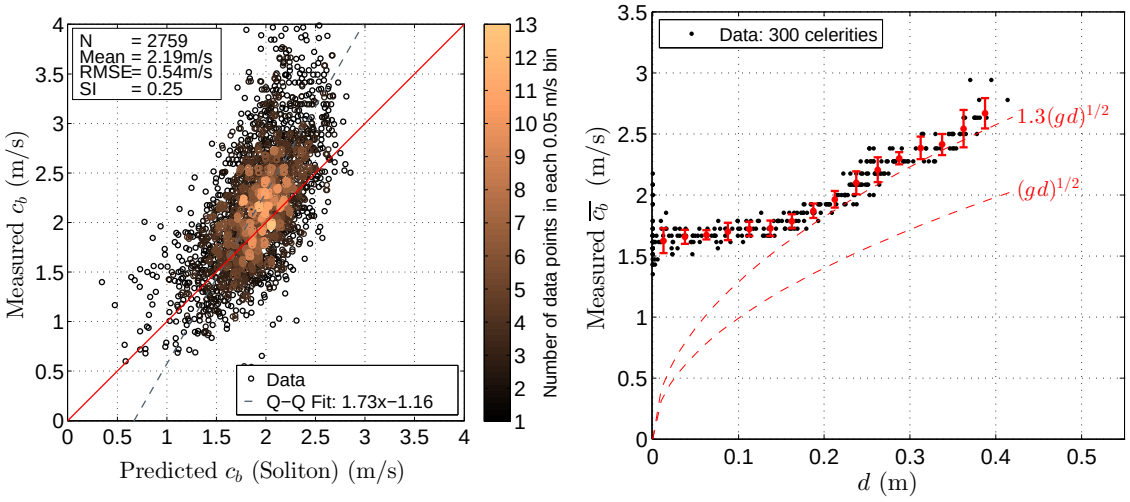


Figure 3.10: Scatter plot of measured wave celerities: a) individual wave celerities against the predictor from the solitary wave theory. Data circles are coloured by their concentration in every 0.05 m/s bins. The wave-period-averaged depth is used for the soliton celerity formulation, following Postacchini and Brocchini (2014). Correlation coefficient r = 0.65.; b) Averaged wave celerities obtained from the cross-correlation of two 10-minute time series, plotted against water depth. Their standard deviation is plotted as red bars, using 0.025m-wide bins. The modified and original linear wave theories in shallow water are represented in red dashed lines.

the best agreement with the present dataset. However, in the shallow water depths investigated here, these values exhibit considerable variability.

- 10-minute averaged wave celerities were also calculated using a cross-correlation technique. These values agree well with the modified shallow-water predictor in depths greater than 0.2 m, becoming almost constant as the water depths decrease landwards. This critical depth also corresponds to that when $T_m$ and $T_{01}$ start to show discrepancies. Since the celerity is a function of the wave period, the two facts could be physically linked. This will be the subject of further investigation, since it could bring new insight into the conditions at the surf-swash boundary.

## Acknowledgements

This work was supported by EPSRC. The three anonymous reviewers are greatly acknowledged for their constructive comments on the manuscript. CEREMA/DREAL Languedoc Roussillon and REFMAR/SHOM are thanked for providing the offshore wave buoy and tide gauge data respectively. Researchers from the institutions involved in this project: Damien Sous (MIO), Frédéric Bouchette (Géosciences Montpellier), François Sabatier, Samuel Meulé (CEREGE), Lise Petitjean (PhD student, MIO and Géosciences Montpellier), and all the other PhD students, are greatly acknowledged for the invitation to participate at this large scale experiment. The survey data used for calibrating the LiDAR was also much appreciated.

## Appendix: Statistical parameters

The different statistical parameters (Root-Mean Square Error, Scatter Index and a correlation coefficient noted r) used in this study are defined in this section. If we denote the two compared series as $X = \{x_1, \cdots, x_n\}$ and $Y = \{y_1, \cdots, y_n\}$, they are defined as follows:

$$RMSE = \sqrt{\frac{1}{n}\sum_{i=1}^{n}(x_i - y_i)^2} \tag{3.2}$$

$$SI = \frac{\sqrt{\frac{1}{n}\sum_{i=1}^{n}(x_i - y_i - \overline{(X-Y)})^2}}{\overline{X}} \tag{3.3}$$

$$r = \frac{\sum_{i=1}^{n}(x_i - \overline{X})(y_i - \overline{Y})}{\sqrt{(\sum_{i=1}^{n}(x_i - \overline{X}))^2(\sum_{i=1}^{n}(y_i - \overline{Y}))^2}} \tag{3.4}$$

## References

Allis, M. J., Peirson, W. L., and Banner, M. L. 2011. Application of LiDAR As a Measurement Tool For Waves. *The Twenty-first International Offshore and Polar Engineering Conference, 19-24 June, Maui, Hawaii, USA*. Vol. 3, pp. 373 – 379.

Almar, R., Bonneton, P., Michallet, H., Cienfuegos, R., Ruessink, B. G., and Tissier, M. 2013. On the use of the radon transform in studying wave dynamics. *Coastal Dynamics '13: Proceedings of the Seventh Conference on Coastal Dynamics, Arcachon, France*, pp. 73 – 82.

Almar, R., Michallet, H., Cienfuegos, R., Bonneton, P., Tissier, M., and Ruessink, G. 2014a. On the use of the Radon Transform in studying nearshore wave dynamics. *Coastal Engineering* 92, pp. 24 – 30. DOI: 10.1016/j.coastaleng.2014.06.008.

Almeida, L. P., Masselink, G., Russell, P. E., and Davidson, M. A. 2015. Observations of gravel beach dynamics during high energy wave conditions using a laser scanner. *Geomorphology* 228, pp. 15 – 27. DOI: 10.1016/j.geomorph.2014.08.019.

Blenkinsopp, C. E., Mole, M. A., Turner, I. L., and Peirson, W. L. 2010. Measurements of the time-varying free-surface profile across the swash zone obtained using an industrial LIDAR. *Coastal Engineering* 57 (11 – 12), pp. 1059 – 1065. DOI: 10.1016/j.coastaleng.2010.07.001.

Bonneton, P. 2004. Wave celerity in the inner surf zone. *Proceedings of the 29th Conference on Coastal Engineering, Lisbon, Portugal*. ASCE AMERICAN SOCIETY OF CIVIL ENGINEERS, p. 392.

Brodie, K. L., Slocum, R. K., and McNinch, J. E. 2012. New insights into the physical drivers of wave runup from a continuously operating terrestrial laser scanner. *Oceans, 2012*, pp. 1 – 8. DOI: 10.1109/OCEANS.2012.6404955.

Catálan, P. A. and Haller, M. C. 2008. Remote sensing of breaking wave phase speeds with application to non-linear depth inversions. *Coastal Engineering* 55 (1), pp. 93 – 111. DOI: 10.1016/j.coastaleng.2007.09.010.

Evans, A. J. 2010. Laser scanning applied to hydraulic modeling. *International Archives of Photogrammetry, Remote Sensing and Spatial Information Sciences, Commission V Symposium, Newcastle upon Tyne, UK*.

Guedes, R. M. C., Bryan, K. R., Coco, G., and Holman, R. A. 2011. The effects of tides on swash statistics on an intermediate beach. *Journal of Geophysical Research: Oceans* 116 (C4). DOI: 10.1029/2010JC006660.

Guedes, R. M., Bryan, K. R., and Coco, G. 2012. Observations of alongshore variability of swash motions on an intermediate beach. *Continental Shelf Research* 48, pp. 61 – 74. DOI: 10.1016/j.csr.2012.08.022.

Harry, M., Zhang, H., Lemckert, C., and Colleter, G. 2010. 3D Spatial Definition of a Water Surface. *The Ninth ISOPE Pacific/Asia Offshore Mechanics Symposium, 14-17 November, Busan, Korea*.

Irish, J. L., Wozencraft, J. M., Cunningham, A. G., and Giroud, C. 2006. Nonintrusive Measurement of Ocean Waves: Lidar Wave Gauge. *Journal of Atmospheric and Oceanic Technology* 23, pp. 1559–1572. DOI: 10.1175/JTECH1936.1.

Park, H. S., Sim, J. S., Yoo, J., and Lee, D. Y. 2011. Breaking wave measurement using Terrestrial LIDAR: validation with field experiment on the Mallipo Beach. *Proceedings 11$^{th}$ International Coastal Symposium*. Vol. SI 64. Journal of Coastal Research, pp. 1718–1721.

Postacchini, M. and Brocchini, M. 2014. A wave-by-wave analysis for the evaluation of the breaking-wave celerity. *Applied Ocean Research* 46, pp. 15 – 27. DOI: 10.1016/j.apor.2014.01.005.

Power, H. E., Hughes, M. G., Aagaard, T., and Baldock, T. E. 2010. Nearshore wave height variation in unsaturated surf. *Journal of Geophysical Research: Oceans* 115 (C8). DOI: 10.1029/2009JC005758.

Raubenheimer, B., Guza, R. T., and Elgar, S. 1996. Wave transformation across the inner surf zone. *Journal of Geophysical Research: Oceans* 101 (C11), pp. 25589 – 25597.

SICK. 2015. Laser Measurement Sensors of the LMS5xx Product Family - Operating Instructions.

Sabatier, F. 2008. Modélisation de l'impact du changement climatique sur l'érosion des dunes. Application à la Camargue. *La Houille Blanche* (1), pp. 40 – 49.

Sabatier, F., Anthony, E. J., Héquette, A., Suanez, S., Musereau, J., Ruz, M.-H., and Regnauld, H. 2009a. Morphodynamics of beach/dune systems: examples from the coast of France. *Géomorphologie: relief, processus, environnement* (1/2009), pp. 3 – 22.

Sabatier, F., Samat, O., Ullmann, A., and Suanez, S. 2009b. Connecting large-scale coastal behaviour with coastal management of the Rhône delta. *Geomorphology* 107 (1–2). Coastal vulnerability related to sea-level rise, pp. 79 – 89. DOI: 10.1016/j.geomorph.2006.09.026.

Sallenger, A. H. and Holman, R. A. 1985. Wave energy saturation on a natural beach of variable slope. *Journal of Geophysical Research: Oceans* 90 (C6), pp. 11939 – 11944. DOI: 10.1029/JC090iC06p11939.

Schäffer, H. A., Madsen, P. A., and Deigaard, R. 1993. A Boussinesq model for waves breaking in shallow water. *Coastal Engineering* 20 (3–4), pp. 185 – 202. DOI: 10.1016/0378-3839(93)90001-O.

Sénéchal, N., Dupuis, H., and Bonneton, P. 2004. Preliminary hydrodynamic results of a field experiment on a barred beach, Truc Vert beach on October 2001. *Ocean Dynamics* 54 (3-4), pp. 408 – 414. DOI: 10.1007/s10236-003-0052-9.

Sénéchal, N., Rey, V., Bonneton, P., and Dupuis, H. 2006. On the Difficulty of Correctly Determining the Characteristic Wave Period in the Surf Zone. *Coastal Dynamics '05: Proceedings of the Fifth Conference on Coastal Dynamics, Barcelona, Spain*, pp. 1 – 12. DOI: 10.1061/40855(214)31.

Sénéchal, N., Dupuis, H., Bonneton, P., Howa, H., and Pedreros, R. 2001. Observation of irregular wave transformation in the surf zone over a gently sloping sandy beach on the French Atlantic coastline. *Oceanologica Acta* 24 (6), pp. 545 – 556. DOI: 10.1016/S0399-1784(01)01171-9.

Stockdon, H. F. and Holman, R. A. 2000. Estimation of wave phase speed and nearshore bathymetry from video imagery. *Journal of Geophysical Research: Oceans* 105 (C9), pp. 22015 – 22033. DOI: 10.1029/1999JC000124.

Svendsen, I. A., Madsen, P. A., and Buhr Hansen, J. 1978. Wave characteristics in the surf zone. *Proceedings of the 16th Conference on Coastal Engineering, Hamburg, Germany*, pp. 520 – 539.

Thornton, E. B. and Guza, R. T. 1982. Energy saturation and phase speeds measured on a natural beach. *Journal of Geophysical Research: Oceans (1978 – 2012)* 87 (C12), pp. 9499 – 9508.

Tissier, M., Bonneton, P., Almar, R., Castelle, B., Bonneton, N., and Nahon, A. 2011. Field measurements and non-linear prediction of wave celerity in the surf zone. *European Journal of Mechanics - B/Fluids* 30 (6), pp. 635 – 641. DOI: 10.1016/j.euromechflu.2010.11.003.

Tissier, M., Bonneton, P., Michallet, H., and Ruessink, B. G. 2015. Infragravity-wave modulation of short-wave celerity in the surf zone. *Journal of Geophysical Research: Oceans* 120 (10), pp. 6799 – 6814. DOI: 10.1002/2015JC010708.

Tissier, M., Almar, R., Bonneton, P., Michallet, H., Birrien, F., Bakker, A. de, and Ruessink, G. 2013. Individual wave celerity in the surf zone of a low-sloping laboratory beach. *Coastal Dynamics '13: Proceedings of the Seventh Conference on Coastal Dynamics, Arcachon, France*.

Tissier, M., Bonneton, P., and Ruessink, G. 2017. Infragravity waves and bore merging. *Proceedings of the Conference on Coastal Dynamics, Helsingør, Denmark*.

Vousdoukas, M. I., Kirupakaramoorthy, T., Oumeraci, H., Torre, M. de la, Wübbold, F., Wagner, B., and Schimmels, S. 2014. The role of combined laser scanning and video techniques in monitoring wave-by-wave swash zone processes. *Coastal Engineering* 83, pp. 150 – 165. DOI: 10.1016/j.coastaleng.2013.10.013.

Wübbold, F, Vousdoukas, M., Hentschel, M, and Wagner, B. 2012. Towards Autonomous Coastal Monitoring using 3D Laser Range Scanners and Camera Vision. *Proceedings of the 33rd Conference on Coastal Engineering, Santander, Spain*.

Yoo, J., Fritz, H. M., Haas, K. A., Work, P. A., and Barnes, C. F. 2011. Depth inversion in the surf zone with inclusion of wave nonlinearity using video-derived celerity. *Journal of Waterway, Port, Coastal, and Ocean Engineering* 137 (2), pp. 95 – 106. DOI: 10.1061/(ASCE)WW.1943-5460.0000068.

## Chapter concluding remarks

In this Chapter, a new surface elevation dataset was collected with a LiDAR scanner in the inner surf and swash zones of Rousty beach, France. An innovative wave-by-wave approach was developed and applied to this dataset: individual wave properties are extracted by detecting the wave crests in the surface elevation timeseries. These wave crests are then tracked until the swash zone, giving the possibility to study cross-shore changes of individual wave properties ($H$, $T$, $c$). Close to the inner surf/swash zone boundary and as waves propagate towards the shoreline, an increasing divergence between individual and spectral wave periods was observed. This has also been observed by previous authors when frequent bore merging occurs, especially in the presence of low-frequency waves, which has the effect of reducing the number of wave crests and hence increases the individual wave period (Sénéchal et al., 2006; Tissier et al., 2017). The scatter observed in the different individual wave properties has implications for the further use of these wave-by-wave analyses in surf zone datasets obtained by LiDAR scanners. Postacchini and Brocchini (2014) reported similar scatter in their dataset of individual wave celerity; this shows the diversity and complexity of processes occurring in the surf zone, such as the presence of low-frequency waves and their effect on shorter wave propagation (see also Tissier et al., 2015). To study the cross-shore evolution of incident wave properties, the potential presence of other physical processes must be identified and accounted for during the analysis if needs be (e.g. through the use of appropriate techniques on the data).

# Chapter 4

## The influence of swash-based reflection on surf zone hydrodynamics: a wave-by-wave approach

Kévin Martins*, Chris E. Blenkinsopp, Rafael Almar and Jun Zang, "The influence of swash-based reflection on surf zone hydrodynamics: a wave-by-wave approach", Coastal Engineering, 122, 2017. DOI: 10.1016/j.coastaleng.2017.01.006

## Abstract

A detailed understanding of the behaviour of waves in the nearshore is essential for coastal engineers as these waves cause beach erosion, coastal flooding and damage to coastal structures. Significantly, the influence of reflected waves is often neglected in surf zone studies, although they are known to influence wave properties and circulation in the nearshore. In this paper, a phase-resolving model is rigorously applied to model conditions from the prototype-scale BARDEXII experiment in order to examine and assess the influence of swash-based reflection on surf zone hydrodynamics at both the individual wave and time-averaged timescales. Surface elevation is separated into incoming and outgoing signals using the Radon Transform and a crest tracking algorithm is used to extract incident and reflected wave properties. It is found that on steep beaches ($\tan\beta > 1:9$) the swash-based reflection - the reflection generated in the swash during the backwash - contributes significantly to the intrawave variability of individual wave properties such as the wave height to water depth ratio $\gamma$, through the generation of quasi-nodes/antinodes system. For $\gamma$ expressed with individual wave heights, variations up to 25% and 40% are obtained for the modelled regular and irregular wave tests, whereas it reaches 15% when it is based on the significant wave height. The outgoing wave field-induced hydrodynamics is also found to affect time-averaged parameters: undertow and horizontal velocity skewness. The undertow is mainly strengthened, particularly in the shoaling region where the outgoing component dominates over the contribution from the incoming wave field. Offshore of the bar, an onshore-directed flow streaming close to the bed is also generated under the outgoing wave field, and is suspected to help in stabilising the bar position. This, along with the influence of the outgoing wave field on the horizontal velocity skewness and the presence of quasi-standing waves, suggests a complex contribution of the hydrodynamics induced by swash-based reflection into sediment transport rates and nearshore bar generation/migration.

# Chapter 4.

## Declaration concerning the article used for this Chapter:

| | |
|---|---|
| Title | The influence of swash-based reflection on surf zone hydrodynamics: a wave-by-wave approach |
| Status | Published and available in Open Access in Coastal Engineering (Elsevier) |
| Details | Kévin Martins*, Chris E. Blenkinsopp, Rafael Almar and Jun Zang, "The influence of swash-based reflection on surf zone hydrodynamics: a wave-by-wave approach", Coastal Engineering, 122, 2017.<br>DOI: 10.1016/j.coastaleng.2017.01.006 |
| Contribution from the authors | K. Martins: Processing of the data and analysis; Setup of the numerical model; Manuscript (70%)<br>C.E. Blenkinsopp: Collection of the LiDAR data; Edited drafts of manuscript (15%)<br>R. Almar: Suggestions for analysis; Edited drafts of manuscript (10%)<br>J. Zang: Edited drafts of manuscript (5%) |
| Statement | This paper reports on original research I conducted during the period of my Higher Degree by Research candidature. |
| Date and Signature | |

## Preamble

In Chapter 3, we presented the first field deployment of LiDAR scanner performed during this PhD. A methodology to study individual wave properties was described and the two following limitations were highlighted during the study:

- The experimental setup: the LiDAR scanner was deployed atop a tower in the swash zone. The dataset was hence limited to small wave heights ($H_s \sim 0.2\,\mathrm{m}$) and very shallow water depths ($h \leq 0.4\,\mathrm{m}$).
- At the wave-by-wave scale, a multitude of processes contribute to the scatter of individual wave properties (e.g. infragravity waves, bore merging and possibly reflection).

These observations motivate the development of a new methodology that allows the analysis of 'true' incident wave properties. The main objective of this Chapter is to develop such a methodology, using a combination of mathematical tools (Radon Transform, Radon, 1917) and the previously developed wave-by-wave methodology presented in Chapter 3.

The dataset used in this chapter consists of the experimental dataset obtained during the prototype-scale BARDEXII experiments (Masselink et al., 2016) and a numerical dataset produced with the CFD toolbox OpenFOAM®. The numerical model was used to reproduce two monochromatic and one irregular wave tests from the BARDEXII experiments and has partly been validated by an innovative LiDAR dataset of breaking waves. The comparison of the numerical and LiDAR datasets with the pressure-derived surface elevation data emphasizes the limitations of linear wave theory to reconstruct wave profiles around the break point. When applied to correct for depth attenuation of the pressure signal, linear wave theory fails to reconstruct the sharp wave crest in highly non-linear conditions, which leads to an underestimation of the wave height and an inaccurate description of the wave skewness.

Thanks to the Radon Transform, the incident and reflected components of the surface elevation can be separated. The wave tracking can then be directly applied to these separated surface elevation fields, allowing the extraction of incident and reflected wave properties in both the shoaling area and the surf zone. The influence of reflected waves on incident wave properties is directly quantified by comparing the wave properties extracted from the incident and total signals. Linear wave theory is also used on the modelled cross-shore current velocities at every location and depth in the wave flume to investigate the influence of reflected waves on time-averaged quantities (undertow, skewness and asymmetry).

# Chapter 4.

## 4.1 Introduction

Wave reflection from beaches and other coastal features is known to influence incident wave-induced hydrodynamics and therefore morphodynamics (Miles et al., 2001; Brocchini and Baldock, 2008).

While there are many studies of structure-induced reflection present in the literature (see Zanuttigh and Meer, 2008, for a relatively recent comparison of extensive datasets), it is evident that prior studies focusing on wave reflection from natural beaches, especially in the sea/swell band ($0.05\,\text{Hz} \leq f \leq 0.5\,\text{Hz}$), are relatively limited. The reflection of monochromatic waves over a slope was first investigated by Iribarren and Nogales (1949), and Miche (1951) and it has been shown that the reflection coefficient of a slope, defined as the ratio between incident and reflected wave height $K = H_r/H_i$, is linked to the surf-similarity parameter (Battjes, 1974):

$$\xi = \tan\beta / \sqrt{H_o/L_o} \tag{4.1}$$

where $\beta$ is the structure or beach slope, and $H_o$ and $L_o$ are the offshore wave height and wavelength, respectively. While the reflected wave phase was found to be only dependent on the offshore wave steepness and the slope (Hughes and Fowler, 1995), the amplitude of reflected waves are substantially influenced by the bottom roughness and permeability, but also the nature of wave transformation across the surf zone (Battjes, 1974; Hughes and Fowler, 1995; Miles and Russell, 2004, and many others). By presenting cross-shore varying reflection coefficients from two field-based experimental datasets, Baquerizo et al. (1997) observed a net increase in reflection coefficients shoreward of the break point, and suggested that when defining the reflection coefficient of a beach, it should be measured as far offshore as possible. Although this approach is appropriate for studying the bulk outgoing wave energy from a beach, it presents several issues. Assessing the outgoing energy further from shore increases the risk of observing additional phenomenon, particularly from non-linear wave interactions (Elgar and Guza, 1985; Bakker et al., 2015), that can lead to reflection coefficients higher than unity (Sheremet et al., 2002). Furthermore and as discussed by Battjes (1974), based on the methodology of Miche (1951), the processes responsible for incident wave energy dissipation in the surf zone (mainly friction and breaking) have to be approximated, while a measurement close to the swash zone would lead to an exact estimation of reflected waves (height and phase), using the local incident properties.

In the few field-based studies focusing on wave reflection in the sea/swell range of frequencies, it was generally demonstrated that reflection could be substantial (Elgar et al., 1994; Miles and Russell, 2004; Almar et al., 2014b). Using an array of 24 bottom-mounted pressure sensors, Elgar et al. (1994) found that up to 18% of the incident sea-swell frequency band was reflected back into the surf zone. These relatively high levels of reflected energy in the surf affect the incident waves in a variety of ways. Fluctuations in the currents velocities due to the reflected wave orbital velocities influence the sediment suspension (Miles et al., 2001), also potentially influencing the velocity skewness, important

for onshore sediment transport (Elfrink et al., 1999; Doering et al., 2000). Instantaneous sea levels are also influenced by the presence of seaward propagating wave crests and troughs, which influence the wave height to depth ratio $\gamma$, due to the presence of quasi-standing waves (Hoque et al., 2002). Many parameterisations are present in the literature to describe the cross-shore variation of this wave parameter, related to the wave energy dissipation (see for example the pioneering work of Battjes and Janssen, 1978). While existing parameterisations of $\gamma$ do not explicitly account for wave reflection, both $\gamma$ and reflection are a function of beach slope and wave number (Raubenheimer et al., 1996; Sénéchal, 2003; Martins et al., 2016). It is known that the beach slope controls the wave reflection to a great extent (see above, and Almar et al., 2014b; Almar et al., 2015). Through observation of the influence of strong backwash flows on the generation of individual reflected waves at the surf-swash boundary, a link might be expected between reflected waves generated by swash flows and the wave height to water depth ratio of individual waves in the surf zone, though no evidence is present in the literature.

A lack of field-based studies of sea/swell reflection on beaches can be explained by the complexity in measuring the energy bulk reflected from a beachface. Several methods to separate incoming from outgoing wave fields exist; see for example Inch et al. (2016) for a recent description. Correlation functions between 2 wave gauges were used (Kajima, 1970; Thornton and Calhoun, 1972, in Goda and Suzuki, 1976) before Goda and Suzuki (1976) introduced the use of Fast-Fourier Transform (FFT) to speed up this process. This was later extended to a larger array of wave gauges - see for example Mansard and Funke (1980), Zelt and Skjelbreia (1992) or Lin and Huang (2004) - which enables the error in the separation process to be reduced (Inch et al., 2016). Other methods such as PUV (Pressure, U horizontal and V vertical current velocities, Guza and Bowen, 1976), or approaches based on long-wave theory described in Guza et al. (1984) use collocated pressure or surface elevation signals, and horizontal current velocities to separate incoming and outgoing signals at a cross-shore location. Using a totally different approach, Almar et al. (2014a) describe the use of the Radon Transform (RT) for nearshore wave studies, with the objective of finding tools to facilitate wave-by-wave analyses. Mostly used in image processing, the RT can be applied to the projection of a cross-shore/temporal diagram $\eta(x,t)$ into points in the Radon (polar) space. This method is therefore particularly suitable in the surf zone as with increasing non-linearities, the wave tracks appear as well-defined lines in such diagrams (e.g. Almar et al., 2013). Almar et al. (2014a) successfully separated incident and reflected long-wave signals from a laboratory dataset and demonstrated that the results compared well with those from a Boussinesq model.

In this study, the RT is applied to the results from a phase-resolving numerical model simulating two monochromatic and one irregular wave tests, performed at prototype-scale in the Delta flume during the BARDEXII project (Masselink et al., 2016). The primary objective is to study the impact of reflected waves on incident wave properties and surf hydrodynamics with a focus on sea/swell waves. For irregular waves, the free surface is actually a sum of wave trains, with different frequency and possibly direction (incident and

reflected). In this regard, a wave-by-wave approach is developed based on the previous work of Martins et al. (2016), allowing individual wave tracking from the shoaling area to the runup limit, and back into the flume after reflection.

The paper is organised as follows. Section 4.2 introduces the experimental and numerical datasets. The numerical model is validated using a large array of instruments, including a Terrestrial Laser Scanner (TLS) that enables the description of the wave shape during breaking. The signal separation in incoming/outgoing components and the wave-by-wave approach used to track individual wave properties are described in Section 4.3. Section 4.4 presents the results on the separation methods and its application for the study of swash-based reflection influence on surf zone hydrodynamics at the individual wave timescale. The concept of swash-based reflection is notably explained through a link with swash events potential energy. The results and the influence of reflection at longer timescales are then discussed in Section 4.5. Finally Section 4.6 provides the conclusions of this study.

## 4.2 Experimental and numerical datasets

### 4.2.1 The BARDEXII experiments

The present study uses experimental data obtained during the 2-month-long BARDEXII experiment (Masselink et al., 2016). In order to study wave processes and cross-shore sediment transport in the surf and swash zones, a coarse sandy beach/barrier system was built in the prototype-scale Delta Flume (Vollenhove, The Netherlands). The A6 and A7 monochromatic test cases (hereafter A6-mono and A7-mono) and A6-01 irregular wave test are the focus of the present study (Masselink et al., 2016). Regular second-order Stokes waves were generated during the A6-mono and A7-mono tests by a second-order wave steering system at $x = 0$ m, with an Active Reflection Compensation system (ARC) for the absorption of reflected waves. For the A6-01 irregular test, a JONSWAP spectrum with a peak enhancement factor of 3.3, was imposed in the wave flume. The initial beach profile of $1 : 15$ slope between $x = 49 - 109$ m evolved under the wave action during Series A1 to A7 to result in the bed profiles presented in Figure 4.1, presenting a much steeper upper beach face, a bar system for the A6-01 and A6-mono, and a terrace for the A7-mono. The wave forcing conditions and beach slope for the different wave tests examined here are presented in Table 4.1.

A large array of instrumentation was used during the experiments, and only part of the experimental dataset is used to validate the numerical model used herein. The positions of the instruments used in the present work are shown in Figure 4.1. A series of pressure transducers (PT) and electro-magnetic current meters (EMCM) both sampled at 20 Hz were located in the shoaling and surf zones to measure the pressure and flow velocity under propagating and breaking waves. Two terrestrial laser scanners were deployed to measure free surface elevations within the flume, the first was positioned in the surf zone at $x = 73.6$ m, 3.9 m above mean sea level (MSL) while the second was deployed at $x = 88.3$ m, 3.8 m above MSL to study the swash zone hydrodynamics and morphodynamics. The TLS

Table 4.1: Wave and beach conditions for the different wave tests. For the monochromatic wave tests, $H_o$ was computed as four times the standard deviation of the surface elevation measured at the wave paddle.

| Run | $H_o$ (m) | $T_p$ (s) | MSL (m) | $\beta_{surf}$ | $\beta_{swash}$ | $\xi_{surf}$ | $\xi_{swash}$ |
|---|---|---|---|---|---|---|---|
| A1-mono | 0.94 | 8 | 3.00 | 1:13 | 1:11 | 0.52 | 0.60 |
| A2-mono | 0.71 | 8 | 3.00 | 1:13 | 1:13 | 0.58 | 0.61 |
| A4-mono | 0.67 | 8 | 3.00 | 1:14 | 1:10 | 0.58 | 0.83 |
| A6-01 | 0.70 | 10.90 | 2.98 | 1:12 | 1:9 | 0.63 | 0.97 |
| A6-mono | 0.74 | 12.10 | 3.00 | 1:15 | 1:8 | 0.64 | 1.10 |
| A7-mono | 0.76 | 12.10 | 3.00 | 1:17 | 1:8 | 0.54 | 1.18 |
| A7T10-mono | - | 10 | 3.00 | 1:17 | 1:8 | 0.49 | 1.07 |
| A7T11-mono | - | 11 | 3.00 | 1:17 | 1:8 | 0.52 | 1.12 |

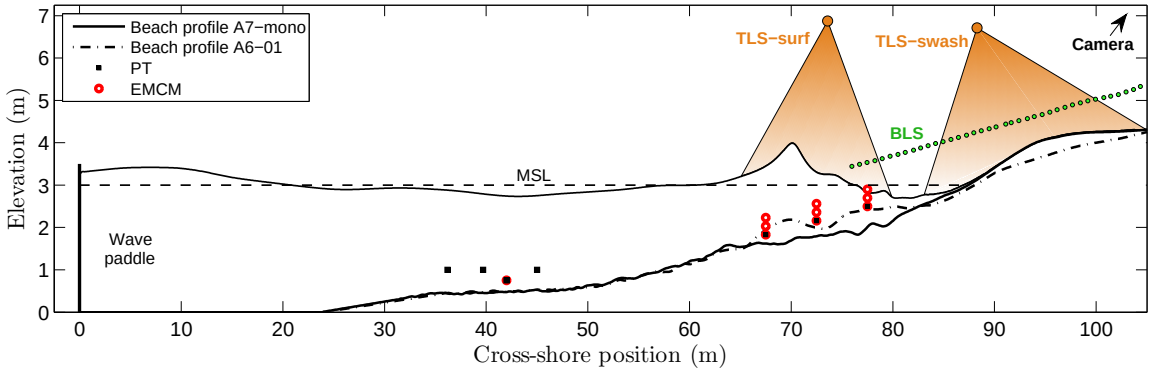


Figure 4.1: Schematic of the experimental setup for the A6-mono, A7-mono and A6-01 wave tests. The two different initial beach profiles are shown. A dataset from the following instruments was used in the present study: 7 pressure transducers (PT) and electro-magnetic current meters (EMCM) located in the shoaling and surf zones and two terrestrial laser scanners (TLS) deployed at 6.8 and 6.9 m above the flume bed (3.8 and 3.9 mMSL, respectively) within the surf and swash zones. The zones covered by the TLS are indicated with the orange cones.

recorded data at an angular resolution of 0.25° and sample rate of 35 Hz; the measurements were processed following Martins et al. (2016) including the correction of the scanner orientation, noise filtering and spatial interpolation onto a regular grid.

TLS data is ideal for wave-by-wave analysis of surf zone processes as the high-spatial and temporal resolutions of the measurements allow for the description of wave geometry and the tracking of individual wave properties through hundreds of cross-shore positions. Physical constraints within the flume limited the elevation of the TLS and hence the horizontal extent of the measurements, however the high resolution of the data enabled the wave shape to be captured in the swash zone and around the primary break point for detailed model validation.

The PT data were used to retrieve the surface elevation using the linear wave theory,

and the classic pressure response factor (see e.g. Bishop and Donelan, 1987):

$$K_p = \frac{\cosh\left(k(\bar{h}+z)\right)}{\cosh\left(k\bar{h}\right)} \tag{4.2}$$

where $\bar{h}$ is the mean water depth, $k$ is the radian wavenumber and $z$ the PT deployment depth. The methodology described by Inch (2014) was followed, using the high frequency cut-off $w_c = 0.564\pi\sqrt{g/\bar{h}}$ (where $g$ is gravity) proposed in Green (1999), to prevent noise amplification. Correcting the signal depth attenuation with linear wave theory is known to lead to an underestimation of the wave crest elevation, especially for highly non-linear waves, see for instance Nielsen (1986), Townsend and Fenton (1996) or Barker and Sobey (1996). Bishop and Donelan (1987) suggested that wave heights could be retrieved within 5%, but no estimation based on wave-by-wave analysis has ever been carried out, thus the impact of the correction at this time scale is unknown. For that reason, the differences at the wave-by-wave scale between the TLS and PT datasets were assessed prior to any model validation.

Figure 4.2a shows the wave profiles measured at $x = 72.5\,\text{m}$, close to the break point, by both instruments for every wave of the A7-mono test case and its ensemble-average, with the modelled surface elevation also shown. In this study, the break point is defined as the point of maximum wave height; for this comparison it was assessed from the wave height evolution (TLS), comparisons between model and data presented further in this paper, and from video data (not shown here) in order to exclude the presence of foam that could increase discrepancies between datasets. It is demonstrated that at the early stage of breaking, the individual wave height is underestimated by approximately 30%. Additionally, considerable differences are observed in the two wave shapes (skewness and steepness): wave non-linearities at the wave-by-wave scale are largely underestimated when using the linear theory to retrieve the surface elevation. For these reasons, the raw pressure signals along the wave flume were used to validate the model. Figure 4.2b shows the ratio of the measured raw pressure to hydrostatic pressure, based on the surface elevation measured by the TLS. It is observed that the two estimates differ significantly before the wave crest where the pressure is higher than hydrostatic and at the crest location, where the measured pressure is well below hydrostatic; a result consistent with previous experimental datasets (Stive, 1980).

Closer to shore, an array of 45 ultrasonic bed level sensors (BLS, see Figure 4.1 for locations) were deployed in the swash zone to measure water depths and monitor high-frequency bed level changes (Turner et al., 2008). Sampling at 4 Hz, the BLS are able to measure water depths and bed-level changes using acoustic signals with an accuracy of the order of 1 millimetre. Finally, an ARGUS video camera system was deployed above the beach, in order to monitor surf, swash and overwash processes. In this study, timestacks from the swash camera were used to track the instantaneous shoreline position for comparison with the simulated results.

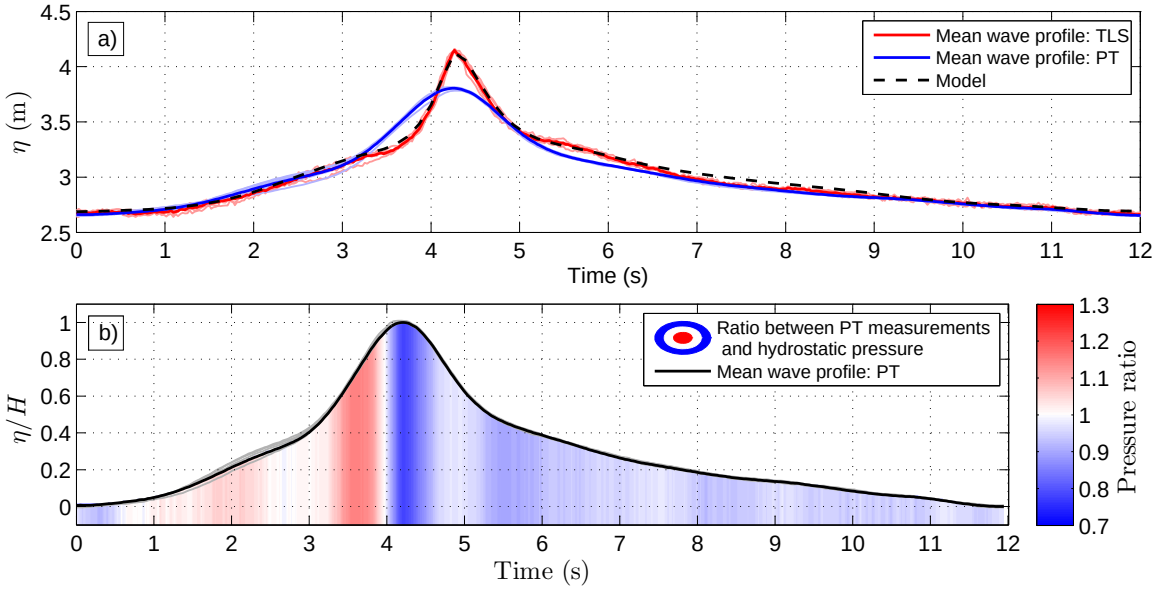


Figure 4.2: Comparison of individual wave profiles obtained from the surf-zone TLS and the PT, at the PT location $x$ = 72.5 m for the A7-mono test. Panel a) shows the wave profile of the modelled waves (light red and blue lines for the TLS and PT, respectively) with the ensemble averaged (thick red and blue lines for the TLS and PT, respectively). The modelled wave profile at that location is also shown as dashed black-line. In panel b), a contour plot of the ratio between the raw measured pressure and hydrostatic pressure based on the surface elevation measured by the TLS is shown: red zones correspond to periods when the pressure is higher than the hydrostatic, and blue zones correspond to periods where it is lower. The ensemble-averaged wave profile is shown as black line, while the gray lines represent individual wave profiles measured by the PT.

### 4.2.2 Numerical model: IHFOAM (Higuera et al., 2013)

The IHFOAM model (Higuera et al., 2013), based on the CFD package OpenFOAM® (v2.1.1 in the present study) was used to generate waves and simulate their propagation across the wave flume. A library for the wave generation and absorption at boundaries was implemented and the solver modified accordingly. The RANS equations described in Higuera et al. (2013) are solved using a VOF (Volume-of-Fluid) method to describe and track the free surface. A rectangular 2D computational mesh for each run was constructed based on survey data, using a cross-shore spacing of $dx$ = 0.05 cm and a varying $dz$, corresponding to a grid of 2100 × 60 = 126000 cells. The 2D mesh was manually created using the '.msh' format based on the window-averaged profile, so that no abrupt changes occur near the bed (see Figure 4.3a). It was then transformed into the OpenFOAM format using the *gmshtofoam* built-in function. The number of vertical layers was chosen such that the cell aspect ratio was approximately unity near the breaking zone (Figure 4.3b) to more accurately resolve the break point (Jacobsen et al., 2014). Sensitivity testing enabled the mesh size to be optimised to obtain a good compromise between CPU time and precision. A desktop PC with 8 GB of RAM and a 3.20 GHz quad-core processor was used to run the simulation, with a typical time step of 0.0005 s, varying to fulfil the Courant–Friedrichs–Lewy (CFL) local restrictions. For an 80 second run, this corresponded to approximately 53 hours of CPU time.

Boundary conditions at the wave paddle were generated using second-order Stokes

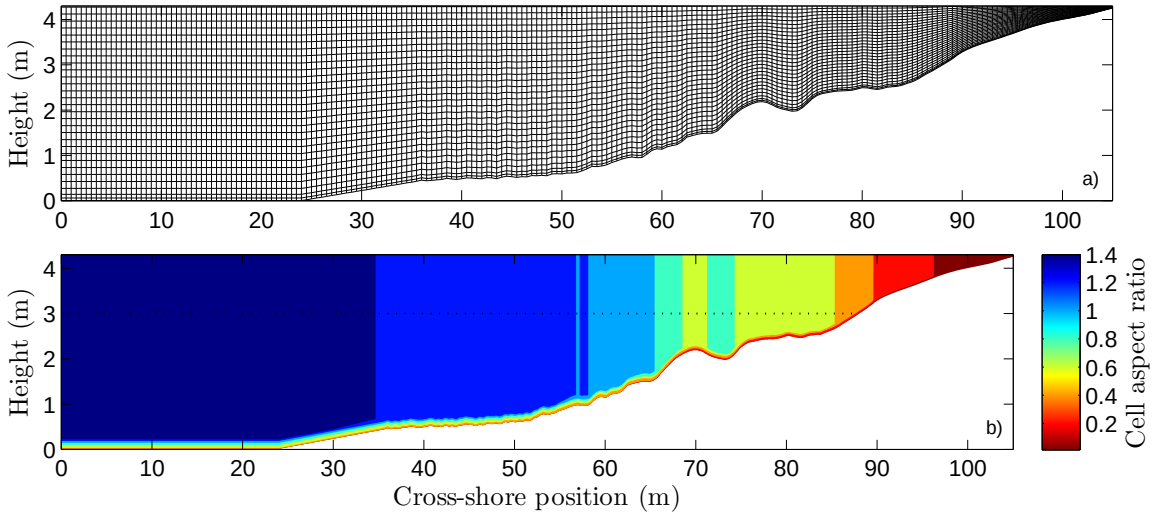


Figure 4.3: Description of the computational mesh: a) rectangle-based computational mesh for the A6-01 wave test, for visual reasons only every 2nd cell in the vertical direction and 10th cell in the horizontal direction are shown; b) contour plot of the cell aspect ratio.

theory (Dean and Dalrymple, 1991) for the A6 and A7 monochromatic wave cases. The A6-01 irregular wave case was generated using the actual wavemaker signal (paddle displacement and surface elevation). The active absorption at the wave paddle (located at $x = 0$, see Figure 4.1) was activated as the Delta flume is equipped with an ARC system, preventing radiated components from being re-reflected towards the artificial beach.

The VOF-based CFD method attributes an $\alpha$ value to the typically two modelled phases of interest, for instance air and water (Berberović et al., 2009). A cell containing only water corresponds to $\alpha = 1$, whereas a cell filled with air corresponds to $\alpha = 0$. The free surface was extracted by integrating $\alpha$ over the water column at a given position. This method is considered particularly suitable for spilling or weakly plunging waves, characterized by relatively low air entrainment. Finally, the $k - \omega$SST turbulence closure model developed by Menter (1994) was used as it was found to better reproduce the surface elevation than the classical $k - \epsilon$ and $k - \omega$ models (Brown et al., 2014). For further details on the model equations, the reader is referred to Higuera et al. (2013).

### 4.2.3 Validation of the numerical model

***Surface elevation and relative pressure in the surf zone***

The detailed surface elevation measurements from the TLS and ultrasonic BLS were used to validate the model predictions of free surface elevation around the break point. Figure 4.4 shows instantaneous comparisons between the TLS and BLS measurements and the modelled water phase for the A7-mono test case at 6 times during the breaking process. Comparisons show good agreement (RSME$<$ 0.06 m, $r^2 > 0.96$) at every stage of the breaking (wave shape evolution and breaking location), with the modelled free surface closely capturing the complex wave geometry resolved from hundreds of point measurements obtained by the TLS. Despite this good model agreement in mean errors (Table 4.2), the existence of short duration, low void fraction, but large magnitude splashes generated

during breaking (landward of $x = 76$ m, see Figure 4.4d) lead to large maximum errors (MAE). These splashes are captured by the TLS once the wave crest propagates landward of $x = 76$ m but are not expected to be resolved by the CFD model. In opposition, the significant MAE observed for the PT (Table 4.2) are due to the poor performance of linear theory to retrieve the surface elevation a this location (Figure 4.2).

To validate the modelled wave transformation across the wave flume the modelled relative pressure was compared with the raw pressure data from the PTs. For conciseness, only results for the 670s-long A6-01 irregular wave test are shown; the statistical errors from all tests are shown in Table 4.2. Figure 4.5 shows a 360 second window of the modelled and measured relative pressure timeseries from the shoaling area to the surf zone. The transformation of the incident waves is well described by the model (RMSE $= 0.02 - 0.04$ dbar and $r^2 = 0.92 - 0.97$), with a good representation of the wave profile changes. Though it is less clear than from a surface elevation timeseries, the more tooth-shaped wave profile after breaking (from $x = 72.5$ m) can clearly be seen. These comparisons show the potential of using the piston-type boundary conditions to generate irregular wave trains in prototype-scale experiments.

Table 4.2: Model skill for reproducing $\eta$ (PT and TLS), $p$ (PT), $u$ and $v$ (EMCM): root-mean square error (RMSE), absolute mean error, maximum absolute error and $r$ the linear correlation coefficient (defined as the ratio between the covariance of the two timeseries, and the product of their standard deviation). For conciseness, only minimum and maximum values along the flume are shown, for every modelled quantity and wave test. For the TLS, statistics are calculated only between $x = 70-78$ m, whereas for the PT, it concerns the PT positions visible in Figure 4.1.

| Quantity | Run | RMSE | AME | MAE | $r^2$ |
|---|---|---|---|---|---|
| $PT - \eta$ | A6-mono | 0.05-0.08 m | 0.04-0.06 m | 0.12-0.45 m | 0.84-0.98 |
| | A7-mono | 0.04-0.06 m | 0.03-0.04 m | 0.12-0.32 m | 0.93-0.98 |
| | A6-01 | 0.03-0.06 m | 0.02-0.04 m | 0.15-0.45 m | 0.85-0.97 |
| $TLS - \eta$ | A6-mono | 0.04-0.08 m | 0.04-0.06 m | 0.10-0.6 m | 0.95-0.99 |
| | A7-mono | 0.03-0.06 m | 0.02-0.04 m | 0.09-0.6 m | 0.96-0.99 |
| | A6-01 | 0.06-0.08 m | 0.04-0.06 m | 0.6-0.8 m | 0.85-0.90 |
| $p$ | A6-mono | 0.02-0.04 dbar | 0.02-0.03 dbar | 0.06-0.11 dbar | 0.98-0.99 |
| | A7-mono | 0.02-0.03 dbar | 0.01-0.02 dbar | 0.06-0.11 dbar | 0.99 |
| | A6-01 | 0.02-0.04 dbar | 0.02-0.03 dbar | 0.10-0.24 dbar | 0.92-0.97 |
| $u$ | A6-mono | 0.06-0.15 m/s | 0.05-0.10 m/s | 0.18-0.55 m/s | 0.89-0.98 |
| | A7-mono | 0.04-0.20 m/s | 0.03-0.17 m/s | 0.11-0.47 m/s | 0.97-0.98 |
| | A6-01 | 0.06-0.27 m/s | 0.05-0.20 m/s | 0.25-1.90 m/s | 0.78-0.96 |
| $v$ | A6-mono | 0.02-0.09 m/s | 0.02-0.07 m/s | 0.12-0.32 m/s | 0.38-0.70 |
| | A7-mono | 0.02-0.09 m/s | 0.02-0.07 m/s | 0.06-0.32 m/s | 0.47-0.84 |
| | A6-01 | 0.02-0.12 m/s | 0.01-0.07 m/s | 0.17-1.52 m/s | 0.19-0.21 |

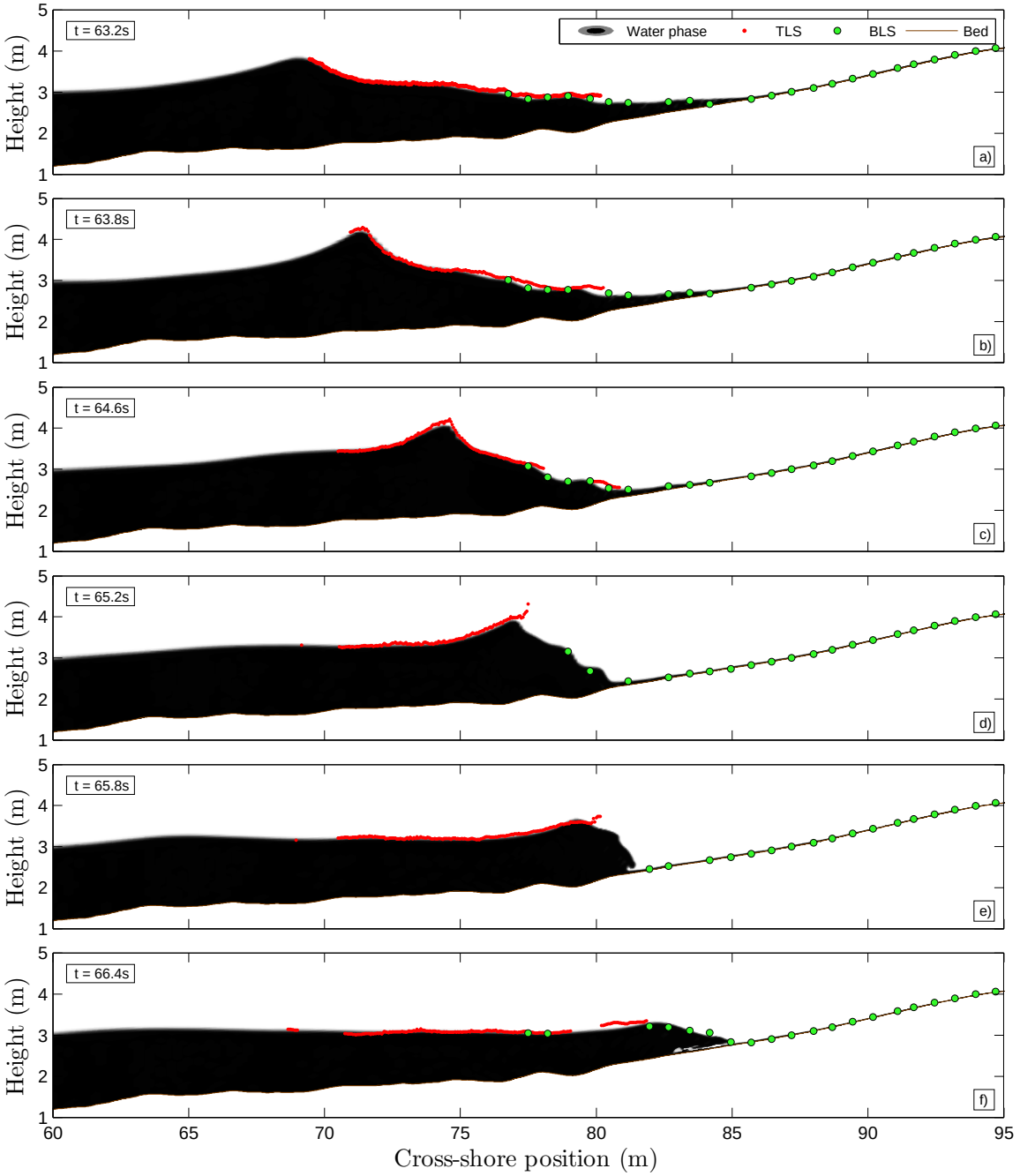


Figure 4.4: Comparison of the modelled water phase from the A7-mono wave test with the instantaneous free-surface elevation measurements from the TLS and the ultrasonic BLS. Six moments of the breaking process are shown.

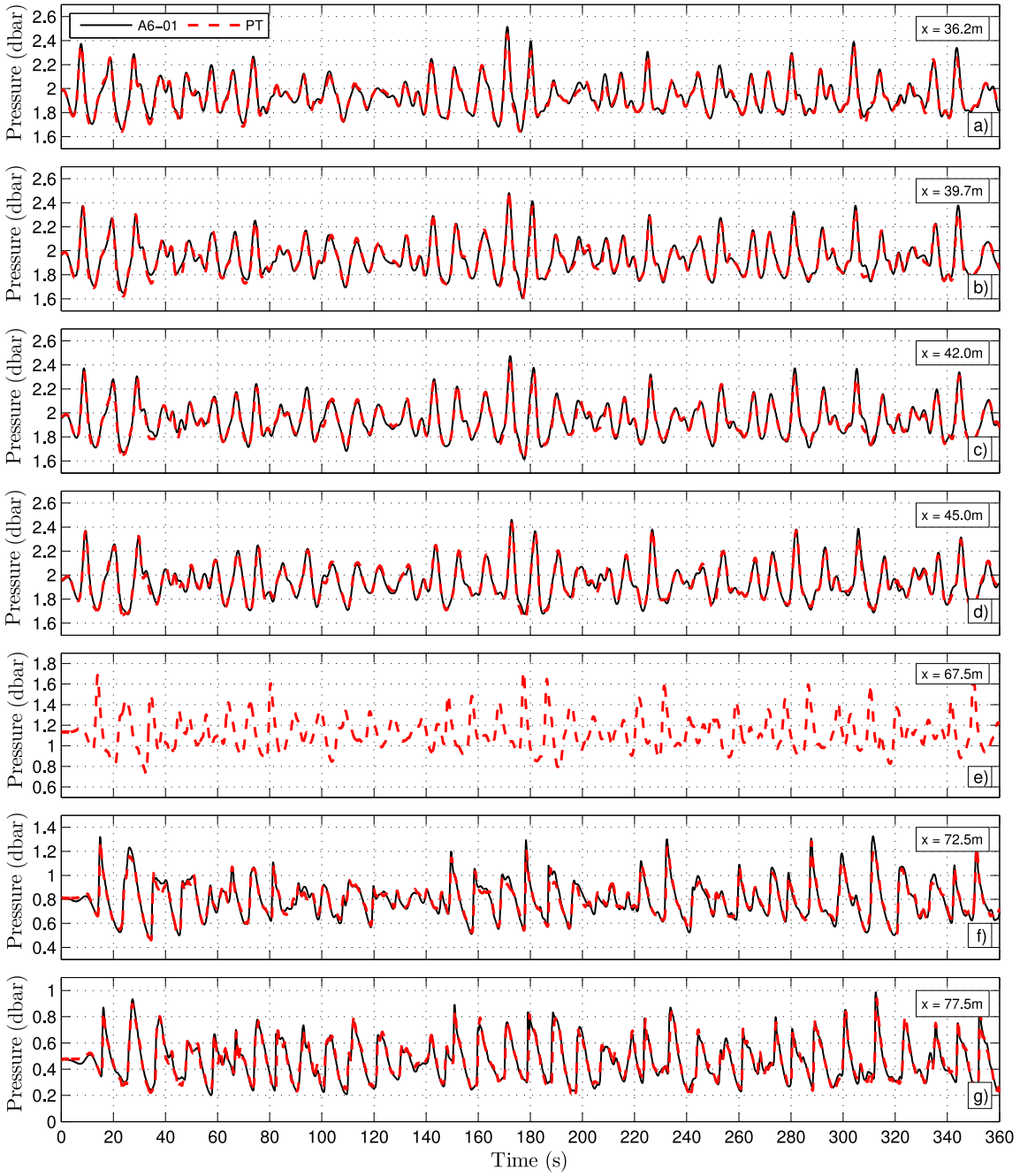


Figure 4.5: Validation of the modelled relative pressure at the PT locations for the A6-01 wave test, for the first 320 s of the simulation. The model and data timeseries are shown at five locations in the shoaling region and two in the surf zone. As seen in Figure 4.1, the pressure sensor located at $x = 67.5$ m is slightly buried, the model therefore cannot provide any signal for this location (out of domain).

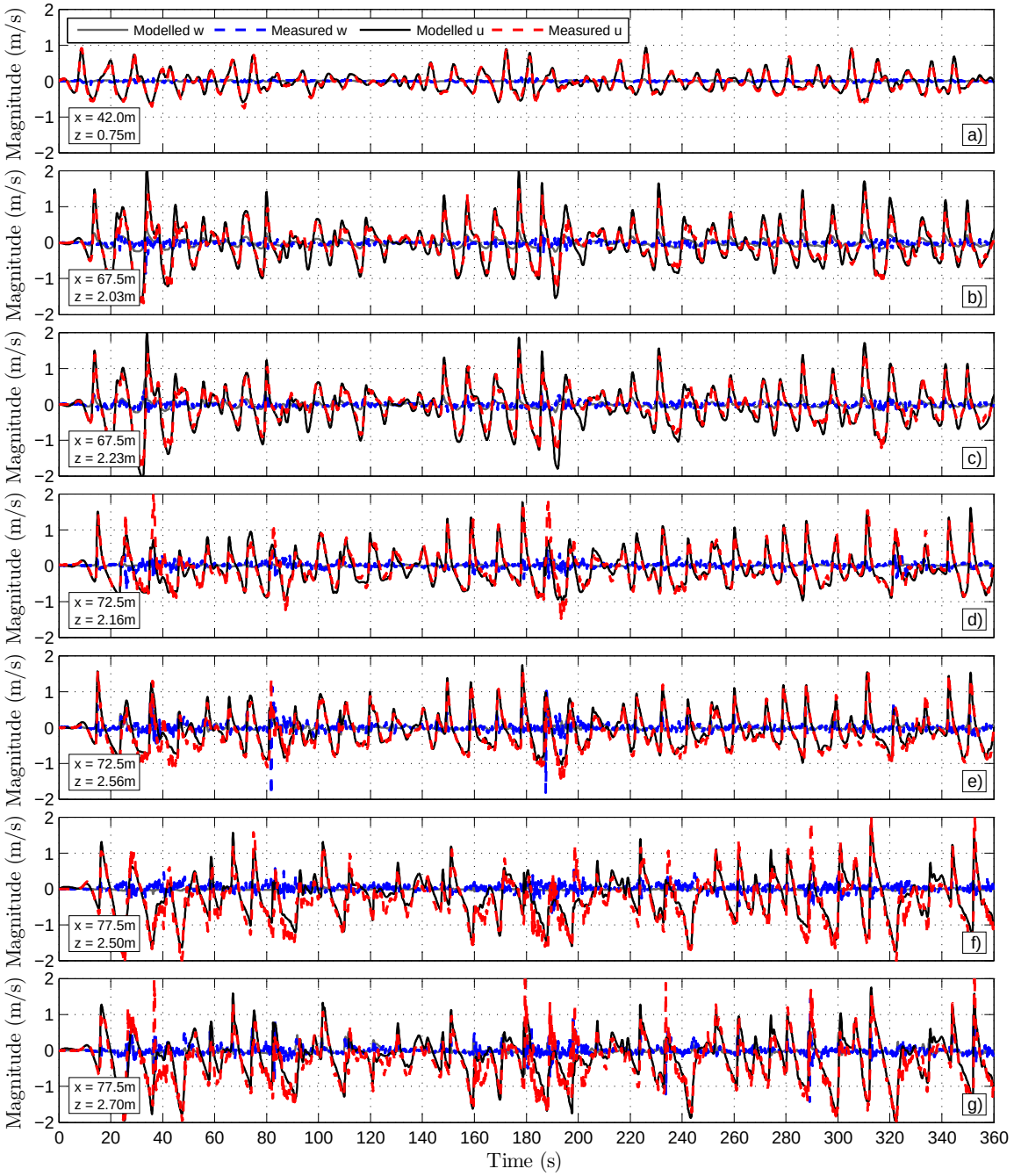


Figure 4.6: Validation of the modelled hydrodynamics at the EMCM locations for the A6-01 wave test, for the first 320 s of the simulation. Modelled horizontal U and vertical V timeseries are shown against measurements at one location in the shoaling region and six in the surf zone.

*Surf and the swash hydrodynamics*

Horizontal and vertical current velocities were measured at various cross-shore locations along the wave flume (see Figure 4.1). These measurements were used to validate the modelled wave-induced hydrodynamics in the shoaling and surf zones. Figure 4.6 shows comparisons of measured and modelled horizontal and vertical velocities for the A6-01 irregular wave test. Overall, the model successfully reproduces the wave-induced hydrodynamics through the shoaling region and surf zone (similar good agreement was found for the regular wave tests, see Table 4.2). More specifically, the high-magnitude current velocities observed after breaking ($x$ = 77.5 m) are well described in the numerical model. Some discrepancies are observed in these comparisons, where measured current velocities are noisy in some locations, e.g. close to the surface at $x$ = 77.5 m and $z$ = 2.70 m. These periods occur during the passage of the two largest wave groups, and could be explained by a high concentration of entrained air bubbles, which are known to introduce noise when using EMCMs (see for example Gailani and Smith, 2000; Elgar et al., 2005; Huang and Hwang, 2015).

As the swash zone is thought to significantly influence surf zone processes (Brocchini and Baldock, 2008), primarily due to its role in reflecting incident wave energy, the ability of the model to reproduce swash zone processes was assessed. The model results were compared against measurements of the shoreline position (ARGUS video camera) and swash depths (BLS and TLS). The cross-shore position of the shoreline was manually extracted from the video timestacks. The modelled shoreline was computed using a 3 cm threshold from the modelled water depths. Both modelled and measured shoreline cross-shore positions were transformed into a vertical elevation using the surveyed beach profile. Figure 4.7 shows the timeseries comparisons of modelled and measured shoreline elevation for the entire A6-01 test, along with a 2-minute subset of the data comparing cross-shore shoreline position and swash depths. Although the modelled runup extent is sometimes slightly overestimated (Figure 4.7a and 4.7b), comparisons show very good agreements between the two datasets. In particular, the timing of the uprush and downrush phases (Figure 4.7b) as well as water volumes (4.7c-e) are accurately reproduced. Figures 4.7c-e highlight some pros and cons of different methods for measuring flow depths in the swash zone (TLS and ultrasonic BLS in this case). In Figure 4.7c, it is observed that there are periods, particularly in the lower swash during backwash where insufficient light is scattered by the water surface and no signal return is detected by the TLS. Reduced ability to detect water depths during backwash and close to the shoreline is common when using TLS, and enhanced here by the reduced persistence of aeration observed in freshwater (e.g. Blenkinsopp and Chaplin, 2011). This effect means that TLS measurements tend to underestimate the shoreline position as observed by (Hofland et al., 2015). By contrast, the measurements from the BLS are much more consistent but are limited by the much reduced spatial resolution, meaning that the wave/bore front is less well resolved.

## 4.3 Methods

### 4.3.1 Separation of the incoming and outgoing signals

In the present study, the influence of reflected waves was studied at two distinct timescales: individual wave timescale and time-averaged over a complete wave test. In order to study the evolution of individual incident wave properties, the Radon Transform (RT) was applied to the modelled free surface elevation to separate the incoming and outgoing signals. The RT was successfully applied to study wave celerity and incident and reflected short and long waves by Almar et al. (2013) and Almar et al. (2014a). The method applies the following transformation (Radon, 1917) to a surface elevation signal $\eta(x,t)$:

$$R(\rho,\theta) = \iint \eta(x,t)\delta(x\cos\theta + t\sin\theta - \rho)dxdt \tag{4.3}$$

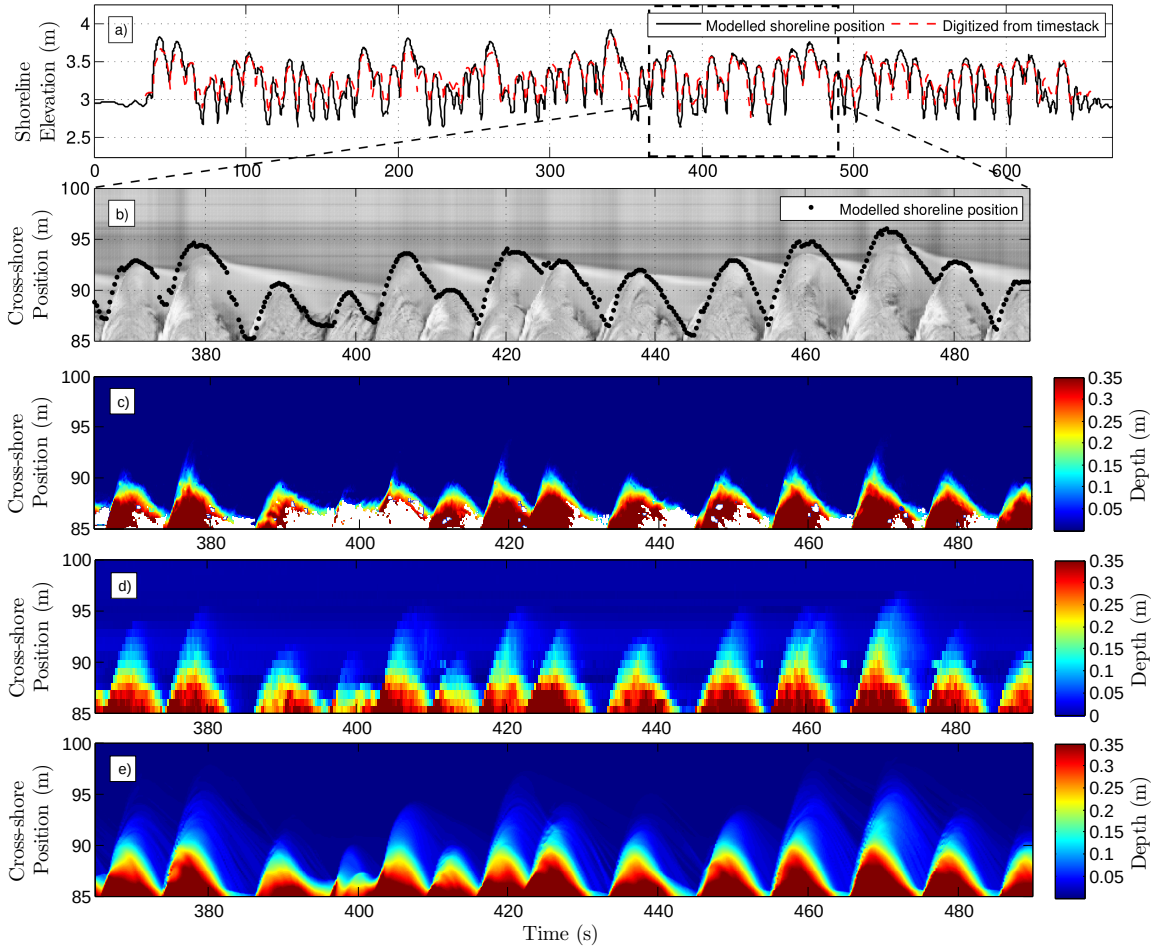


Figure 4.7: Validation of the model in the swash zone: a) Modelled shoreline elevation and digitised shoreline elevation from the ARGUS video camera timestack are shown for the entire wave test, b) ARGUS Video camera timestack along with the modelled shoreline cross-shore position for a 2 min window, c) Water depths measured by the swash zone TLS, d) Water depths measured by the array of ultrasonic BLS and e) Modelled water depths.

where $x$ represents the cross-shore dimension, and $t$ is time, $\delta$ is the Dirac function, $\rho$ and $\theta$ the distance and angle from origin of the integration line defined by $\rho = x\cos\theta + t\sin\theta$ (Almar et al., 2014a). As described in Almar et al. (2014a), lines in the Cartesian spatio-temporal space ($\eta(x,t)$ diagram) are represented by points in the Radon space.

More interestingly for the present study, when a wave reflects off the beach, it is also visible as a line in the aforementioned $\eta(x,t)$ diagram. By integrating the Radon signal over the correct angles with the inverse RT (Almar et al., 2014a), the separation of the incoming and outgoing signals is made possible. The result enables the modelled surface elevation to be described as:

$$\eta(x,t) = \eta_{inc}(x,t) + \eta_{out}(x,t) \tag{4.4}$$

where the *'inc'* and *'out'* subscripts refer to the incoming and outgoing components respectively. An example of this process is shown in Figure 4.8 for the A7-mono test which demonstrates the strength of this method: incident (Figure 4.8b) and reflected waves (Figure 4.8c) clearly appear as lines in the $\eta(x,t)$ diagram. Note that in this study, a difference is made between 'reflected' wave and 'outgoing' signal. While at the wave-by-wave time scale it is evident that the wave propagating seaward from the beach upper slope is generated through reflection, it is not clear how other signals propagating seaward are originated, especially at longer time scales (e.g. non-linear interactions). The term 'reflected wave' is therefore only used to describe seaward propagating waves generated at the boundary between the swash backwash and the inner surf that can be tracked (swash-based reflection). The same reasoning is applied to differentiate 'incident' wave from 'incoming' signal.

The separation based on the RT was compared in the frequency domain to the commonly used method of Guza et al. (1984) (hereafter Guza84). The Guza84 method was developed from long-wave theory and uses collocated surface elevation and horizontal current velocities signals to separate the incoming and outgoing components of surface elevation or horizontal current velocities. The use of this linear theory-based method is motivated by two reasons: 1) a performance comparison with the RT to assess the model capacity in reproducing the wave spectra and 2) the observed poor performance of the RT to resolve mean flow velocities after separation. While the RT was found to satisfactorily separate incoming and outgoing signals (for both $\eta$ and $u$), mean incoming and outgoing cross-shore flow velocities close to zero were found when time-averaged. The two possible explanations are the introduction of noise in the high frequencies, which makes the average of the whole signal tend to zero, or the less sharp 'lines' in the $u(x,t)$ diagram, compared to the $\eta(x,t)$ diagram observable in Figure 4.8a.

For this reason, linear theory was used to separate surface elevation and horizontal current velocity in order to study the influence of reflection on time-averaged surf zone parameters (undertow, wave setup and horizontal velocity skewness). Modelled horizontal current velocities were extracted from the results of the A6-01 test along the wave flume at various heights above the bed ranging from 0.01 m to 1.8 m (non-dimensional height $z' = z/\bar{h} \in [0, 0.6]$) using the Guza84 method (Miles et al., 1996). After performing the aforementioned current separation, horizontal current velocities were averaged over the

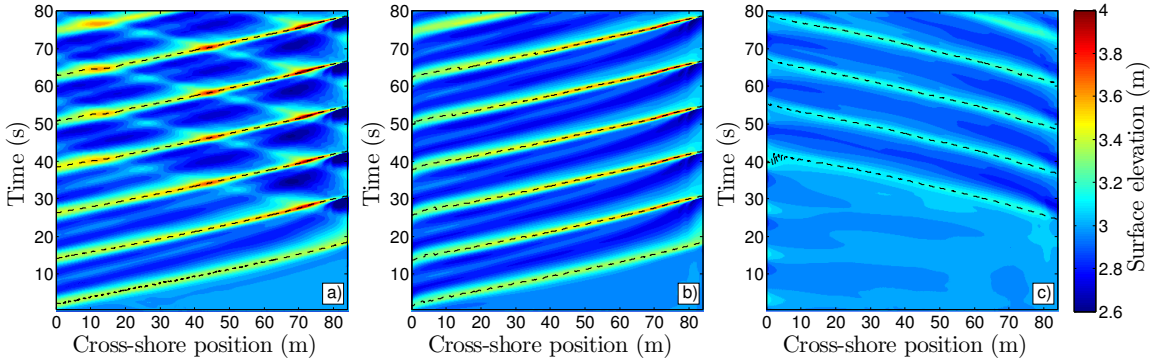


Figure 4.8: Incoming/outgoing signal separation of the modelled surface elevation using the RT: a) $\eta(x,t)$ diagram of the modelled surface elevation for the A7-mono wave test; b) $\eta_{inc}(x,t)$ diagram of the incoming signal; c) $\eta_{ref}(x,t)$ diagram of the outgoing signal. In every panel, the dashed black lines show the individual waves path, tracked with the methodology presented in Section 4.3.2.

entire test to compute the mean cross-shore current velocities (undertow) and velocity skewness defined as $S_k = \overline{u^3}/\overline{u^2}^{3/2}$, where $\overline{.}$ is the time-averaging operator.

### 4.3.2 Wave-by-wave approach

The results at the individual wave time scale presented in this paper rely on a wave-by-wave analysis, performed separately on the extracted incoming and outgoing signals. At every cross-shore position between $x = 0$ and 84 m, local peaks in the surface elevation timeseries (corresponding to wave crests) are identified to enable the extraction of individual wave properties (e.g. $H$,$T$), following an improved version of the methodology presented in Martins et al. (2016). Previous work has been undertaken to study individual wave properties; see for example recent studies of Power et al. (2010) and Power et al. (2015), Postacchini and Brocchini (2014). These methods are based on peak-to-peak analysis which bypasses the need for low-pass filtering but cannot deal with the superposition of waves travelling in either the same or opposing directions.

The present algorithm starts by extracting wave properties at an initial cross-shore position (e.g. $x = 0$ m, for incident waves) using peak analysis: wave crests are detected and wave troughs are defined as the minimum reached between two crests. Wave height $H$ is then defined as the height difference between crest and trough levels, and the wave period $T$ corresponds to the time between the two troughs surrounding this wave crest. From this initial position, every detected wave (or a manually-selected subset) can be tracked. At each new cross-shore position, the time of wave crest detection at the previous cross-shore position is compared to the detection time at the new location. If a wave crest is detected within a reasonable physical range (based on wave celerity), it is kept as the new position. If no value is found, wave tracking is ceased. The same methodology can be applied to both incoming and outgoing signals, with the values for the physical range set accordingly. The result of this wave tracking algorithm on the A7-mono test is shown in Figure 4.8.

Using two separate analyses, this methodology was performed on the total $\eta(x,t)$ and incoming $\eta_{inc}(x,t)$ signals. The following individual wave properties were extracted: crest height $C$, wave height $H$, period $T$, and depth under preceding trough $h_{tr}$. The analysis

performed on the incoming signal allows for the retrieval of incident wave properties, by removing the effect/component of reflected waves from the total signal. Reflected wave properties were also extracted from the outgoing $\eta_{out}(x,t)$ signal in order to assess the incoming/outgoing energy ratio and study their characteristics as a function of the incident wave properties.

## 4.4 Results

### 4.4.1 Inter-comparison of separation methods

Model and experimental data from the A6-01 irregular wave test were compared in the frequency domain by applying the RT on the modelled free surface elevation and the Guza84 method on the collocated PT/EMCM data. Figure 4.9 shows the comparison of the total, incoming and outgoing signals at four cross-shore locations: $x$ = 42, 67.5, 72.5 and 77.5 m. At all positions, and for both sea-swell and infragravity ranges of frequencies, the comparisons show good agreement. Although the amount of energy is small, more incoming energy at the infragravity frequencies (0.005 Hz $\leq f \leq$ 0.05 Hz) is estimated in the PT data at $x$ = 42 m (Figure 4.9b). This could be explained by two factors and it is not certain which prevails: an underestimation in the model of the transfer of energy to sub-harmonics between $x$ = 0 and 42 m or a more efficient absorption of outgoing waves at the numerical paddle than in the real flume. The energy peaks and the spectrum tail along the wave flume are well represented everywhere else, indicating that the model is able to simulate the breaking process and the transfer of energy to higher/lower frequencies. Similar performance has been observed by Morgan et al. (2010) in their modelling of wave transformation over submerged bar with up to 8th order harmonics correctly simulated.

The observed agreement between the RT and the Guza84 approach are somewhat surprising for two main reasons: 1) the previously observed differences at the wave-by-wave scale between the pressure-derived surface elevation and the model output close to break point (around 30% of $H$, Figure 4.2) is not evident in the spectral domain, and 2) while the Guza84 method, is thought to be inappropriate for use in highly non-linear surf zone waves, the current results indicate that it can be applied in the surf zone with reasonable results.

### 4.4.2 Intrawave variability of wave heights and wave height to water depth ratio

Figure 4.10a and 4.10b present the cross-shore evolution of the modelled individual wave height $H$ for the total and incoming signals, from the A6-mono and A7-mono tests. Similar to that observed in the $\eta(x,t)$ diagram presented in Figure 4.8a, the reflected components of the waves are clearly observable in the cross-shore evolution of $H$. In the total signal $\eta(x,t)$ diagram (Figure 4.8a), the first modelled wave after reflection influences the second, third and fourth incident waves at cross-shore positions of approximately $x$ = 71 m, 44 m and 14 m. The surface elevation at these locations is temporarily increased due to the presence of a reflected wave crest, and this leads to an apparent net increase in $H$ from total signal at

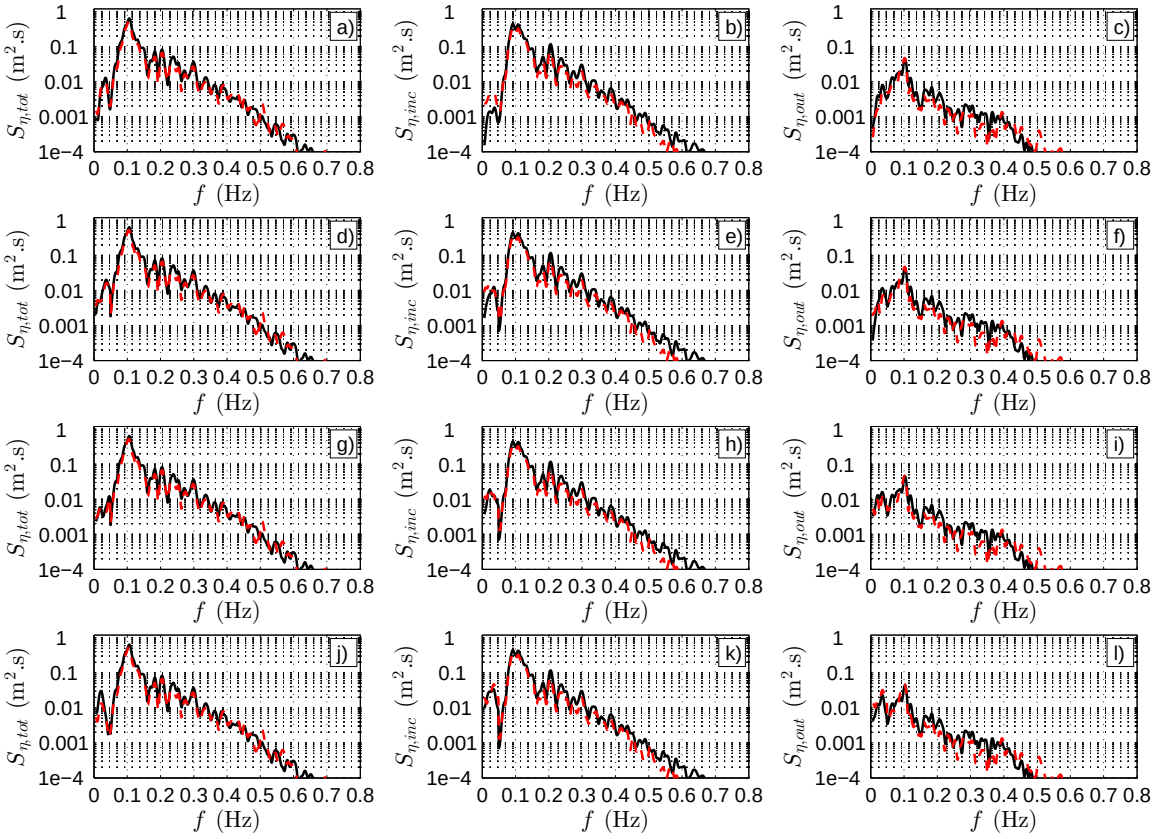


Figure 4.9: Comparison of the modelled surface elevation spectra (black line) along the wave flume against measurements from pressure-derived data (red dashed line), for total (left column), incoming (central column) and outgoing (right column). The modelled total signal was separated using the RT, while the measured total signal was separated with the Guza84 method. Comparisons are performed at the following cross-shore locations: a-b-c) $x$ = 42 m, d-e-f) $x$ = 67.5 m), g-h-i) $x$ = 72.5 m) and j-k-l) $x$ = 77.5 m).

these cross-shore locations, while the values from the incoming signals obtained from the RT present gradually increasing $H$ values in the shoaling region, as it should be expected. Similarly, the passage of troughs also influence $H$ values by decreasing the surface elevation temporarily.

The observed effect of reflected waves on individual wave height is also present in $\gamma$ values which are expressed as $\gamma = H/\bar{h}$ (Figure 4.10c and 4.10d). Since the first modelled wave is propagating in a calm wave flume, its properties are not altered by any reflected component: $\gamma_{tot}$ and $\gamma_{inc}$ should therefore be similar. This is observed in Figure 4.10a and 4.10b where the incoming and total values match at all positions (gray lines and dots), and in the scatter plots of Figure 4.10c and 4.10d, where gray dots are close to the 1:1 agreement. While for the subsequent waves in the test there are differences between $\gamma_{tot}$ and $\gamma_{inc}$ values of up to 35% in the shoaling area, this reduces to around 25% closer to the break point, which is defined as the location of the maximum wave height for each propagating wave ($x$ = 71 m, for both monochromatic tests).

A similar wave-by-wave approach was performed for the A6-01 irregular test case and the results can be observed in Figure 4.11. Figure 4.11a shows the cross-shore evolution of $\gamma_{s,tot}$ and $\gamma_{s,inc}$, based on significant wave height $H_s$ and mean water depth. In the shoaling

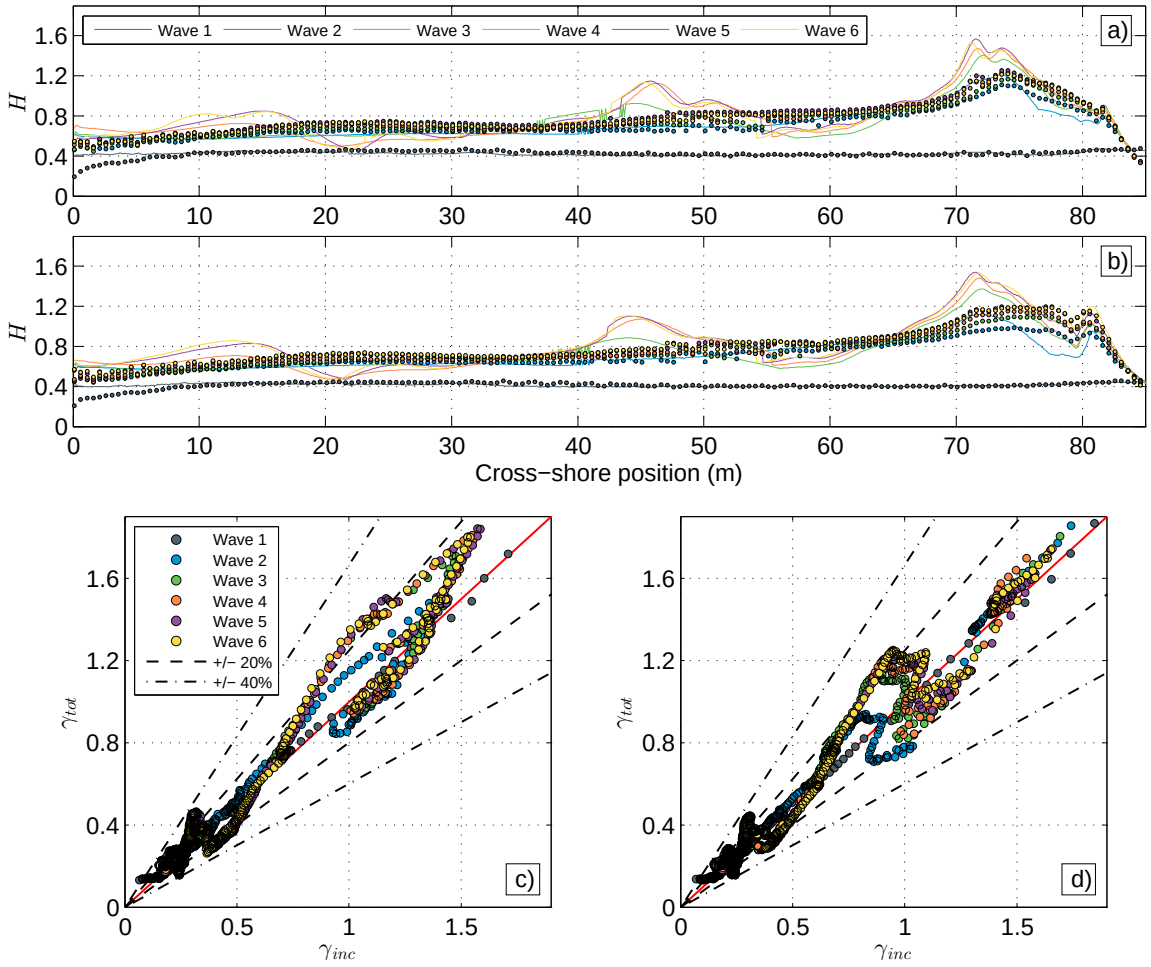


Figure 4.10: Results from the wave-by-wave analysis on modelled total and incoming signals ($\eta(x,t)$ and $\eta_{inc}(x,t)$) from the A6-mono and A7-mono wave tests. Panels a) and b) represent the wave height evolution extracted from the total (continuous lines) and incoming (dots) signals for the A6-mono and A7-mono wave tests respectively. Panels c) and d) represent the corresponding $\gamma$ scatter plots for the A6-mono and A7-mono wave tests respectively (values from the total signal against values from incoming signal). In the four panels, the 6 modelled waves are shown, and the same colours are used in the line/dots for the wave numbering; ±20% and ±40% lines are also represented in the scatter plots as dashed and dot-dashed lines respectively.

area, the two ratios present identical evolution, demonstrating little influence of reflection on averaged breaker indexes in that zone. Just offshore of the bar, the values computed from the incoming signals are slightly larger than those from the total signal, while over the bar the opposite occurs. The most significant difference is visible on the terrace ($x = 75 - 78$ m), where incoming values are approximately 15% greater.

Individual $\gamma$ and $\gamma_{tr} = H/h_{tr}$, where $h_{tr}$ is the water depth below the wave trough, are shown in Figure 4.11b-e for incoming and total signals. Overall, the values computed from the incoming signal are less variable; this can be seen from the slightly smaller error bars and more 'organized' lines, showing lower intrawave variability. The scatter plots of Figures 4.11f and 4.11g allow a comparison of the different definitions of $\gamma$ and suggest that variations up to 20% and 40% are common for $\gamma$ and $\gamma_{tr}$ respectively which is comparable to that found for the monochromatic cases (Figure 4.10c and 4.10d).

The alternate effect of reflected wave crests and troughs on the incident waves for the irregular wave test is similar to that observed for the monochromatic wave tests. This behaviour supports the concept of quasi-standing waves previously observed by Hoque et al. (2002) for shorter waves. The interactions of two progressive waves travelling in opposite direction, with the same period but different amplitude (due to wave breaking and friction), generates quasi-antinodes and quasi-nodes at the location where the incident and reflected waves are in phase and out of phase respectively. This concept has been investigated for the A6-01 irregular wave test. Figure 4.12 shows the cross-shore evolution of the ratio of total and incoming variance density spectra $S_\eta / S_{\eta_{inc}}$ for sea/swell frequencies. This ratio indicates the presence of reflected wave energy: a ratio greater than 1 corresponds to the presence of a reflected wave crest, while a ratio lower than 1 corresponds to the presence of a reflected wave trough. For relatively low frequencies ($f \leq 0.2$ Hz), a node/antinode pattern is observed along the wave flume. In particular, for the frequency of the monochromatic wave tests ($f = 0.083$ Hz), a very similar node/antinode system as observed in Figure 4.10 is found during the irregular wave run: antinodes due to superposed crests are found at around $x = 75$ m, $x = 53$ m and $x = 24$ m, and discrepancies are mainly explained by the different foreshore slope (Table 4.1). It was suggested for the monochromatic wave tests that partially standing waves were responsible for the intrawave variability of $H$ and hence $\gamma$ (Figure 4.10). The results presented in Figure 4.12 suggest that similar behaviour is observed for irregular waves, and for relatively high frequencies.

### 4.4.3 Generation of swash-based reflections

The reflected waves studied here in the sea/swell frequency are thought to be 'generated' primarily by the seaward propagating mass fluxes present in the strong swash backwashes. The term swash-based is therefore used to describe this type of reflection. This concept has been investigated by relating the energy of the tracked reflected waves to the maximum potential energy present in the swash preceding the 'generation' of that reflected wave. The two energy concepts are expressed as follows:

$$E_{ref} = \rho g \int_0^L \eta_{ref}^2(x) dx \tag{4.5}$$

$$\max_t E_{p,swash}(t) = \rho g \int_0^{R(t)} h(x,t) z(x,t) dx \tag{4.6}$$

where $L$ is the wavelength, $R(t)$ is the time-varying shoreline position, $h(x,t)$ the water depth and $z(x,t)$ the height above the reference for null potential energy taken as MSL. In the potential energy formulation from equation 4.6, $z(x,t)$ is the mid flow depth: $z(x,t) = z_{bed}(x) + h(x,t)/2$, where $z_{bed}(x)$ is the bed elevation at the cross-shore position $x$. A sketch describing the terminology used in Equation 4.5 and 4.6 is presented in Figure 4.13.

Figure 4.14 shows the comparison of the two energy expressions for a range of both validated and unvalidated test cases. Although not validated in this paper, the A1-mono, A2-mono and A4-mono wave tests from the BARDEXII experiments were run for this

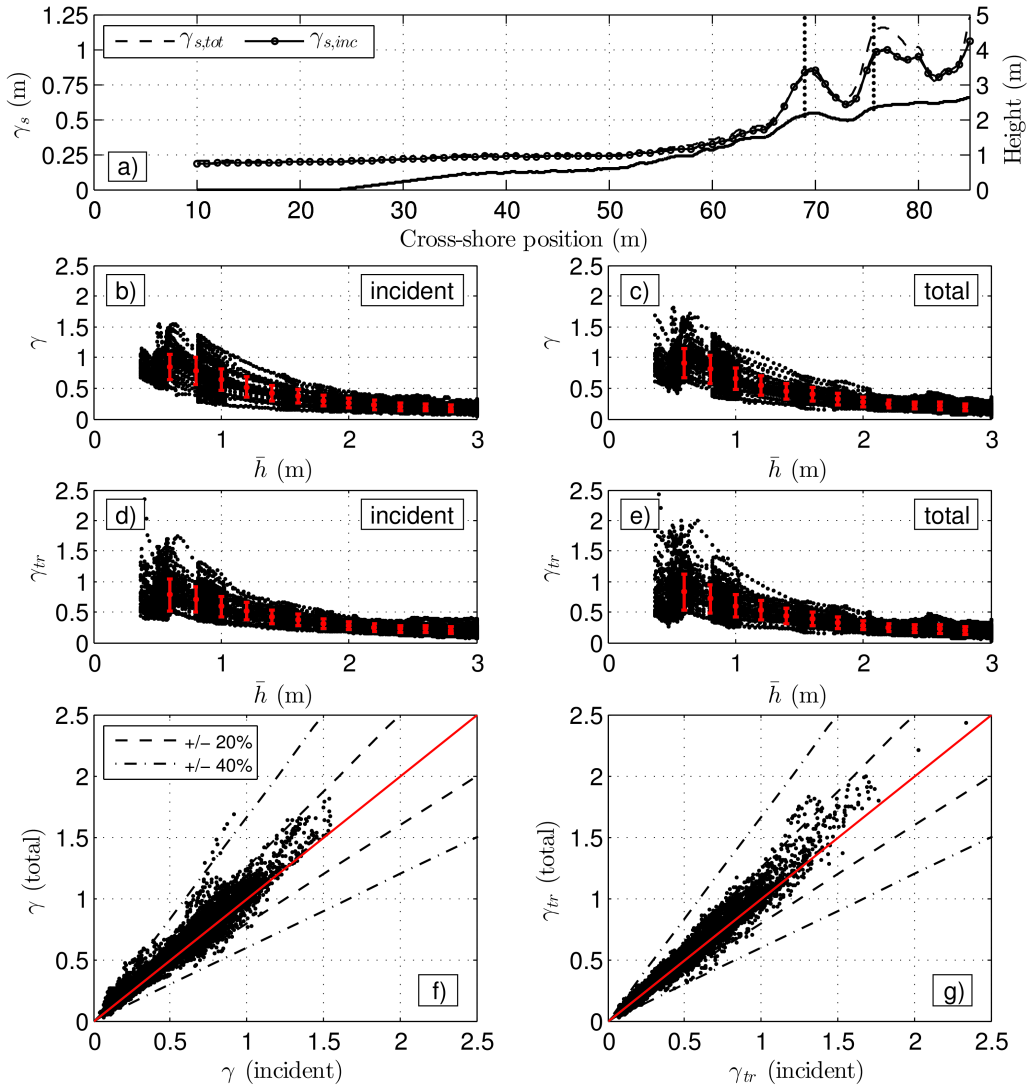


Figure 4.11: Results from the wave-by-wave analysis on the total and incoming signals ($\eta(x,t)$ and $\eta_{inc}(x,t)$) from the A6-01 irregular wave test. Panel a) shows the cross-shore evolution of the significant wave height to depth ratio $\gamma_s$ computed from the total (dashed line) and incoming (circled line) signals respectively. The two break points defined as the maximum significant wave height are also shown as vertical dotted lines. Panels b) and c) show the individual $\gamma$ values computed from the total and incoming signal. Panels d) and e) show the individual $\gamma_{tr}$ values computed from the total and incoming signal using the water depth below trough $h_{tr}$. For these 4 scatter plots, standard deviation of the mean are shown as error bars, using bins of 0.2 m. Panels f) and g) represent the corresponding $\gamma$ and $\gamma_{tr}$ scatter plots. In these, ±20% and ±40% lines are also represented as dashed and dot-dashed lines respectively.

investigation in order to have a wider range of beach and wave characteristics (see Table 4.1). Additionally, two further monochromatic cases using the same $H_s$ and beach conditions as A7-mono, but with different wave periods were modelled (see Table 4.1). For every regular case, the ensemble-averaged energy from the tracked reflected wave (Equation 4.5, estimated between $x = 15\,\text{m}$ and $x = 15 + L\,\text{m}$) is compared to the ensemble-averaged potential energy contained in the preceding swash event (Equation 4.6). For the irregular run, a subset of 5 individual waves was extracted. For the beach slopes and wave conditions examined here, a clear correlation between the two energy formulations is observed in Figure 4.14 with the potential energy in a swash event consistently double that of the

reflected wave that this event generates.

This result suggests that it is possible to estimate the energy and height of individual reflected waves based on the monitoring of foreshore bed levels and the time-varying surface elevations (leading to water depths and swash excursion, the two required parameters). Field deployments of TLS in the swash zone such as in Martins et al. (2016) and Almeida et al. (2015) could use this relationship to estimate the bulk of energy reflected from the beach. Further investigation is required to completely validate this hypothesis, and to explain the presence of the 0.5 coefficient of proportionality observed in Figure 4.14, though this is thought to be closely linked to the beach gradient and hence the mass flux in the backwash.

### 4.4.4 Cross-shore evolution of reflection coefficients

To the authors' knowledge, Baquerizo et al. (1997) were the first to study the cross-shore variation of the reflection coefficient in the sea/swell range of frequencies, defined as the ratio of incoming and outgoing wave energy. Using various methods to separate incoming and outgoing signals, they measured increasing reflection coefficient values through the surf zone and suggested that to minimize the uncertainty introduced by this variation, representative values should be estimated seaward of the break point. A numerical model based on an energy balance, taking into account the incident wave dissipation and reflection from slope was developed by Baquerizo et al. (1998) to predict local reflection coefficients. Although it showed very good agreement seaward of the break point it overestimated the reflection coefficient in the surf zone. Discrepancies in the surf zone are thought to be due to the expression of the reflected wave energy fluxes, directly linked to the incoming fluxes and the rate of dissipation. To illustrate this, the energy fluxes defined using linear theory as $F = H^2 c$, where $c$ is the wave celerity (Baquerizo et al., 1998), for the incident and reflected waves from the A6-mono and A7-mono tests are shown in Figure 4.15a. While the energy fluxes of reflected waves are approximately constant, meaning that waves are deshoaling as $c$ increases with increasing depths, the incident waves show a net increase in energy flux landward of $x = 40 - 50$ m. This occurs when wave celerity cannot be described anymore by linear wave theory and corresponds to where wave non-linearities become important (high Ursell number). This overestimation in the incident wave energy fluxes when non-linearities become significant leads, for a given dissipation rate, to an overestimation of the reflected wave energy as defined by Baquerizo et al. (1998). This is consistent with the larger reflected fluxes found in the surf zone by Baquerizo et al. (1997) (see their Figure 8).

The direct ratio between incident and reflected individual wave heights is shown in Figure 4.15b, for both monochromatic tests. It is shown that up to the break point ($x = 71$ m), the ratio remains reasonably constant with a slight decreasing trend for both tests. This is explained by the shoaling incident waves dominating over the deshoaling reflected waves, observed in Figure 4.15a. Landward of the break point $x = 71 - 75$ m, and as previously found by Baquerizo et al. (1998), the ratio rapidly increases due to the sudden decrease in the wave height after breaking. It is hard to infer from the present dataset what would

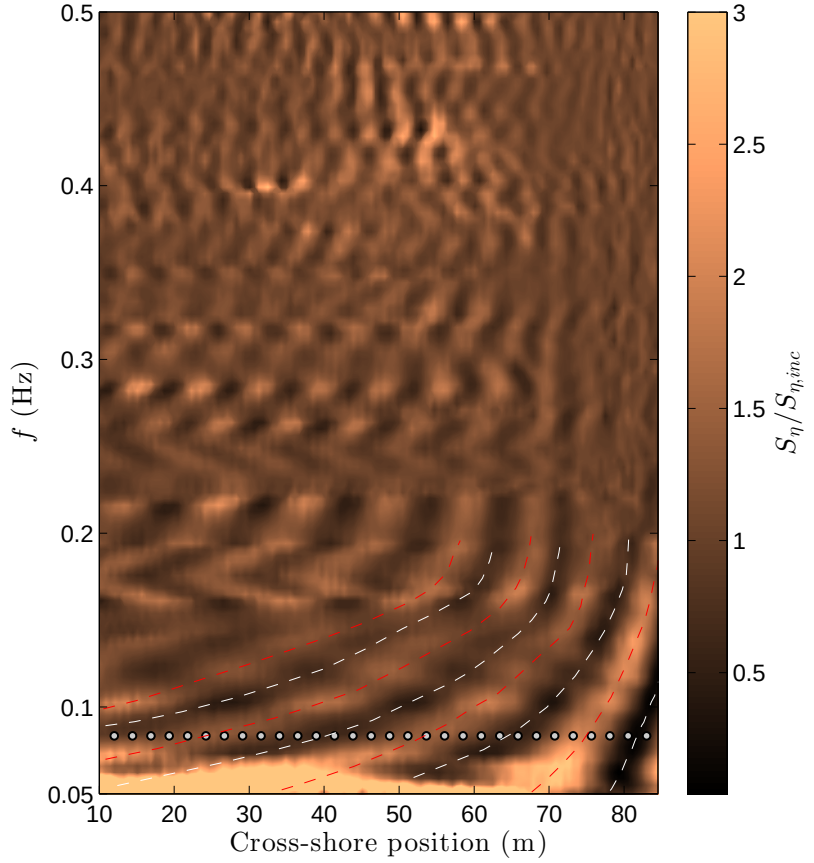


Figure 4.12: Cross-shore evolution of the ratio of variance density spectra computed on total and incoming surface elevation signals. For $f \leq 0.2$ Hz and for each frequency, the locations of two types of antinodes are shown as white (incident and reflected wave troughs superposed) and red (incident and reflected wave crests superposed) dashed lines. The frequency corresponding to the A6-mono and A7-mono wave tests is also shown by the grey dots.

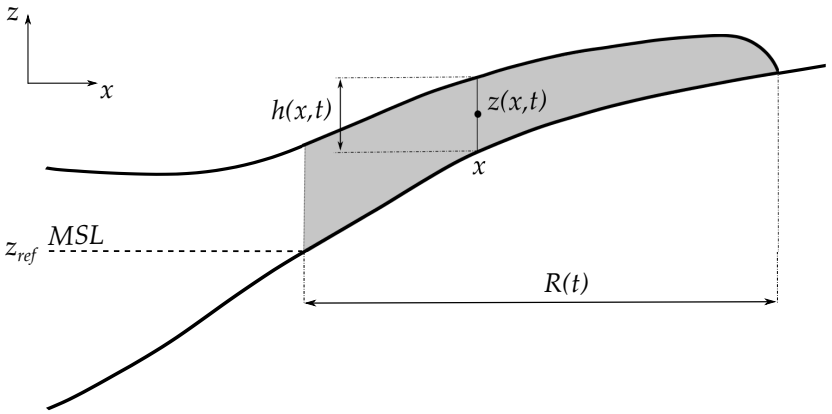


Figure 4.13: Sketch of a typical swash event, at a time $t$. Mean Sea Level (MSL) defines the elevation reference $z_{ref}$ for the potential energy definition in Equation 4.6. The intersection between MSL and the bed also defines the origin to estimate the time-varying horizontal shoreline position $R(t)$. $x$ defines the cross-shore location, $h(x,t)$ the water depth at $x$ and time $t$, $z(x,t)$ the middle point of the water column at $x$.

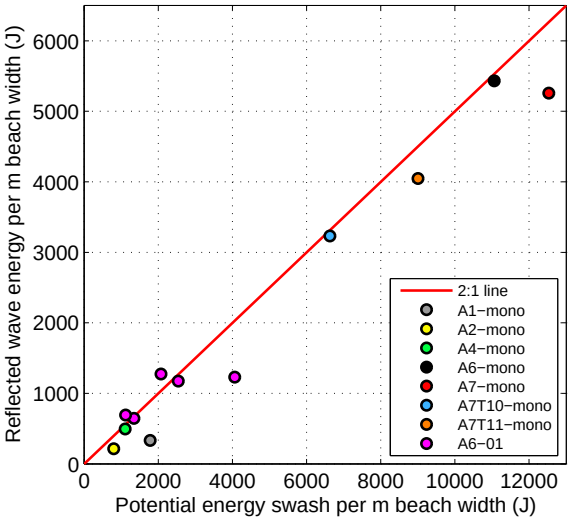


Figure 4.14: Comparison between reflected wave energy (Equation 4.5) and maximum potential energy in the preceding swash event (Equation 4.6) for a range of validated and unvalidated test cases detailed in Table 4.1.

happen with a wider surf zone and at distances further from the break point. It is natural though to hypothesise an increase of $H_{ref}/H_{inc}$ towards a value which is a function of the wave steepness and the foreshore slope. The energy dissipation rate and the width of the surf zone after break point indeed limit the maximum $H_{inc}$ that can be reflected from a beach, for a given foreshore slope and incident wavelength (Miche, 1951; Battjes, 1974).

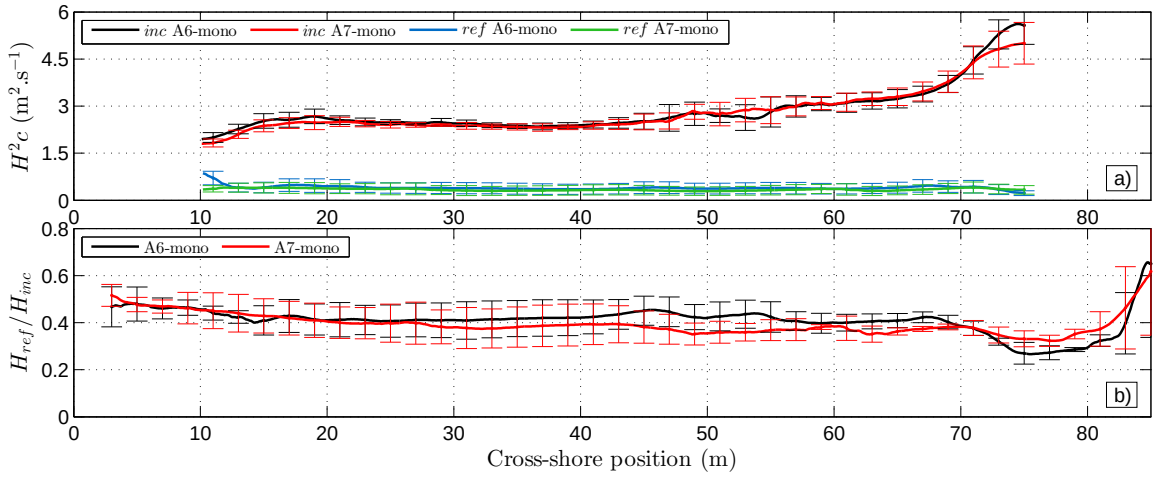


Figure 4.15: Cross-shore evolution of reflection coefficient based on individual wave properties: a) individual wave incident and reflected energy fluxes and b) individual incident and reflected wave height ratio for the A6-mono and A7-mono tests. The value for each run represents the ensemble-average of the four first waves, since only four reflected waves could be tracked (as seen in Figure 4.2c). Standard deviation of the ensemble-average values are shown every two meters in the cross-shore direction, as error bars. For the fluxes expression, wave celerity was estimated for each wave on an individual basis, using the tracking method described in Section 4.3.2.

## 4.5 Discussion

### 4.5.1 Break point

The differences observed in the $\gamma$ values under the presence of reflected waves can be of great significance for numerical models or the parameterisation of wave energy across the surf zone. For instance, a shift seaward or landward of the break point due to the presence of reflected waves will change the energy dissipation patterns across the surf zone, and can affect the position of bar for models supported by the break point hypothesis for sandbar generation (Mariño-Tapia et al., 2007).

For both monochromatic wave tests, $H$ computed from the total signal reaches its maximum at the same location ($x$ = 71m), see Figure 4.10a and 4.10b. However, if only the incoming signal is considered, the maximum wave height is reached around $x = 74\,\text{m}$ for both tests, though it is noted that no strong peak is observed for A7-mono and the wave height remains constant over the low-sloping terrace. If the break point is defined as the location of maximum wave height as used in this study, the results suggest that the incident wave break point occurs further landward. Although no evidence of a direct influence from the reflected wave field on the wave energy dissipation or the breaking onset of incident waves is shown, the detection of the break point with the present definition is affected and therefore biased by the presence of reflected waves.

For the irregular wave test, the presence of reflected waves does not seem to influence the location of the break point as it is observed that the peak values of total and incoming significant wave height computed over sea/swell range of frequencies $H_s$ occur at the same location: $x = 68.5\,\text{m}$ and $x = 75.4\,\text{m}$ (Figure 4.11a). At the inner breakpoint, there is a discrepancy of up to 15% between the gamma values derived from the total and incoming signals and therefore the presence of reflected wave may explain previously observed discrepancies between existing breaker index datasets (Robertson et al., 2013). Further effort is therefore required to account for the influence of wave reflection on gamma in order to obtain a better description of cross-shore evolution of incident wave height under reflective conditions.

### 4.5.2 Influence of wave reflection on time-averaged surf zone parameters

The results presented in Figure 4.12 suggest that wave reflection in the sea/swell range of frequencies in a reflective environment can influence the surf hydrodynamics at the wave-by-wave scale through the formation of multiple quasi-node/antinode system, affecting orbital velocities. Further influence at longer timescales is discussed here, in terms of undertow, wave setup and horizontal velocity skewness.

***Undertow***

Horizontal current velocities from the A6-01 test were separated using linear theory (see Section 4.3.1), and time-averaged to obtain the contribution of both incoming and outgoing wave-induced hydrodynamics on the undertow. Figure 4.16 shows the result of this separation by illustrating the contribution of the outgoing wave field on the undertow along

the wave flume. At the four locations where current velocities measurements are available ($x$ = 42, 67.5, 72.5 and 77.5 m), modelled mean horizontal flow magnitude is shown against measurements (Figure 4.16a-d). The ratio $|\overline{U_{out}}|/|\overline{U_{inc}}|$ shown as a contour plot in Figure 4.16e represents the relative contribution of the outgoing wave field on the mean return flow. Although, over-predicted in the mid-column at $x$ = 67.5 m and slightly underestimated at $x$ = 77.5 m, the modelled undertow shows good agreement with data, in terms of magnitude and vertical structure.

Consistent with previous work (Putrevu and Svendsen, 1993), the vertical structure of the undertow evolves with the water depth across the shoaling area and the surf zone. Where non-linearities are small ($\gamma_s \sim O(0.2)$ and low Ursell number), the undertow is weak, and rather vertical-uniform close to the bed. In this region, the undertow is dominated by the outgoing wave field (Figure 4.16e), which triggers an offshore-directed mean horizontal current. With reducing depth and hence increasing non-linearities (between $x$ = 35 m and 50 m) the waves are shoaling and the undertow remains weak and seaward directed. In this region the incoming and outgoing wave field contribute roughly equally to the mean flows ($|\overline{U_{out}}|/|\overline{U_{inc}}| \approx 1$ in Figure 4.16e). As waves propagate closer to the bar crest, the beach becomes much steeper, and the undertow magnitude becomes much stronger, with its maximum reached at mid-depth.

The ratio shown in Figure 4.16e exhibits a narrow band in the lower 10 cm of the water column and seaward of the bar (focussing on the region between $x$ = 66 m and 69 m immediately adjacent to the bed where $|\overline{U_{out}}|/|\overline{U_{inc}}| \approx 0.4$) where reflection seems to have an important influence on the undertow. In this narrow band, the mean flow induced by outgoing waves is onshore-directed close to the bed (Figure 4.16b), and has the effect of almost balancing the offshore-directed mean flow induced by the incoming wave field, leading to almost zero mean flow adjacent to the bed. This is thought to have an influence on bar morphology and will be further discussed in Section 4.6. Except in this narrow band, the incoming wave field is mostly responsible for the mean return flow around the bar location, indicated by the region where $|\overline{U_{out}}|/|\overline{U_{inc}}|$ is close to zero between $x$ = 62 and 72 m.

The strengthening of the undertow by the outgoing wave field, can partially be explained by the offshore-oriented Stokes drift that it generates and a change in the wave setup (Mendez et al., 1998). Indeed, Figure 4.17a) suggests that the presence of reflected waves significantly reduces the setdown generated by the breaking of incident waves in the region $x = 72 - 80$ m. Landward and seaward of this region, the setup induced by the outgoing field predominates over that from the incoming field, which is consistent with the observations made on the undertow (Figure 4.16d). The undertow is known to influence cross-shore sediment transport, as it plays an important role in the offshore/onshore bar migration (Dyhr-Nielson and Sørensen, 1970; Thornton et al., 1996) and/or in the resuspension of sediment in the water column (Fredsøe and Deigaard, 1992). Figure 4.16 for instance suggests that the presence of the outgoing wave field helps to stabilise the bar by weakening the offshore directed mean flow at the bottom of the water column. Although it

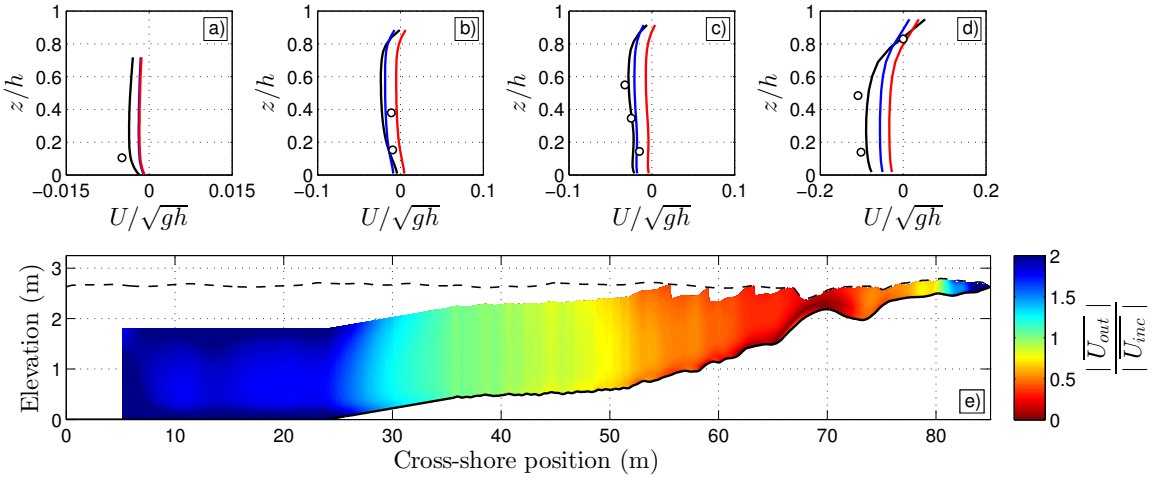


Figure 4.16: Vertical structure of the modelled undertow along the flume for the A6-01 wave test. The top panels show the modelled undertow from total (black line), incoming (blue line) and outgoing (red line) signals at: a) $x = 42$ m, b) $x = 67.5$ m, c) $x = 72.5$ m and d) $x = 77.5$ m. Experimental data from the EMCM are shown as circles. Panel e) shows a contour plot of the outgoing signal contribution on the undertow structure, compared to the incoming contribution. The black dashed line corresponds to the minimum surface elevation reached, and any data from above that limit has been removed to not bias the time-average.

is consistently offshore-directed, the present results show that the nature of the undertow - at least in reflective environments - is more complex that it was thought before, e.g. in terms of temporal structure with a contribution from incident and reflected waves acting with different phasing.

***Skewness***

Flow skewness and wave asymmetry have been shown by many researchers to contribute to onshore-directed sediment fluxes, therefore balancing the effect that undertow has on surf zone morphodynamics, see for instance Elfrink et al. (1999), Elgar et al. (2001), and Silva et al. (2011). Figure 4.17b shows the surface elevation asymmetry - defined as $A_s = -\overline{\mathcal{I}m(\mathcal{H}(\eta))^3}/\overline{\eta^2}^{3/2}$ where $\mathcal{I}m$ is the imaginary part of the Hilbert transform $\mathcal{H}$ of the surface elevation - and Figure 4.17c-e show the flow velocity skewness along the wave flume, computed from the total, incoming and outgoing wave-induced velocity fields. Two striking observations emerge from this analysis: 1) near-zero skewness from the incoming component on top of the bar and on the terrace (Figure 4.17c), and 2) the negative skewness of the outgoing field (Figure 4.17d) that therefore generates a negative total skewness over the terrace ($x = 75 - 82$ m, see Figure 4.17b). The positive skewness seaward of the bar trough and negative skewness landward, along with strong surface elevation asymmetry observed in Figure 4.17a are thought to explain the 'filling' of the trough observed after the A6-01 test under similar wave conditions (Masselink et al., 2016). This is consistent with the findings of Grasso et al. (2011).

Although, no obvious influence of the multiple quasi-node/antinode system can be observed in the different skewness fields, it is thought to be of importance. Bowen (1980) suggested that nodes/antinodes of standing infragravity waves and their associated drift velocities could trigger the generation/migration of bar towards an equilibrium profile.

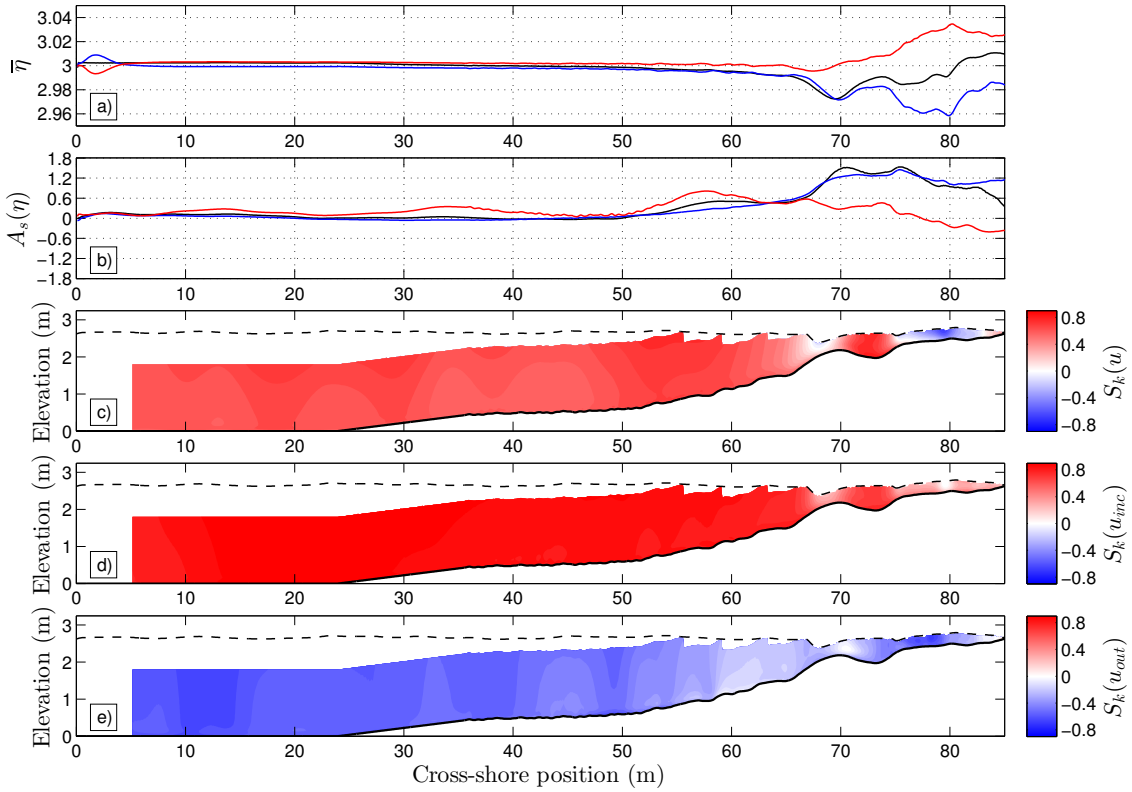


Figure 4.17: Evolution of modelled time-averaged surf zone parameters along the wave flume. Panel a) shows the modelled time-averaged surface elevation (wave setup) for the total, incoming and outgoing signal (black, blue and red lines respectively). Panel b) shows the surface elevation asymmetry for the total, incoming and outgoing signal (black, blue and red lines respectively). Panels c), d) and e) show contour plots of the skewness computed from the total, incoming and outgoing horizontal velocity fields, respectively. The black dashed line in panels c-e) corresponds to the minimum surface elevation reached, and any data from above that limit has been removed to not bias the skewness computation.

This was confirmed numerically by Bernabeu et al. (2003) who obtained improved model skill in predicting beach equilibrium profiles by accounting for wave reflection. Further verification was obtained in field conditions for sea/swell frequencies by Sánchez-Badorrey et al. (2008) who observed the generation of a multiple bar-trough system in front of a newly installed seawall which matched the quasi-node/antinode positions of the peak frequency. Similarly, Alsina et al. (2012) observed a reduced offshore bar migration rate when conditions in the swash were more dissipative: if reflection occurs earlier, the antinode location slightly shifts offshore compared to the location for a more dissipative swash, generating a different sediment convergent point. Alternatively, this can also be explained by the more intense backwashes observed that potentially suspend more sediment in the inner surf. Combined with the stronger undertow under more reflective conditions (Figure 4.16), it can possibly promote higher offshore-directed sediment transport rates. As noted by Grasso et al. (2011), despite recent effort in that regard, it is difficult to isolate individual physical processes that might affect sediment transport rates in the surf zone. Although rarely considered as such, wave reflection in the sea/swell range of frequencies in reflective environments is clearly playing a role in the surf zone hydrodynamics at various time scale, which in turn affect the morphodynamics.

## 4.6 Conclusions

In this paper, a RANS numerical model based on the IHFOAM library (Higuera et al., 2013) has been validated and used to study the influence of swash-based wave reflection in the sea/swell range of frequencies on surf zone hydrodynamics at the wave-by-wave and wave tests temporal scales. A TLS dataset of breaking waves has been used for the first time to validate the modelled wave shape at various stage of breaking. This highlighted the important wave-by-wave discrepancies (wave height and skewness) when using linear theory to retrieve the surface elevation from the measured pressure signal, close to the break point.

The RT was successfully applied to the modelled free surface elevation to separate incoming and outgoing signals. A wave tracking algorithm was used to isolate individual waves and demonstrated that reflected waves induce intrawave variability of individual incident wave properties such as the wave height, and the wave height to water depth ratio, through the generation of quasi-standing waves. Variations of up to 35% and 15% are observed for individual and spectral values of wave height to water depth ratios respectively. This renders the extraction and the study of incident wave properties more difficult, and must be considered when parameterising wave reflection in numerical models of nearshore circulation. By tracking individual reflected waves, a direct link between the potential energy of swash flows and the reflected wave energy has been demonstrated. This has two main implications: 1) the potential to use measurements of swash depths to estimate the energy of individual reflected waves, and 2) a good representation of swash mass fluxes is required to accurately model surf zone hydrodynamics (Torres-Freyermuth et al., 2010).

Using the Guza84 approach, the incoming and outgoing components of the modelled horizontal flow velocities were computed along the wave flume in order to study the contribution of each component to the mean return flow (undertow) and higher velocity moments (skewness). It was demonstrated that the presence of strong reflective conditions were promoting the undertow, by strengthening its magnitude almost everywhere in the wave flume except offshore of the bar crest, where the outgoing components induce an onshore-directed streaming close to the bed. This phenomenon, added to the convergence points created by the observed quasi-standing waves and the influence of reflection on velocity skewness is thought to influence sediment transport rates and their variation along the beach profile, contributing to bar generation/migration.

## Acknowledgements

This work was supported by the University of Bath, through a URS scholarship, and by the EPSRC-funded project EP/N019237/1 "Waves in Shallow Water: A new approach based on high-frequency remote sensing and wave-by-wave analysis". The two anonymous reviewers are greatly acknowledged for their constructive comments on the paper. The BARDEXII data set used in this study is available from `www.hydralab.info`, and it was obtained with the support by the European Community's 7th Framework Programme

through the grant to the budget of the Integrating Activity HYDRALAB IV, contract no. 261520.

## References

Almar, R., Bonneton, P., Michallet, H., Cienfuegos, R., Ruessink, B. G., and Tissier, M. 2013. On the use of the radon transform in studying wave dynamics. *Coastal Dynamics '13: Proceedings of the Seventh Conference on Coastal Dynamics, Arcachon, France*, pp. 73 – 82.

Almar, R., Michallet, H., Cienfuegos, R., Bonneton, P., Tissier, M., and Ruessink, G. 2014a. On the use of the Radon Transform in studying nearshore wave dynamics. *Coastal Engineering* 92, pp. 24 – 30. DOI: 10.1016/j.coastaleng.2014.06.008.

Almar, R., Catalan, P., Ibaceta, R., Blenkinsopp, C., Cienfuegos, R., Villagran, M., Aguilera, J. C., and Castelle, B. 2014b. Swash zone based reflection during energetic wave conditions at a dissipative beach: towards a wave-by-wave approach. *Proceedings of the 34th Conference on Coastal Engineering, Seoul, Korea*.

Almar, R., Ibaceta, R., Blenkinsopp, C., Catalan, P., Cienfuegos, R., Viet, N., Thuan, D., UU, D. V., Lefebvre, J.-P., Laryea, W., et al. 2015. Swash-based wave energy reflection on natural beaches. *Coastal Sediments 2015: The Proceedings of the Coastal Sediments 2015*. World Scientific.

Almeida, L. P., Masselink, G., Russell, P. E., and Davidson, M. A. 2015. Observations of gravel beach dynamics during high energy wave conditions using a laser scanner. *Geomorphology* 228, pp. 15 – 27. DOI: 10.1016/j.geomorph.2014.08.019.

Alsina, J. M., Cáceres, I., Brocchini, M., and Baldock, T. E. 2012. An experimental study on sediment transport and bed evolution under different swash zone morphological conditions. *Coastal Engineering* 68, pp. 31 – 43. DOI: 10.1016/j.coastaleng.2012.04.008.

Bakker, A. T. M. de, Herbers, T. H. C., Smit, P. B., Tissier, M. F. S., and Ruessink, B. G. 2015. Nonlinear Infragravity–Wave Interactions on a Gently Sloping Laboratory Beach. *Journal of Physical Oceanography* 45 (2), pp. 589 – 605. DOI: 10.1175/JPO-D-14-0186.1.

Baquerizo, A., Losada, M. A., and Smith, J. M. 1998. Wave Reflection from Beaches: A Predictive Model. *Journal of Coastal Research* 14 (1), pp. 291 – 298.

Baquerizo, A., Losada, M. A., Smith, J. M., and Kobayashi, N. 1997. Cross-shore variation of wave reflection from beaches. *Journal of waterway, port, coastal, and ocean engineering* 123 (5), pp. 274 – 279.

Barker, C. H. and Sobey, R. J. 1996. Irregular wave kinematics from a pressure record. *Proceedings of the 25th Conference on Coastal Engineering, Orlando, Florida*, pp. 1034 – 1047.

Battjes, J. A. 1974. Surf similarity. *Proceedings of the 14th Conference on Coastal Engineering, Copenhagen, Denmark*, pp. 466 – 480.

Battjes, J. A. and Janssen, J. P.F. M. 1978. Energy loss and set-up due to breaking of random waves. *Proceedings of the 16th Conference on Coastal Engineering, Hamburg, Germany*, pp. 569 – 587.

Berberović, E., Hinsberg, N. P. van, Jakirlić, S., Roisman, I. V., and Tropea, C. 2009. Drop impact onto a liquid layer of finite thickness: Dynamics of the cavity evolution. *Phys. Rev. E* 79 (3), p. 036306. DOI: 10.1103/PhysRevE.79.036306.

Bernabeu, A. M., Medina, R., and Vidal, C. 2003. Wave reflection on natural beaches: an equilibrium beach profile model. *Estuarine, Coastal and Shelf Science* 57 (4), pp. 577 – 585. DOI: 10.1016/S0272-7714(02)00393-1.

Bishop, C. T. and Donelan, M. A. 1987. Measuring waves with pressure transducers. *Coastal Engineering* 11 (4), pp. 309 – 328. DOI: 10.1016/0378-3839(87)90031-7.

Blenkinsopp, C. E. and Chaplin, J. R. 2011. Void fraction measurements and scale effects in breaking waves in freshwater and seawater. *Coastal Engineering* 58 (5), pp. 417 – 428. DOI: 10.1016/j.coastaleng.2010.12.006.

Bowen, A. J. 1980. Simple Models of Nearshore Sedimentation, Beach Profiles and Longshore Bars. *The Coastline of Canada, Geological Survey of Canada*, pp. 1 – 11.

Brocchini, M. and Baldock, T. E. 2008. Recent advances in modeling swash zone dynamics: Influence of surf-swash interaction on nearshore hydrodynamics and morphodynamics. *Reviews of Geophysics* 46 (3). DOI: 10.1029/2006RG000215.

Brown, S. A., Magar, V., Greaves, D. M., and Conley, D. C. 2014. An evaluation of RANS turbulence closure models for spilling breakers. *Proceedings of the 34th Conference on Coastal Engineering, Seoul, Korea*.

Dean, R. G. and Dalrymple, R. A. 1991. *Water wave mechanics for engineers and scientists*. Advanced Series on Ocean Engineering: Volume 2, World Scientific.

Doering, J. C., Elfrink, B., Hanes, D. M., and Ruessink, B. G. 2000. Parameterization of Velocity Skewness under Waves and its Effect on Cross-Shore Sediment Transport. *Proceedings of the 27th Conference on Coastal Engineering, Sydney, Australia*, pp. 1383 – 1397.

Dyhr-Nielson, M. and Sørensen, T. 1970. Some sand transport phenomena on coasts with bars. *Proceedings of the 12th Conference on Coastal Engineering, Washington, D.C.*, pp. 855 – 865.

Elfrink, B., Rakha, K. A., Deigaard, R., and Brøker, I. 1999. Effect of near-bed velocity skewness on cross shore sediment transport. *Proceedings of the 4th International Symposium on Coasting Engineering and Science of Coastal Sediment Processes (ASCE), Hauppauge, New York, United States*, pp. 33 – 47.

Elgar, S. and Guza, R. T. 1985. Observations of bispectra of shoaling surface gravity waves. *Journal of Fluid Mechanics* 161, pp. 425 – 448. DOI: 10.1017/S0022112085003007.

Elgar, S., Herbers, T. H. C., and Guza, R. T. 1994. Reflection of Ocean Surface Gravity Waves from a Natural Beach. *Journal of Physical Oceanography* 24 (7), pp. 1503 – 1511. DOI: 10.1175/1520-0485(1994)024<1503:ROOSGW>2.0.CO;2.

Elgar, S., Gallagher, E. L., and Guza, R. T. 2001. Nearshore sandbar migration. *Journal of Geophysical Research: Oceans* 106 (C6), pp. 11623 – 11627. DOI: 10.1029/2000JC000389.

Elgar, S., Raubenheimer, B., and Guza, R. T. 2005. Quality control of acoustic Doppler velocimeter data in the surfzone. *Measurement Science and Technology* 16 (10), p. 1889. DOI: 10.1088/0957-0233/16/10/002.

Fredsøe, J. and Deigaard, R. 1992. *Mechanics of coastal sediment transport*. Advanced Series on Ocean Engineering: Volume 3, World Scientific.

Gailani, J. Z. and Smith, S. J. 2000. *Sediment Transport Analysis from OBS/EMCM During Storms*. Tech. rep. DTIC Document.

Goda, Y. and Suzuki, T. 1976. Estimation of incident and reflected waves in random wave experiments. *Proceedings of the 15th Conference on Coastal Engineering, Honolulu, Hawaii*, pp. 828 – 845.

Grasso, F., Michallet, H., and Barthélemy, E. 2011. Sediment transport associated with morphological beach changes forced by irregular asymmetric, skewed waves. *Journal of Geophysical Research: Oceans* 116 (C3). C03020. DOI: 10.1029/2010JC006550.

Green, M. O. 1999. Test of sediment initial-motion theories using irregular-wave field data. *Sedimentology* 46 (3), pp. 427 – 441. DOI: 10.1046/j.1365-3091.1999.00221.x.

Guza, R. T., Thornton, E. B., and Holman, R. A. 1984. Swash on steep and shallow beaches. *Proceedings of the 19th Conference on Coastal Engineering, Houston, Texas*, pp. 708 – 723.

Guza, R. T. and Bowen, A. J. 1976. Resonant Interactions for Waves Breaking on a Beach. *Proceedings of the 15th Conference on Coastal Engineering, Honolulu, Hawaii*, pp. 560 – 579.

Higuera, P., Lara, J. L., and Losada, I. J. 2013. Realistic wave generation and active wave absorption for Navier-Stokes models: Application to OpenFOAM®. *Coastal Engineering* 71, pp. 102 – 118. DOI: 10.1016/j.coastaleng.2012.07.002.

Hofland, B., Diamantidou, E., Steeg, P. van, and Meys, P. 2015. Wave runup and wave overtopping measurements using a laser scanner. *Coastal Engineering* 106, pp. 20 – 29. DOI: 10.1016/j.coastaleng.2015.09.003.

Hoque, M. A., Asano, T., and Neshaei, M. A. L. 2002. Effect of Reflective Structures on Undertow Distribution. *Proceedings of the Fourth International Symposium on Ocean Wave Measurement and Analysis, Waves 2001, San Francisco, California, United States*, pp. 1042 – 1051. DOI: 10.1061/40604(273)106.

Huang, Z.-C. and Hwang, K.-S. 2015. Measurements of surface thermal structure, kinematics, and turbulence of a large-scale solitary breaking wave using infrared imaging techniques. *Coastal Engineering* 96, pp. 132 – 147. DOI: 10.1016/j.coastaleng.2014.12.005.

Hughes, S. A. and Fowler, J. E. 1995. Estimating wave-induced kinematics at sloping structures. *Journal of waterway, port, coastal, and ocean engineering* 121 (4), pp. 209 – 215.

Inch, K. 2014. Surf Zone Hydrodynamics: Measuring Waves and Currents. *Geomorphological Techniques, Chap. 3, Sec. 2.3*. British Society of Geomorphology.

Inch, K., Davidson, M., Masselink, G., and Russell, P. 2016. Accurate Estimation of Wave Reflection on a High Energy, Dissipative Beach. *Journal of Coastal Research* SI 75, pp. 877 – 881.

Iribarren, C. R. and Nogales, C. 1949. Protection des ports. *XVIIth International Navigation Congres* 1 (14).

Jacobsen, N. G., Fredsoe, J., and Jensen, J. H. 2014. Formation and development of a breaker bar under regular waves. Part 1: Model description and hydrodynamics. *Coastal Engineering* 88, pp. 182 – 193. DOI: 10.1016/j.coastaleng.2013.12.008.

Kajima, R. 1970. Estimation of incident wave spectrum in the sea area influenced by reflection. *Proceedings of the 12th Conference on Coastal Engineering, Washington, D.C.* Pp. 9 – 16.

Lin, C.-Y. and Huang, C.-J. 2004. Decomposition of incident and reflected higher harmonic waves using four wave gauges. *Coastal Engineering* 51 (5–6), pp. 395 – 406. DOI: 10.1016/j.coastaleng.2004.04.004.

Mansard, E. P. D. and Funke, E. R. 1980. The measurement of incident and reflected spectra using least squares method. *Proceedings of the 17th Conference on Coastal Engineering, Sydney, Australia*, pp. 154 – 172.

Mariño-Tapia, I. J., Russell, P. E., O'Hare, T. J., Davidson, M. A., and Huntley, D. A. 2007. Cross-shore sediment transport on natural beaches and its relation to sandbar migration patterns: 1. Field observations and derivation of a transport parameterization. *Journal of Geophysical Research: Oceans* 112 (C3). DOI: 10.1029/2005JC002893.

Martins, K., Blenkinsopp, C. E., and Zang, J. 2016. Monitoring Individual Wave Characteristics in the Inner Surf with a 2-Dimensional Laser Scanner (LiDAR). *Journal of Sensors, 2016*, pp. 1 – 11. DOI: 10.1155/2016/7965431.

Masselink, G., Ruju, A., Conley, D., Turner, I., Ruessink, G., Matias, A., Thompson, C., Castelle, B., Puleo, J., Citerone, V., and Wolters, G. 2016. Large-scale Barrier Dynamics Experiment II (*BARDEX II*): Experimental design, instrumentation, test program, and data set. *Coastal Engineering* 113, pp. 3 – 18. DOI: 10.1016/j.coastaleng.2015.07.009.

Mendez, F. J., Losada, I. J., Dalrymple, R. A., and Losada, M. A. 1998. Effects of wave reflection and dissipation on wave-induced second order magnitudes. *Proceedings of the 26th Conference on Coastal Engineering, Copenhagen, Denmark*, pp. 537 – 500.

Menter, F. R. 1994. Two-equation eddy-viscosity turbulence models for engineering applications. *AIAA Journal* 32 (8), pp. 1598 – 1605. DOI: 10.2514/3.12149.

Miche, A. 1951. Le pouvoir réfléchissant des ouvrages maritimes exposés à l'action de la houle. *Annales des Ponts et Chaussées* 121, pp. 285 – 319.

Miles, J. R. and Russell, P. E. 2004. Dynamics of a reflective beach with a low tide terrace. *Continental Shelf Research* 24 (11), pp. 1219 – 1247. DOI: 10.1016/j.csr.2004.03.004.

Miles, J. R., Russell, P. E., and Huntley, D. A. 1996. Sediment Transport and Wave Reflection Near a Seawall. *Proceedings of the 25th Conference on Coastal Engineering, Orlando, Florida*, pp. 2612 – 2624.

Miles, J. R., Russell, P. E., and Huntley, D. A. 2001. Field Measurements of Sediment Dynamics in Front of a Seawall. *Journal of Coastal Research* 17 (1), pp. 195 – 206.

Morgan, G. C. J., Zang, J., Greaves, D., Heath, A., Whitlow, C., and Young, J. 2010. Using the rasInterFoam CFD model for wave transformation and coastal modelling. *Proceedings of the 32nd Conference on Coastal Engineering, Shanghai, China*.

Nielsen, P. 1986. Local approximations: a new way of dealing with irregular waves. *Proceedings of the 20th Conference on Coastal Engineering, Taipei, Taiwan*, pp. 633 – 646.

Postacchini, M. and Brocchini, M. 2014. A wave-by-wave analysis for the evaluation of the breaking-wave celerity. *Applied Ocean Research* 46, pp. 15 – 27. DOI: 10.1016/j.apor.2014.01.005.

Power, H. E., Hughes, M. G., Aagaard, T., and Baldock, T. E. 2010. Nearshore wave height variation in unsaturated surf. *Journal of Geophysical Research: Oceans* 115 (C8). DOI: 10.1029/2009JC005758.

Power, H. E., Hughes, M. G., and Baldock, T. E. 2015. A novel method for tracking individual waves in the surf zone. *Coastal Engineering* 98, pp. 26 – 30. DOI: 10.1016/j.coastaleng.2015.01.006.

Putrevu, U. and Svendsen, I. A. 1993. Vertical structure of the undertow outside the surf zone. *Journal of Geophysical Research: Oceans* 98 (C12), pp. 22707 – 22716. DOI: 10.1029/93JC02399.

Radon, J. 1917. Über die Bestimmung von Funktionen durch ihre Integralwerte längs gewisser Mannigfaltigkeiten. *Akad. Wiss.* 69, pp. 262 – 277.

Raubenheimer, B., Guza, R. T., and Elgar, S. 1996. Wave transformation across the inner surf zone. *Journal of Geophysical Research: Oceans* 101 (C11), pp. 25589 – 25597.

Robertson, B., Hall, K., Richard, Z., and Nistor, I. 2013. Breaking waves: review of characteristic relationships. *Coastal Engineering Journal* 55 (01), p. 1350002. DOI: 10.1142/S0578563413500022.

Sánchez-Badorrey, E., Losada, M. A., and Rodero, J. 2008. Sediment transport patterns in front of reflective structures under wind wave-dominated conditions. *Coastal Engineering* 55 (7–8), pp. 685 – 700. DOI: 10.1016/j.coastaleng.2007.11.005.

Sénéchal, N. 2003. "Etude de la propagation des vagues au-dessus d'une bathymétrie complexe en zone de surf". PhD thesis. École doctorale sciences du vivant, géosciences, sciences de l'environnement, Université de Bordeaux I.

Sheremet, A., Guza, R. T., Elgar, S., and Herbers, T. H. C. 2002. Observations of nearshore infragravity waves: Seaward and shoreward propagating components. *Journal of Geophysical Research: Oceans* 107 (C8), pp. 10–1 – 10–10. DOI: 10.1029/2001JC000970.

Silva, P. A., Abreu, T., A, D. A. van der, Sancho, F., Ruessink, B. G., Werf, J. van der, and Ribberink, J. S. 2011. Sediment transport in nonlinear skewed oscillatory flows: Transkew experiments. *Journal of Hydraulic Research* 49 (sup1), pp. 72 – 80. DOI: 10.1080/00221686.2011.592681.

Stive, M. J. F. 1980. Velocity and pressure field of spilling breakers. *Proceedings of the 17th Conference on Coastal Engineering, Sydney, Australia*, pp. 547 – 566.

Thornton, E. B., Humiston, R. T., and Birkemeier, W. 1996. Bar/trough generation on a natural beach. *Journal of Geophysical Research: Oceans* 101 (C5), pp. 12097 – 12110. DOI: 10.1029/96JC00209.

Thornton, E. B. and Calhoun, R. J. 1972. Spectral resolution of breakwater reflected waves. *Journal of the Waterways, Harbors and Coastal Engineering Division* 98 (4), pp. 443 – 460.

Torres-Freyermuth, A., Lara, J. L., and Losada, I. J. 2010. Numerical modelling of short- and long-wave transformation on a barred beach. *Coastal Engineering* 57 (3), pp. 317 – 330. DOI: 10.1016/j.coastaleng.2009.10.013.

Townsend, M. and Fenton, J. D. 1996. A comparison of analysis methods for wave pressure data. *Proceedings of the 25th Conference on Coastal Engineering, Orlando, Florida*, pp. 575 – 588.

Turner, I. L., Russell, P. E., and Butt, T. 2008. Measurement of wave-by-wave bed-levels in the swash zone. *Coastal Engineering* 55 (12), pp. 1237 – 1242. DOI: 10.1016/j.coastaleng.2008.09.009.

Zanuttigh, B. and Meer, J. W. van der. 2008. Wave reflection from coastal structures in design conditions. *Coastal Engineering* 55 (10), pp. 771 – 779. DOI: 10.1016/j.coastaleng.2008.02.009.

Zelt, J. A. and Skjelbreia, J. E. 1992. Estimating incident and reflected wave fields using an arbitrary number of wave gauges. *Proceedings of the 23rd Conference on Coastal Engineering, Venice, Italy*, pp. 777 – 789.

## Chapter concluding remarks

In this Chapter, we investigated the influence of reflected waves on the hydrodynamics of the shoaling and surf zones at the wave-by-wave and time-averaged temporal scales using the results from a CFD numerical model. After being generated at the inner surf/swash zone boundary from the energy of the preceding backwash, reflected waves propagate back through the surf zone and interact with incident waves. This has consequences at both the wave-by-wave scale (intra-wave variability of $\gamma$) and the time-averaged temporal scale (effect on the undertow, cross-shore velocity skewness and surface asymmetry). The first point confirms the observation made in Chapter 3 that other physical processes (here reflection) are partly responsible for the scatter of individual wave properties (e.g. $\gamma$). The numerical model used in this Chapter was partly validated using an innovative LiDAR dataset of breaking waves obtained during the prototype-scale BARDEXII experiments. Comparisons of this LiDAR dataset with pressure-derived surface elevation computed with linear wave theory showed large differences at the wave-by-wave scale (up to 30% of $H$), demonstrating the limitations of the latter approach to get accurate individual wave properties around the break point. This also raises questions about datasets acquired with pressure transducers in the outer surf zone to investigate wave height distribution or wave breaking properties: the wave height can be greatly underestimated and considerable differences in the wave profile (wave skewness) are also observed. LiDAR scanners offer a great alternative for measuring wave breaking properties as no transformation of the signal is required and the wave spatial information is also measured. This is the subject of Chapter 5.

# Chapter 5

## High-resolution monitoring of wave transformation in the surf zone using a lidar scanner array

This chapter is based on two research papers: an article published in Coastal Engineering (Elsevier) and an article published in the Proceedings of the Conference on Coastal Dynamics 2017, held in Helsingør, Denmark. The first article provides a detailed description of the field experiments performed within the WASH[1] project at Saltburn-by-the-Sea, UK. The second article, whose reference is given later, presents more results following the innovative approach presented in the first paper. The first has been published in Coastal Engineering: "Use by an author [···] inclusion in a thesis or dissertation, [···] (with full acknowledgment of the original publication of the Article)" (Source: https://authors.elsevier.com/authorform/staticpage/definitions.do?lang=English# prePrint).

Kévin Martins, Chris E. Blenkinsopp*, Hannah E. Power, Brittany Bruder, Jack A. Puleo and Erwin W. J. Bergsma, "High-resolution monitoring of wave transformation in the surf zone using a LiDAR scanner array", Coastal Engineering, 128, 2017.
DOI: 10.1016/j.coastaleng.2017.07.007

## Abstract

Understanding of breaking and broken waves is key for the prediction of nearshore sediment transport and coastal hazards, however the difficulty of obtaining measurements of highly unsteady nearshore waves has limited the availability of field data. This paper reports on a novel field experiment designed to capture the time-varying free-surface throughout the surf and swash zones that was conducted on a dissipative sandy beach using an array of 2D LiDAR scanners. Three scanners were deployed from the pier at Saltburn-by-the-Sea, UK for a 6 day period to monitor the surface elevation of nearshore waves from the break point to the runup limit at temporal and spatial resolutions (order of centimetres) rarely achieved in field conditions. The experimental setup and the procedure to obtain a continuous time series of surface elevation and wave geometry is described. A new method to accurately determine the break point location is presented and compared to existing methodologies.

[1] WAves in SHallow waters, EPSRC-funded project (blog: http://blogs.bath.ac.uk/wash/)

# Chapter 5.

## Declaration concerning the article used for this Chapter:

| | |
|---|---|
| Title | High-resolution monitoring of wave transformation in the surf zone using a LiDAR scanner array |
| Status | Published and available in Open Access in Coastal Engineering (Elsevier) |
| Details | Kévin Martins, Chris E. Blenkinsopp*, Hannah E. Power, Brittany Bruder, Jack A. Puleo, Erwin W. J. Bergsma, "High-resolution monitoring of wave transformation in the surf zone using a LiDAR scanner array", Coastal Engineering, 128, 2017.<br>DOI: 10.1016/j.coastaleng.2017.07.007 |
| Contribution from the authors | K. Martins: Planning and conduction of the field experiments; Processing of the data and analysis; Manuscript (50%)<br>C.E. Blenkinsopp: Planning and conduction of the field experiments; Manuscript (20%)<br>H.E. Power: Assistance during the field experiments; Manuscript (9%)<br>B. Bruder: Assistance during the field experiments; Manuscript (9%)<br>J.A. Puleo: Assistance during the field experiments; Manuscript (9%)<br>E.W.J. Bergsma: Manuscript (3%) |
| Statement | This paper reports on original research I conducted during the period of my Higher Degree by Research candidature. |
| Date and Signature | |

## Preamble

***Methodology and objectives***

This Chapter describes the field experiments performed in Saltburn-by-the-Sea, UK, within the frame of the WASH (WAves in SHallow waters) EPSRC-funded project. During these experiments, an array of 2D LiDAR scanners was deployed from a pier to capture the wave propagation from the shoaling region to the swash zone.

The results of Chapter 4 demonstrated that the traditional approach commonly used in field conditions and consisting of applying linear wave theory to a pressure signal is unable to correctly reproduce individual wave profiles in highly non-linear conditions. A consistent underestimation of wave heights from pressure-derived signals acquired around the break point questions the validity of wave height distributions obtained with this method in the surf zone (e.g. Power et al., 2016). Understanding how individual waves are distributed in the surf zone is fundamental as wave height distributions are an important aspect of numerical models of irregular wave transformation (Battjes and Janssen, 1978; Thornton and Guza, 1983; Dally, 1990). Knowledge of extreme waves in the nearshore is also essential for the design of structures (e.g., see Goda, 2010). Furthermore, the inability of the method to reproduce individual and potentially time-averaged wave skewness can be problematic as wave skewness plays an important role in surf zone morphodynamics (e.g. Hoefel and Elgar, 2003; Grasso et al., 2011). One of the goals of this Chapter is to present an innovative approach for accurately measuring breaking wave properties. The following research objectives/questions are addressed:

- Obtain a comprehensive surface elevation dataset of waves propagating in the shoaling region and through the surf zone with an array of LiDAR scanners.
- Track individual wave properties throughout their propagation within the surf zone, and in particular, extract these properties at the break point
- Study wave geometry (skewness and asymmetry) at various temporal scales.

The first part of this Chapter consists of the article published in Coastal Engineering and titled: "High-resolution monitoring of wave transformation in the surf zone using a LiDAR scanner array". After presenting the experimental setup, the paper focuses on the technique to detect the break point and on the method to extract geometric properties of waves from the LiDAR dataset. The second part of the Chapter consists of additional results presented at the Coastal Dynamics Conference 2017 (Helsingør, Denmark). In this part, wave skewness and asymmetry are studied at various temporal scales and a link with cross-shore current velocity is demonstrated.

As for any field experiment, the planning and preparation period was essential to ensure its success. Since the research article format does not allow for the description of these phases, more details are given in this Preamble. Saltburn pier (see Figure 5.1 of the article) was chosen as it is one of the few piers in the UK which are exposed to relatively consistent medium to long period swell conditions. The predominantly North-East swell direction means that waves propagate parallel to the pier, which is oriented

~18°NE. Additionally the macrotidal character of this part of the British coast allows for full beach surveys at every low tide, which is an essential aspect for the study of nearshore wave transformation. Two principal questions therefore remained: 1) which period of the year should the field trip be planned? and 2) how can we optimize the experimental setup of the LiDAR array?

***Period of the field experiments***

The start of the WASH project in early 2016 and the very small wave conditions in summer restricted the field experiments to be performed over a period from March to May 2016. The wave climate during this period was assessed using offshore wave data (Tyne Tees buoy, see Figure 5.1 of the article for the location) and surf reports[2] from the local surf school at Saltburn. Aided by pictures taken on the beach for the surf reports, the wave conditions measured at Tyne Tees could be linked to the local surf conditions: parameters such as the wave directionality (relative to the pier) or the surf zone width could be assessed.

Figure 5.P1 shows the wave roses at Tyne Tees during March and April over the period 2007-2015. Two observations can be made from these roses:

- Waves arrive predominantly from the North/North-East (NNE) direction,
- More energetic conditions for the preferred direction (NNE quadrant) are observed in March

The wave height $H$, peak period $T_p$ and direction $\theta_p$ were the main information extracted from the surf reports. Figure 5.P2 shows the wave conditions at the Tyne Tees buoy for the period over which surf reports were available (October 2015 to January 2016). Except for the swell event around the 21/12/15 ($T_p = 12\,\text{s}$, $\theta_p = 0\,°$), both the observed wave direction (Figure 5.P2b) and peak period (Figure 5.P2c) match well with the wave conditions measured by the buoy. Interestingly, the visually observed wave height corresponds roughly to half the significant wave height measured at Tyne Tees.

Pictures taken on the days of the surf reports were used to assess the conditions as 'suitable' or 'not suitable' for the LiDAR deployment. The two main criteria were the surf zone width and the wave direction. Conditions were considered suitable when the surf zone was shorter than ~100 m in width so that it could be entirely covered by an array of three LiDAR scanners. Additionally, waves were required to propagate approximately parallel to the pier to minimise interaction with the pier itself and optimise the data for the study of wave transformation (corresponding to a wave direction of $\theta_p \sim 18\,°$). This analysis suggested that optimal conditions were present with waves from the NNE and a wave height smaller than 1 m at pier, corresponding to $H \leq 2\,\text{m}$ at Tyne Tees. From the 9 year-long dataset available it was determined that optimum conditions were 10% more likely during April than March. Furthermore storm conditions were observed to occur less frequently during April. The choice to perform the field experiments during the second week of April was therefore motivated by these observations.

[2]Example available here: http://magicseaweed.com/Saltburn-Beach-Surf-Report/24/

*Deploying an array of 2D LiDAR scanners*

The objective of the LiDAR deployment described in this Chapter was to capture the wave propagation from the shoaling area to the swash zone. This means that the scanners need to be located at a sufficient distance from each other to ensure enough coverage. However, a compromise has to be reached in order to ensure the absence of possible gaps due to high grazing angle (Martins et al., 2016).

For the dataset collected during the Rousty experiments, Martins et al. (2016) noted that a grazing (or attack) angle of $\alpha \sim 13.5°$ was the minimum angle for acquiring consistent measurements from the LiDAR for wave-by-wave analysis. This information should be taken with care in the present context as the level of aeration around the break point and in the swash zone can be different. Also, it only concerned waves travelling towards the LiDAR. A pilot study was performed by Chris Blenkinsopp in 2012 with the assistance of José Beya (Universidad de Valparaíso, Chile) on a nearshore pier in Chile. A quality analysis was performed on this unpublished dataset to investigate the spatial extent provided by the LiDAR scanner when deployed on a pier. This is presented in Figure 5.P3 and involved counting the number of returned signals as a function of the incident angle $\alpha$.

Small differences are observed between the seaward and landward directions in terms of measurement quality. More measurements are generally obtained landward of the LiDAR over the 6 log files considered. This is mainly due to more consistent wave breaking at this location. Each side of the LiDAR, three zones can roughly be observed:

- For $\alpha \in [50°, 90°]$, the signal quality is independent of the cross-shore direction (and hence $\alpha$) and is probably a function of the amount of foam present at the water surface.

- For $\alpha \in [30°, 50°]$, the quality of the signal slowly decreases as a function of the cross-shore direction, probably due to an increasing number of shadow areas (e.g. laser beam obstructed by the presence of a wave crest).
- For $\alpha \leq 30°$, the quality of the signal rapidly decreases as a function of the cross-shore direction. Angles $\alpha \leq 10°$ do not provide any signal return.

Considering the little differences noted between the first two zones, the $\alpha \sim 25 - 30°$ boundary was chosen to maximise cross-shore coverage but minimise the risk of data gaps. The minimal pier height - found close to shore - was visually estimated to be around 7 m, which with an overlapping area between adjacent scanners of 5 m, corresponds to a distance between scanners of 20 m.

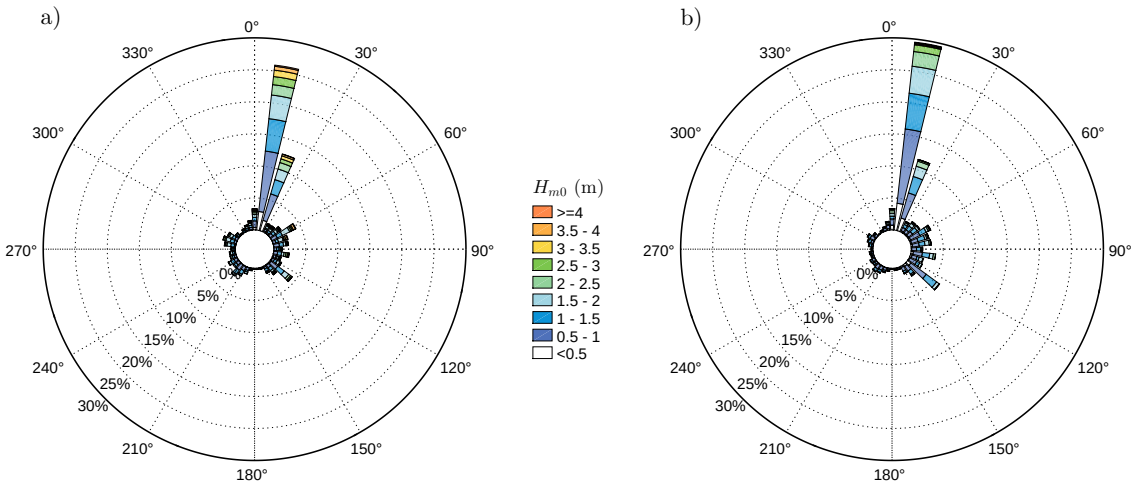


Figure 5.P1: Wave roses for the Tyne Tees wave buoy (25 km North of Saltburn-by-the-Sea, UK, see Figure 5.1) for March (panel a) and April (panel b) over the period 2007-2015. The angular resolution is 10° (36 divisions used) and the corresponding significant wave height $H_s$ is coloured by intensity.

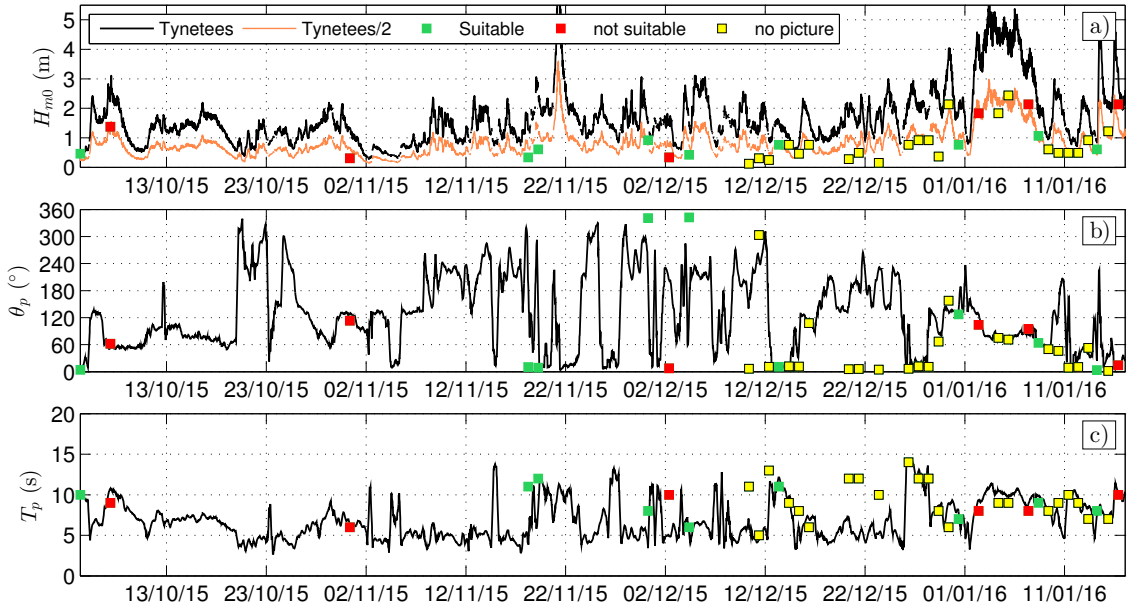


Figure 5.P2: Timeseries of the wave conditions measured at offshore buoy of Tyne Tees, compared to the visually assessed conditions in the Saltburn surf reports. The measured significant wave height $H_{m0}$ is shown in panel a), while the peak direction $\theta_p$ and peak period $T_p$ are shown in panels b) and c) respectively.

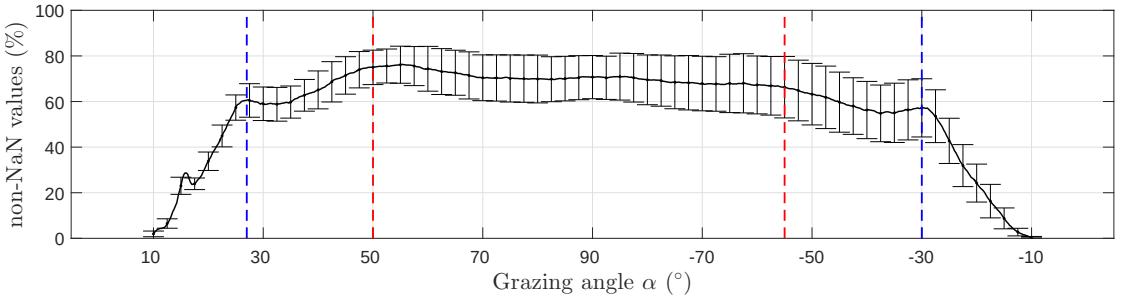


Figure 5.P3: Quality assessment of the LiDAR data from the Chile pilot study in function of the grazing angle $\alpha$. The black line corresponds to the mean returned signals (non Not a Number, NaN) over 6 log files and the error bars are the standard deviations. The red and blue dashed lines demark the first and second zones described in text.

## 5.1 Introduction

The surf zone is the most energetic area of the nearshore, characterised by the presence of breaking and broken waves. Depth-induced wave breaking is a complex physical process, which leads to dissipation of energy through a variety of processes including the injection of air (e.g. Blenkinsopp and Chaplin, 2007) and turbulence (e.g. Longo et al., 2002) into the water column as well as the generation of splashes and noise (Carey and Fitzgerald, 1993).

Due to the difficulty of obtaining high quality data in the energetic surf zone, existing field data are primarily from major field experiments: for example DUCK (Ebersole and Hughes, 1987), DELILAH (Birkemeier et al., 1990) and SUPERDUCK (Rosati et al., 1990) in the USA and more recently in Europe with the ECORS experiments (Sénéchal et al., 2011). Although the coastal community's knowledge of nearshore processes and wave transformation has greatly benefited from these experiments, they were generally limited by the cross-shore resolution of the measurements. Wave breaking involves a rapid transformation of wave geometry, and the break point constantly moves over time due to changing wave conditions and variation of mean water levels. The deployment of in situ instruments such as photopoles, pressure transducers or wave gauges can therefore only bring limited insight into the rapid changes in shape that a wave undergoes around the break point. As well as being non intrusive, remote sensors can generally cover larger scale with a better spatial resolution (e.g. RaDAR or video imaging, Holman and Haller, 2013) and can easily be deployed and maintained at the coast. However, most remote sensors are not capable of directly measuring the wave geometry.

Recent studies have demonstrated the ability of LiDAR scanners to obtain accurate measurements of the water surface and depth-averaged velocity at hundreds of points within the swash zone of a sandy beach (Blenkinsopp et al., 2012), and also the morphodynamics of gravel beaches (Almeida et al., 2015). In deeper water, the study of waves propagating in the inner surf zone of a dissipative sandy beach was made possible by deploying a tower-mounted LiDAR scanner close to the shoreline (Martins et al., 2016) or on a dune (Brodie et al., 2015). Brodie et al. (2015) demonstrate the potential of LiDAR scanners to monitor inner surf zone waves with high spatial extent and resolution by comparing the estimated spectral and third moment wave properties to pressure transducer data. More recently, Martins et al. (2017d) show that it is possible with a LiDAR scanner to accurately capture the shape of individual breaking waves (wave height, skewness and asymmetry), underlining significant differences between pressure-derived surface elevation and the scanner dataset.

Accurate detection of the break point is desired because it defines the seaward limit of the surf zone, where the behaviour of propagating waves changes significantly from a progressive surface wave to a bore, characterised by high levels of aeration and energy dissipation (Svendsen et al., 1978). Methods to define the break point based on wave geometry obtained from in situ gauges (e.g. Stokes limiting steepness of $H/L < 1/7$) or surface elevation vertical velocity $\partial\eta/\partial t$ have been used in deep water (Babanin, 2011). In shallower waters where spatial resolution is key, other methods mostly based on remote-

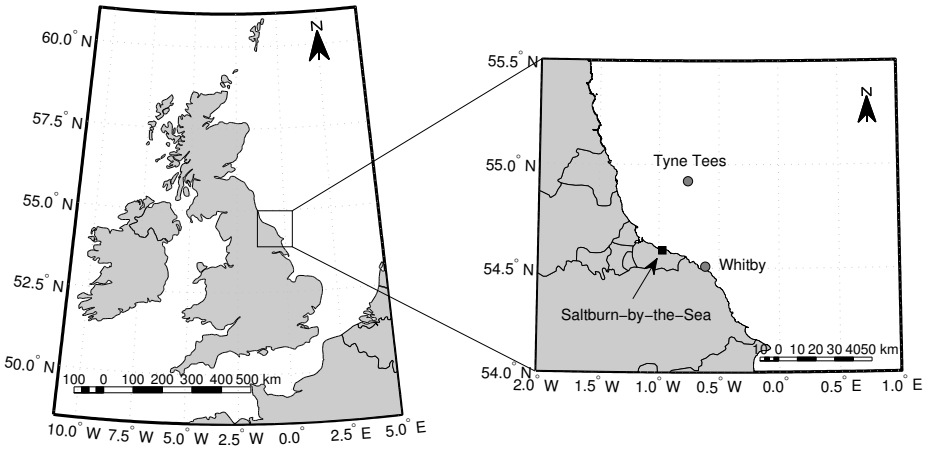


Figure 5.1: Map of the UK, zoomed around the field site area. The location of Saltburn-by-the-Sea is shown as the black square in the zoomed map, while the nearshore (Whiby) and offshore (Tyne Tees) buoys are shown as the grey dots. This part of the coastline is oriented to 18°NE in the North Sea.

sensing techniques (video methods Haller and Catalán, 2009, infrared imagery Carini et al., 2015 and microwave backscattering from breakers Catalán et al., 2014) have been used. Here, a new method to extract the break point from the high-resolution LiDAR dataset is discussed and compared to other commonly used criteria.

## 5.2 Methodology

### 5.2.1 Field site and wave conditions

A field experiment was undertaken between 7th April and 13th April, 2016 at Saltburn-by-the-Sea, on the North East coast of England (Figure 5.1). The beach at Saltburn is home to a 206 m long pier which was used to facilitate the experimental methodology described below (Figure 5.2). This part of the UK coastline is macrotidal: the measured tidal range at the harbour at Whitby reached a maximum of 5.42 m on 08/04 decreasing to 3.47 m on 13/04. The beach at Saltburn consists of a wide, sandy low gradient intertidal beach ($\tan\beta \sim 1:65$) backed by a steeper cobble slope ($\tan\beta \sim 1:6$). Between low and mid-tide, conditions are dissipative whereas when the mean water level reaches the lower part of the cobble slope, conditions become more reflective. The measurements described below focused on the period from mid to high tide and thus captured both dissipative and reflective conditions.

The wave climate at Saltburn is bi-modal with a combination of Northerly swell and Easterly wind-sea waves: deepwater average wave peak period ($T_p$) measured at the Tyne Tees Waverider buoy in 65 m water depth (see Figure 5.1 for the buoy location) are 9.4 s and 6.2 s respectively for these two direction quadrants. Figure 5.3 shows the nearshore wave conditions during the experiment measured by the Whitby Waverider buoy (17 m depth, see Figure 5.1 for the buoy location) and by a pressure transducer installed at the offshore limit of the pier. Throughout the course of the experiments, the significant wave height $H_s$ at the end of the pier remained relatively constant around 1 m (Figure 5.3a). However, wave direction and period changed abruptly on 11/04, when Easterly wind seas became

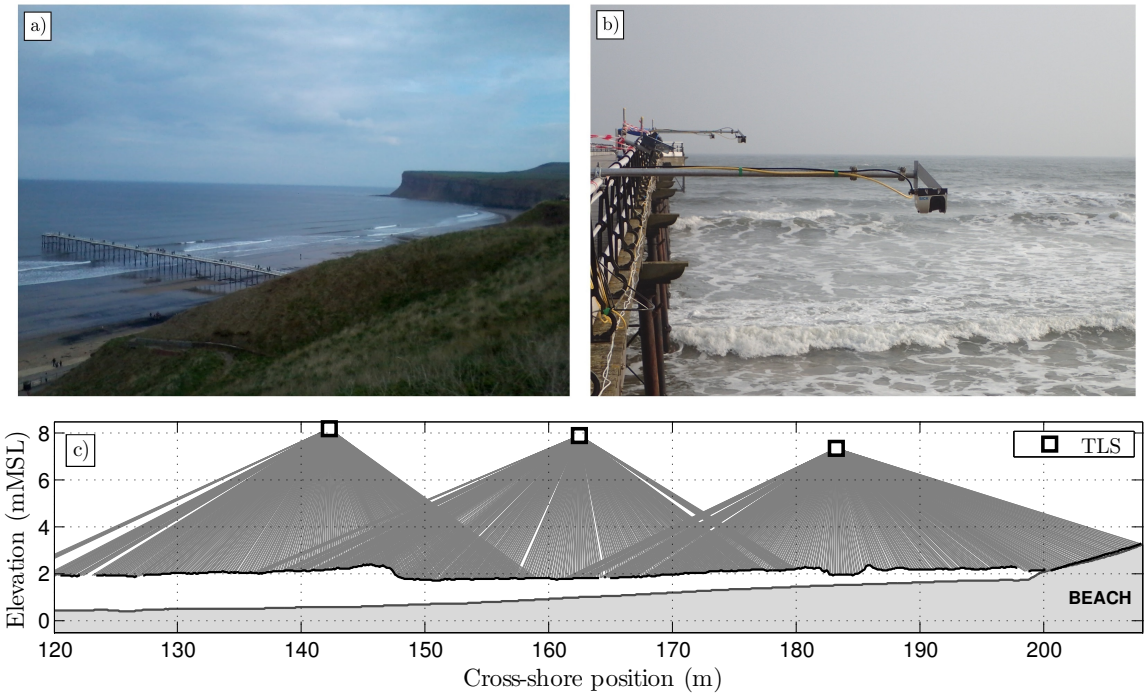


Figure 5.2: Field site and LiDAR scanners deployment. Panel a) shows the Saltburn beach pier, protected from the Eastern seas by a cliff. Panel b) shows the LiDAR scanners deployment: deployed in the first third of the pier, the scanners were deployed 2.5 m away from the pier, using a 'T' shaped scaffolding system relying on the pier railing system. Panel c) shows a schematic of the setup with an example of post-processed free surface elevation (black thick line while individual measurements are shown as light gray lines). The beach profile (thick gray line) corresponds to the surveyed profile during the previous low tide.

predominant over the Northerly swell (Figure 5.3b-c).

### 5.2.2 Experimental setup

Three SICK LMS511 commercial 2D LiDAR scanners were cantilevered over the side of the pier on braced scaffold poles extending 2.5 m from the safety railing (Figure 5.2b). The LiDAR scanners were positioned 20 m apart along the pier and at a height from the sand surface ranging from 5.9 m to 7.6 m, which enabled measurements of the free-surface data along an approximately 100 m long cross-shore transect, depending on surf zone width. Data were recorded continuously during each mid-high-mid tide cycle at a frequency of 25 Hz and an angular resolution of 0.1667°. Figure 5.2c displays the cross shore profile of the experimental set up, along with an example of the LiDAR measurements.

The LiDAR scanners were positioned on the East side of the pier such that the majority of wave rays did not pass beneath the pier before reaching the LiDAR scanning profile. Optimal conditions for the study of the cross-shore transformation of surf zone waves occurred during Northerly swell conditions (09/04 and 10/04) when after refraction, incoming waves propagate parallel to the pier (oriented to 18°NE in the North Sea). Additionally, by deploying the scanners 2.5 m from the pier structure, the influence of splashes from the pier legs was minimised, though in fact, due to the relatively small diameter of the pier legs, little splashing was observed.

In addition to the LiDAR scanners, one RBR pressure transducer (PT) was deployed

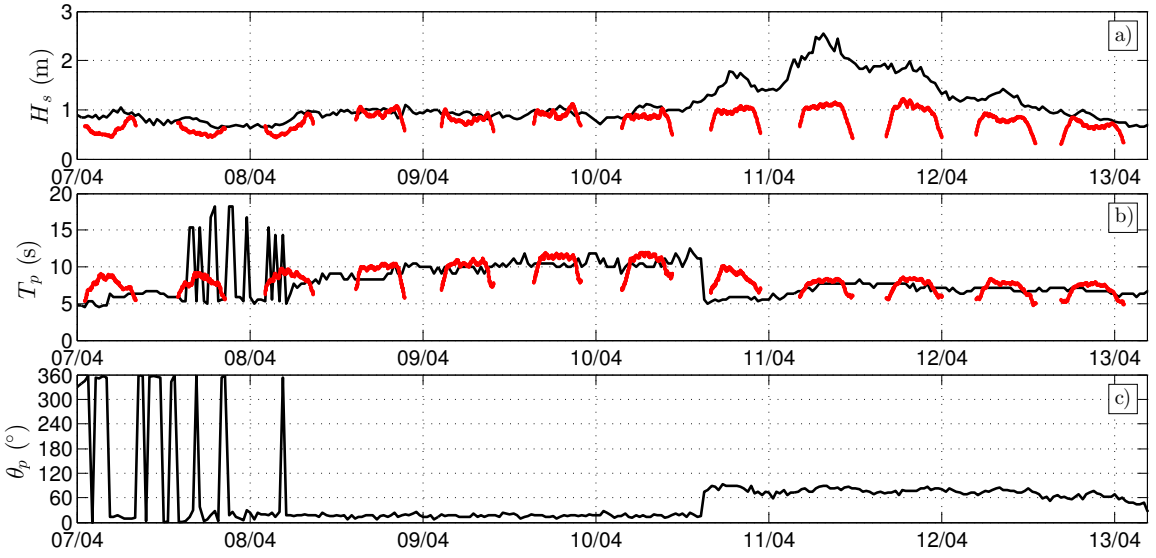


Figure 5.3: Nearshore wave conditions during the field experiment: a) Significant wave height $H_s$, b) Peak period $T_p$ and c) Peak direction $\theta_p$. In every panel measured conditions at Whitby buoy (courtesy of http://www.channelcoast.org/) are shown as black lines, while the conditions measured at the seaward edge of the pier by the pressure transducer are shown as red lines (only $H_s$ and $T_p$).

at $x = 16$ m, and sampled at 2 Hz ($x = 0$ m taken as the offshore limit of the pier, and $x$ is positive towards shore). Finally, beach profiles were measured using a total station and RTK GPS at every low tide.

### 5.2.3 Processing of the LiDAR data

As demonstrated by Blenkinsopp et al. (2010) and Blenkinsopp et al. (2012), successful detection of an air-water interface by LiDAR requires the presence of foam or bubbles at the surface. Each LiDAR scanner consistently detected the free-surface at hundreds of locations along a cross-shore transect spanning $40 - 50$ m. The spatial resolution varied with distance from the LiDAR but was generally 0.02 m beneath the scanner and up to 0.25 m at the outer edges of each LiDAR scan (see Figure 5.2c).

A combined dataset of surface elevation comprising the three individual LiDAR datasets was used to track waves across the surf zone. The location of each scanner was first surveyed using a total station. After geo-location, each of the individual LiDAR scanner datasets underwent a series of transformations (see Martins et al., 2016, for further detail): roll angle correction using surveys of beach profile, despiking and spatial interpolation into a 0.1-m regular cross-shore grid. This series of steps provides a time-series of water surface profiles for each of the three scanners as indicated in Figure 5.2c. A linear weighting function was used in the regions where there was overlapping LiDAR data ($x = 142$ to 162 m and $x = 162$ to 182 m) to prioritise the data with a smaller angle of incidence with the free surface. At any position where the data from one of the instruments was invalid, for example when the line-of-sight to a wave trough was obscured by the wave crest, the measurement from the other scanner only was used.

The differences observed between the LiDAR measurements in the overlapping areas

have been quantified in terms of Root-Mean Square Errors (RMSE) between individual LiDAR datasets. Consistency between adjacent instruments was observed throughout the experiment, with the largest average *RMSE* over an overlap region being 0.037 m, which is just four times the order of magnitude of the noise observed from a single sensor measuring a dry surface (Martins et al., 2016), and comparable to the local variation of the water surface due to 3D effects and splashes. Although lower standard deviations over the overlap regions was observed for swell conditions (09/04 and 10/04), no clear trend of the observed *RMSE* between instrument datasets with the wave conditions (Figure 5.3) was found.

## 5.3 Detection of the break point

Identifying the break point location in any free surface dataset is difficult due to the rapid and relatively limited spatial extent of the breaking process. A new method (hereafter referred to as gradient variance method; GVM) is described in Section 5.3.2. GVM uses the high-resolution dataset obtained from the LiDAR scanners to detect the evolution of small features in the broken wave front. The ability of GVM to detect the break point was compared to a range of other break point criteria for a dataset of 116 waves:

- location of maximum wave height $H$ (Svendsen and Buhr Hansen, 1976),
- location where the rate of change of surface elevation $\partial\eta/\partial t$ exceeds a threshold (equivalent to the rate of rise in Longuet-Higgins and Smith, 1983),
- location of maximum wave skewness $S_k$ (Svendsen, 2006),
- location of minimum wave asymmetry $A_t$ (Svendsen, 2006)

$H$ and the rate of change of surface elevation should reach their maximum at break point, because the wave steepness reaches its maximum at the break point location. Similarly, the wave skewness should reach its maximum while the asymmetry decreases significantly at the break point.

The ground truth method consists of the visual assessment of the break point from measured wave profile animations. The break point was visually estimated for each individual wave at the crest location when one of the following signs was apparent (Cowell, 1982) spray at the wave crest, wave front close to the wave crest about to overturn (vertical) and/or a disturbance or high frequency peaks in the wave front (suggesting a spilling-type of breaker). As the ground truth method is subjective to the user, the same analysis was performed by four people on a reduced subset of 41 waves. The *RMSE* between the user's datasets had minimum (maximum) values of 1.5 m (2.6 m), with corresponding standard deviation values of 1.4 m (2.2 m).

### 5.3.1 Wave-by-wave approach

To detect the break point, GVM relies on a previously developed wave-by-wave approach that involves tracking individual waves from the shoaling region and through the surf zone (Martins et al., 2016; Martins et al., 2017d). In this wave-by-wave approach, wave crests were identified by detecting peaks in the surface elevation timeseries at each cross-shore

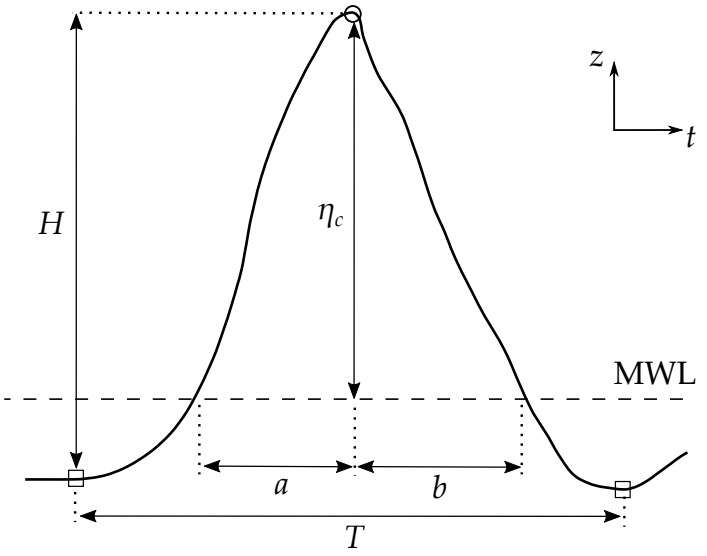


Figure 5.4: Nomenclature adopted for the definition of spatial and temporal individual wave parameters: based on Mean Water Level (*MWL*), $\eta_c$ defines the crest height elevation above *MWL*, $H$ the distance between wave crest and preceding trough. The parameters a and b represent the time elapsed for the surface elevation to reach the crest elevation from up-crossing *MWL* and the time elapsed for the surface elevation to down-cross *MWL* from the crest elevation. The squares represent the two surrounding troughs, defining the individual wave period of the wave. The crest is designated by a circle.

grid location. Starting at an initial cross-shore location, the wave crests were then tracked through the surf zone and at each cross-shore location, and the following individual wave properties were extracted: individual wave height $H$, wave period $T$ and trough levels $h_t$, along with spatial (Eq. 5.1) and temporal (Eq. 5.2) definitions of wave asymmetry:

$$A_s = \eta_c/H \tag{5.1}$$

$$A_t = a/b \tag{5.2}$$

where the parameters in Eq. 5.1 and 5.2 are defined in Figure 5.4 (Adeyemo, 1968). The vertical spatial asymmetry was used to define the individual wave skewness:

$$S_k = A_s - 0.5 \tag{5.3}$$

which has a value close to zero when the wave profile is centred on the Mean Water Level (*MWL*). In the analysis described here, wave periods are defined by the time elapsed between the passages of the two troughs surrounding the wave crests at a same location (Figure 5.4).

### 5.3.2 Break point detection using the gradient variance method

The principle of GVM to detect the break point takes advantage of the ability of the LiDAR to capture small-scale features in the broken wave front. Figure 5.5 shows timestack examples of surface elevation and surface elevation spatial gradient (based on central differences) of a breaking wave from 10/04. Prior to the break point ($x$ = 158 m), the surface elevation around the crest of the shoaling wave is smooth (Figure 5.5a) and the corresponding spatial

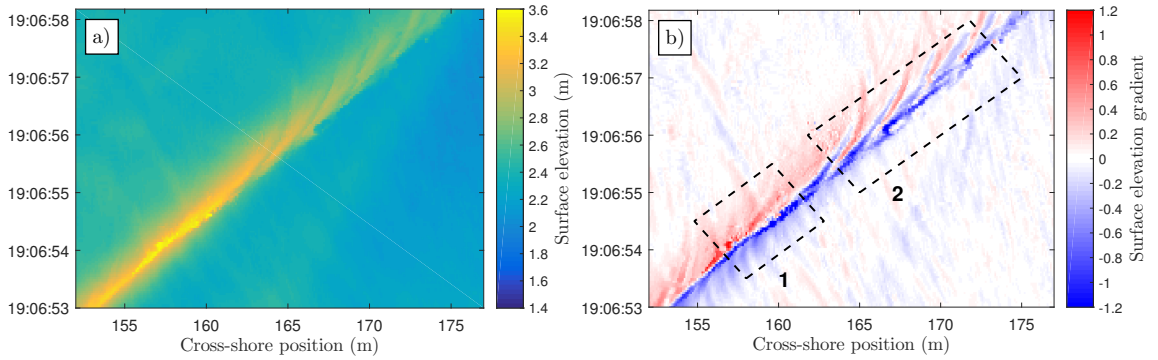


Figure 5.5: Example of surface elevation timestack of a breaking wave: a) shows the surface elevation in the Saltburn Mean Sea Level (*MSL*) datum, while b) shows the corresponding spatial surface elevation gradient $\partial\eta/\partial x$. The two dashed rectangles in panel b) represent the two distinct phases during the breaking process: 1 corresponds to the breaking onset, with the maximum wave height and minimum gradient in front of the wave reached; 2 corresponds to the early stage of propagation as a bore.

gradients in front and behind the wave crest are relatively constant, and respectively negative and positive (Figure 5.5b). At the onset of breaking, the surface elevation reaches its maximum (Figure 5.5a), and the maximum absolute gradient is reached at the wave front face (phase 1 in Figure 5.5b). While the wave keeps breaking, higher frequency peaks are generated in the roller region (phases 2 in Figure 5.5b). These peaks appear as alternately positive and negative gradient stripes close to the wave crest which exhibit nearly regular patterns both in time and space. Figure 5.6a illustrates further this phenomenon with the example of a wave profile evolution.

To estimate the break point location of a tracked wave, the surface elevation spatial gradients at every point in the wave profile between the wave crest and an elevation $0.8H$ below the crest on the wave front face are extracted. This process is performed at every cross-shore position, at the moment when the wave crest passes that position (see example in Figure 5.6a). The variance of these spatial gradients is then computed and used as a proxy for the break point detection: the variance increases considerably at the breaking onset, and remains much higher than when shoaling due to the roller activity (see example in Figure 5.6b). Note that the variance of the gradients is calculated only to $0.8H$ below the crest because when tracking waves individually, the wave trough - defined as minimum reached between two wave crests - can be relatively distant from the subsequent crest due to the presence of higher frequency waves. The first cross-shore location where the surface elevation gradients variance reaches the empirical threshold of 0.2 defines the break point.

## 5.4 Results

### 5.4.1 Performance of the break point detection methods

The different methods to assess the break point outlined in Section 5.3 were compared in terms of performance against the ground truth method for 116 individual waves from the 08/04, 09/04, 10/04 and 11/04 to cover the range of wave conditions experienced during the experiments. Figure 5.7 shows a scatter plot of the estimated break point locations using all methods. From their fit to the 1:1 line, it is evident that for the chosen ground truth

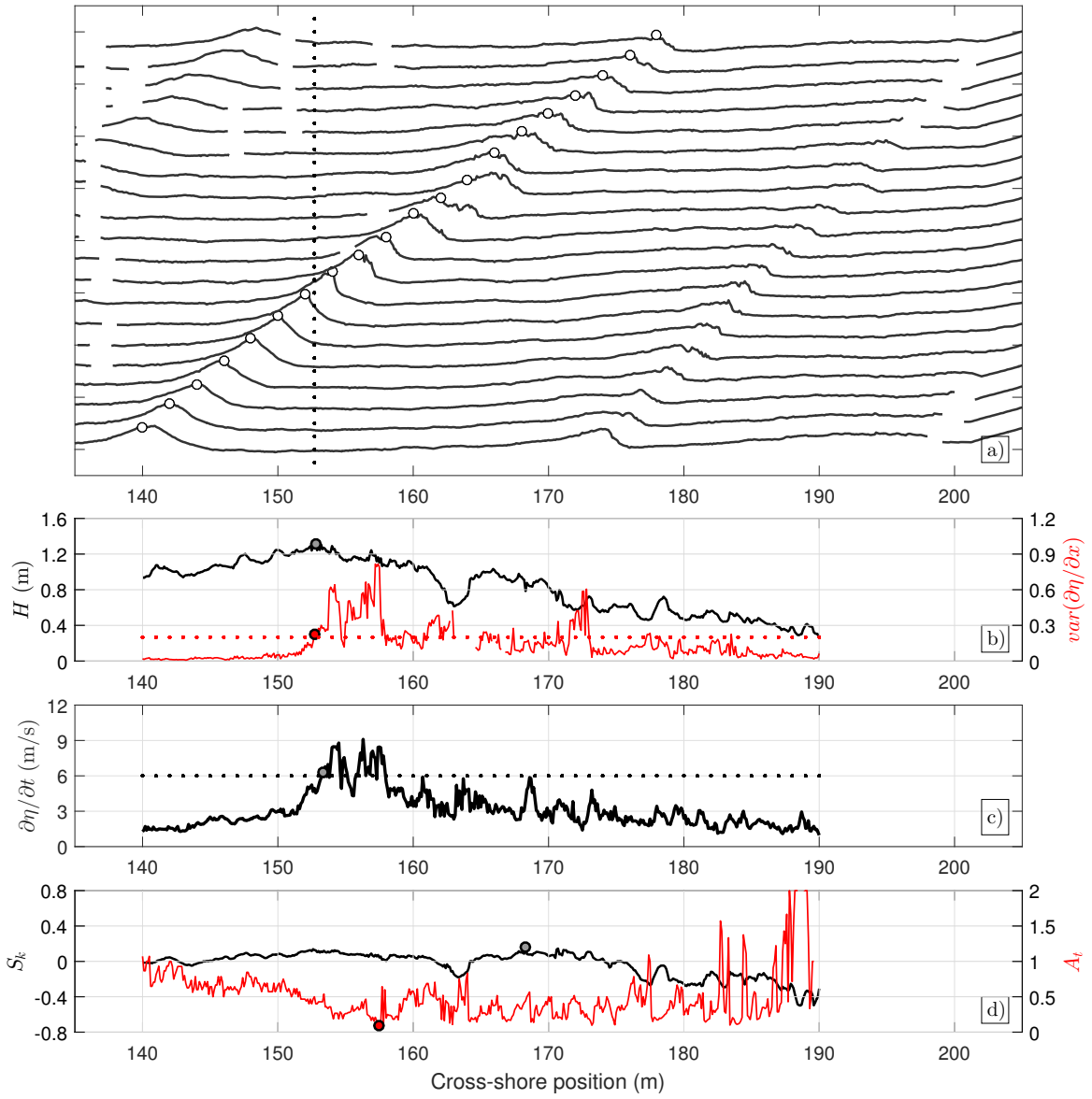


Figure 5.6: Propagation of a breaking wave on 09/04. Panel a) shows the wave profile evolution through the surf zone: a complete profile is shown at the time when the maximum water surface elevation (wave crest) is detected at 2 m cross-shore increments. The break point location is shown as vertical dotted line. Panel b) shows the cross-shore evolution of the individual wave height $H$ (black line), shown with the variance of the surface elevation gradient in front of the wave (red line). The red dotted threshold line of 0.2 is also shown. The break points are shown as grey and red dot for the $H$-based method and GVM respectively. Panel c) shows the maximal surface elevation rate of change in front of the wave. The threshold line used for this method (6 m/s) is shown as dotted black line Panel d) shows the individual wave skewness ($S_k$) and wave time asymmetry ($A_t$) as black and red lines respectively. The break points are shown as grey and red dot for the $S_k$-based and $A_t$-based methods respectively.

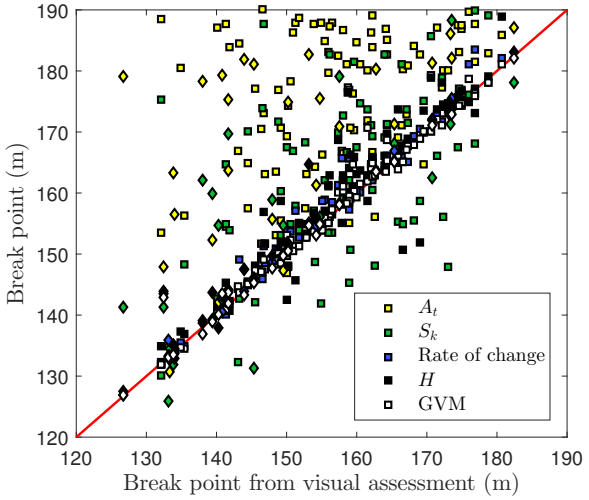


Figure 5.7: Scatter plot of the different methods for the break point assessment. For a subset of 116 manually picked individual waves, the detected break point from each method is shown against the ground truth method (visual assessment from LiDAR data animations). Data from the 09/04 and 10/04 (plunging and spilling breaker types) are shown as squares while the rest of the data (predominantly spilling breakers) are represented using diamonds.

method, three methods stand out: GVM, the velocity-based (using a threshold of 6 m/s) and $H$-based methods. GVM provide the best fit with the smallest $RMSE$ when compared to the ground truth method (1.75 m), followed by the method based on the rate of change of surface elevation and the $H$-based method with $RMSE$ of 2.44 m and 4.52 m respectively.

The $S_k$-based and $A_t$-based methods provide the least accurate estimates of the break point, with $RMSE$ of 13.62 and 22.52 m respectively. Although these two methods give different $RMSE$, the standard deviation is high and of the same order (around 13 m). The reason is that the $S_k$-based method often predicts a breakpoint seaward of the visually observed location, whereas the individual time asymmetry becomes minimal only at the break point or after during the bore propagation, meaning that the $A_t$-based method almost never predicts the break point earlier than it actually occurs. An example of this can be seen in Figure 5.6d, where $A_t$ decreases until breaking ($x$ = 152.7 m), but reaches its minimum value farther landward ($x$ = 158 m). In other cases, this can be even farther landward in the inner surf, as developed bores can be steep, and their asymmetry small, as suggested by the presence of multiple small values in Figure 5.6d. The absence of a defined peak at or near the break point for the $S_k$ parameter in part explains the discrepancies observed with the $S_k$-based method. Instead, the peak values in the cross-shore were often caused by the superposition of incident and reflected waves in either the shoaling or surf zones.

### 5.4.2 Sensitivity analysis of breaker detection methods

The sensitivity of GVM to the chosen threshold was investigated by performing the same analysis with two other thresholds of 0.15 and 0.3. With these two thresholds, $RMSE$ of 2.16 and 4.69 m were obtained. The chosen value of 0.2 is therefore close to the optimal value for this ground truth method. The poorer performance obtained with the 0.3 threshold can be primarily explained by the time needed for the gradient variance to increase for spilling

waves, tending to delay the detection of the break point.

The criterion for the method based on the rate of change of surface elevation was also examined. This parameter is expected to reach its maximum at the moment of breaking, however the presence of high-frequency peaks in the roller region generated during the breaking process not only leads to the good performance of the GVM, but also implies steep and rapidly-changing features in the front of the wave. When these changes are faster than those due to a steepening or breaking wave, the maximum rate of change in the wave path can therefore be located well away from the actual break point. This is illustrated in Figure 5.6c, where multiple peaks are present after the break point, and the greatest peak does not correspond to the break point location. Similar to the $A_t$-based method, this criterion tends to predict the break point landward of its true location (Figure 5.7). The choice of the up-crossing threshold method rather than the maximum location decreased the *RMSE* for this method from 6.61 m to 2.44 m. A drawback of this method lies in the lower rate of change observed for spilling waves. No break point could be detected for 9 of the 116 waves, because the surface elevation rate of change never exceeded the threshold. A more robust threshold accounting for the individual wave celerity is desirable (Longuet-Higgins and Smith, 1983), but at present, estimating the individual wave celerity based on a timeseries at a single point remains a challenge.

Although the maximum value of the wave height to water depth ratio $\gamma = H/h$ is sometimes used to define the break point, it was recently observed to increase in the inner surf zone, with the possibility of reaching higher values than at break point (Power et al., 2010). This parameter was also found to be affected by the presence of higher/lower frequency waves such as those reflected at high tide (Martins et al., 2017d) or the formation of jets/splashes after breaking that can reach higher elevation than the crest itself at break point. A reduction in *RMSE* of 1.87 m to estimate the break point was obtained by using the maximum wave height $H$ rather than $\gamma$.

## 5.5 Concluding remarks

This paper reports on a field experiment undertaken in April 2016 at Saltburn-by-the-Sea, UK. Three 2D LiDAR scanners were deployed 20 m apart along the pier to obtain a complete surface elevation dataset throughout the surf and swash zones. A detailed field dataset of breaking waves was obtained, with data covering up to 100 m of the surf zone at a frequency of 25 Hz and a spatial resolution ranging from 0.02 to 0.25 m.

A new method to estimate the break point location from the detailed wave profile measurements is presented. It uses previously developed tracking algorithms and the high spatial and temporal resolution of the LiDAR dataset to assess the break point based on the variance of the surface elevation gradients in front of a tracked wave crest. Good ability to detect the break point location was obtained against a visual assessment of LiDAR data (*RMSE* = 1.75 m). Good performances were also obtained by the methods based on surface elevation rate of changes and on the wave height. The other methods based on geometrical considerations ($S_k$, $A_t$) tend to delay or detect the break point farther landward (Figure 5.7).

The error in break point location is mostly explained by the increasing non-linearities in the wave shape after breaking.

Finally, the discrepancies observed in the break point location, and those found in the breaker parameters possibly explain the difficulty in obtaining simple relations between offshore wave parameters, beach slope and wave properties at the break point noted by Robertson et al. (2013). The ability to obtain high resolution data using a LiDAR and the analysis methods presented here may provide a good opportunity to make progress with this problem.

## Acknowledgements

The authors would like to acknowledge the financial assistance provided by the Engineering and Physical Sciences Research Council (EP/N019237/1). Kévin Martins was supported by the University of Bath, through a URS scholarship. The assistance of Perveen Mian and her colleagues at Redcar and Cleveland Council in facilitating access to the site is greatly appreciated. B. Bruder and J. Puleo were supported by SERDP (MR-2503) and the University of Delaware. We would also like to thank Aline Pieterse (University of Delaware, USA) for her assistance during the experiment.

## References

Adeyemo, M. 1968. Effect of beach slope and shoaling on wave asymmetry. *Proceedings of 11th Conference on Coastal Engineering, London, United Kingdom*, pp. 145 – 172.

Almeida, L. P., Masselink, G., Russell, P. E., and Davidson, M. A. 2015. Observations of gravel beach dynamics during high energy wave conditions using a laser scanner. *Geomorphology* 228, pp. 15 – 27. DOI: 10.1016/j.geomorph.2014.08.019.

Babanin, A. 2011. *Breaking and Dissipation of Ocean Surface Waves*. Cambridge University Press. DOI: 10.1017/CBO9780511736162.

Birkemeier, W., Donoghue, C., Long, C., Hathaway, K., and Baron, C. 1990. *DELILAH nearshore experiment: Summary report*. Tech. rep. CHL-97-4-24, US Army Corps of Engineers. Field Research Facility.

Blenkinsopp, C. E and Chaplin, J. R. 2007. Void fraction measurements in breaking waves. *Proceedings of the Royal Society of London A: Mathematical, Physical and Engineering Sciences* 463 (2088), pp. 3151 – 3170. DOI: 10.1098/rspa.2007.1901.

Blenkinsopp, C. E., Mole, M. A., Turner, I. L., and Peirson, W. L. 2010. Measurements of the time-varying free-surface profile across the swash zone obtained using an industrial LIDAR. *Coastal Engineering* 57 (11 – 12), pp. 1059 – 1065. DOI: 10.1016/j.coastaleng.2010.07.001.

Blenkinsopp, C. E., Turner, I. L., Allis, M. J., Peirson, W. L., and Garden, L. E. 2012. Application of LiDAR technology for measurement of time-varying free-surface profiles in a laboratory wave flume. *Coastal Engineering* 68, pp. 1 – 5. DOI: 10.1016/j.coastaleng.2012.04.006.

Brodie, K. L., Raubenheimer, B., Elgar, S., Slocum, R. K., and McNinch, J. E. 2015. Lidar and Pressure Measurements of Inner-Surfzone Waves and Setup. *Journal of Atmospheric and Oceanic Technology* 32 (10), pp. 1945 – 1959. DOI: 10.1175/JTECH-D-14-00222.1.

Carey, W. M. and Fitzgerald, J. W. 1993. "Low Frequency Noise from Breaking Waves". *Natural Physical Sources of Underwater Sound: Sea Surface Sound (2)*. Ed. by B. R. Kerman. Dordrecht: Springer Netherlands, pp. 277 – 304. DOI: 10.1007/978-94-011-1626-8_22.

Carini, R. J., Chickadel, C. C., Jessup, A. T., and Thomson, J. 2015. Estimating wave energy dissipation in the surf zone using thermal infrared imagery. *Journal of Geophysical Research: Oceans* 120 (6), pp. 3937 – 3957. DOI: 10.1002/2014JC010561.

Catalán, P. A., Haller, M. C., and Plant, W. J. 2014. Microwave backscattering from surf zone waves. *Journal of Geophysical Research: Oceans* 119 (5), pp. 3098 – 3120. DOI: 10.1002/2014JC009880.

Cowell, P. J. 1982. *Breaker stages and surf structure on beaches*. Tech. rep. Coastal Studies Unit Technical Report No. 82/7, Sydney, Australia.

Ebersole, B. A. and Hughes, S. A. 1987. *DUCK85 Photopole Field Experiment*. Tech. rep. ADA188477, DTIC Document.

Haller, M. C. and Catalán, P. A. 2009. Remote sensing of wave roller lengths in the laboratory. *Journal of Geophysical Research: Oceans* 114 (C7). C07022. DOI: 10.1029/2008JC005185.

Holman, R. and Haller, M. C. 2013. Remote Sensing of the Nearshore. *Annual Review of Marine Science* 5 (1). PMID: 22809186, pp. 95 – 113. DOI: 10.1146/annurev-marine-121211-172408.

Longo, S., Petti, M., and Losada, I. J. 2002. Turbulence in the swash and surf zones: a review. *Coastal Engineering* 45 (3–4). Surface and Swash Zone Mechanics, pp. 129 – 147. DOI: 10.1016/S0378-3839(02)00031-5.

Longuet-Higgins, M. S. and Smith, N. D. 1983. Measurement of breaking waves by a surface jump meter. *Journal of Geophysical Research: Oceans* 88 (C14), pp. 9823 – 9831. DOI: 10.1029/JC088iC14p09823.

Martins, K., Blenkinsopp, C. E., and Zang, J. 2016. Monitoring Individual Wave Characteristics in the Inner Surf with a 2-Dimensional Laser Scanner (LiDAR). *Journal of Sensors, 2016*, pp. 1 – 11. DOI: 10.1155/2016/7965431.

Martins, K., Blenkinsopp, C. E., Almar, R., and Zang, J. 2017d. The influence of swash-based reflection on surf zone hydrodynamics: a wave-by-wave approach. *Coastal Engineering* 122, pp. 27 – 43. DOI: 10.1016/j.coastaleng.2017.01.006.

Power, H. E., Hughes, M. G., Aagaard, T., and Baldock, T. E. 2010. Nearshore wave height variation in unsaturated surf. *Journal of Geophysical Research: Oceans* 115 (C8). DOI: 10.1029/2009JC005758.

Robertson, B., Hall, K., Richard, Z., and Nistor, I. 2013. Breaking waves: review of characteristic relationships. *Coastal Engineering Journal* 55 (01), p. 1350002. DOI: 10.1142/S0578563413500022.

Rosati, J. D., Gingerich, K. J., and Kraus, N. C. 1990. *Superduck surf zone sand transport experiment*. Tech. rep. ADA225690, DTIC Document.

Sénéchal, N., Abadie, S., Gallagher, E., MacMahan, J., Masselink, G., Michallet, H., Reniers, A., Ruessink, G., Russell, P., Sous, D., Turner, I., Ardhuin, F., Bonneton, P., Bujan, S., Capo, S., Certain, R., Pedreros, R., and Garlan, T. 2011. The ECORS-Truc Vert'08 nearshore field experiment: presentation of a three-dimensional morphologic system in a macro-tidal environment during consecutive extreme storm conditions. *Ocean Dynamics* 61 (12), pp. 2073 – 2098. DOI: 10.1007/s10236-011-0472-x.

Svendsen, I. A. 2006. *Introduction to Nearshore Hydrodynamics*. Advanced series on ocean engineering. World Scientific.

Svendsen, I. A. and Buhr Hansen, J. 1976. Deformation up to breaking of periodic waves on a beach.

Svendsen, I. A., Madsen, P. A., and Buhr Hansen, J. 1978. Wave characteristics in the surf zone. *Proceedings of the 16th Conference on Coastal Engineering, Hamburg, Germany*, pp. 520 – 539.

# Chapter 5.

## Preamble to the second part

Although individual wave skewness and asymmetry can not be used as a proxy for the break point detection, both properties showed interesting cross-shore evolution in the research article above (e.g., see Figure 5.7). These results raise an interesting question on whether or not individual wave skewness and asymmetry correlate with the same properties at the time-averaged scale. The second part of this Chapter presents additional analyses performed on the LiDAR dataset collected in Martins et al. (2017b), and aim at studying wave geometric properties and investigate their link at different temporal scales.

In addition to the LiDAR measurements, pressure and cross-shore current velocity data were acquired at five and three cross-shore locations respectively. Figure 5.2c of the research article above has been modified in Figure 5.8 to show the complete cross-shore experimental setup. The flow velocity data were collected at elevations from the bed ranging from 0.10 to 0.15 m from the sea bed using three Nortek Acoustic Doppler Velocimeters (ADV) sampled at 16 Hz. Each ADV is equipped with an internal pressure sensor, but the two most onshore ADVs were also synchronized with an external pressure transducer (PT) and Optical Backscatter Sensor (OBS). In these additional analyses, a potential link between the sea surface elevation skewness and asymmetry and that of the cross-shore current velocities is investigated, with the aim of predicting flow characteristics close to the sea bed from remotely-sensed water surface characteristics.

The results given in the second part of this Chapter were presented at the Coastal Dynamics Conference in Helsingør, Denmark. Here, we only include the results and discussion parts of the Conference paper as it largely overlaps with the preceding research article. However, the reader is also invited to read further information in Martins et al. (2017c):

Kévin Martins, Chris E. Blenkinsopp*, Erwin W. J. Bergsma, Hannah E. Power, Brittany Bruder and Jack A. Puleo and , "Remote-sensing of wave transformation in the surf zone", Proceedings of the Conference on Coastal Dynamics 2017, Helsingør, Denmark.
PDF: http://coastaldynamics2017.dk/onewebmedia/033_Martins_Kevin.pdf

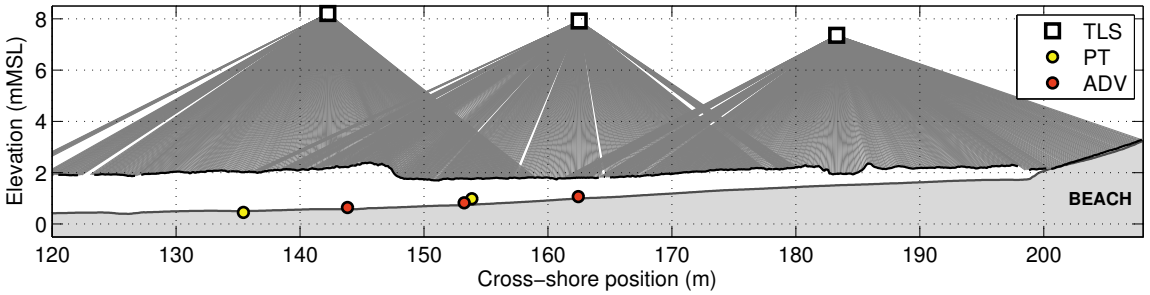


Figure 5.8: LiDAR scanners deployment: schematic of the full experimental setup with an example of post-processed free surface elevation (black thick line while individual measurements are shown as light gray lines). The beach profile (thick gray line) corresponds to the surveyed profile during the previous low tide.

## 5.6 On the surface elevation and cross-shore current skewness and asymmetry

### 5.6.1 Definitions

As described in the previous paper, wave skewness $S_k$ and asymmetry $A_s$ are a measure of the wave non-linearity. It can hence be used to characterize the wave geometry in the surf zone: highly skewed waves are characterized by a narrower crest and broader trough while highly asymmetric waves generally have a steep front and gradually sloping back, as is the case with propagating bores.

At the time-averaged temporal scale, the surface elevation skewness and asymmetry are defined as follows:

$$S_k = \frac{\overline{(\eta(t) - \bar{\eta})^3}}{\overline{(\eta(t) - \overline{\eta})^2}^{3/2}} \tag{5.4}$$

$$A_s = \frac{\overline{\mathcal{I}m(\mathcal{H}(\eta(t) - \bar{\eta}))^3}}{\overline{(\eta(t) - \overline{\eta})^2}^{3/2}} \tag{5.5}$$

where $\mathcal{I}m(\mathcal{H}(\,.\,))$ is the imaginary part of the Hilbert transform and $\overline{(\,.\,)}$ is the time-averaged operator (Berni et al., 2013). The wave skewness and asymmetry were calculated for both pressure-derived and LiDAR surface measurements, using 20 minute-long data windows. Similarly, the skewness and asymmetry of the cross-shore bottom current velocity $u$ measured at the three cross-shore locations were calculated (replacing $\eta$ by $u$ in Equations 5.4 and 5.5). In that way, skewness and asymmetry at the surface can be related to that of the current close to the bottom. At the wave-by-wave scale, we use the same temporal framework as described before, although more detailed here (Adeyemo, 1968; Cowell, 1982):

$$D = a/b \tag{5.6}$$

$$A_s = 2(a + b)/T \tag{5.7}$$

$$S_k = 2\eta_c/H - 1 \tag{5.8}$$

We also extend the analysis to the spatial domain by looking at the wave front and back angle denoted $\theta_{front}$ and $\theta_{back}$ respectively. These angles are estimated by calculating the slope of a line fitting a section of the wave profile. The section of the wave profile starts from the detected and tracked wave crest, and extends to the first point 65% of $H$ below the crest level at the wave front for $\theta_{front}$, and behind it for $\theta_{back}$. These spatial frameworks and temporal frameworks are illustrated in the sketches of Figure 5.9.

### 5.6.2 Surface elevation first and third order moments

The additional results use data obtained around high tide at the four tidal cycles during 09/04 and 10/04. Figure 5.10 shows the comparison of the significant wave height $H_{m0}$, wave asymmetry $A_s$ and skewness $S_k$ measured by the LiDAR and pressure transducers

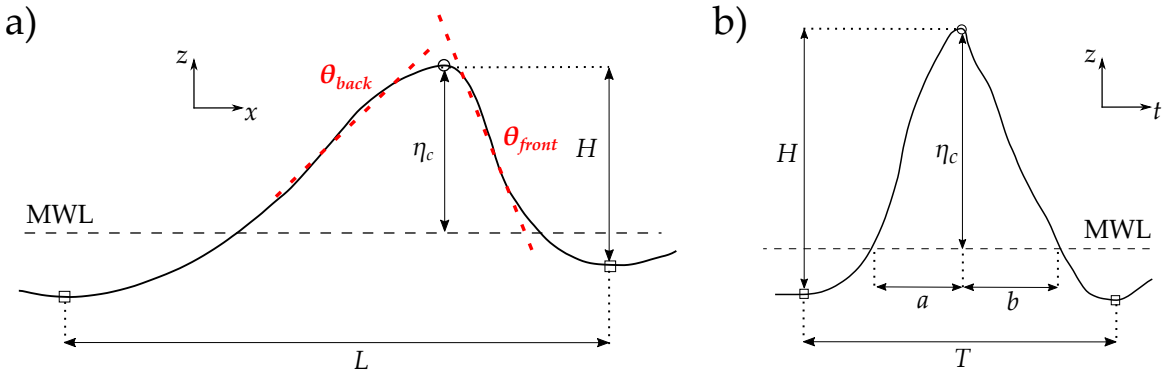


Figure 5.9: Nomenclature adopted for the definition of spatial (Panel a) and temporal (Panel b) individual wave parameters: based on the Mean Water Level (*MWL*), $\eta_c$ defines the crest height elevation above *MWL*, $H$ the distance between wave crest and preceding trough. The quantities $a$ and $b$ represent the time elapsed for the surface elevation to reach the crest elevation from up-crossing *MWL* and the time elapsed for the surface elevation to down-cross *MWL* from the crest elevation. The squares represent the two surrounding troughs, defining the individual wave period of the wave. The crest is designated by a circle.

at the three ADV locations (Figure 5.8). These parameters were calculated using moving windows of 20 minutes, to allow for a more continuous description throughout the tide. A threshold of 75% non-NaN values over that window was used for the LiDAR dataset. This explains that some data are missing at high tide, when there was less consistent wave breaking over the two most offshore ADV.

The significant wave height measured by the PT and LiDAR show very good agreement (Figure 5.10a, 5.10d and 5.10g), at every location and every stage of the tide. This is consistent with the results from Brodie et al. (2015) who obtained similar results in their field dataset. Despite the very likely differences between pressure-derived and the remotely-sensed wave height at the wave-by-wave scale (e.g. Martins et al., 2017d), the spectral parameters present good agreement, consistent with the conclusion of Bishop and Donelan (1987) that the significant wave height could be retrieved within 5% of error with pressure transducers.

Comparison of time-averaged wave asymmetry from the PT and LiDAR (Figure 5.10b, 5.10e and 5.10h) also show good agreement at all stages of the tide. During the flooding and ebbing period (wave height to water depth ratio $\gamma \in [0.45; 0.55]$), $A_s$ exhibits a peak value and then decreases to reach its minimum values around high tide. However, the wave skewness estimated from the LiDAR scanner is consistently greater than that estimated from the pressure-derived signal: a very good correlation ($r = 0.9$ and Scatter Index of 0.07) is found for the relation $S_{k,LiDAR} = 1.2S_{k,PT}$. Considering the physical explanation that is given to the wave skewness, a possible explanation at this stage of the analysis could be that the underestimation of individual wave height in the pressure-derived dataset at the onset of breaking or soon after affect the time-averaged parameter.

### 5.6.3 Relation between surface and bottom cross-shore velocity

Wave skewness and asymmetry (Equations 5.4 and 5.5) respectively) estimated from the surface elevation $\eta$ and bottom current velocity $u$ were compared to investigate the possibility of predicting third-moments of the cross-shore current velocity from a surface elevation

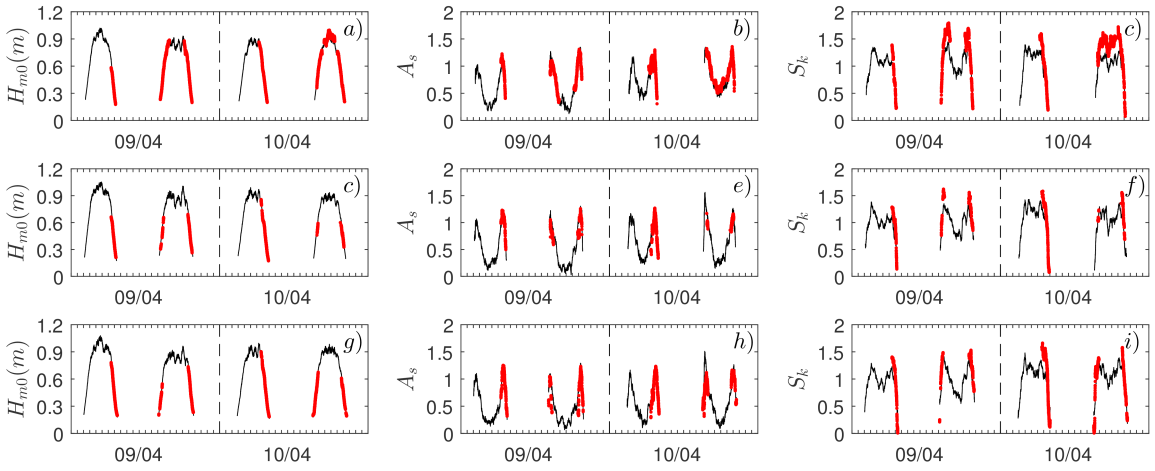


Figure 5.10: Comparison between pressure-derived (black line) and LiDAR (red points) significant wave height $H_{m0}$, wave asymmetry $A_s$ and skewness $S_k$. Panels a-c) show the data at the onshore ADV location ($x$ = 162 m), while panels d-f) and g-i) show the data at the middle ($x$ = 153 m) and offshore ($x$ = 144 m) ADV locations respectively.

signal.

Two different comparisons were performed: 1) $A_s$ and $S_k$ compared with no specific processing on $\eta$ or $u$; 2) $A_s$ and $S_k$ compared with a Fourier low-pass filter on $\eta$, with the cutoff frequency chosen as three times the peak frequency $f_p$. This was attempted as Berni et al. (2013) showed that three Fourier components were enough to accurately describe the free-stream velocity under skewed and asymmetric waves. The results are first displayed in Figure 5.11 as a timeseries for the data from the offshore ADV location. It is observed that during the four tides of interest (09/04 and 10/04), the asymmetry and skewness calculated from the filtered surface elevation signal is in much better agreement with that from the current velocity than when estimated with the full $\eta$ spectrum. The major improvements principally concern the periods when the water is relatively shallow (flooding and ebbing), where due to the presence of bores, $S_k$ presents values of up to twice that at high tide, and up to ten times for $A_s$.

The ADV data (with and without frequency cutoff) as well as the LiDAR data (with frequency cutoff) from every cross-shore location and all tides are displayed in Figure 5.12. It is shown that the wave asymmetry and skewness estimated from the filtered surface elevation derived from PTs and LiDARs closely match those for the bottom current velocity. For the ADV data, besides the fact that the mean data points estimated from the filtered signal are closer to the 1:1 line, standard deviations are also smaller. Considerable deviation between these filtered signal datasets and the current velocity dataset is still observed for very low values of $A_s$ ($A_s < 0.1$) and especially very low values of $S_k$ ($S_k < 0.15$), although there is considerable scatter for these ranges of values. This suggests that at low tide (Figure 5.11), both the cross-shore current asymmetry and skewness will typically be underestimated when based on surface elevation measurements. The presence of strong infragravity waves observed at this stage of the tide very likely explain this phenomenon.

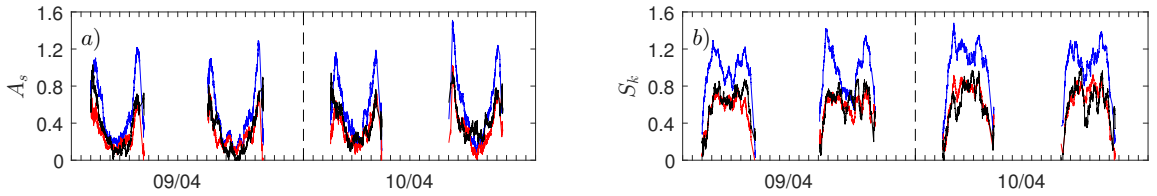


Figure 5.11: Timeseries comparison of third-order wave moments data estimated from pressure and velocity measurements at the offshore ADV location: panel a) shows $A_{s,u}$ (black line) against $A_{s,\eta}$ based on the full spectrum of $\eta$ (blue line) and $A_{s,\eta}$ based on the $\eta$ with a cutoff frequency of $3f_p$ (red line); panel a) shows $S_{k,u}$ (black line) against $S_{k,\eta}$ based on the full spectrum of $\eta$ (blue line) and $S_{k,\eta}$ based on the $\eta$ with a cutoff frequency of $3f_p$ (red line).

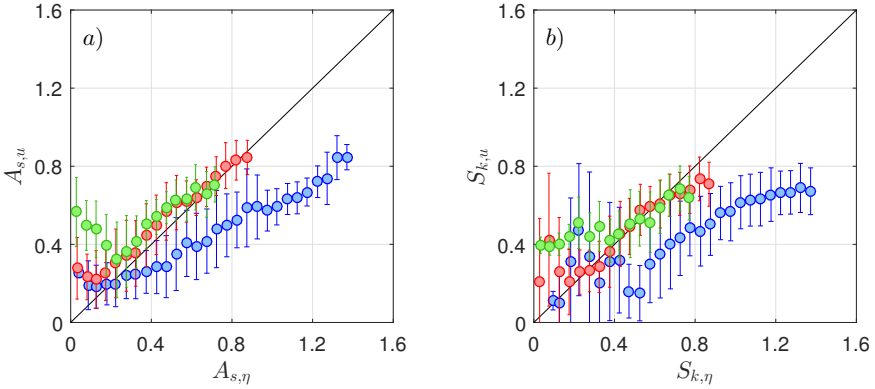


Figure 5.12: Comparison of all third-order wave moments data estimated from LiDAR, pressure and velocity measurements: panel a) shows $A_{s,u}$ against $A_{s,\eta}$ while panel b) shows $S_{k,u}$ against $S_{k,\eta}$. In each subplot, red dots correspond to data from the ADV using the frequency cutoff on $\eta$, while the full spectrum was used for the blue data. Green data correspond to the LiDAR scanner, with the same frequency cutoff. Bins of 0.05 in the $x$-direction were used to calculate the mean and standard deviation, represented as error bars. The 1:1 line is shown as black line.

## 5.7 Wave-by-wave analysis of wave skewness and asymmetry

To further compare the pressure, velocity and surface elevation datasets, a wave-by-wave analysis has been performed on the pressure-derived and LiDAR surface elevation signals, and on the cross-shore current velocity signal (Equations 5.6-5.8). The analysis presented here focuses on the data obtained at the onshore ADV location. Figure 5.13 displays the different parameters studied: $D$, $A_s$ and $S_k$, along with the front and back wave angles $\theta_{front}$ and $\theta_{back}$. For each of these wave properties, the mean was computed using moving windows of 60 waves, and the shaded area represents the standard deviation over these 60 waves.

The first observation that can be made is that there is a good overall agreement between all datasets, for every tide (Figure 5.13a-c). Especially, the mean individual wave properties extracted from surface elevation and the current velocity signal show very similar evolution, without the need of a low-pass filter for the surface elevation. The wave deformation $D$ presents very similar values over the course of the experiments (Figure 5.13a): values generally range from 0.3 at low tide and increase to 0.8-0.9 at high tide. Values from the LiDAR scanner present more scattered data at high tide probably because it detects a broader range of surface wave frequencies: the presence of very short waves along with

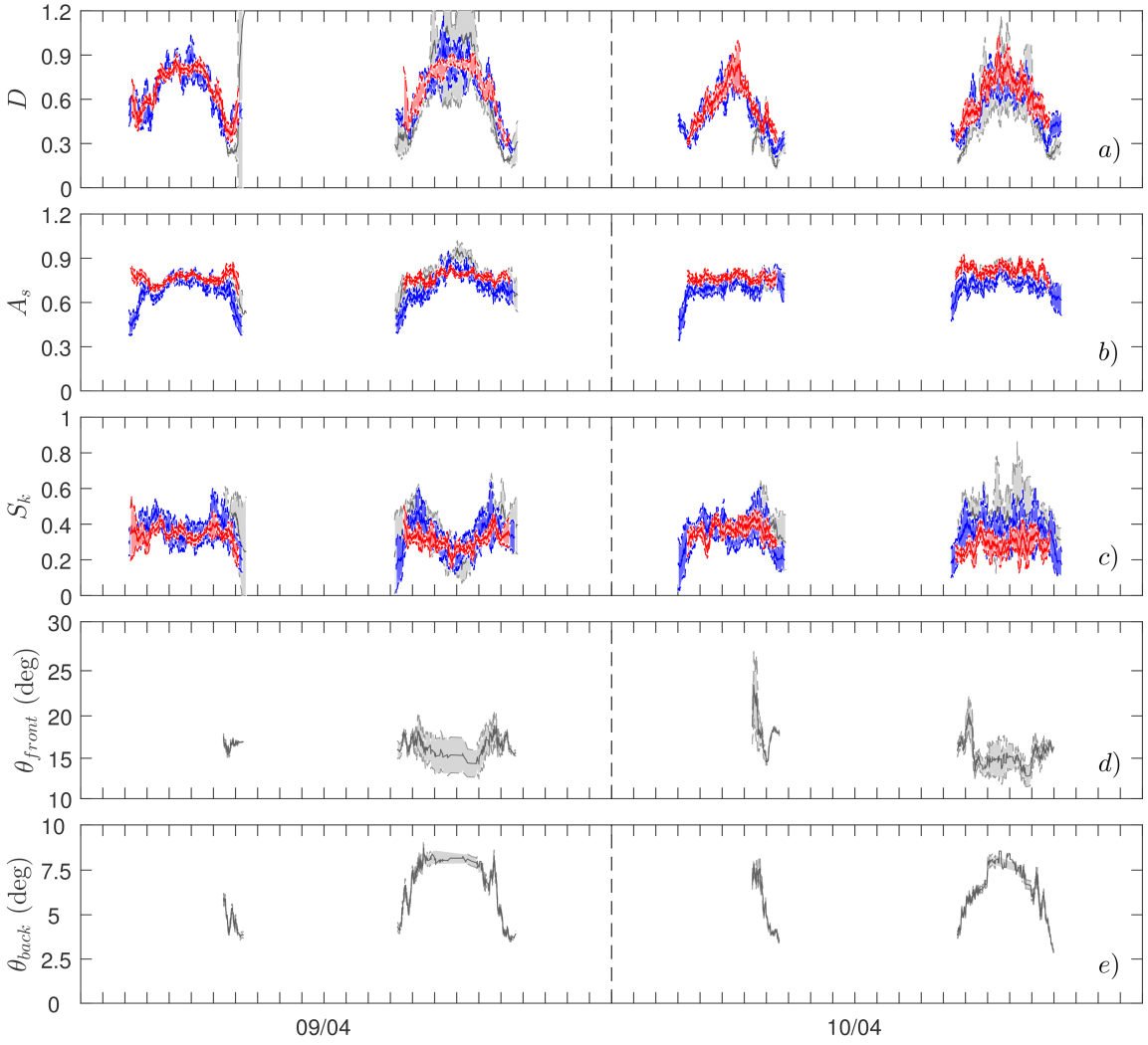


Figure 5.13: Comparison between pressure-derived and LiDAR data at the wave-by-wave scale: wave deformation $D$, wave asymmetry $A_s$ and skewness $S_k$. Panels d-e) show the individual wave front and back angles respectively. For each wave properties, the mean (continuous line) is calculated using a moving window of 60 waves, and she shaded area correspond to the standard deviation. Pressure-derived data is shown as blue, current data is shown as red and LiDAR data is shown as gray.

longer non-broken waves makes the range of values reached by $D$ greater.

The wave-by-wave asymmetry presents less scatter than other properties (Figure 5.13b), although we note more divergence between the datasets. When based on surface elevation, $A_s$ increases to values around 0.8 at high tide, which is consistent with its definition (Equation 5.7) and the evolution of $D$. Indeed, the ratio of the wave crest propagation phase duration ($\eta > h_w$) and that of the trough propagation phase ($\eta < h_w$) reaches its maximum at high tide. That is expected as unbroken waves will have a much more symmetrical profile at high tide than bores. During ebb or flooding, $A_s$ decreases: the crest is narrower (in time) compared to the trough. This narrowness does not appear in the current velocity-derived $A_s$ that exhibits more constant values. This could be explained by the presence of infragravity waves: although their influence on the surface elevation is reduced by using the local definition of $h_w$, they more strongly influence the underlying current.

The wave-by-wave skewness displays some interesting features (Figure 5.13c), especially during the second tide of 09/04. It is low in shallow waters (low tide) even in the presence of infragravity waves thanks to the use of $h_w$, and show peak values at some time during both flood and ebb periods, before decreasing at high tide. Similar behaviour was observed for the time-averaged $A_s$ (Figure 5.10b, 5.10e and 5.10h). The breaking regime explains this behaviour, and it is illustrated in Figure 5.13d and 5.13e, with the measured front and back wave angles. The peaks in $S_k$ coincide with a net increase in the back wave angle and a slight increase in the values and the amount of variation of the front angle: we pass from the presence of only broken waves, to a regime where wave breaking occurs at this location. It is worth noting that the mean front wave angles are in agreement with the values of Almar et al. (2012) and are much larger than those reported in Carini et al. (2015), who estimated $\theta_{front}$ by using the celerity given by linear wave theory and the time elapsed between the passage of the preceding wave trough and the wave crest at a certain location (see also Zhang et al., 2017).

## 5.8 Conclusions

During these experiments, three LiDAR scanners were deployed along a pier to generate a unique surface elevation dataset of shoaling, breaking and broken waves. In the present study, a link between the wave-by-wave and the time-averaged scales is found. The wave-by-wave parameters estimated on the pressure-derived, current velocity and LiDAR datasets are consistent with expected results throughout the tide cycle. The wave-by-wave skewness is the parameter at the individual wave scale that relates the most to time-averaged parameters, and in particular to the wave asymmetry $A_s$. The presence of noise and waves with a frequency greater than the peak frequency in the surface elevation signal was found to increase the time-averaged skewness. A frequency cutoff of three times the peak frequency applied to the surface elevation enables good estimates of the third-order cross-shore current velocity moments. This opens up the possibility for interesting LiDAR applications for the remote sensing of third-order moments of nearshore current. Finally, the LiDAR provides the possibility to measure the surface slopes of surf zone waves. For this particular dataset, the angles measured at the front are larger than the values usually used in numerical models of nearshore wave transformation based on the energy balance concept (e.g. Flores et al., 2016). Further analysis is required to understand the link between surface slope and wave properties, but provides the potential to give improvements in such modelling.

## References

Adeyemo, M. 1968. Effect of beach slope and shoaling on wave asymmetry. *Proceedings of 11th Conference on Coastal Engineering, London, United Kingdom*, pp. 145 – 172.

Almar, R., Cienfuegos, R., Catalán, P. A., Michallet, H., Castelle, B., Bonneton, P., and Marieu, V. 2012. A new breaking wave height direct estimator from video imagery. *Coastal Engineering* 61, pp. 42 – 48. DOI: 10.1016/j.coastaleng.2011.12.004.

Berni, C., Barthélemy, E., and Michallet, H. 2013. Surf zone cross-shore boundary layer velocity asymmetry and skewness: An experimental study on a mobile bed. *Journal of Geophysical Research: Oceans* 118 (4), pp. 2188 – 2200. DOI: 10.1002/jgrc.20125.

Bishop, C. T. and Donelan, M. A. 1987. Measuring waves with pressure transducers. *Coastal Engineering* 11 (4), pp. 309 – 328. DOI: 10.1016/0378-3839(87)90031-7.

Brodie, K. L., Raubenheimer, B., Elgar, S., Slocum, R. K., and McNinch, J. E. 2015. Lidar and Pressure Measurements of Inner-Surfzone Waves and Setup. *Journal of Atmospheric and Oceanic Technology* 32 (10), pp. 1945 – 1959. DOI: 10.1175/JTECH-D-14-00222.1.

Carini, R. J., Chickadel, C. C., Jessup, A. T., and Thomson, J. 2015. Estimating wave energy dissipation in the surf zone using thermal infrared imagery. *Journal of Geophysical Research: Oceans* 120 (6), pp. 3937 – 3957. DOI: 10.1002/2014JC010561.

Cowell, P. J. 1982. *Breaker stages and surf structure on beaches*. Tech. rep. Coastal Studies Unit Technical Report No. 82/7, Sydney, Australia.

Duncan, J. H. 1981. An Experimental Investigation of Breaking Waves Produced by a Towed Hydrofoil. *Proceedings of the Royal Society of London A: Mathematical, Physical and Engineering Sciences* 377 (1770), pp. 331 – 348. DOI: 10.1098/rspa.1981.0127.

Flores, R. P., Catalán, P. A., and Haller, M. C. 2016. Estimating surfzone wave transformation and wave setup from remote sensing data. *Coastal Engineering* 114, pp. 244 – 252. DOI: 10.1016/j.coastaleng.2016.04.008.

Martins, K., Blenkinsopp, C. E., Power, H. E., Bruder, B., Puleo, J. A., and Bergsma, E. W. J. 2017b. High-resolution monitoring of wave transformation in the surf zone using a LiDAR scanner array. *Coastal Engineering* 128, pp. 37 – 43. DOI: 10.1016/j.coastaleng.2017.07.007.

Martins, K., Blenkinsopp, C. E., Bergsma, E. W. J., Power, H. E., Bruder, B., and Puleo, J. A. 2017c. Remote-sensing of wave transformation in the surf zone. *Proceedings of the Conference on Coastal Dynamics, Helsingør, Denmark*.

Martins, K., Blenkinsopp, C. E., Almar, R., and Zang, J. 2017d. The influence of swash-based reflection on surf zone hydrodynamics: a wave-by-wave approach. *Coastal Engineering* 122, pp. 27 – 43. DOI: 10.1016/j.coastaleng.2017.01.006.

Zhang, C., Zhang, Q., Zheng, J., and Demirbilek, Z. 2017. Parameterization of nearshore wave front slope. *Coastal Engineering* 127, pp. 80 – 87. DOI: http://dx.doi.org/10.1016/j.coastaleng.2017.06.008.

## Chapter concluding remarks

During the field experiments performed at Saltburn-by-the-Sea, continuous surface elevation measurements of shoaling, breaking and broken waves were obtained with an array of three LiDAR scanners. This dataset probably constitutes the most highly detailed measurements of breaking waves in field conditions.

The focus of this Chapter is the cross-shore evolution of the geometric properties of surf zone waves, with a particular interest on the wave skewness and asymmetry, which are first studied at the wave-by-wave scale. Although a clear signature is observed in values of $S_k$ and $A_s$ at the different stages of propagation (shoaling, breaking and broken waves), it is not sufficiently pronounced to accurately detect the break point. A new methodology to accurately detect the break point from LiDAR scanner data was presented: it uses the activity of the wave face, captured in detail by the scanners, as a proxy. This new method can be used to create new field datasets of geometric properties of breaking waves.

The skewness and asymmetry of the free surface and cross-shore current velocity were also analysed at the time-averaged scale. In the present dataset, a low-pass filter at $3f_p$ on the free surface elevation signal (from PT and LiDAR) yields a good estimate of the free-stream cross-shore velocity third-order moments. This is a very interesting and promising result as these quantities play an important role in morphological changes in the surf zone. Finally, the wave front angle is directly estimated for the first time in field conditions. Interestingly, it shows much higher angles than generally assumed; this will be further investigated in the last chapter of this thesis as it is an important variable in the parameterization of the energy dissipation rates (Duncan, 1981).

# Chapter 6

## Energy dissipation in the inner surf zone: new insights from lidar-based roller geometry measurements

Kévin Martins*, Chris E. Blenkinsopp, Rolf Deigaard, Hannah E. Power, "Energy dissipation in the inner surf zone: new insights from LiDAR-based roller geometry measurements", Journal of Geophysical Research (*under review*).

## Abstract

In the surf zone, breaking waves dissipate their energy and control cross-shore and longshore sediment transport rates through the nearshore mean circulation. Consequently it is vital to develop better understanding of the wave breaking process. In this paper, we extract geometrical roller properties from an innovative LiDAR field dataset of broken waves to obtain new insights into wave energy dissipation in the inner surf zone. We use a roller model to show that most existing roller area formulations in the literature lead to large overestimation of the wave energy dissipation, which is found to be close to, but smaller than, the energy dissipation in a hydraulic jump of the same height. Using previously published results from deep-water wave breaking studies, we propose a scaling law for energy dissipation in the inner surf zone, which achieves satisfactory results at both the time-averaged and wave-by-wave scales. Finally, the use of linear wave theory for expressing the wave flux is discussed. It is believed that the incorrect use of linear wave theory across the whole surf zone and inappropriate roller properties (e.g. roller angle) have been responsible for concealing incorrect formulations of wave energy dissipation in the inner part of the surf zone.

## Declaration concerning the article used for this Chapter:

| | |
|---|---|
| Title | Energy dissipation in the inner surf zone: new insights from LiDAR-based roller geometry measurements |
| Status | Submitted the 17/08/2017 to Journal of Geophysical Research: Oceans (AGU) |
| Details | Kévin Martins*, Chris E. Blenkinsopp, Rolf Deigaard, Hannah E. Power, "Energy dissipation in the inner surf zone: new insights from LiDAR-based roller geometry measurements" |
| Contribution from the authors | K. Martins: Processing of the data and analysis; Numerical model development; Manuscript (70%)<br>C.E. Blenkinsopp: Manuscript and Guidance in the analysis (15%)<br>R. Deigaard: Guidance in the model and analysis (10%)<br>H.E. Power: Manuscript (5%)<br>The authors from Chapter 5 are once again acknowledged for making the collection of this dataset possible. Discussions with José Beya (Universidad de Valparaíso) and James Duncan (University of Maryland, MD) greatly contributed to the quality of the manuscript and the good conduction of the analysis. |
| Statement | This paper reports on original research I conducted during the period of my Higher Degree by Research candidature. |
| Date and Signature | |

## Preamble

In Chapter 5, the first direct measurements of wave angles performed by LiDAR scanners in field conditions were presented. Although non-broken, breaking and broken waves were not separated on a wave-by-wave basis, the measured ensemble-averaged wave angles were much larger than the value generally assumed in numerical models using the surface roller concept (Svendsen, 1984a) for parameterizing the wave-breaking-induced energy dissipation ($\tan\theta = 0.1$, e.g., Dally and Brown, 1995; Walstra et al., 1996; Reniers and Battjes, 1997; Ruessink et al., 2001). Some studies employing the surface roller model (e.g., Dally and Brown, 1995; Haller and Catalán, 2009; Flores et al., 2016) use empirical relations linking the roller properties to that of the broken wave, which were found by Duncan (1981) during his hydrofoil experiment. However, this hydrofoil dataset and the relations that were derived have never been compared to field measurements of surface roller and wave properties, mainly because roller properties are very challenging to measure. As suggested in Chapter 5, LiDAR scanners offer the possibility to extract and study surface roller properties. In this Chapter, we aim to develop a new methodology to create the first field dataset of surface roller geometric properties (angle $\theta$ and length $L_r$) from the LiDAR dataset acquired in Martins et al. (2017b). The following research objectives/questions were addressed:

- Develop a robust methodology based on the previous tracking algorithm to extract wave and surface roller geometric properties.
- Compare the new field dataset to the empirical relations of Duncan (1981).
- Investigate energy dissipation with the surface roller concept: at what rate does a broken wave in the inner surf zone dissipate its energy? Can we accurately model it?

Thanks to the ability of the LiDAR scanners to directly measure the surface roller angle and length, the number of unknowns in the classic roller model first developed by Svendsen (1984a) is reduced to the mean void fraction in the roller (represented by the quantity $\rho_r/\rho$) and the roller area $A$. This dataset hence offers a unique opportunity to study the sensitivity of the model to these two parameters. In this Chapter, a roller numerical model is set up and used to compare the energy dissipation rates obtained with the different roller area formulations present in the literature with measurements. Finally, a scaling law for the energy dissipation rates in inner surf zone is proposed and has the advantage that it only uses the wave celerity and its period.

# Chapter 6.

## 6.1 Introduction

The surf zone is the part of the nearshore where waves are breaking due to the decreasing depth. A considerable amount of incident wave energy is dissipated at the break point and subsequently in the inner surf zone where the waves continue to break, which drives the mean circulation on the beach (Svendsen, 1984a; Stive and Wind, 1986; Deigaard et al., 1991). A better understanding of wave breaking processes is necessary to enable better prediction of beach erosion and coastal hazards.

Over the last few decades, numerical models based on the full Navier-Stokes equations have been increasingly used to study wave breaking processes thanks to ever-improving computational capabilities (e.g., Jacobsen et al., 2012; Higuera et al., 2013; Deike et al., 2016). However, they remain a limited tool for many engineering applications as they require high computational cost and it is often difficult to obtain the correct boundary conditions for the domain being modelled. For these reasons, phase-averaged wave transformation models are often used due to their efficiency but also their accuracy, thanks to the efforts made to parameterize the different physical processes related to wave generation, propagation, and breaking/decay (Cavaleri et al., 2007). Full spectral models were developed to describe wave generation and propagation in the deep ocean (e.g., Booij and Holthuijsen, 1987; Tolman, 1989; Benoit et al., 1996) and, although breaking processes in both deep and shallow water still need to be better parameterized (e.g., the review of Salmon et al., 2015; Cavaleri et al., 2007), these models show satisfactory results when applied in the presence of depth-induced breaking (e.g., Vink, 2001; Zheng et al., 2008; Goda, 2008; Filipot and Cheung, 2012; Grunnet et al., 2014).

A simpler class of parametric models is commonly used in the surf zone (e.g., Apotsos et al., 2008). These models rely on the energy balance concept (Battjes and Janssen, 1978; Stive, 1984; Svendsen, 1984a), which states that the majority of incident wave energy is transferred into turbulent kinetic energy through various processes (including entrainment of air and friction) with only a fraction of it being dissipated directly into heat (Svendsen, 2006). Depending on the beach and wave conditions, the majority of remaining incident energy is either reflected from the beach (Elgar et al., 1994; Baquerizo et al., 1997; Martins et al., 2017d) or transports sediment in the surf and swash zones (Masselink and Puleo, 2006). Svendsen (1984a) and then Deigaard and Fredsøe (1989) showed that accounting for the surface roller is a fundamental element of energy balance-based models in the surf zone. The surface roller is a turbulent mass of mixed air and water advected by the breaking wave that greatly contributes to the energy flux and radiation stress balance in the surf zone due to its added mass and momentum and thus affects the mean circulation (Longuet-Higgins and Stewart, 1964; Svendsen et al., 1978; Svendsen, 1984a; Stive and Wind, 1986; Deigaard and Fredsøe, 1989; Nairn et al., 1990; Deigaard, 1993; Rattanapitikon and Shibayama, 2000; Bae et al., 2013). Energy balance models are capable of predicting wave bulk properties (e.g. the wave height $H$) as well as wave-induced quantities such as set-up/set-down and longshore and cross-shore mean currents more efficiently than CFD models (e.g., Nairn et al., 1990; Dally and Brown, 1995; Lippmann et al., 1996; Apotsos

et al., 2008). The roller concept has also been successfully implemented in Boussinesq-type flow models (e.g., Schäffer et al., 1993; Cienfuegos et al., 2010).

In his seminal experiments on steady breakers generated by hydrofoils, Duncan (1981, hereinafter D81) highlighted the link between the roller geometry (roller angle $\theta$, length $L_r$ and surface area $A$, see Figure 6.1) and the energy dissipated by the breaker. Prior attempts to model the energy dissipation in spilling breakers used formulations derived from hydraulic jump theory (Le Méhauté, 1962; Hwang and Divoky, 1970; Battjes and Janssen, 1978; Svendsen et al., 1978). The relations obtained by D81 have been applied to remotely sensed roller lengths to estimate bulk surf zone quantities (e.g., Haller and Catalán, 2009; Carini et al., 2015; Flores et al., 2016). The lack of direct roller angle measurements in field or laboratory conditions explains the common choice to make $\theta$ constant in any modelling attempt, although a cross-shore variation is expected in the surf zone (Zhang et al., 2014). Another shortcoming to this modelling approach concerns the transition region, also referred to as the outer surf zone (Svendsen, 1984a, hereinafter S84), in which waves undergo a rapid transformation after breaking. The length of this region, which extends from the break point to the transition point where we can consider the broken wave a fully developed bore (Basco and Yamashita, 1986; Nairn et al., 1990; Kweon and Goda, 1996), remains an unknown. The typical modelling approach therefore considers the roller to be fully developed immediately after the break point, suggesting that the breaking wave instantaneously propagates in the inner part of the surf zone (Svendsen, 1984a). The errors introduced by such approximations potentially hide the inaccuracy of the current parameterisation of energy dissipation in the inner surf zone. A consequence of this is that surface roller models heavily rely on calibration on a case-by-case basis (e.g., Lippmann et al., 1996; Walstra et al., 1996; Apotsos et al., 2008; Flores et al., 2016).

In this paper, we present a novel field dataset of inner surf zone waves obtained from an array of 2D LiDAR scanners (Martins et al., 2017b). 2D LiDAR are able to directly measure the surface elevation profiles of broken waves at high spatial and temporal resolutions making them ideal for obtaining the geometrical properties of surface rollers as they vary in space and time. Using this data, we investigate the accuracy of commonly-used formulations of energy dissipation in the inner surf zone at the individual and wave group time scales. The paper is organised as follows. Section 6.2 reviews the concept of surface rollers introduced by S84, and its application to modelling wave transformation in the inner surf zone. The field dataset and the methodology developed to analyse the broken wave geometries from the LiDAR data are presented in Section 6.3. The measured geometrical properties are compared to those found by D81 during his hydrofoil experiments in Section 6.4. We also compare the energy dissipation terms computed using various roller area formulations which are then tested in a roller model to investigate the effect of the choice of the roller area formulation on wave incident energy flux modelling. In Section 6.5, we present an attempt to scale the energy dissipation in the inner surf using local wave properties. Finally, different energy flux formulations are discussed in Section 6.6, and we explain how using linear wave theory can lead to erroneous energy dissipation.

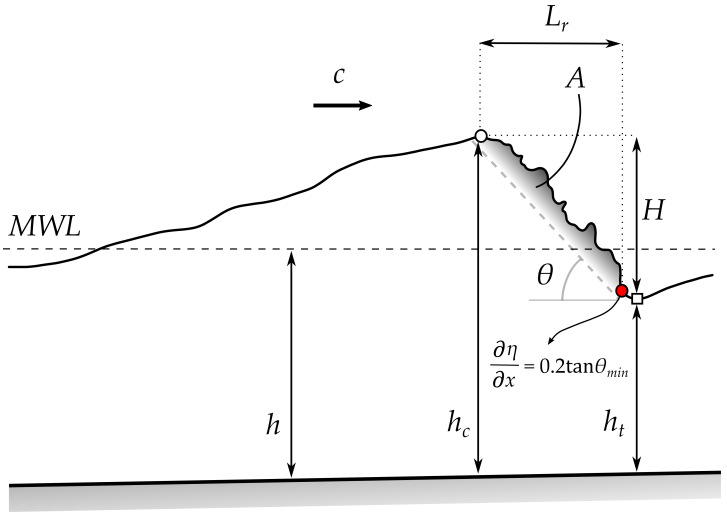


Figure 6.1: Definition sketch of the broken wave (bore) geometry. The mean water depth $h$ is defined as the vertical distance between the bed and Mean Water Level (*MWL*). The bore propagates at speed $c$ in water depth $h_t$ and has a height $H$, corresponding to the distance between the crest (white dot) and the preceding trough (white square). The instantaneous water depth below the bore crest is expressed as $h_c = H + h_t$. The surface roller (active region of the broken wave) is defined from the wave crest (white dot) to the bore toe (red dot), defined as the point where $\frac{\partial \eta}{\partial x} = 0.2 \tan \theta_{min}$, where $\theta_{min}$ is the minimum angle found in the wave face. The surface roller has an angle with the horizontal of $\theta$ and a length $L_r$. Finally, the area of the surface roller is noted $A$.

## 6.2 Surf zone energy budget modelling

### 6.2.1 Surface rollers

The energy balance for waves in the surf zone states that the spatial variation of the time-averaged incident wave energy flux $E_f$ is equal to the amount of energy dissipated per unit area during breaking. If we consider a shore-normal wave propagating in one spatial dimension, the model is defined as:

$$\frac{\partial E_f}{\partial x} = -D \tag{6.1}$$

where $D$ is the amount of energy per unit area dissipated or transformed during the breaking process, as discussed by Svendsen (2006) (e.g., Battjes and Janssen, 1978; Svendsen, 1984a; Nairn et al., 1990; Dally and Brown, 1995). Note that $D > 0$ by convention. $D$ incorporates the effects from multiple physical processes that occur during breaking (see, Carini et al., 2015, and the references therein): production of heat, noise and turbulent kinetic energy; the entrainment of bubbles in the water column; production of spray at the surface; and the suspension and/or entrainment of sediment due to friction effects at the bed. Except for the production of turbulent kinetic energy, most of the other effects are generally neglected, even when the models extend seaward of the inner region into the shoaling zone (Svendsen, 1984a; Nairn et al., 1990; Deigaard et al., 1991; Dally and Brown, 1995). Blenkinsopp and Chaplin (2007) showed, however, that between 6.5 and 14% of the total wave energy could be dissipated due to the entrainment of air during wave breaking. This potentially explains

the failure of parametric models to represent the energy dissipation in the transition region, especially for plunging waves. The effect is generally compensated in the inner surf by adjusting other parameters (Lippmann et al., 1996; Walstra et al., 1996; Haller and Catalán, 2009; Flores et al., 2016).

By considering surface rollers as a mass of mixed water and air centred on the Mean Water Level (*MWL*), and moving at the same celerity $c$ as the carrier wave (see also, Tajima, 1996), S84 separated the incident wave energy flux into a wave and a roller contribution as follows:

$$E_f = E_{f,w} + E_{f,r} \tag{6.2}$$

with

$$E_{f,w} = \rho g c \frac{1}{T} \int_0^T \eta^2 dt \tag{6.3}$$

$$E_{f,r} = \frac{1}{2} \rho_r \frac{A}{T} c^2 \tag{6.4}$$

where $\rho$ is the water density, $g$ is the gravity constant, $T$ is the wave period, $\eta$ is the time-varying surface elevation, and $\rho_r$ and $A$ the surface roller density and area. It is worth noting that the term $E_{f,r}$ is actually the surface roller kinetic energy. Although different hypotheses on the broken wave characteristics led S84 to Equation 6.2), we observe that this relation can also be obtained if we assume that the kinetic energy of the wave is equal to the potential energy. Although this assumption has not been thoroughly verified in the inner surf zone for a wide range of wave and beach conditions, some relatively recent experimental studies show evidence that this is an accurate assumption (e.g., Huang et al., 2009). By further assuming that all the energy dissipation occurs in the roller but that energy can still be exchanged between the wave and the roller, Equations 6.1 and 6.2 can be combined:

$$\frac{\partial E_{f,w}}{\partial x} + \frac{\partial E_{f,r}}{\partial x} = -D_r \tag{6.5}$$

where $D_r$ is the energy dissipated in the surface roller (see also e.g., Lippmann et al., 1996; Dally and Brown, 1995; Haller and Catalán, 2009). Following the seminal work of Le Méhauté (1962) on non-saturated breakers and that of Svendsen et al. (1978), S84 assumed that the energy dissipation in broken waves was equal to that of a hydraulic jump of the same height (Svendsen, 2006):

$$D_r = D_{HJ} = \frac{1}{4} \rho g h \frac{H^3}{h_c h_t T} \tag{6.6}$$

where $h$ is the mean water depth, and $h_c$ and $h_t$ are the water depths below crest and trough respectively (see Figure 6.1 for a definition sketch of the broken wave geometry). The presence of a coefficient $B$ of the order of unity is often used to calibrate this type of dissipation model for regular or irregular waves (e.g., Le Méhauté, 1962; Battjes and Janssen, 1978; Thornton and Guza, 1983).

From his hydrofoil experiments, D81 related the steady breaker energy dissipation to the Reynolds stresses at the boundary between the roller and the underlying layers of fluid. Averaged over the wave period, this reads:

$$D_r = D_\tau = \overline{\tau c} = \rho_r g A \frac{\sin\theta}{T} \tag{6.7}$$

where $\theta$ is the surface roller angle (see Figure 6.1).

### 6.2.2 Influence of roller geometry on dissipation

The roller model (Equation 6.5) relies heavily on the geometrical properties of the bore ($\theta$, $L_r$ and $A$, see Figure 6.1) which appear in both the roller kinetic energy (Equation 6.4) and the dissipation terms if $D_\tau$ is used (Equation 6.7). However, direct measurements in both field or laboratory conditions of roller geometry to use in Equation 6.7 are scarce. Roller lengths $L_r$ have been estimated from video imagery in studies by Haller and Catalán (2009), and more recently by Carini et al. (2015) and Flores et al. (2016). Haller and Catalán (2009) obtained a good match between the remotely-sensed roller lengths and those modelled by the roller model described above. In the model, the energy dissipation was inferred from measured wave heights using linear wave theory. Additionally, a range of constant wave angles was used to assess the model sensitivity. To estimate the wave angle in the dataset of Haller and Catalán (2009), Zhang et al. (2014) used the time elapsed between the *MWL* upcrossing and the passage of the crest at a given location, assuming a constant celerity from solitary wave theory. A similar method was used by Carini et al. (2015) but using the trough level and the celerity from linear wave theory. These estimates are valuable but can be considered quite coarse given that average wave celerity has been shown to be 1.14 times that estimated by linear wave theory in the surf zone (Tissier et al., 2011), and that the preceding trough can be located well away from the bore toe (e.g. D81). Nonetheless, Zhang et al. (2014) reported wave slopes $\tan\theta$ greater than 0.2, which is at least twice the value generally adopted ($\tan\theta = 0.1$, e.g., Dally and Brown, 1995; Walstra et al., 1996; Reniers and Battjes, 1997; Ruessink et al., 2001). These higher values are in better agreement with the experimental results of D81 and Govender et al. (2002) or the simulations of Haller and Catalán (2009), and seem more realistic when compared to the known critical wave steepness of $\tan\theta \sim 0.58$ for wave breaking initiation in deep water (Longuet-Higgins and Fox, 1977).

Considerable uncertainty also exists in the surface roller area $A$, which is a very difficult quantity to consistently and accurately measure (Duncan, 1981; Govender et al., 2002). In addition to $\rho_r$, $A$ is the only surface roller quantity that is not measured in this study. The difficulty in measuring the roller area has led to the existence of numerous formulations in the literature as shown in Table 6.1. A simple sensitivity analysis assuming $H \sim O(1)$, $L_r \sim O(1)$, $\tan\theta \sim O(0.1)$, and the beach slope $\tan\beta \sim O(0.01)$ demonstrates that it is possible to have an order of magnitude difference between the formulations of D81 and Tajima (1996). When $D_\tau$ (Equation 6.7) is used for the dissipation terms in Equation 6.5, we note that $A$ appears in both sides of Equation 6.5, which probably tends to reduce the effect

Table 6.1: List of expressions for the surface roller area $A$ from existing literature.

| Studies | Expression | Observations |
|---|---|---|
| Duncan (1981) | $A = 0.11\left(\frac{L_r}{\cos\theta}\right)^2$ | Relation found during the hydrofoil experiments. Note that the horizontal projection of the roller/wave interface is used here ($L_r$), hence the cosine presence. |
| Engelund (1981) | $A = \frac{H^3}{4h\tan\theta}$ | This relation was derived by Deigaard et al. (1991) to match the dissipation of a hydraulic jump of the same height, based on the results of Engelund (1981). |
| Svendsen (1984a) | $A = 0.9H^2$ | Based on the reanalysis of Duncan (1981). |
| Okayasu et al. (1986) | $\frac{A}{HL} = 0.06 - 0.07$ | $L$ is the wavelength. A coefficient $k$ exists in the original version to account for the bore development ($k = 1$ here since we consider fully developed bores). |
| Tajima (1996) | $A = B\tan\beta H_*^2$ | $B$ is a coefficient taken as 140 in Tajima (1996), and $H_*^2$ the equivalent linear wave height (i.e. same energy flux). |

of inaccuracies in $A$ when choosing a formulation (Table 6.1). However, in the inner surf zone, by comparing Equations 6.4 and 6.7, we expect $D_\tau$ to be much larger than the roller contribution, meaning that an inaccurate formulation of $A$ has a more pronounced effect on the energy dissipation parameterisation.

## 6.3 Methods

### 6.3.1 Field site and experimental set-up

The present study uses LiDAR data collected during the field experiments performed at Saltburn-by-the-Sea, UK (see Figure 6.2) during April 2016 (Martins et al., 2017b,c). The field experiments and the raw data processing are described in these two references, but some basic information is repeated here. Three eye-safe 2D LiDAR scanners (SICK LMS511) were deployed along a pier to measure the time-varying free surface elevation of shoaling, breaking and broken waves at 25 Hz (see Figure 6.2b). The three individual datasets were processed following the methods of Martins et al. (2016) and then merged into a unique surface elevation dataset using linear weighting functions: at a given cross-shore location, priority is given to the nearest LiDAR scanner as it provides the most accurate measurement at that location. Figure 6.2c displays the full cross-shore experimental setup where in addition to the scanners, three RBR pressure transducers (PT) and three Nortek Acoustic Doppler Velocimeters (ADV) were deployed and sampled at 2 Hz and 16 Hz respectively. An example of the final LiDAR dataset is also shown in Figure 6.2c and illustrates the spatial resolution of the datasets (0.1-m cross-shore grid).

As a result of the macrotidal environment in this part of the North Sea, every phase of the nearshore wave transformation could be measured: from propagating bores in the inner surf zone during flood or ebb phases to shoaling and breaking waves during high tides. The present study focuses on wave propagation in the inner surf zone, where waves propagate as fully developed bores after the transition point. We only use data from the

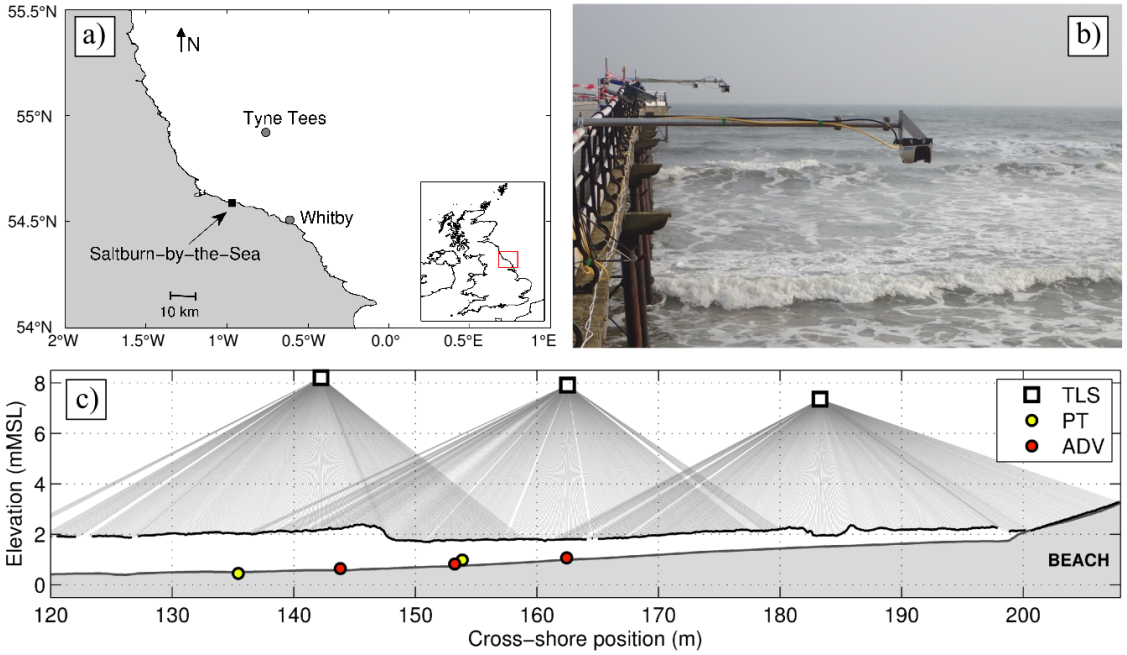


Figure 6.2: Field site and LiDAR scanner deployment. The regional map around Saltburn-by-the-Sea, UK, is shown in panel a). The location of the nearshore (Whitby) and offshore (Tyne Tees) wave buoys are shown by the grey dots. Panel b) shows the LiDAR scanner deployment on the nearshore pier: the scanners were deployed 2.5 m away from the pier, using a 'T' shaped scaffolding system fixed to the pier railing. Panel c) shows a schematic of the experimental set-up with an example of post-processed free surface elevation (black thick line while individual measurements are shown as light grey lines). The beach profile (thick grey line) corresponds to the surveyed profile during the previous low tide (10/04/16).

09/04/2016 and 10/04/2016 (shore-normal propagating swell with $T_p \sim 10-11$ s, $H_s = 1$ m), during periods when the maximum runup position was located just seaward of the steep gravel upper beachface located around $x = 195$ m (see Figure 6.2c). This was to minimize the influence of reflected waves on the geometrical properties of incident waves.

### 6.3.2 Wave-by-wave analysis: extraction of roller properties

Individual waves are tracked in the surf zone and their geometrical properties are extracted with the algorithms developed in Martins et al. (2016) and Martins et al. (2017b,c). The tracking works by detecting the wave crests as maxima in the surface elevation timeseries. Individual wave heights $H$ are then computed as the vertical distance between the crest and preceding trough elevations ($h_c$ and $h_t$ respectively, see Figure 6.1), and the wave period $T$ is defined as the time elapsed between the passage of the two troughs either side of a crest at a given cross-shore location. In the LiDAR dataset, we define the surface roller as the part of the wave profile from the wave crest, through the breaking region (where $\partial\eta/\partial x < 0$) to the roller toe. For fully developed bores, the roller toe location will be close to and seaward of the preceding trough. Here we use a surface gradient upcrossing value set at 20% of the minimum surface elevation gradient value found in the breaking region to define the roller toe (see illustration in Figure 6.1). We then estimate the roller angle $\theta$ by fitting a line to the surface roller profile (from the detected wave crest to the roller toe).

To accurately measure the incident wave energy flux, good estimates of the wave

celerity are required (Svendsen et al., 2003); here the wave tracks are used directly to obtain individual wave celerities. The general approach for estimating wave celerity $c_i$ relies in the following estimate: $c_i \approx \Delta x/\Delta t$ where $\Delta x$ is the distance travelled by the wave in the time $\Delta t$. Suhayda and Pettigrew (1977) were the first to apply this principle in field conditions to estimate individual wave celerities using video cameras and photopoles every three metres in the surf zone. Using a different approach, Yoo et al. (2011) used the Radon Transform (Radon, 1917) on video timestacks to estimate individual wave celerities in the surf zone for depth-inversion purposes. Lines in a timestack image (e.g. crests) appear as single points in Radon space (Yoo et al., 2011; Almar et al., 2014a); the inverse Radon then enables the retrieval of the wave celerity (Almar et al., 2014a). After comparing the performance of these two methods and their sensitivity to spatial and temporal windows, a different approach for this study was designed to take advantage of the spatial resolution of the dataset. A linear fit to the wave trajectory was fitted over a 5 m window (2.5 m either side of the point where the celerity is estimated) and the slope of the trajectory fit was taken as the individual wave celerity.

## 6.4 Results

### 6.4.1 Surface Roller Geometry

The relations obtained by D81 during his hydrofoil experiments are often applied in the surf zone to estimate wave energy dissipation (e.g., Haller and Catalán, 2009; Carini et al., 2015; Flores et al., 2016), even though their applicability in this region remains unclear. In this Section, we compare these relations to the dataset discussed here consisting of 38 manually selected waves, measured in the inner surf zone using the methodology described in Section 6.3.2. These waves were selected as no gaps in the dataset were present and as there was no apparent interaction with incident or reflected waves.

An example of a tracked wave is shown in Figure 6.3 to clarify the methodology used to extract the roller angle (Section 6.3.2). We first observe that the bore front angle varies considerably in the inner surf zone and is much higher than the constant value of 5.7° typically used (e.g., Dally and Brown, 1995; Reniers and Battjes, 1997; Ruessink et al., 2001; Flores et al., 2016). Figure 6.3e shows a rapid initial reduction in roller angle from 25° to 18° in the first 8 m post-breaking. This is followed by a period of relatively constant roller angle in the range 16° to 22° between $x$ = 131 and 160 m, followed by a rapid reduction in roller angle between $x$ = 165 and $x$ = 170 m of about 10° associated with an increase in the rate of wave height decay (Figure 6.3b). This corresponds to where the beach slope is the greatest, as seen in the evolution of $h_t$ (Figure 6.3b). The general trend over the passage of the wave is that high roller angles coincide with greater dissipation, which is evidenced by a more rapid reduction of $H$. Interestingly, we note a delay between high roller angles and high roller lengths values: peaks in $L_r$ appear about 5 m after those observed in $\theta$. This highlights the unsteadiness of breaking and broken waves in a natural environment in contrast to the steady-state breakers generated and observed by D81.

Figure 6.4 presents data from all 38 waves in the analysed dataset. Figure 6.4a illustrates

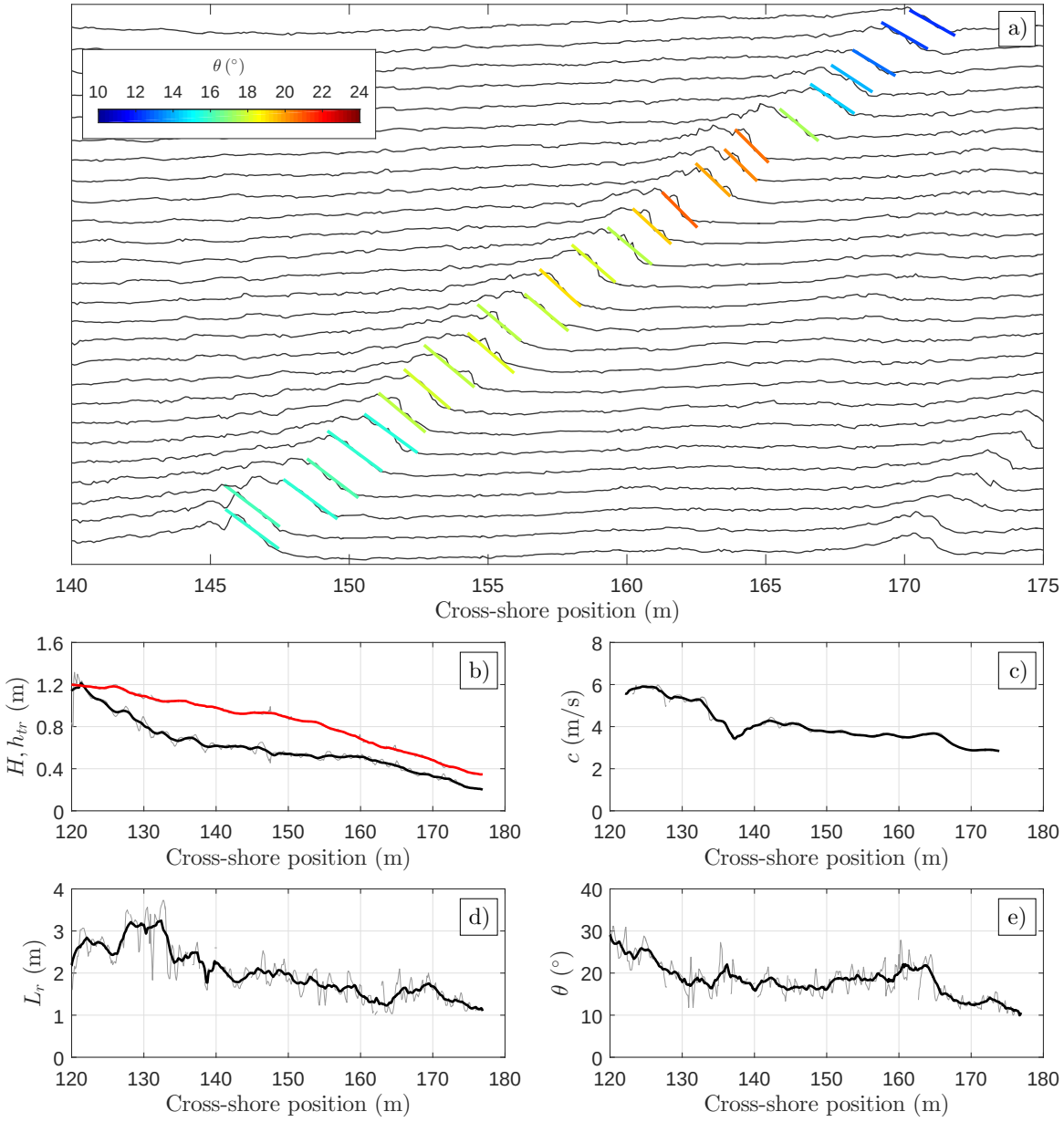


Figure 6.3: Example of a tracked bore in the inner surf zone on 09/04. Panel a) shows the wave profile changes every metre along a section of the full wave track between $x$ = 145 and 170 m. The linear fit of the bore front is added at every location, coloured by the roller angle. Panels b-e) show the cross-shore evolution of the individual wave height $H$ (black line) and local water depth $h_{tr}$ (red line), celerity c, the roller length $L_r$ and angle $\theta$ respectively. The raw measurement is shown as a thin grey line, while the moving window-averaged ($\Delta x$ = 2 m) signal is shown as black thick line (red for $h_{tr}$).

the depth-limited character of the individual waves in the inner surf zone at Saltburn: a good correlation ($r^2$ = 0.87) is found between the individual wave height $H$ and the period-averaged water depth $h_w$. The roller slope is then shown as a function of the wave height in Figure 6.4b, and the product $L_r \tan\theta$ against the surf zone similarity parameter in Figure 6.4c. There appears to be a linear trend between $\tan\theta$ and $H$, however more data from other sites and with different conditions are required to draw robust conclusions on possible parameterizations of $\theta$ as a function of local wave and beach parameters.

The relation $H = 0.6c^2/g$ obtained by D81 is compared to the present inner surf data

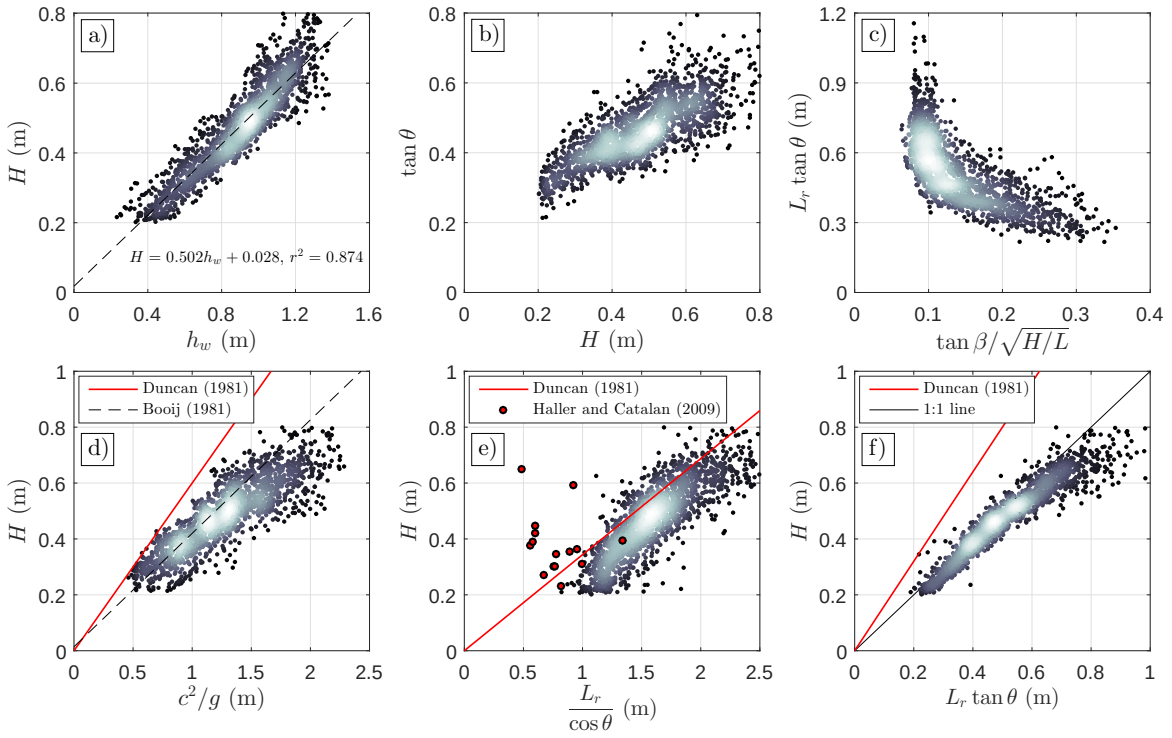


Figure 6.4: Individual wave properties of the 38 inner surf zone waves constituting the present dataset. In each panel, data are shown as a scatter plot coloured by the cloud point density: the brighter region is the densest area whereas darker dots show sparser data points. Panel a) first shows the individual wave height $H$ against the period-averaged water depth $h_w$. Panel b) shows the bore front slope $\tan\theta$ as a function of $H$. Panel c) shows the quantity $L_r \tan\theta$ as a function of the local Iribarren number ($\tan\beta$ is the local beach slope and $L$ a wave length estimated as $cT$). Panels d-f) show the comparison of $c^2/g$, $L_r/\cos\theta$ and $L_r \tan\theta$ against $H$ and the results from Duncan (1981).

in Figure 6.4d. For any broken wave height, we observe a consistent overestimation of the observed $c^2/g$ values compared to the relation of D81. The steady-state breakers generated by D81 had a propagation speed imposed by the displacement of the hydrofoil. However, in the surf zone, amplitude dispersion is generally observed to be important due to increasing wave non-linearities (e.g., Svendsen et al., 1978; Catálan and Haller, 2008; Tissier et al., 2011). To verify this effect on the dataset, the non-linear wave celerity predictor of Booij (1981) was tested here:

$$\frac{c^2_{Booij}}{g} = \frac{1}{k}\tanh\left(k\left(h_w + \frac{H}{2}\right)\right) \tag{6.8}$$

In shallow water, the hyperbolic tangent can be approximated as follows (error <0.7% for the present dataset):

$$\frac{c^2_{Booij}}{g} \approx h_w + \frac{H}{2} \tag{6.9}$$

Using the linear relation found between $H$ and $h_w$ in Figure 6.4a, we obtain the simple linear relation:

$$\frac{c^2_{Booij}}{g} \approx 2.49H - 0.06 \tag{6.10}$$

Accounting for the wave non-linearity in the celerity provides a much better estimate of

the quantity $c^2/g$ than with the formulation of D81, reducing the root-mean square error ($RMSE$) from 0.86 to 0.25 m/s and the scatter index ($SI$) from 1.74 to 0.21.

The measured roller length $L_r/\cos\theta$ is relatively well correlated ($r^2 = 0.68$) to the wave height, and are slightly longer than that predicted by the relation $L_r/\cos\theta = 2.91H$ from the dataset of D81 (Figure 6.4e). From Figure 6.4f, we can see that the measured values of $L_r \tan\theta$ are also greater than that obtained by D81 ($H = 1.6L_r \tan\theta$). The fact that the dataset only consists of fully developed bores explains this behaviour: a simple analysis of the roller geometry in Figure 6.1 shows that if $L_r$ is correctly measured, we should get $L_r \tan\theta \approx H$. This is verified in the present dataset with $r^2 = 0.89$, a $RMSE$ of 0.06 m and $SI$ of 0.13, showing that the procedure for the extraction of the roller length and angle is robust. In contrast, the surface roller covered only a fraction of the wave face during the hydrofoil experiments performed by D81 (see Figures 1 and 3 in Duncan, 1981) leading to relatively shorter roller lengths. This also explains the greater values of $L_r/\cos\theta$ obtained in Figure 6.4e compared to D81.

### 6.4.2 Influence of roller area on energy dissipation rate

Figure 6.5 presents the cross-shore evolution of the surface roller area based on the formulations given in Table 6.1. Values of $A$ are computed using the ensemble-averaged properties of a wave group from the 09/04 consisting of 6 consecutive and similar waves (see Appendix). The original coefficients for the formulations from Tajima (1996) and Okayasu et al. (1986) lead to values about 6 and 10 times larger than those from Engelund (1981), confirming the sensitivity analysis presented in 6.2.2 which suggested that $A$ could vary by an order of magnitude depending on the formulation used. Although the relation found

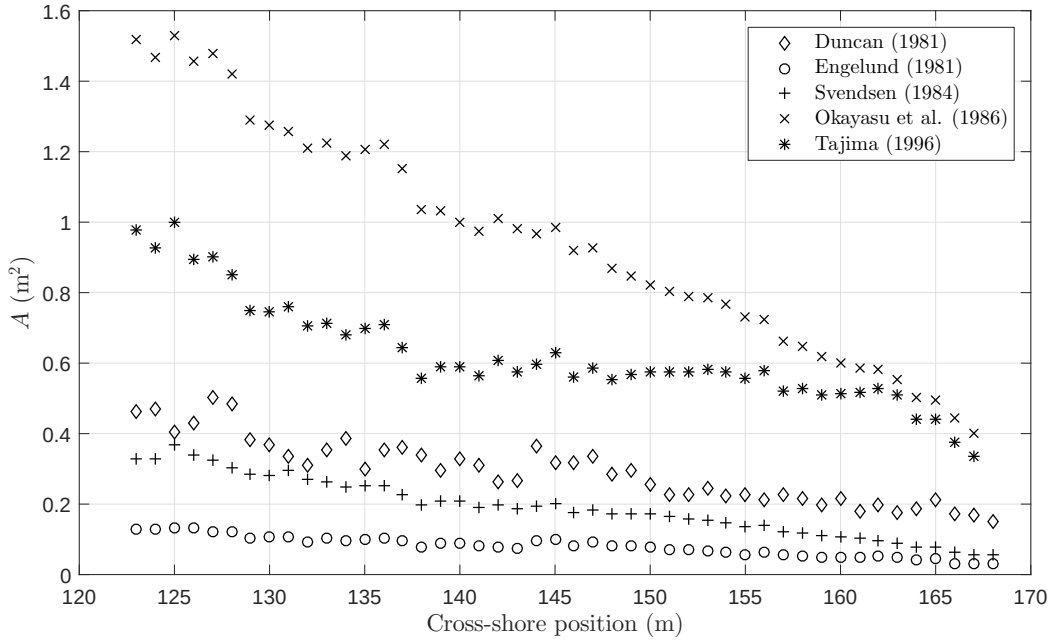


Figure 6.5: Cross-shore evolution of the surface roller area computed from the formulations of Table 6.1 using the ensemble-averaged properties of a wave group from 09/04/2016 (composed of 6 consecutive and similar waves, see Appendix).

by S84 is based on the dataset obtained by D81, it consistently predicts a smaller roller surface area than the original relation of D81. The difference between the two formulations increases closer to shore, where $L_r/\cos\theta$ tends to get larger compared to $H$ in the field when compared with the dataset of D81 (Figure 6.4e). The roller area model developed by Deigaard et al. (1991) based on Engelund (1981) gave the smallest estimates of $A$: roughly half that of S84 and a third of D81.

These differences in the predictions of roller area based on wave and morphology parameters, directly affect the dissipation term $D_\tau$ (Equation 6.7). In Figure 6.6, we compare $D_\tau$ computed for the whole dataset of 38 waves with the roller area formulations in Table 6.1 against the dissipation $D_{HJ}$ estimated for a hydraulic jump of the same height (Equation 6.6). The relation from Engelund (1981) was derived by Deigaard et al. (1991) to match the dissipation of a hydraulic jump of the same height, based on the results of Engelund (1981). This is confirmed by the data (Figure 6.6a), and a reduction of the roller density $\rho_r$ from $\rho$ to $0.8\rho$ and $0.6\rho$ leads to dissipation values 20% and 40% smaller respectively. It is worth mentioning that for the formulation of Engelund (1981), $\rho_r$ should be seen as the tuning coefficient $B$ mentioned earlier, as strictly, a change in the roller density would affect the roller thickness but would still lead to the same amount of energy dissipation as in a hydraulic jump of the same height (Engelund, 1981). When computed with the surface

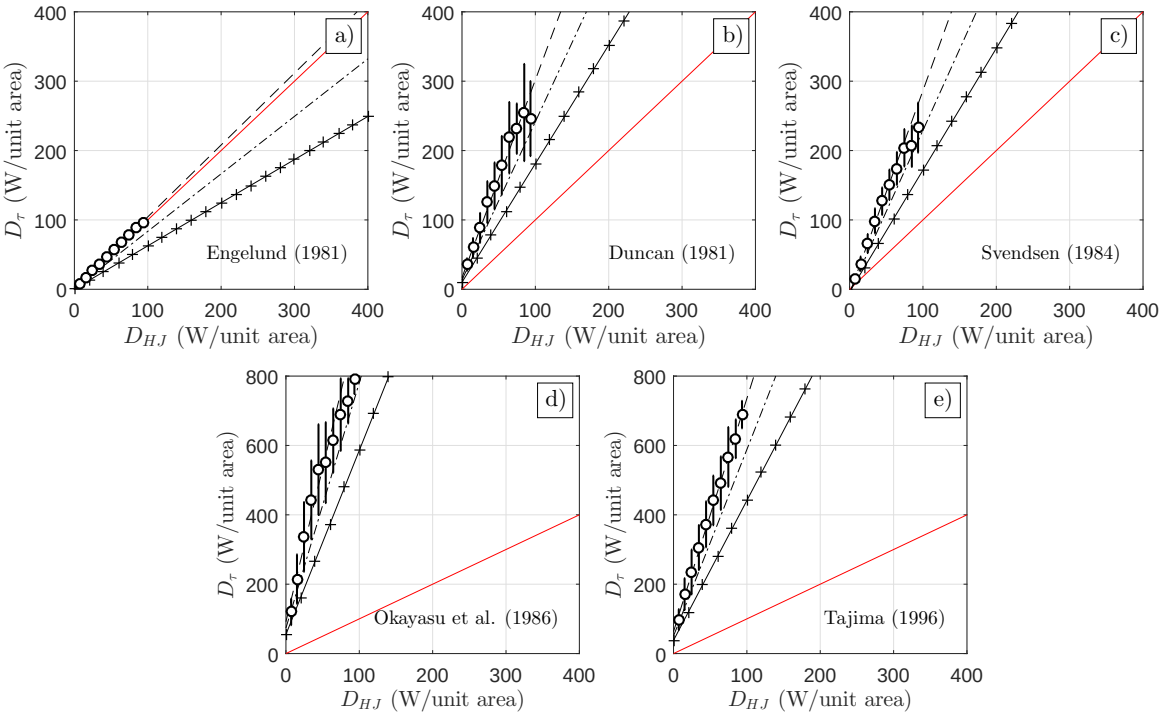


Figure 6.6: Comparison between the energy dissipation $D_\tau$ (Equation 6.5) computed for every roller area formulation (Table 6.1) against the energy dissipation $D_{HJ}$ of a hydraulic jump of the same height. For the formulations of Okayasu et al. (1986) and Tajima (1996), the original coefficients were used. In every panel, the data computed with $\rho_r = \rho$ (white dots) correspond to the mean per 10 W/unit area bins. The standard deviation over that bin is represented by the vertical black lines. To show the influence of the choice of $\rho_r$ on $D_\tau$, the linear fit obtained with $\rho_r = \rho$ (black dashed line), $\rho_r = 0.8\rho$ (black dash-dotted line) and $\rho_r = 0.6\rho$ (black line with + symbols).

roller area formulations of D81 and S84, $D_\tau$ predicts a dissipation rate 1.5 to 3 times greater than that of a hydraulic jump of the same height, depending on the choice of $\rho_r$ (Figure 6.6b-c). In particular, for $\rho_r = 0.8\rho$ which will lead to the best fit with data (Section 4.3), $D_\tau$ is approximately a factor of 2 larger than $D_{HJ}$. In contrast, the formulations of Okayasu et al. (1986) and Tajima (1996) with the original tuning coefficients provide dissipation about 8 and 7 times greater than for an equivalent height hydraulic jump respectively.

### 6.4.3 Consequences for modelling purposes

The roller area formulations listed in Table 6.1 lead to dissipation $D_\tau$ 0.6 to 8 times greater than that for a hydraulic jump of the same height, depending on the value of $\rho_r$. Here, we develop a finite difference modelling approach to estimate the incident wave energy flux $E_{f,w}$ (Equation 6.2). Starting at an initial position $x_0$, the model uses measured wave quantities ($H$, $c$, $\theta$ and $L_r$) and local quantities ($h_w$, $h_{tr}$) to compute the roller contribution (Equation 6.4) and the energy dissipation terms ($D_{HJ}$ from Equation 6.6 and $D_\tau$ from Equation 6.7) to then feed into Equation 6.5. At any cross-shore location $x_i$, the discretization used for Equation 6.5 reads:

$$(E_{f,w})_i = (E_{f,w})_{i-1} - \delta x (D_r)_{i-1} - (E_{f,r})_i + (E_{f,r})_{i-1} \tag{6.11}$$

where the subscripts $i$ and $i-1$ refer to the evaluation of the quantity at the successive grid points $x_i$ and $x_{i-1}$ respectively. $\delta x = x_i - x_{i-1}$ is the spatial discretization step, taken here as 0.1 m. This numerical scheme introduces a local error of $O(\delta x^2)$, meaning that the numerical method is of order 1 over the whole surf zone. This is considered satisfactory for the present application considering the range of values for the energy flux and the roller concept approximations.

The model is tested here on the ensemble-averaged data obtained from the same wave group used in Figure 6.5, composed of 6 consecutive and similar waves (see Appendix). As observed in 6.4.2, an energy dissipation at least twice that of a hydraulic jump of the same height was observed for the roller area formulations of D81 and S84, yielding unrealistic simulations of the energy budget across the surf zone when compared to the data. To fit the data a factor of 0.32 and 0.41 was applied to the roller area formulations of D81 and S84 respectively, so that:

$$A = 0.035 \left(L_r / \cos\theta\right)^2 \tag{6.12}$$

$$A = 0.369 H^2 \tag{6.13}$$

Note that the coefficients of Equations 6.12 and 6.13 were calculated with $\rho_r = 0.8\rho$ as this provided the best fit to data when using the roller area formulation of Engelund (1981), and is within the range of previous observations (Longuet-Higgins and Turner, 1974; Duncan, 1981; Govender et al., 2009; Rojas and Loewen, 2010). Consequently, the coefficients in Equations 6.12 and 6.13 will therefore slightly differ if a different mean void fraction is used. The computed dissipation terms are shown in Figure 6.7a while Figure 6.7b shows

the cross-shore evolution of the simulated incident wave energy. Very good results are obtained with the formulation from Engelund (1981) ($RMSE$ = 46.13 W per unit area) and that of Equation 6.13 ($RMSE$ = 34.70 W per unit area). The modified version of D81 (Equation 6.12) has the worst performance (if we exclude the dissipation from a hydraulic jump) with $RMSE$ of 91.36 W per unit area. The striking difference between the modified version of D81 (Equation 6.12) and the other formulations is that D81 fails to describe the change in dissipation regime occurring around $x$ = 140 m, mainly because it does not take $H$ into account. It is worth noting that, although both the Engelund (1981) and S84 (Equation 6.13) formulations lead to the same amount of energy around $x$ = 165 m, the modified formulation of S84 (Equation 6.13) better predicts the energy dissipation over the whole surf zone, especially between $x$ = 135 and $x$ = 150 m where a better match with the data is obtained.

The results obtained with the formulation of Engelund (1981) could be improved by using a variable void fraction in the roller, as it would be expected to vary in the cross-shore direction with the wave properties and the breaking intensity. Because there is no evidence to support this hypothesis at present, the constant value of $\rho_r = 0.8\rho$ was used here. It is noted that the formulations of Okayasu et al. (1986) and Tajima (1996) give similar results to Equation 6.12 if the coefficients in the original formulations are changed from 0.65 and 140 to 0.065 and 30 respectively (curves not shown here).

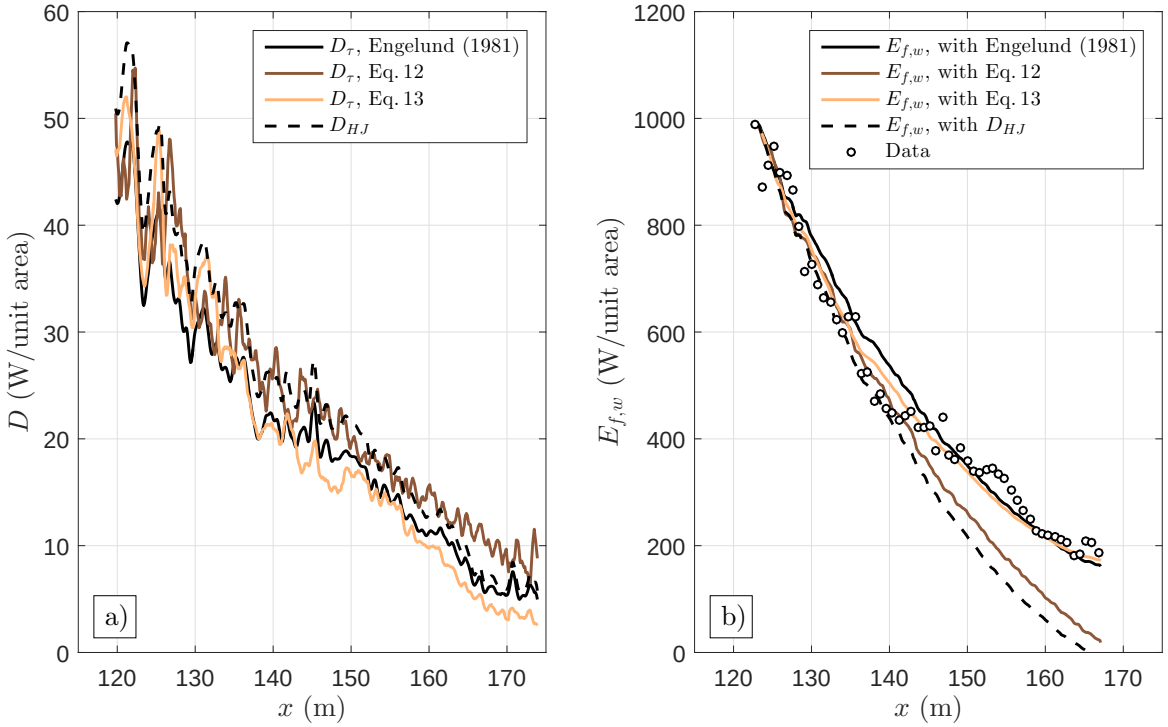


Figure 6.7: Results from the roller model against the wave group ensemble-averaged data, using $\rho_r = 0.8\rho$ (same wave group as Figure 6.5, see also Appendix). Panel a) shows the dissipations terms $D_\tau$ computed using the roller area formulations from Engelund (1981) and the modified formulations of D81 (Equation 6.12) and S84 (Equation 6.13). The dissipation term $D_{HJ}$ of a hydraulic jump of the same height is also shown. Panel b) shows the cross-shore evolution of the modelled incident wave energy flux (Equation 6.3) computed with the dissipation terms from panel a).

## 6.5 Scaling wave breaking energy dissipation in the inner surf zone

Roller models represent a considerable simplification of the breaking process in the inner surf zone. The interaction between surf zone turbulent flows and incident waves (Teixeira and Belcher, 2002) or simply the generation of turbulence during wave breaking (see e.g., Nairn et al., 1990) are very often simplified or not even considered in such model (as it is the case herein). Therefore, a primary source of error when using this type of model is due to the assumption that the dissipation term $D$ in Equation 6.5 is associated solely with the roller. D81 was the first to express the total energy dissipation as a simple function of the wave celerity to the fifth power:

$$D = b\rho\frac{c^5}{g} \tag{6.14}$$

where $b$ is a dissipation coefficient of the form $\alpha/\sin\theta$ (where $\alpha$ is a constant), which takes values in the range 0.031 to 0.066 in the dataset of D81. Later, Melville (1994) found lower values of $b$ in the range 0.004 to 0.012, with $b$ increasing with the wave slope. Interestingly, a simple approximation of the hydraulic jump energy dissipation rate (with $c \sim 1.14\sqrt{gh}$, Tissier et al., 2011) leads to:

$$\epsilon_{HJ} \sim \frac{1}{4}\rho g\frac{H^3}{h}c = \frac{1}{4}\rho\frac{H^3}{h^3}\frac{g^2h^2}{g}c \sim \rho\frac{\gamma^3}{5.2}\frac{c^5}{g} \tag{6.15}$$

which for the present dataset corresponds to $b$ within 0.01 and 0.015, roughly a third of the values from D81, but well within the range of values obtained by Melville (1994). Drazen et al. (2008) performed an extensive analysis of several experimental datasets to further understand the variation of this parameter (e.g., Melville, 1994; Drazen et al., 2008; Romero et al., 2012), and highlighted the dependence of $b$ on $(Hk)^{5/2}$. It is worth noting that in this expression for $b$, Drazen et al. (2008) defined $H$ as the height of the 'active' or 'overturning' part of the wave, which is equal to $H$ as defined in Figure 6.1 (fully developed bores in the inner surf zone). This type of parameterisation is promising for use in the surf zone, as it reduces the number of assumptions made in terms of energy dissipation, while still relying on the wave characteristics and broken wave geometry.

The performance of the two formulations for $b$ was investigated here at the wave group and wave-by-wave scales; the optimum coefficients for both formulations were found to be:

$$b = 1.24(Hk)^{5/2} \tag{6.16}$$

$$b = 0.0011/\sin\theta \tag{6.17}$$

where, $k$ has been calculated using the measured surf zone quantity $cT$. Figure 6.8 shows the cross-shore evolution of the dissipation coefficient $b$, computed with the properties of the same wave group as for the roller model in Figure 6.7. Despite showing two very distinct behaviours, we observe that the two formulations of $b$ yield values in the range of

that observed for unsteady breaking waves (Drazen et al., 2008). Equation 6.16 predicts a dissipative coefficient which decreases gradually between $x = 120$ and 150 m, where the beach slope is mild ($\sim 1:80$) before decreasing more rapidly as the beach steepens landward of $x = 150$ m ($\sim 1:30$). Equation 6.17 predicts the opposite behaviour. This difference in behaviour for $b$ is observed in dissipation terms (Figure 6.9a), with Equation 6.16 predicting more energy dissipation than Equation 6.17 until $x = 135$ m; the trend changes after this location. Although the incident wave energy is better modelled with Equation 6.16 (Figure 6.9b) in the most dissipative part (up to $x = 140$ m), both formulations for $b$ lead to similar skill score overall (*RMSE* of 41.4 and 39.8 W/unit area for Equations 6.16 and 6.17 respectively).

The same order of accuracy is obtained at the wave-by-wave scale, see Figure 6.10. The six waves constituting the wave group are modelled individually and if we exclude the 5th wave (Figure 6.10e), the *RMSE* ranges from 36.5 to 61.9 W/unit area when Equation 6.16 is used, while it varies from 60 to 126 W/unit area when Equation 6.17 is used. The greater model skill displayed by Equation 6.16 can be explained by the fact that the dissipation coefficient $b$ increases with the wave steepness, which qualitatively agrees with the observations in the dataset (see Figure 6.3 for an example). By contrast, Equation 6.17 predicts an increasing dissipation coefficient $b$ for decreasing roller angle, which is not observed in the present dataset.

## 6.6 Discussion on the energy flux formulation in the surf zone

Using a detailed dataset of broken waves, it has been shown that it is possible to correctly simulate energy dissipation in the inner surf zone with the roller model initially developed by S84, using the total wave energy in its integral form (Equation 6.3). Despite the work

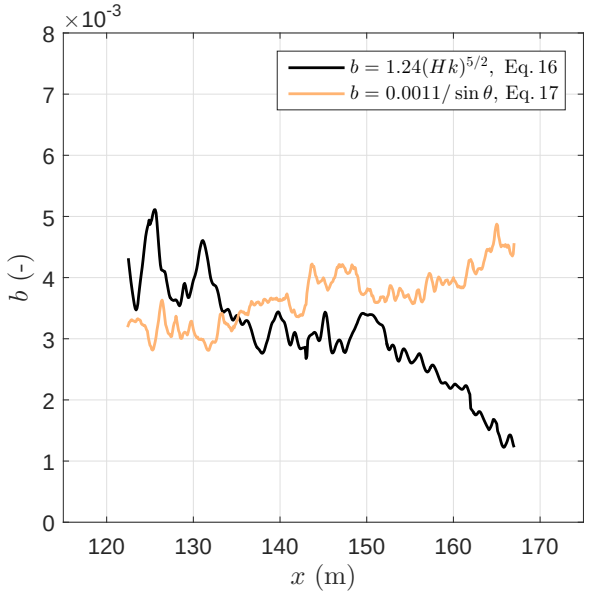


Figure 6.8: Cross-shore evolution of the dissipation coefficient $b$ in Equation 6.14), computed with the wave group ensemble-averaged data (same wave group as Figure 6.5) with the formulation of D81 (Equation 6.16) and that found later by Drazen et al. (2008) (Equation 6.17).

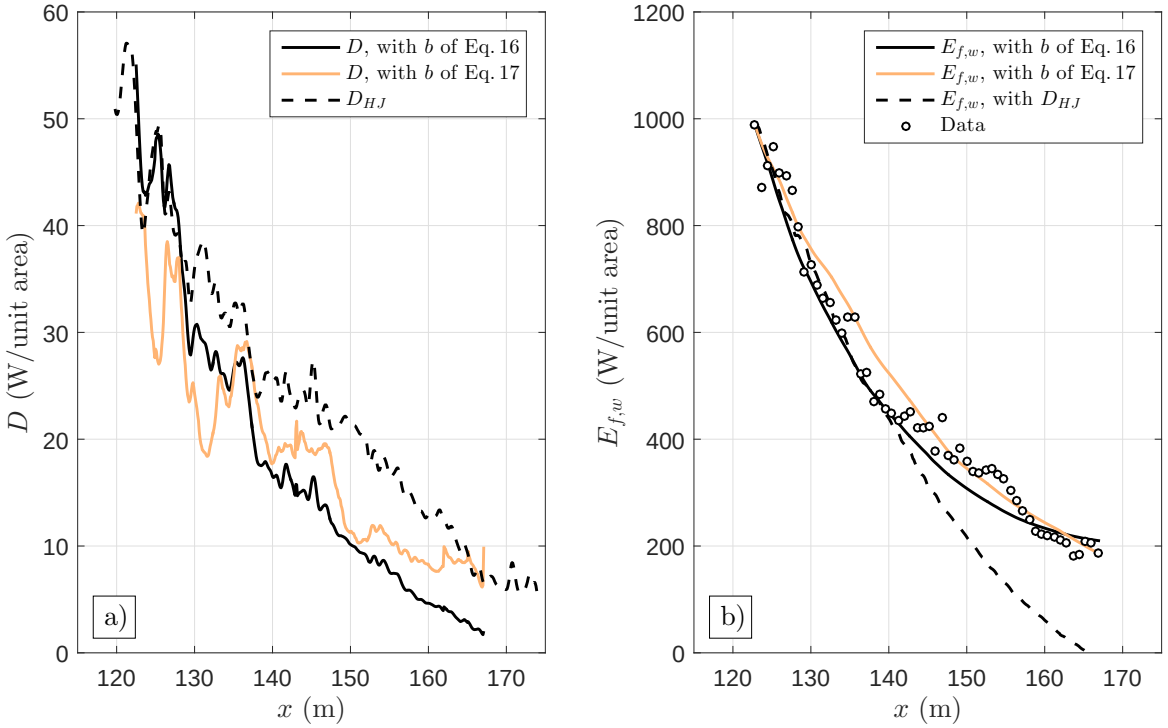


Figure 6.9: Results from the energy balance model of Equation 6.14 against the wave group ensemble-averaged data (same wave group as Figure 6.5, see also Appendix). Panel a) shows the dissipations terms $D$ computed using the two formulations for $b$ (Equations 6.16 and 6.17). The dissipation term $D_{HJ}$ of a hydraulic jump of the same height is also shown as indication. Panel b) shows the cross-shore evolution of the modelled incident wave energy (Equation 6.14) computed with the dissipation terms from panel a).

of S84 and Stive (1984), linear wave theory is generally used to express the energy budget in the surf zone, in the form $1/8\rho g H^2$ or $1/8\rho g H_{rms}^2$. Here, we explain why this approach can be be a very coarse approximation, leading to incorrect estimations of the wave energy dissipation.

In the present dataset and at the wave group scale, we have the following relation (see Appendix):

$$E_w = \frac{1}{2}E_{w,lin} = \rho g \frac{1}{T}\int_0^T \eta^2 dt = \frac{1}{16}\rho g H^2 \tag{6.18}$$

meaning that there is approximately a factor 2 difference between the total wave energy flux computed from the integral form (Equation 6.2) and that given by linear theory. This suggests that in very shallow water, and in the presence of highly non-linear and skewed waves, the energy flux from linear wave theory does not describe the energy flux in a satisfactory manner. This has recently been noted by Martins et al. (2017d) for shoaling waves, but also by many previous researchers at any position in the surf zone (e.g., Svendsen et al., 1978; Svendsen, 1983, 1984a; Stive, 1984; Basco and Yamashita, 1986; Buhr Hansen, 1990; Svendsen et al., 2003; Huang et al., 2009). The increase in wave steepness and skewness generally observed in the surf zone leads to increasing discrepancies between $\frac{1}{T}\int_0^T \eta^2 dt$ and $H^2/8$. This is characterized by the wave shape parameter $B_0$ introduced by

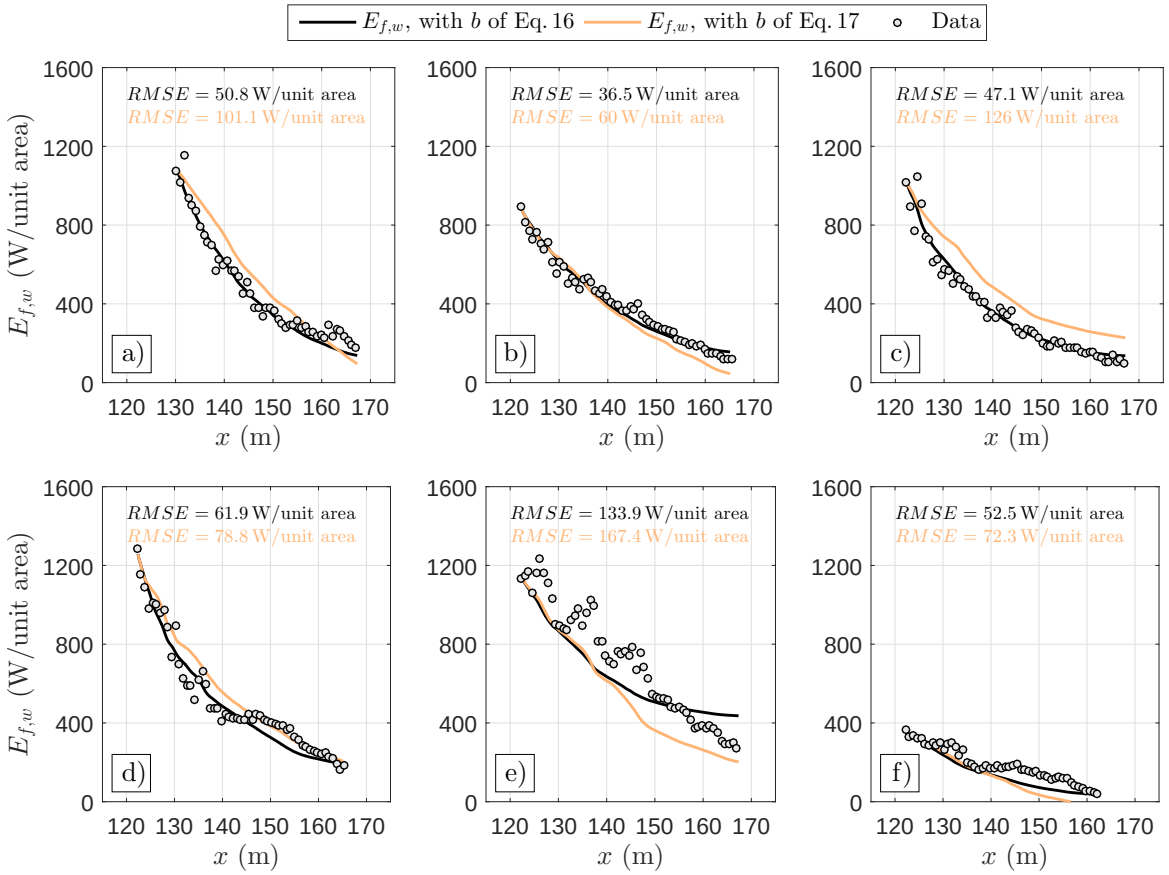


Figure 6.10: Results from the energy balance model of Equation 6.14 at the wave-by-wave scale against measurements from the same wave group as Figures 6.5, 6.7 and 6.9. If we number the individual waves by order of apparition (see Figure 6.12), panels a, b, c, d, e and f show the modelled wave energy flux for the waves number 1, 2, 3, 4, 5 and 6 respectively.

S84 (noted $A_F$ in Stive, 1984):

$$B_0 = \frac{1}{T}\int_0^T \left(\frac{\eta}{H}\right)^2 dt \tag{6.19}$$

In practice and as described by S84, $\rho g c H^2 B_0$ should be taken as the wave energy flux if linear wave theory is to be used. In deep water and for linear waves, $B_0$ takes a value of 1/8. In shallower water, $B_0$ is generally found to vary in the cross-shore direction: it is close to 1/8 in the shoaling region (Basco and Yamashita, 1986), rapidly decreases towards the break point and then slowly varies in the inner surf zone to a value close to a typical value of 0.075 due to a more asymmetric wave profile (Svendsen, 1983, 1984a; Basco and Yamashita, 1986; Buhr Hansen, 1990; Svendsen, 2006). For the data presented here, $B0$ values for individual waves are smaller than 0.1 and $B_0$ is typically found to decrease with increasing wave skewness (see the example shown in Figure 6.11), where skewness is computed as:

$$S_k = \frac{\langle(\eta - \langle\eta\rangle)^3\rangle}{\langle(\eta - \langle\eta\rangle)^2\rangle^{3/2}} \tag{6.20}$$

At the time-averaged scale, the relation given by Equation 6.18 shows that $B_0$ takes the value 1/16. It is worth noting that if $H_{rms} \sim H/\sqrt{2}$ is used instead of $H$ in the energy flux

formulation from linear wave theory, $B_0$ also takes a value of 1/16, which agrees with the current data (Equation 6.18 and see also Appendix) and is close to the typical value of 0.075 (Svendsen, 1983). This confirms the fact that in the inner surf zone, linear wave theory better describes the wave energy flux when $H_{rms}$ is used rather than $H$.

The variation of $B_0$ from almost 1/8 in the shoaling area to half that value in the inner surf zone highlights the effect of choosing a single $B_0$ value to describe the wave energy flux throughout the region of wave transformation, which is implicit when applying linear wave theory. In relatively deep water ($h/h_b > 1.5 - 2$, with $h_b$ the depth at breaking, Basco and Yamashita, 1986), $H$ should be used in the expression for the energy flux as $H_{rms}$ will lead to an underestimation of the incident energy budget by a factor close to 2. By contrast, in the inner surf zone, $H_{rms}$ will yield a more accurate description of the incident energy flux while $H$ will overestimate it by a factor close to 2 (Svendsen, 1984a, and this dataset). In a modelling exercise, an incorrect estimation of the energy budget, say wave height measurements, has a direct impact on the amount of energy dissipation required to match measured data. It is thought that the choice of a constant $B_0$ along with the lack of measured roller geometry has led to the use of unrealistic values for the roller angle in previous studies in order to match model results to observations (e.g., Flores et al., 2016, who used an angle as low as $\theta = 5.7°$ everywhere in the surf zone, which is a factor 2 to 6 smaller than the values measured in this study).

## 6.7 Concluding remarks

In this paper, we present a high-resolution LiDAR dataset from which roller geometrical properties ($H$, $\theta$ and $L_r$) could be extracted. This reduced the number of tunable parameters in the roller model of Svendsen (1984a) to the roller area $A$ and the mean void fraction in the roller represented by the ratio $\rho_r/\rho$. The choice of $A$ appears to be paramount for accurately describing the wave breaking energy dissipation in the inner surf zone (Figure 6.6 and 6.7).

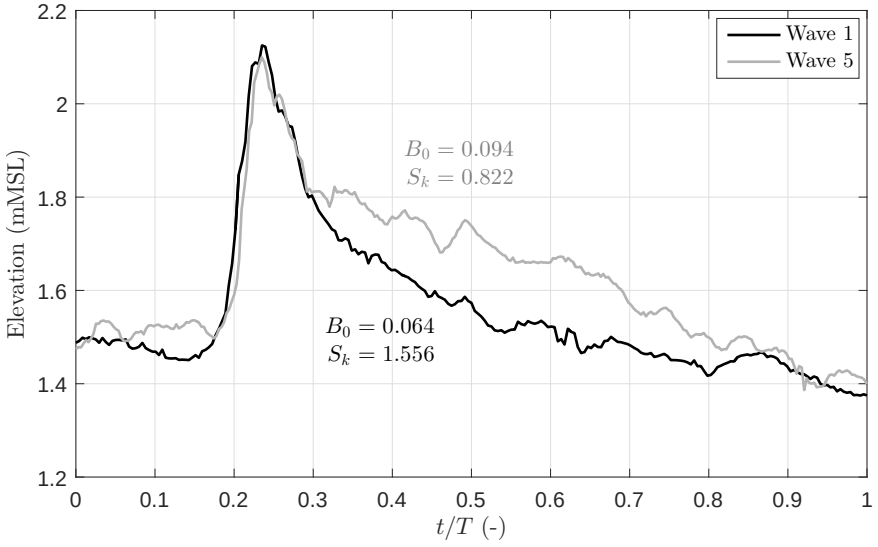


Figure 6.11: Temporal wave profile at $x$ = 130 m of the individual wave number 1 and 5 of the wave group (see Appendix).

The roller area formulation obtained by Duncan (1981) and that later derived by Svendsen (1984a) had to be modified to yield sensible estimates of the energy dissipation in the inner surf zone for the current dataset. The main reason for this lies in the dataset upon which both original formulations have been built. Indeed, the results of 6.4.1 suggest that the relations between wave and roller geometrical quantities from the hydrofoil experiments (Duncan, 1981) do not necessarily apply in a natural inner surf zone. This is in agreement with the observations made by Melville (1994) and Drazen et al. (2008) who found a greater dissipation in the hydrofoil waves of D81 than in 'classic' unsteady breaking waves, corresponding to higher $b$ values. The reason probably lies in the greater celerity imposed on the hydrofoil-generated wave compared to natural unsteady breakers (Figure 6.4d), which induces greater energy dissipation.

The roller area derived by Deigaard et al. (1991) using the work of Engelund (1981) and the modified formulation of Svendsen (1984a) (Equation 6.13) yielded the best predictions of incident energy dissipation with the roller model. This confirms many past observations that broken waves in the inner surf zone dissipate energy at a similar, but generally smaller rate to hydraulic jumps of the same height (Le Méhauté, 1962; Hwang and Divoky, 1970; Svendsen et al., 1978; Battjes and Janssen, 1978; Svendsen, 1984a; Svendsen et al., 2003). The roller density $\rho_r$ appears as a tunable parameter which has a value of $0.8\rho$ to best-fit the present data.

The scaling law (Equation 6.14) first described by Duncan (1981) relating the energy dissipation to the wave celerity was also tested against our dataset. The dissipation coefficient $b$ given by Drazen et al. (2008) appears to accurately describe the wave energy dissipation in the inner surf zone at both wave group and wave-by-wave scales. This is very promising as the energy dissipation could be adopted in a spectral model to simulate energy dissipation in the inner surf zone. However, robust descriptions of the break point location and wave celerity over the whole surf zone are still required (e.g., Svendsen et al., 2003).

Finally, we reiterate the conclusions previously found in the past regarding the use of linear wave theory to describe the wave energy flux in the surf zone. The present findings as well as many past studies show evidence that the choice of a unique $B_0$, implicitly assumed when using wave energy flux from linear wave theory, is not adequate as it does not represent the local wave energy flux correctly. A direct consequence is that it also affects the quantity of dissipated energy required to match an energy balance model with measured data by using non-physical roller parameters.

## Appendix: Comparison of the formulations for the total wave energy in the inner surf

For part of the present analysis, a wave group of 6 waves has been isolated as it was composed of very similar waves and no gaps were present in the data. In this Appendix, we present this wave group, and show that at the wave group scale, we have $B_0 \approx 1/16 = 0.0625$.

Figure 6.12a shows the surface elevation timestack, displaying the six well-defined wave tracks. The methodology of 6.3.2 has been followed to extract the individual wave

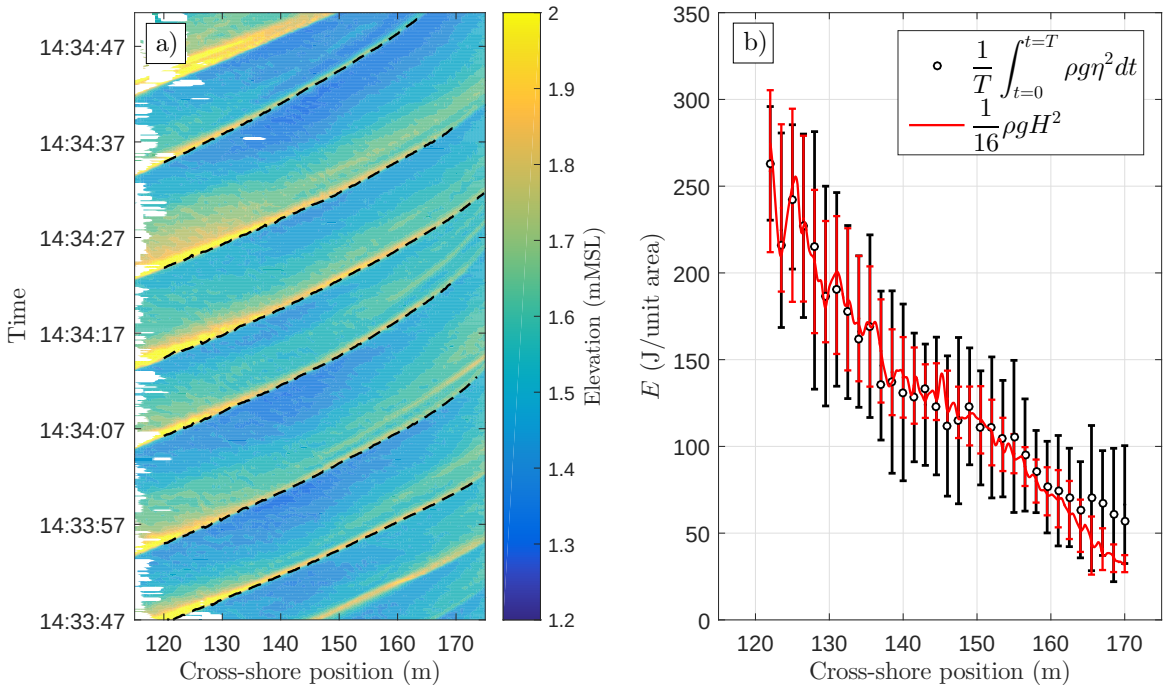


Figure 6.12: Presentation of the wave group selected for the analysis. Panel a) shows the surface elevation timestack in the Mean Sea Level (*MSL*) referential. The wave crest tracks are shown as black dashed lines. Panel b) compares the ensemble-averaged total wave computed with the integral form (Equation 6.21) and that modified from linear wave theory (Equation 6.22). For both energy formulation, the standard deviation is shown as error bar in the same colour.

properties. These properties were ensemble-averaged to compute the total wave energy using the following two formulations:

$$E_w = \rho g \frac{1}{T}\int_0^T \eta^2 dt \tag{6.21}$$

$$\frac{1}{2}E_{w,lin} = \frac{1}{16}\rho g H^2 \tag{6.22}$$

The results from the two formulations are presented in Figure 6.12b; they show very good agreement at the wave group scale ($RMSE$ = 12.05 J/unit area). This means that for the present dataset of inner surf zone waves at the time-averaged scale, $B_0$ has a value of 1/16 = 0.0625. However, at the wave-by-wave scale, significant differences are observed; these can be observed in the greater standard deviations obtained with the integral form (Equation 6.21). There are two potential reasons for this:

- There can be a great variability in shape from one wave to another, see Figure 6.11 for example, and Equation 6.22 does not account for the wavelength or frequency, nor for the wave breaking 'history', whereas Equation 6.21 does.

- Calculating an integral over such a high-resolution dataset is evidently sensitive to the temporal boundaries. Therefore, the location of the individual wave troughs has the potential to affect the amount of energy estimated.

## Acknowledgements

The authors would like to acknowledge the financial assistance provided by the Engineering and Physical Sciences Research Council (EP/N019237/1). Kévin Martins was supported by the University of Bath, through a University Research Services (URS) scholarship. Assistance during the field experiments from Jack Puleo, Brittany Bruder and Aline Pieterse (University of Delaware, US), is greatly appreciated. José Beya (Universidad de Valparaíso, Chile) and James Duncan (University of Maryland, MD, US) are greatly acknowledged for fruitful exchanges.

## References

Almar, R., Michallet, H., Cienfuegos, R., Bonneton, P., Tissier, M., and Ruessink, G. 2014a. On the use of the Radon Transform in studying nearshore wave dynamics. *Coastal Engineering* 92, pp. 24 – 30. DOI: 10.1016/j.coastaleng.2014.06.008.

Apotsos, A., Raubenheimer, B., Elgar, S., and Guza, R. T. 2008. Testing and calibrating parametric wave transformation models on natural beaches. *Coastal Engineering* 55 (3), pp. 224 – 235. DOI: 10.1016/j.coastaleng.2007.10.002.

Bae, J. S., Kim, H.-J., and Choi, J. 2013. Surface Roller Effect Affecting on Shear Fluctuations of a SandyDuck Experiment under a Random Wave Environment. *Journal of Coastal Research* 165, pp. 1491 – 1496. DOI: 10.2112/SI65-252.1.

Baquerizo, A., Losada, M. A., Smith, J. M., and Kobayashi, N. 1997. Cross-shore variation of wave reflection from beaches. *Journal of waterway, port, coastal, and ocean engineering* 123 (5), pp. 274 – 279.

Basco, D. and Yamashita, T. 1986. Toward a simple model of the wave breaking transition region in the surf zones. *Proceedings of the 20th Conference on Coastal Engineering, Taipei, Taiwan*, pp. 955 – 970.

Battjes, J. A. and Janssen, J. P.F. M. 1978. Energy loss and set-up due to breaking of random waves. *Proceedings of the 16th Conference on Coastal Engineering, Hamburg, Germany*, pp. 569 – 587.

Benoit, M., Marcos, F., and Becq, F. 1996. Development of a third generation shallow-water wave model with unstructures spatial meshing. *Proceedings of the 25th Conference on Coastal Engineering, Orlando, Florida*, pp. 465 – 478.

Blenkinsopp, C. E and Chaplin, J. R. 2007. Void fraction measurements in breaking waves. *Proceedings of the Royal Society of London A: Mathematical, Physical and Engineering Sciences* 463 (2088), pp. 3151 – 3170. DOI: 10.1098/rspa.2007.1901.

Booij, N. 1981. "Gravity waves on water with non-uniform depth and current". PhD thesis. Technische Hogeschool, Delft (Netherlands).

Booij, N. and Holthuijsen, L. H. 1987. Propagation of ocean waves in discrete spectral wave models. *Journal of Computational Physics* 68 (2), pp. 307 – 326. DOI: 10.1016/0021-9991(87)90060-X.

Buhr Hansen, J. 1990. Periodic waves in the surf zone: Analysis of experimental data. *Coastal Engineering* 14 (1), pp. 19 – 41. DOI: 10.1016/0378-3839(90)90008-K.

Carini, R. J., Chickadel, C. C., Jessup, A. T., and Thomson, J. 2015. Estimating wave energy dissipation in the surf zone using thermal infrared imagery. *Journal of Geophysical Research: Oceans* 120 (6), pp. 3937 – 3957. DOI: 10.1002/2014JC010561.

Catálan, P. A. and Haller, M. C. 2008. Remote sensing of breaking wave phase speeds with application to non-linear depth inversions. *Coastal Engineering* 55 (1), pp. 93 – 111. DOI: 10.1016/j.coastaleng.2007.09.010.

Cavaleri, L., Alves, J.-H.G. M., Ardhuin, F., Babanin, A., Banner, M., Belibassakis, K., Benoit, M., Donelan, M., Groeneweg, J., Herbers, T. H. C., Hwang, P., Janssen, P. A.E. M., Janssen, T., Lavrenov, I. V., Magne, R., Monbaliu, J., Onorato, M., Polnikov, V., Resio, D., Rogers, W. E., Sheremet, A., Smith, J. M., Tolman, H. L., Vledder, G. van, Wolf, J., and Young, I. 2007. Wave modelling – The state of the art. *Progress in Oceanography* 75 (4), pp. 603 – 674. DOI: 10.1016/j.pocean.2007.05.005.

Cienfuegos, R., Barthélemy, E., and Bonneton, P. 2010. Wave-Breaking Model for Boussinesq-Type Equations Including Roller Effects in the Mass Conservation Equation. *Journal of Waterway, Port, Coastal, and Ocean Engineering* 136 (1), pp. 10 – 26. DOI: 10.1061/(ASCE)WW.1943-5460.0000022.

Dally, W. R. and Brown, C. A. 1995. A modeling investigation of the breaking wave roller with application to cross-shore currents. *Journal of Geophysical Research: Oceans* 100 (C12), pp. 24873 – 24883. DOI: 10.1029/95JC02868.

Deigaard, R. 1993. A note on the three-dimensional shear stress distribution in a surf zone. *Coastal Engineering* 20 (1), pp. 157 – 171. DOI: 10.1016/0378-3839(93)90059-H.

Deigaard, R. and Fredsøe, J. 1989. Shear stress distribution in dissipative water waves. *Coastal Engineering* 13 (4), pp. 357 – 378. DOI: 10.1016/0378-3839(89)90042-2.

Deigaard, R., Justesen, P., and Fredsøe, J. 1991. Modelling of undertow by a one-equation turbulence model. *Coastal Engineering* 15 (5), pp. 431 – 458. DOI: 10.1016/0378-3839(91)90022-9.

Deike, L., Melville, W. K., and Popinet, S. 2016. Air entrainment and bubble statistics in breaking waves. *Journal of Fluid Mechanics* 801, pp. 91 – 129. DOI: 10.1017/jfm.2016.372.

Drazen, D. A., Melville, W. K., and Lenain, L. 2008. Inertial scaling of dissipation in unsteady breaking waves. *Journal of Fluid Mechanics* 611, 307–332. DOI: 10.1017/S0022112008002826.

Duncan, J. H. 1981. An Experimental Investigation of Breaking Waves Produced by a Towed Hydrofoil. *Proceedings of the Royal Society of London A: Mathematical, Physical and Engineering Sciences* 377 (1770), pp. 331 – 348. DOI: 10.1098/rspa.1981.0127.

Elgar, S., Herbers, T. H. C., and Guza, R. T. 1994. Reflection of Ocean Surface Gravity Waves from a Natural Beach. *Journal of Physical Oceanography* 24 (7), pp. 1503 – 1511. DOI: 10.1175/1520-0485(1994)024<1503:ROOSGW>2.0.CO;2.

Engelund, F. 1981. *A simple theory of hydraulic jumps*. Tech. rep. Inst. Hydrodyn. Hydraul. Eng. (ISVA), Tech. Univ. Denmark, Progress Rep, 54: 29 – 32.

Filipot, J.-F. and Cheung, K. F. 2012. Spectral wave modeling in fringing reef environments. *Coastal Engineering* 67, pp. 67 – 79. DOI: 10.1016/j.coastaleng.2012.04.005.

Flores, R. P., Catalán, P. A., and Haller, M. C. 2016. Estimating surfzone wave transformation and wave setup from remote sensing data. *Coastal Engineering* 114, pp. 244 – 252. DOI: 10.1016/j.coastaleng.2016.04.008.

Goda, Y. 2008. Overview on the applications of random wave concept in coastal engineering. *Proceedings of the Japan Academy, Series B* 84 (9), pp. 374 – 385. DOI: 10.2183/pjab.84.374.

Govender, K., Mocke, G. P., and Alport, M. J. 2002. Video-imaged surf zone wave and roller structures and flow fields. *Journal of Geophysical Research: Oceans* 107 (C7), pp. 9–1 – 9–21. DOI: 10.1029/2000JC000755.

Govender, K., Michallet, H., Alport, M., Pillay, U., Mocke, G., and Mory, M. 2009. Video DCIV measurements of mass and momentum fluxes and kinetic energies in laboratory waves breaking over a bar. *Coastal Engineering* 56 (8), pp. 876 – 885. DOI: 10.1016/j.coastaleng.2009.04.002.

Grunnet, N., Martins, K., Deigaard, R., and Drønen, N. 2014. Surf zone hydrodynamics - comparison of modelling and field data. *Proceedings of the 34th Conference on Coastal Engineering, Seoul, Korea*.

Haller, M. C. and Catalán, P. A. 2009. Remote sensing of wave roller lengths in the laboratory. *Journal of Geophysical Research: Oceans* 114 (C7). C07022. DOI: 10.1029/2008JC005185.

Higuera, P., Lara, J. L., and Losada, I. J. 2013. Realistic wave generation and active wave absorption for Navier-Stokes models: Application to OpenFOAM®. *Coastal Engineering* 71, pp. 102 – 118. DOI: 10.1016/j.coastaleng.2012.07.002.

Huang, Z.-C., Hsiao, S.-C., Hwung, H.-H., and Chang, K.-A. 2009. Turbulence and energy dissipations of surf-zone spilling breakers. *Coastal Engineering* 56 (7), pp. 733 – 746. DOI: 10.1016/j.coastaleng.2009.02.003.

Hwang, L.-S. and Divoky, D. 1970. Breaking wave setup and decay on gentle slopes. *Proceedings of the 12th Conference on Coastal Engineering, Washington, D.C.* Pp. 377 – 389.

Jacobsen, N. G., Fuhrman, D. R., and Fredsøe, J. 2012. A wave generation toolbox for the open-source CFD library: OpenFoam®. *International Journal for Numerical Methods in Fluids* 70 (9), pp. 1073 – 1088. DOI: 10.1002/fld.2726.

Kweon, H.-M. and Goda, Y. 1996. A parametric model for random wave deformation by breaking on arbitrary beach profiles. *Proceedings of the 25th Conference on Coastal Engineering, Orlando, Florida*, pp. 261 – 274.

Le Méhauté, B. 1962. On non-saturated breakers and the wave run-up. *Proceedings of the 12th Conference on Coastal Engineering, Mexico City, Mexico*, pp. 77 – 92.

Lippmann, T. C., Brookins, A. H., and Thornton, E. B. 1996. Wave energy transformation on natural profiles. *Coastal Engineering* 27 (1), pp. 1 – 20. DOI: 10.1016/0378-3839(95)00036-4.

Longuet-Higgins, M. S. and Fox, M. J. H. 1977. Theory of the almost-highest wave: the inner solution. *Journal of Fluid Mechanics* 80 (4), pp. 721 – 741. DOI: 10.1017/S0022112077002444.

Longuet-Higgins, M. S. and Stewart, R. W. 1964. Radiation stresses in water waves; a physical discussion, with applications. *Deep Sea Research and Oceanographic Abstracts* 11 (4), pp. 529 – 562. DOI: 10.1016/0011-7471(64)90001-4.

Longuet-Higgins, M. S. and Turner, J. S. 1974. An 'entraining plume' model of a spilling breaker. *Journal of Fluid Mechanics* 63 (1), pp. 1 – 20. DOI: 10.1017/S002211207400098X.

Martins, K., Blenkinsopp, C. E., and Zang, J. 2016. Monitoring Individual Wave Characteristics in the Inner Surf with a 2-Dimensional Laser Scanner (LiDAR). *Journal of Sensors, 2016*, pp. 1 – 11. DOI: 10.1155/2016/7965431.

Martins, K., Blenkinsopp, C. E., Power, H. E., Bruder, B., Puleo, J. A., and Bergsma, E. W. J. 2017b. High-resolution monitoring of wave transformation in the surf zone using a LiDAR scanner array. *Coastal Engineering* 128, pp. 37 – 43. DOI: 10.1016/j.coastaleng.2017.07.007.

Martins, K., Blenkinsopp, C. E., Bergsma, E. W. J., Power, H. E., Bruder, B., and Puleo, J. A. 2017c. Remote-sensing of wave transformation in the surf zone. *Proceedings of the Conference on Coastal Dynamics, Helsingør, Denmark*.

Martins, K., Blenkinsopp, C. E., Almar, R., and Zang, J. 2017d. The influence of swash-based reflection on surf zone hydrodynamics: a wave-by-wave approach. *Coastal Engineering* 122, pp. 27 – 43. DOI: 10.1016/j.coastaleng.2017.01.006.

Masselink, G. and Puleo, J. A. 2006. Swash-zone morphodynamics. *Continental Shelf Research* 26 (5). Swash-Zone Processes, pp. 661 – 680. DOI: 10.1016/j.csr.2006.01.015.

Melville, W. K. 1994. Energy Dissipation by Breaking Waves. *Journal of Physical Oceanography* 24 (10), pp. 2041–2049. DOI: 10.1175/1520-0485(1994)024<2041:EDBBW>2.0.CO;2.

Nairn, R., Roelvink, J. A., and Southgate, H. 1990. Transition zone width and implications for modeling surfzone hydrodynamics. *Proceedings of the 22nd Conference on Coastal Engineering, Delft, The Netherlands*, pp. 68 – 81.

Okayasu, A., Shibayama, T., and Mimura, N. 1986. Velocity field under plunging waves. *Proceedings of the 20th Conference on Coastal Engineering, Taipei, Taiwan*, pp. 660 – 674.

Radon, J. 1917. Über die Bestimmung von Funktionen durch ihre Integralwerte längs gewisser Mannigfaltigkeiten. *Akad. Wiss.* 69, pp. 262 – 277.

Rattanapitikon, W. and Shibayama, T. 2000. Simple model for undertow profile. *Coastal Engineering Journal* 42 (01), pp. 1–30. DOI: 10.1142/S057856340000002X.

Reniers, A. J.H. M. and Battjes, J. A. 1997. A laboratory study of longshore currents over barred and non-barred beaches. *Coastal Engineering* 30 (1), pp. 1 – 21. DOI: 10.1016/S0378-3839(96)00033-6.

Rojas, G. and Loewen, M. R. 2010. Void fraction measurements beneath plunging and spilling breaking waves. *Journal of Geophysical Research: Oceans* 115 (C8).

Romero, L., Melville, W. K., and Kleiss, J. M. 2012. Spectral Energy Dissipation due to Surface Wave Breaking. *Journal of Physical Oceanography* 42 (9), pp. 1421–1444. DOI: 10.1175/JPO-D-11-072.1.

Ruessink, B. G., Miles, J. R., Feddersen, F., Guza, R. T., and Elgar, S. 2001. Modeling the alongshore current on barred beaches. *Journal of Geophysical Research: Oceans* 106 (C10), pp. 22451 – 22463. DOI: 10.1029/2000JC000766.

Salmon, J. E., Holthuijsen, L. H., Zijlema, M., Vledder, G. P. van, and Pietrzak, J. D. 2015. Scaling depth-induced wave-breaking in two-dimensional spectral wave models. *Ocean Modelling* 87, pp. 30 – 47. DOI: 10.1016/j.ocemod.2014.12.011.

Schäffer, H. A., Madsen, P. A., and Deigaard, R. 1993. A Boussinesq model for waves breaking in shallow water. *Coastal Engineering* 20 (3–4), pp. 185 – 202. DOI: 10.1016/0378-3839(93)90001-O.

Stive, M. J. F. 1984. Energy dissipation in waves breaking on gentle slopes. *Coastal Engineering* 8 (2), pp. 99 – 127. DOI: 10.1016/0378-3839(84)90007-3.

Stive, M. J. F. and Wind, H. G. 1986. Cross-shore mean flow in the surf zone. *Coastal Engineering* 10 (4), pp. 325 – 340. DOI: 10.1016/0378-3839(86)90019-0.

Suhayda, J. N. and Pettigrew, N. R. 1977. Observations of wave height and wave celerity in the surf zone. *Journal of Geophysical Research* 82 (9), pp. 1419 – 1424. DOI: 10.1029/JC082i009p01419.

Svendsen, I. A. 1983. "Wave heights and set-up in a surf zone". *Hydraulic Engineering Reports*. University of Delaware.

Svendsen, I. A. 1984a. Mass flux and undertow in a surf zone. *Coastal Engineering* 8 (4), pp. 347 – 365. DOI: 10.1016/0378-3839(84)90030-9.

Svendsen, I. A. 2006. *Introduction to Nearshore Hydrodynamics*. Advanced series on ocean engineering. World Scientific.

Svendsen, I. A., Madsen, P. A., and Buhr Hansen, J. 1978. Wave characteristics in the surf zone. *Proceedings of the 16th Conference on Coastal Engineering, Hamburg, Germany*, pp. 520 – 539.

Svendsen, I. A., Qin, W., and Ebersole, B. A. 2003. Modelling waves and currents at the LSTF and other laboratory facilities. *Coastal Engineering* 50 (1), pp. 19 – 45. DOI: 10.1016/S0378-3839(03)00077-2.

Tajima, Y. 1996. "Surf zone hydrodynamics". MA thesis. Massachusetts Institute of Technology.

Teixeira, M. A. C. and Belcher, S. E. 2002. On the distortion of turbulence by a progressive surface wave. *Journal of Fluid Mechanics* 458, pp. 229 – 267. DOI: 10.1017/S0022112002007838.

Thornton, E. B. and Guza, R. T. 1983. Transformation of wave height distribution. *Journal of Geophysical Research: Oceans* 88 (C10), pp. 5925 – 5938. DOI: 10.1029/JC088iC10p05925.

Tissier, M., Bonneton, P., Almar, R., Castelle, B., Bonneton, N., and Nahon, A. 2011. Field measurements and non-linear prediction of wave celerity in the surf zone. *European Journal of Mechanics - B/Fluids* 30 (6), pp. 635 – 641. DOI: 10.1016/j.euromechflu.2010.11.003.

Tolman, H. L. 1989. *The numerical model WAVEWATCH: a third generation model for hindcasting of wind waves on tides in shelf seas*. Tech. rep. 89-2. ISSN 0169-6548. Faculty of civil engineering, Delft University of Technology.

Vink, A. S. 2001. "Transformation of wave spectra across the surf zone". MA thesis. Technical University of Delft.

Walstra, D. J. R., Mocke, G. P., and Smit, F. 1996. Roller contribution as inferred from inverse modelling techniques. *Proceedings of the 25th Conference on Coastal Engineering, Orlando, Florida*, pp. 1205 – 1218.

Yoo, J., Fritz, H. M., Haas, K. A., Work, P. A., and Barnes, C. F. 2011. Depth inversion in the surf zone with inclusion of wave nonlinearity using video-derived celerity. *Journal of Waterway, Port, Coastal, and Ocean Engineering* 137 (2), pp. 95 – 106. DOI: 10.1061/(ASCE)WW.1943-5460.0000068.

Zhang, C., Chen, Y., Zheng, J., and Demirbilek, Z. 2014. Variation of wave roller slope in the surf zone. *Proceedings of the 34th Conference on Coastal Engineering, Seoul, Korea*. DOI: 10.9753/icce.v34.waves.12.

Zheng, J., Mase, H., Demirbilek, Z., and Lin, L. 2008. Implementation and evaluation of alternative wave breaking formulas in a coastal spectral wave model. *Ocean Engineering* 35 (11), pp. 1090 – 1101. DOI: 10.1016/j.oceaneng.2008.05.001.

## Chapter concluding remarks

This Chapter - the last of this PhD thesis - brings some answers to one of the most complex problems of the nearshore: at what rate do broken waves dissipate energy in the inner surf zone? The results obtained with the roller model of Svendsen (1984b) combined with novel measurements surface roller properties confirm many past studies that broken waves dissipate their energy at a slightly smaller rate than hydraulic jumps of the same height. However, and as always in research, these results bring many new questions that should be addressed in the future. Three principal questions emerge and are as follows:

- Can we parameterize surface roller angles as a function of the broken wave and beach properties?
- Is the assumption $E_p = E_k$ valid in the surf zone for any wave and beach conditions?
- Does the proposed scaling law for energy dissipation in the inner surf zone work for other wave and beach conditions?

It seems impossible to hypothesise on the second and third points without further investigation, however, some recent work by Zhang et al. (2017) suggest that it might be possible to parameterize $\theta$. Although the authors did not differentiate non-broken and broken waves, they express the wave angle as a function of the wave steepness and the Ursell number. Further analysis of the present datasets might show that the relations found by Zhang et al. (2017) are applicable to surface rollers.

# Chapter 7

# Conclusions and further work

## 7.1 Conclusions

In this thesis, 2D LiDAR scanners were used to collect high spatial and temporal resolution measurements of surf zone waves. For the first time, an array of three scanners was deployed along a nearshore pier to measure wave transformation from the shoaling region to the swash zone. Thanks to the great details of the wave profiles captured by the scanners, the cross-shore evolution of geometric properties of breaking and broken waves was studied at various temporal scales. In this Conclusions Chapter, the findings are summarized and discussed with respect to the initial objectives. Finally, the results of this study are placed in a wider context and some future investigations with or without LiDAR scanners are proposed.

### 7.1.1 A Wave-by-wave approach to study wave properties

Following the recent work of Power et al. (2010) and Postacchini and Brocchini (2014), waves were individually defined by detecting maxima in the surface elevation timeseries and minima for the surrounding troughs. This method does not require the definition of a mean water level, which is a considerable advantage for the shallowest regions of the surf zone where low-frequency energy often dominates (e.g, see Chapter 3). Taking advantage of the high spatial resolution of the LiDAR datasets, tracking algorithms were then developed to follow the evolution of particular waves. This approach was presented and validated against statistical wave parameters in Chapter 3. An interesting feature in the cross-shore evolution of the mean individual wave period was observed: close to shore, it exhibited larger values than the spectral period. More recent studies (Tissier et al., 2017; García-Medina et al., 2017) demonstrated that bore merging was responsible for this phenomenon (i.e. a broken wave catching up with the preceding wave). This phenomenon will need further investigation in the future as it occurs at the boundary between the inner surf and the swash zones, hence affecting the amount of energy entering the swash zone.

The individual wave properties presented in Chapter 3, and especially the scatter that they exhibit, raise interesting and important questions. The variety of the processes occurring in the surf zone at various temporal scales explain this scatter and suggest that wave properties obtained in previous dataset may contain the effect from other physical

processes such as low-frequency waves or reflected waves (cf. Chapter 4). Indeed, the presence of low-frequency waves strongly influences the local water depth that a particular wave experiences, leading to modifications of the incident wave celerity (Tissier et al., 2015) but also its local energy dissipation rates. Consequently, it is still very difficult to predict the celerity of individual waves using a non-linear celerity predictor.

In Chapter 4, a combination of experimental and numerical datasets was used to study wave reflection processes at various temporal scales. Ingoing and outgoing surface elevation signals were separated with the Radon Transform (Radon, 1917; Yoo et al., 2011; Almar et al., 2014a). First, the mechanism at the origin of wave reflection was highlighted: reflected waves are generated by the mass flux of the preceding swash and propagate back into the surf zone. Next, the wave-by-wave analysis of Chapter 3 was performed on the separated surface elevation fields and demonstrated that the interactions between incident and reflected waves contribute to the scatter of $\gamma$ in the surf zone. Similar to low-frequency waves that induce intra-wave variability of individual wave celerity (Tissier et al., 2015), wave reflection in the sea-swell frequency band induces intra-wave variability of individual $\gamma$ values. These individual reflected waves were also found to have an impact on time-averaged surf zone quantities such as the undertow, the wave setup, the wave asymmetry and the cross-shore current velocity skewness.

### 7.1.2 LiDAR scanner arrays for the study of surf zone waves

The most innovative aspect of this PhD project consists of the field experiment performed at the nearshore pier of Saltburn-by-the-Sea, UK, which involved the deployment of an array of three LiDAR scanners above the water surface. The objective to collect a unique surface elevation dataset covering up to 100 m of surf zone posed serious challenges. A previous unpublished LiDAR dataset collected at a nearshore pier in Chile was successfully used to estimate the optimal separation distance between adjacent LiDARs. Next, each individual LiDAR dataset was processed following the methodology described in Chapter 3 (Martins et al., 2016). For more accuracy, the geo-localization of the scanners was performed by reflector-less total station surveys. Finally, a weight function method based on the distance from each instrument location was applied to construct the unique surface elevation dataset from the three individual datasets.

In Chapter 4, the comparisons of surface elevation derived from the pressure signal with direct measurements from the LiDAR scanner showed the limitation of the common approach to use linear wave theory in highly non-linear conditions. The dataset acquired during the field experiment at Saltburn allows for the direct measurement of breaking wave properties. A new method to detect the break point from high-resolution LiDAR datasets was first presented in Chapter 5 (Martins et al., 2017b). Aided by visual estimations of the break point, this technique was found to be more efficient than classic methods such as that based on the location of maximum wave height or those using the geometric measurements of waves (e.g. $S_k$ and $A_s$).

The surface elevation and cross-shore current velocity asymmetry and skewness were

studied at the wave-by-wave and time-averaged scales. At the time-averaged scale, a relation between the free-stream third order moments and those measured at the surface by both the scanner and the pressure-derived signals was demonstrated. This has the exciting potential application of linking changes in morphology and wave conditions with third-order moments of the free surface via the application of long-term remote sensing using LiDAR, as we know that the wave acceleration skewness is an important factor for beach morphology (e.g., Hoefel and Elgar, 2003; Grasso et al., 2011; Dubarbier et al., 2015). At the wave-by-wave scale, surface and current wave properties showed similar characteristics (for both skewness and asymmetry), except in the shallowest parts of the inner surf zone where infragravity waves are suspected to bias the properties from the velocity signal. The individual wave skewness was the individual wave property that was found to relate the most to the time-averaged wave skewness and asymmetry.

### 7.1.3 Energy dissipation rates of broken waves in the surf zone

In Chapter 6, the first direct measurements in field conditions of geometric properties of surface rollers ($\theta$ and $L_r$) were presented. This dataset was used together with the roller model first described by Svendsen (1984b) to investigate energy dissipation rates in broken waves propagating in the inner surf zone.

The geometric properties of surface rollers were first compared to the empirical relationships linking surface roller and broken wave properties, and obtained by Duncan (1981). The differences found between the two datasets suggest that the relations obtained by Duncan (1981) during his hydrofoil experiments do not hold in natural inner surf zones. There are two main reasons for this: 1) the unsteadiness of the breaking process compared to the steady-state breakers in the experiments of Duncan (1981) and 2) the breaker celerity imposed by the hydrofoil compared to the wave celerity in the surf zone, where amplitude dispersion is important. This has direct implication on the parameterization of energy dissipation rates in inner surf zone broken waves as the increased celerity provokes a greater dissipation than in reality. This also reflected in the observations of greater roller area. Consequently, the roller area formulation from Duncan (1981) and that later derived with the same dataset by Svendsen (1984b) led to an overestimation of the energy dissipation when used in a roller model. In the inner surf zone, waves were found to dissipate their energy at a similar, but smaller, rate than hydraulic jumps of the same height, which is consistent with many past studies.

## 7.2 Implications and perspectives for the future

### 7.2.1 Wave-by-wave analysis

In this thesis, many tools to track individual waves and extract their geometric properties across the surf zone are developed. This is only allowed thanks to the high-resolution surface elevation datasets collected by LiDAR scanner.

With this wave-by-wave approach, precious information on wave reflection processes, measurements of breaking and broken wave geometries as well as a better understanding

of energy dissipation rates could be obtained. Although synthetic and laboratory datasets were used, recent studies have also applied such an approach for studying runup and extracting wave height at breaking (Padilla and Alsina, 2017; García-Medina et al., 2017). In the future, this methodology could be applied to LiDAR dataset such as that acquired in Chapter 5 to obtain accurate estimation of wave height distributions in the surf zone.

The presence of multiple physical processes occurring at different temporal scales can, however, be misleading and particular care should be taken. Indeed, it is demonstrated in Chapters 3 and 4 that incident waves potentially interact with low-frequency and reflected waves. Without accounting for these processes in the analysis (e.g. the Radon Transform for wave reflection), individual wave properties can 'incorporate' their effect. Here, intra-wave variability of $\gamma$ is shown to be due to the presence of reflected waves in the sea/swell band of frequencies.

In conclusion, wave-by-wave approaches such as those presented in this thesis are useful as they enable new insights from high-resolution data, especially when they are combined with traditional analysis at longer time scales. However, they should be interpreted with care as individual waves can exhibit a considerable scatter induced by the effect of various physical processes such as wave reflection and the presence of low-frequency waves (e.g., see Tissier et al., 2015; Martins et al., 2017d).

### 7.2.2 The use of linear wave theory in the surf zone

At several stages of the present work, serious limitations of linear wave theory in surf zone applications are highlighted. In the validation stage of the OpenFOAM® model used in Chapter 4, the pressure signal is transformed into surface elevation using the classic depth correction method (e.g., Bishop and Donelan, 1987). Differences of up to 30% in the individual wave height are obtained around the break point, as well as significant differences in the wave profile skewness. At the wave-by-wave scale, this is unacceptable as it leads to an incorrect and non-physical description of various wave quantities. Besides providing incorrect measurements for validating models, the observed underestimation of individual nearshore wave heights from pressure-derived measurements casts serious doubt on the reliability of previously reported wave height distributions in the surf zone from PTs (e.g., Power and Baldock, 2017). Wave height distributions in the surf zone are an important component of nearshore wave propagation models (e.g., Battjes and Janssen, 1978; Thornton and Guza, 1983; Apotsos et al., 2008), they thus have to be as accurate as possible. One of the conclusions of this work is that LiDAR scanners represent a great opportunity to obtain accurate measurements of wave heights across the whole surf zone at the wave-by-wave scale, without any assumptions on the measurements.

Secondly, and maybe more importantly, concerns are raised in Chapter 6 regarding the expression for the wave energy flux in the surf zone, generally taken from linear wave theory. Despite the seminal work of Svendsen (1984b) and Stive (1984), linear wave theory is still used in the same manner across the entire surf zone. The variation in shape that waves experience in the surf zone is not accounted for in the simple expression from linear

wave theory, which solely uses the wave height. In expectation of more comprehensive experiments, the empirical formulations from Buhr Hansen (1990) on the $B_0$ parameter of Svendsen (1984b) provide better estimates of the wave energy budget (e.g., see Svendsen et al., 2003). The incorrect use of linear wave theory when inferring wave heights from energetic-based models are thought responsible for the use of non-physical roller properties and energy dissipation parameterizations.

## 7.3 Recommendation for further work

During this study, some important results were obtained and these improved our understanding of wave transformation in the shoaling and surf zones. As always, many of these results either brought new research questions or relied on hypotheses that could not be verified. In this section, the principal research directions that emerged from the present work are addressed.

### 7.3.1 Influence of swash-based reflection on surf zone morphodynamics

In Chapter 4, reflected waves were observed to influence the time-averaged surf zone hydrodynamic quantities, such as the undertow. Along with a clear signature in the undertow in the seaward part of the bar, the existence of node/antinode systems in the sea/swell band of frequencies suggests that swash-based wave reflection has an effect on long-term surf morphodynamics. Recent laboratory-based investigations on the spatial evolution of ripples, which generate and migrate under reflective conditions (Cobos et al., 2017), tend to validate this hypothesis. In light of the present results, the nature of the undertow seems more complex than just an offshore mean-current driven by the excess of mass fluxes under progressive waves. The phase shift of the reflected waves influencing the local current conditions must play an important role, and perturbation in the incident wave boundary layers might also exist. Interactions between reflected and incident waves close to the bed might lead to stronger pressure gradients that were recently shown to have an influence on bed morphology by destabilizing it (Berni et al., 2017; Anderson et al., 2017; Michallet et al., 2017). More experiments, e.g. looking at bar generation/migration in relation to foreshore slopes and wave dominant conditions, should be performed to understand the long-term influence of swash-based reflection on surf zone morphology.

### 7.3.2 Hypothesis on the mechanical wave energy of surf zone waves

The surface roller concept first described and applied by Svendsen (1984b) was used in Chapter 6 (Martins et al., submitted) to model the energy dissipation due to wave breaking. Although the results obtained were consistent with previous studies in terms of energy dissipation rates, the hypothesis made implicitly in the model that $E_p = E_k$ everywhere in the surf zone cannot be verified in the field. This hypothesis has to be further investigated in laboratory conditions, and for a wide range of wave and beach conditions so that a wide spectrum of wave breaking types are covered. Additionally, this investigation could provide more insights on void ratio, turbulence generation and spreading in the region of the surface roller.

### 7.3.3 LiDAR applications

With LiDAR scanners, the potential for future nearshore wave studies seems extensive and very exciting. We believe that they have the potential to become the norm in any 'high-frequency' field experiment as they provide both wave and beach measurements at high spatial and temporal resolution. Possible applications include:

- Collecting a more comprehensive dataset of roller geometries from a range of beach and wave conditions with the aim of parametrizing surface roller length and angle.
- Extending the analysis of wave geometric properties to the swash zone, e.g. to study wave properties at bore collapse (Bergsma et al., submitted).
- Monitoring third-order moments of the surface elevation and relate it to bathymetric changes in the long-term.
- The study of swash zone morphodynamics at the swash event scale.

In the following, two other potential further use of LiDAR scanner are discussed in more details.

The application of the new break point detection method on the dataset collected in Chapter 5 (Martins et al., 2017b) is a unique opportunity to obtain a comprehensive field dataset of breaking wave properties, including parameters such as breaker index, the wave skewness and wave asymmetry but also wave angles. Indeed, spatial information on the wave shape are directly measured by the scanners, which is an interesting added value as these measurements are generally obtained only by video imagery in down-scaled laboratory conditions. Just after the break point, the wave enters the transition zone, where it experiences rapid changes. At the moment, there is no quantitative dataset of surface elevation in field conditions in this region. Instead, most of the knowledge is mainly based on visual observations and point-based measurements (cf. Chapter 2). LiDAR datasets could be used to obtain a better understanding of wave transformation in this transition region and answer questions such as: how wide is this region? Can geometric wave properties be used to clearly separate outer and inner surf zone? Can we parameterize the energy dissipation in this region of the surf zone?

LiDAR scanners have the ability to estimate wave celerity and height at the same time. This has direct application in the search for a non-linear wave celerity predictor, for depth-inversion purposes. Estimation of wave phases is also possible with video camera systems, at both the wave-by-wave and time-averaged scales. However, wave geometry cannot be directly estimated over the whole domain, which has the effect of considerably reducing the accuracy of depth-inversion techniques in region of high wave non-linearities (e.g., Bergsma et al., 2016). A combination of these two technologies has the potential to extend the accuracy obtained in intermediate depths by video imagery through to the inner surf zone. Secondly, it was seen in Chapter 6 that wave celerity was a proxy for wave energy dissipation in the inner surf zone. By tracking waves from both video imagery and LiDAR datasets, the dissipation field can potentially be estimated in two dimensions. This could provide valuable estimates of the surf zone mean circulation.

# Bibliography


Abshire, J. B., 2010. *NASA's Space Lidar Measurements of Earth and Planetary Surfaces*. NASA Goddard Space Flight Center; Greenbelt, MD, United States.

Airy, G. B., 1845. "Tides and waves". *Encyclopaedia Metropolitana*. Vol. 5.

Allis, M. J., Peirson, W. L., and Banner, M. L., 2011. Application of LiDAR As a Measurement Tool For Waves. *The Twenty-first International Offshore and Polar Engineering Conference, 19-24 June, Maui, Hawaii, USA*. Vol. 3, pp. 373 – 379.

Almar, R., Cienfuegos, R., Catalán, P. A., Michallet, H., Castelle, B., Bonneton, P., and Marieu, V., 2012. A new breaking wave height direct estimator from video imagery. *Coastal Engineering* 61, pp. 42 – 48. DOI: 10.1016/j.coastaleng.2011.12.004.

Almar, R., Michallet, H., Cienfuegos, R., Bonneton, P., Tissier, M., and Ruessink, G., 2014a. On the use of the Radon Transform in studying nearshore wave dynamics. *Coastal Engineering* 92, pp. 24 – 30. DOI: 10.1016/j.coastaleng.2014.06.008.

Almar, R., Catalan, P., Ibaceta, R., Blenkinsopp, C., Cienfuegos, R., Villagran, M., Aguilera, J. C., and Castelle, B., 2014b. Swash zone based reflection during energetic wave conditions at a dissipative beach: towards a wave-by-wave approach. *Proceedings of the 34th Conference on Coastal Engineering, Seoul, Korea*.

Almeida, L. P., Masselink, G., Russell, P. E., and Davidson, M. A., 2015. Observations of gravel beach dynamics during high energy wave conditions using a laser scanner. *Geomorphology* 228, pp. 15 – 27. DOI: 10.1016/j.geomorph.2014.08.019.

Almeida, L. P., Masselink, G., Russell, P., Davidson, M., Poate, T., McCall, R., Blenkinsopp, C., and Turner, I., 2013. Observations of the swash zone on a gravel beach during a storm using a laser-scanner (Lidar). *Journal of Coastal Research*, pp. 636 – 641. DOI: 10.2112/SI65-108.1.

Alsina, J. M. and Cáceres, I., 2011. Sediment suspension events in the inner surf and swash zone. Measurements in large-scale and high-energy wave conditions. *Coastal Engineering* 58 (8), pp. 657 – 670. DOI: 10.1016/j.coastaleng.2011.03.002.

Alsina, J. M., Falchetti, S., and Baldock, T. E., 2009. Measurements and modelling of the advection of suspended sediment in the swash zone by solitary waves. *Coastal Engineering* 56 (5–6), pp. 621 – 631. DOI: 10.1016/j.coastaleng.2009.01.007.

Alsina, J. M., Cáceres, I., Brocchini, M., and Baldock, T. E., 2012. An experimental study on sediment transport and bed evolution under different swash zone morphological conditions. *Coastal Engineering* 68, pp. 31 – 43. DOI: 10.1016/j.coastaleng.2012.04.008.

Anderson, D., Cox, D., Mieras, R., Puleo, J. A., and Hsu, T.-J., 2017. Observations of wave-induced pore pressure gradients and bed level response on a surf zone sandbar. *Journal of Geophysical Research: Oceans* 122 (6), pp. 5169 – 5193. DOI: 10.1002/2016JC012557.

Apotsos, A., Raubenheimer, B., Elgar, S., and Guza, R. T., 2008. Testing and calibrating parametric wave transformation models on natural beaches. *Coastal Engineering* 55 (3), pp. 224 – 235. DOI: 10.1016/j.coastaleng.2007.10.002.

Ardhuin, F., 2012. "Les vagues: un compartiment important du systême terre". Lecture notes.

Astier, J., Astruc, D., Lacaze, L., and Eiff, O., 2012. Investigation of the swash zone evolution at wave time scale. *Proceedings of the 33rd Conference on Coastal Engineering, Santander, Spain*.

Baquerizo, A., Losada, M. A., Smith, J. M., and Kobayashi, N., 1997. Cross-shore variation of wave reflection from beaches. *Journal of waterway, port, coastal, and ocean engineering* 123 (5), pp. 274 – 279.

Basco, D. R., 1983. Surfzone currents. *Coastal Engineering* 7 (4), pp. 331 – 355. DOI: 10.1016/0378-3839(83)90003-0.

Basco, D. R., 1985. A Qualitative Description of Wave Breaking. *Journal of Waterway, Port, Coastal, and Ocean Engineering* 111 (2), pp. 171–188. DOI: 10.1061/(ASCE)0733-950X(1985)111:2(171).

Basco, D. and Yamashita, T., 1986. Toward a simple model of the wave breaking transition region in the surf zones. *Proceedings of the 20th Conference on Coastal Engineering, Taipei, Taiwan*, pp. 955 – 970.

Battjes, J. A., 1974. Surf similarity. *Proceedings of the 14th Conference on Coastal Engineering, Copenhagen, Denmark*, pp. 466 – 480.

Battjes, J. A., 1988. Surf-Zone Dynamics. *Annual Review of Fluid Mechanics* 20 (1), pp. 257 – 291. DOI: 10.1146/annurev.fl.20.010188.001353.

Battjes, J. A. and Janssen, J. P.F. M., 1978. Energy loss and set-up due to breaking of random waves. *Proceedings of the 16th Conference on Coastal Engineering, Hamburg, Germany*, pp. 569 – 587.

Beji, S., 1995. Note on a nonlinearity parameter of surface waves. *Coastal Engineering* 25 (1), pp. 81 – 85. DOI: 10.1016/0378-3839(94)00031-R.

Beji, S. and Battjes, J. A., 1993. Experimental investigation of wave propagation over a bar. *Coastal Engineering* 19 (1), pp. 151 – 162. DOI: 10.1016/0378-3839(93)90022-Z.

Bergamasco, F., Torsello, A., Sclavo, M., Barbariol, F., and Benetazzo, A., 2017. WASS: An open-source pipeline for 3D stereo reconstruction of ocean waves. *Computers & Geosciences* 107 (Supplement C), pp. 28 – 36. DOI: 10.1016/j.cageo.2017.07.001.

Bergsma, E. W. J., Conley, D. C., Davidson, M. A., and O'Hare, T. J., 2016. Video-based nearshore bathymetry estimation in macro-tidal environments. *Marine Geology* 374, pp. 31 – 41. DOI: 10.1016/j.margeo.2016.02.001.

Bergsma, E. W. J., Blenkinsopp, C. E., Martins, K., Almar, R., and Almeida, L. P., submitted. Bore collapse and wave run-up on a sandy beach. *Submitted to Continental Shelf Research*.

# Bibliography


Berni, C., Michallet, H., and Barthélemy, E., 2017. Effects of horizontal pressure gradients on bed destabilization under waves. *Journal of Fluid Mechanics* 812, pp. 721 – 751. DOI: 10.1017/jfm.2016.805.

Birkemeier, W., Donoghue, C., Long, C., Hathaway, K., and Baron, C., 1990. *DELILAH nearshore experiment: Summary report*. Tech. rep. CHL-97-4-24, US Army Corps of Engineers. Field Research Facility.

Bishop, C. T. and Donelan, M. A., 1987. Measuring waves with pressure transducers. *Coastal Engineering* 11 (4), pp. 309 – 328. DOI: 10.1016/0378-3839(87)90031-7.

Blenkinsopp, C. E and Chaplin, J. R, 2007. Void fraction measurements in breaking waves. *Proceedings of the Royal Society of London A: Mathematical, Physical and Engineering Sciences* 463 (2088), pp. 3151 – 3170. DOI: 10.1098/rspa.2007.1901.

Blenkinsopp, C. E. and Chaplin, J. R., 2008. The effect of relative crest submergence on wave breaking over submerged slopes. *Coastal Engineering* 55 (12), pp. 967 – 974. DOI: 10.1016/j.coastaleng.2008.03.004.

Blenkinsopp, C. E. and Chaplin, J. R., 2011. Void fraction measurements and scale effects in breaking waves in freshwater and seawater. *Coastal Engineering* 58 (5), pp. 417 – 428. DOI: 10.1016/j.coastaleng.2010.12.006.

Blenkinsopp, C. E., Mole, M. A., Turner, I. L., and Peirson, W. L., 2010. Measurements of the time-varying free-surface profile across the swash zone obtained using an industrial LIDAR. *Coastal Engineering* 57 (11 – 12), pp. 1059 – 1065. DOI: 10.1016/j.coastaleng.2010.07.001.

Blenkinsopp, C. E., Turner, I. L., Masselink, G., and Russell, P. E., 2011. Swash zone sediment fluxes: Field observations. *Coastal Engineering* 58 (1), pp. 28 – 44. DOI: 10.1016/j.coastaleng.2010.08.002.

Blenkinsopp, C., Matias, A., Howe, D., Castelle, B., Marieu, V., and Turner, I., 2016. Wave runup and overwash on a prototype-scale sand barrier. *Coastal Engineering* 113. Barrier Dynamics Experiment II: sediment processes across a large-scale sand barrier, pp. 88 – 103. DOI: 10.1016/j.coastaleng.2015.08.006.

Blenkinsopp, C. E., Turner, I. L., Allis, M. J., Peirson, W. L., and Garden, L. E., 2012. Application of LiDAR technology for measurement of time-varying free-surface profiles in a laboratory wave flume. *Coastal Engineering* 68, pp. 1 – 5. DOI: 10.1016/j.coastaleng.2012.04.006.

Borgman, L. E., 1979. "Directional Wave Spectra from Wave Sensors". *Ocean Wave Climate*. Ed. by M. Earle and A. Malahoff. Vol. 8. Marine Science. Springer US, pp. 269–300. DOI: 10.1007/978-1-4684-3399-9_12.

Briganti, R., Torres-Freyermuth, A., Baldock, T. E., Brocchini, M., Dodd, N., Hsu, T.-J., Jiang, Z., Kim, Y., Pintado-Patiño, J. C., and Postacchini, M., 2016. Advances in numerical modelling of swash zone dynamics. *Coastal Engineering* 115. Swash-zone Processes, pp. 26 – 41. DOI: 10.1016/j.coastaleng.2016.05.001.

Brocchini, M., 2006. Integral swash-zone models. *Continental Shelf Research* 26 (5). Swash-Zone Processes, pp. 653 – 660. DOI: 10.1016/j.csr.2006.02.002.

Brocchini, M. and Baldock, T. E., 2008. Recent advances in modeling swash zone dynamics: Influence of surf-swash interaction on nearshore hydrodynamics and morphodynamics. *Reviews of Geophysics* 46 (3). DOI: 10.1029/2006RG000215.

Brock, J. C. and Purkis, S. J., 2009. The Emerging Role of Lidar Remote Sensing in Coastal Research and Resource Management. *Journal of Coastal Research* 25 (6), pp. 1–5.

Brodie, K. L., Slocum, R. K., and McNinch, J. E., 2012. New insights into the physical drivers of wave runup from a continuously operating terrestrial laser scanner. *Oceans, 2012*, pp. 1 – 8. DOI: 10.1109/OCEANS.2012.6404955.

Brodie, K. L., Raubenheimer, B., Elgar, S., Slocum, R. K., and McNinch, J. E., 2015. Lidar and Pressure Measurements of Inner-Surfzone Waves and Setup. *Journal of Atmospheric and Oceanic Technology* 32 (10), pp. 1945 – 1959. DOI: 10.1175/JTECH-D-14-00222.1.

Buhr Hansen, J., 1990. Periodic waves in the surf zone: Analysis of experimental data. *Coastal Engineering* 14 (1), pp. 19 – 41. DOI: 10.1016/0378-3839(90)90008-K.

Butt, T., Russell, P., Puleo, J., Miles, J., and Masselink, G., 2004. The influence of bore turbulence on sediment transport in the swash and inner surf zones. *Continental Shelf Research* 24 (7), pp. 757 – 771. DOI: 10.1016/j.csr.2004.02.002.

Carey, W. M. and Fitzgerald, J. W., 1993. "Low Frequency Noise from Breaking Waves". *Natural Physical Sources of Underwater Sound: Sea Surface Sound (2)*. Ed. by B. R. Kerman. Dordrecht: Springer Netherlands, pp. 277 – 304. DOI: 10.1007/978-94-011-1626-8_22.

Carini, R. J., Chickadel, C. C., Jessup, A. T., and Thomson, J., 2015. Estimating wave energy dissipation in the surf zone using thermal infrared imagery. *Journal of Geophysical Research: Oceans* 120 (6), pp. 3937 – 3957. DOI: 10.1002/2014JC010561.

Carvalho, J. and Parente, C., 2000. Directional wave measurements using a slope array system. *Applied Ocean Research* 22 (2), pp. 95 – 101. DOI: 10.1016/S0141-1187(99)00028-0.

Catálan, P. A. and Haller, M. C., 2008. Remote sensing of breaking wave phase speeds with application to non-linear depth inversions. *Coastal Engineering* 55 (1), pp. 93 – 111. DOI: 10.1016/j.coastaleng.2007.09.010.

Cavaleri, L, 1980. Wave measurement using pressure transducer. *Oceanologica Acta* 3 (3), pp. 339 – 346.

Chanson, H. and Jaw-Fang, L., 1997. Plunging jet characteristics of plunging breakers. *Coastal Engineering* 31 (1), pp. 125 – 141. DOI: 10.1016/S0378-3839(96)00056-7.

Chardón-Maldonado, P., Pintado-Patiño, J. C., and Puleo, J. A., 2016. Advances in swash-zone research: Small-scale hydrodynamic and sediment transport processes. *Coastal Engineering* 115, pp. 8 – 25. DOI: 10.1016/j.coastaleng.2015.10.008.

Cobos, M., Chiapponi, L., Longo, S., Baquerizo, A., and Losada, M. A., 2017. Ripple and sandbar dynamics under mid-reflecting conditions with a porous vertical breakwater. *Coastal Engineering* 125, pp. 95 – 118. DOI: 10.1016/j.coastaleng.2017.04.006.

Cowell, P. J., 1982. *Breaker stages and surf structure on beaches*. Tech. rep. Coastal Studies Unit Technical Report No. 82/7, Sydney, Australia.

# Bibliography


Dally, W. R., 1990. Random breaking waves: A closed-form solution for planar beaches. *Coastal Engineering* 14 (3), pp. 233 – 263. DOI: 10.1016/0378-3839(90)90026-S.

Dally, W. R. and Brown, C. A., 1995. A modeling investigation of the breaking wave roller with application to cross-shore currents. *Journal of Geophysical Research: Oceans* 100 (C12), pp. 24873 – 24883. DOI: 10.1029/95JC02868.

Dean, R. G. and Dalrymple, R. A., 1991. *Water wave mechanics for engineers and scientists*. Advanced Series on Ocean Engineering: Volume 2, World Scientific.

Deane, G. B., 1997. Sound generation and air entrainment by breaking waves in the surf zone. *The Journal of the Acoustical Society of America* 102 (5), pp. 2671–2689. DOI: 10.1121/1.420321.

Deigaard, R., 1993. A note on the three-dimensional shear stress distribution in a surf zone. *Coastal Engineering* 20 (1), pp. 157 – 171. DOI: 10.1016/0378-3839(93)90059-H.

Deike, L., Melville, W. K., and Popinet, S., 2016. Air entrainment and bubble statistics in breaking waves. *Journal of Fluid Mechanics* 801, pp. 91 – 129. DOI: 10.1017/jfm.2016.372.

Divoky, D., Le Méhauté, B., and Lin, A., 1970. Breaking waves on gentle slopes. *Journal of Geophysical Research* 75 (9), pp. 1681 – 1692. DOI: 10.1029/JC075i009p01681.

Dubarbier, B., Castelle, B., Marieu, V., and Ruessink, G., 2015. Process-based modeling of cross-shore sandbar behavior. *Coastal Engineering* 95, pp. 35 – 50. DOI: http://dx.doi.org/10.1016/j.coastaleng.2014.09.004.

Duncan, J. H., 1981. An Experimental Investigation of Breaking Waves Produced by a Towed Hydrofoil. *Proceedings of the Royal Society of London A: Mathematical, Physical and Engineering Sciences* 377 (1770), pp. 331 – 348. DOI: 10.1098/rspa.1981.0127.

Duncan, J. H., 2001. Spilling breakers. *Annual Review of Fluid Mechanics* 33 (1), pp. 519 – 547. DOI: 10.1146/annurev.fluid.33.1.519.

Duncan, J. H., Qiao, H., Philomin, V., and Wenz, A., 1999. Gentle spilling breakers: crest profile evolution. *Journal of Fluid Mechanics* 379, 191–222. DOI: 10.1017/S0022112098003152.

Dyhr-Nielson, M. and Sørensen, T., 1970. Some sand transport phenomena on coasts with bars. *Proceedings of the 12th Conference on Coastal Engineering, Washington, D.C.*, pp. 855 – 865.

Ebersole, B. A. and Hughes, S. A., 1987. *DUCK85 Photopole Field Experiment*. Tech. rep. ADA188477, DTIC Document.

Elfrink, B. and Baldock, T., 2002. Hydrodynamics and sediment transport in the swash zone: a review and perspectives. *Coastal Engineering* 45 (3). Surface and Swash Zone Mechanics, pp. 149 – 167. DOI: 10.1016/S0378-3839(02)00032-7.

Elgar, S., Herbers, T. H. C., and Guza, R. T., 1994. Reflection of Ocean Surface Gravity Waves from a Natural Beach. *Journal of Physical Oceanography* 24 (7), pp. 1503 – 1511. DOI: 10.1175/1520-0485(1994)024<1503:ROOSGW>2.0.CO;2.

Erikson, L., Larson, M., and Hanson, H., 2005. Prediction of swash motion and run-up including the effects of swash interaction. *Coastal Engineering* 52 (3), pp. 285 – 302. DOI: 10.1016/j.coastaleng.2004.12.001.

Esteva, D. and Harris, D., 1970. Comparison of pressure and staff wave gage records. *Proceedings of the 12th Conference on Coastal Engineering, Washington, D.C.* Pp. 101 – 116.

Evans, A. J., 2010. Laser scanning applied to hydraulic modeling. *International Archives of Photogrammetry, Remote Sensing and Spatial Information Sciences, Commission V Symposium, Newcastle upon Tyne, UK*.

Führboter, A., 1970. Air Entrainment and Energy Dissipation in Breakers. *Proceedings of the 12th Conference on Coastal Engineering, Washington, D.C.* Pp. 101 – 116.

Flores, R. P., Catalán, P. A., and Haller, M. C., 2016. Estimating surfzone wave transformation and wave setup from remote sensing data. *Coastal Engineering* 114, pp. 244 – 252. DOI: 10.1016/j.coastaleng.2016.04.008.

Folsom, R. G., 1947. Sub-surface pressures due to oscillatory waves. *Eos, Transactions American Geophysical Union* 28 (6), pp. 875 – 881. DOI: 10.1029/TR028i006p00875.

García-Medina, G., Haller, H. T. Özkan, Holman, R. A., and Ruggiero, P., 2017. Large runup controls on a gently sloping dissipative beach. *Journal of Geophysical Research: Oceans*. DOI: 10.1002/2017JC012862.

Goda, Y., 2010. *Random Seas and Design of Maritime Structures*. Advanced series on ocean engineering. World Scientific.

Goda, Y. and Suzuki, T., 1976. Estimation of incident and reflected waves in random wave experiments. *Proceedings of the 15th Conference on Coastal Engineering, Honolulu, Hawaii*, pp. 828 – 845.

Grace, R. A., 1978. Surface wave heights from pressure records. *Coastal Engineering* 2, pp. 55 – 67. DOI: 10.1016/0378-3839(78)90005-4.

Grasso, F., Michallet, H., and Barthélemy, E., 2011. Sediment transport associated with morphological beach changes forced by irregular asymmetric, skewed waves. *Journal of Geophysical Research: Oceans* 116 (C3). C03020. DOI: 10.1029/2010JC006550.

Grasso, F., Castelle, B., and Ruessink, B. G., 2012. Turbulence dissipation under breaking waves and bores in a natural surf zone. *Continental Shelf Research* 43, pp. 133 – 141. DOI: 10.1016/j.csr.2012.05.014.

Grilli, S. T., Svendsen, I. A., and Subramanya, R., 1997. Breaking Criterion and Characteristics for Solitary Waves on Slopes. *Journal of Waterway, Port, Coastal, and Ocean Engineering* 123 (3), pp. 102 – 112. DOI: 10.1061/(ASCE)0733-950X(1997)123:3(102).

Guard, P. A. and Baldock, T. E., 2007. The influence of seaward boundary conditions on swash zone hydrodynamics. *Coastal Engineering* 54 (4), pp. 321 – 331. DOI: 10.1016/j.coastaleng.2006.10.004.

Guza, R. T. and Thornton, E. B., 1980. Local and shoaled comparisons of sea surface elevations, pressures, and velocities. *Journal of Geophysical Research: Oceans* 85 (C3), pp. 1524 – 1530. DOI: 10.1029/JC085iC03p01524.

Guza, R. T. and Thornton, E. B., 1982. Swash oscillations on a natural beach. *Journal of Geophysical Research: Oceans* 87 (C1), pp. 483 – 491. DOI: 10.1029/JC087iC01p00483.

Guza, R. T. and Bowen, A. J., 1976. Resonant Interactions for Waves Breaking on a Beach. *Proceedings of the 15th Conference on Coastal Engineering, Honolulu, Hawaii*, pp. 560 – 579.

# Bibliography


Haller, M. C. and Catalán, P. A., 2009. Remote sensing of wave roller lengths in the laboratory. *Journal of Geophysical Research: Oceans* 114 (C7). C07022. DOI: 10.1029/2008JC005185.

Hamm, L., Madsen, P. A., and Peregrine, D. H., 1993. Wave transformation in the nearshore zone: A review. *Coastal Engineering* 21 (1), pp. 5–39. DOI: 10.1016/0378-3839(93)90044-9.

Harry, M., Zhang, H., Lemckert, C., and Colleter, G., 2010. 3D Spatial Definition of a Water Surface. *The Ninth ISOPE Pacific/Asia Offshore Mechanics Symposium, 14-17 November, Busan, Korea*.

Higuera, P., Lara, J. L., and Losada, I. J., 2013. Realistic wave generation and active wave absorption for Navier-Stokes models: Application to OpenFOAM®. *Coastal Engineering* 71, pp. 102–118. DOI: 10.1016/j.coastaleng.2012.07.002.

Hoefel, F. and Elgar, S., 2003. Wave-Induced Sediment Transport and Sandbar Migration. *Science* 299 (5614), pp. 1885–1887. DOI: 10.1126/science.1081448.

Hofland, B., Chen, X., Altomare, C., and Oosterlo, P., 2017. Prediction formula for the spectral wave period Tm-1,0 on mildly sloping shallow foreshores. *Coastal Engineering* 123, pp. 21–28. DOI: http://dx.doi.org/10.1016/j.coastaleng.2017.02.005.

Holman, R. and Haller, M. C., 2013. Remote Sensing of the Nearshore. *Annual Review of Marine Science* 5 (1). PMID: 22809186, pp. 95–113. DOI: 10.1146/annurev-marine-121211-172408.

Holman, R., Plant, N., and Holland, T., 2013. cBathy: A robust algorithm for estimating nearshore bathymetry. *Journal of Geophysical Research: Oceans* 118 (5), pp. 2595–2609. DOI: 10.1002/jgrc.20199.

Holthuijsen, L., 2007. *Waves in Oceanic and Coastal Waters*. Cambridge University Press.

Hom-ma, M., Horikawa, K., and Komori, S., 1966. Response characteristics of underwater wave gauge. *Proceedings of 10th Conference on Coastal Engineering, Tokyo, Japan*, pp. 99–114.

Hoque, A. and Aoki, S.-I., 2005. A Quantitative Analysis of Energy Dissipation among Three Typical Air Entrainment Phenomena. *Environmental Fluid Mechanics* 5 (4), pp. 325–340. DOI: 10.1007/s10652-005-3258-1.

Hotta, S, Mizuguchi, M, and Isobe, M, 1982. A field study of waves in the nearshore zone. *Proceedings of the 17th Conference on Coastal Engineering, Sydney, Australia*, pp. 38–57.

Howe, D., 2016. "Bed shear stress under wave runup on steep slopes". PhD thesis. Water Research Laboratory, Faculty of Engineering, UNSW.

Hughes, M. G., Aagaard, T., Baldock, T. E., and Power, H. E., 2014. Spectral signatures for swash on reflective, intermediate and dissipative beaches. *Marine Geology* 355, pp. 88–97. DOI: 10.1016/j.margeo.2014.05.015.

Huntley, D. A., 1976. Long-period waves on a natural beach. *Journal of Geophysical Research* 81 (36), pp. 6441–6449. DOI: 10.1029/JC081i036p06441.

Huntley, D. A., Guza, R. T., and Bowen, A. J., 1977. A universal form for shoreline run-up spectra? *Journal of Geophysical Research* 82 (18), pp. 2577 – 2581. DOI: 10.1029/JC082i018p02577.

Hwang, L.-S. and Divoky, D., 1970. Breaking wave setup and decay on gentle slopes. *Proceedings of the 12th Conference on Coastal Engineering, Washington, D.C.* Pp. 377 – 389.

Hwang, P. A., Walsh, E. J., Krabill, W. B., Swift, R. N., Manizade, S. S., Scott, J. F., and Earle, M. D., 1998. Airborne remote sensing applications to coastal wave research. *Journal of Geophysical Research: Oceans* 103 (C9), pp. 18791 – 18800. DOI: 10.1029/98JC00895.

Hwang, P. A., Wang, D. W., Walsh, E. J., Krabill, W. B., and Swift, R. N., 2000a. Airborne Measurements of the Wavenumber Spectra of Ocean Surface Waves. Part I: Spectral Slope and Dimensionless Spectral Coefficient. *Journal of Physical Oceanography* 30 (11), pp. 2753–2767. DOI: 10.1175/1520-0485(2001)031<2753:AMOTWS>2.0.CO;2.

Hwang, P. A., Wang, D. W., Walsh, E. J., Krabill, W. B., and Swift, R. N., 2000b. Airborne Measurements of the Wavenumber Spectra of Ocean Surface Waves. Part II: Directional Distribution*. *Journal of Physical Oceanography* 30 (11), pp. 2768–2787. DOI: 10.1175/1520-0485(2001)031<2768:AMOTWS>2.0.CO;2.

Iafrati, A., 2011. Energy dissipation mechanisms in wave breaking processes: Spilling and highly aerated plunging breaking events. *Journal of Geophysical Research: Oceans* 116 (C7). C07024. DOI: 10.1029/2011JC007038.

Inch, K., 2014. Surf Zone Hydrodynamics: Measuring Waves and Currents. *Geomorphological Techniques, Chap. 3, Sec. 2.3*. British Society of Geomorphology.

Iribarren, C. R. and Nogales, C., 1949. Protection des ports. *XVIIth International Navigation Congres* 1 (14).

Irish, J. L., Wozencraft, J. M., Cunningham, A. G., and Giroud, C., 2006. Nonintrusive Measurement of Ocean Waves: Lidar Wave Gauge. *Journal of Atmospheric and Oceanic Technology* 23, pp. 1559–1572. DOI: 10.1175/JTECH1936.1.

Jacobsen, N. G., Fuhrman, D. R., and Fredsøe, J., 2012. A wave generation toolbox for the open-source CFD library: OpenFoam®. *International Journal for Numerical Methods in Fluids* 70 (9), pp. 1073 – 1088. DOI: 10.1002/fld.2726.

Kuznetsov, S. and Saprykina, Y., 2012. Secondary waves in coastal zone: physical mechanisms of formation and possible application for coastal protection. *Proceedings of the 33rd Conference on Coastal Engineering, Santander, Spain*.

Kweon, H.-M. and Goda, Y., 1996. A parametric model for random wave deformation by breaking on arbitrary beach profiles. *Proceedings of the 25th Conference on Coastal Engineering, Orlando, Florida*, pp. 261 – 274.

Le Méhauté, B., 1962. On non-saturated breakers and the wave run-up. *Proceedings of the 12th Conference on Coastal Engineering, Mexico City, Mexico*, pp. 77 – 92.

Lin, C. and Hwung, H. H., 1992. External and internal flow fields of plunging breakers. *Experiments in Fluids* 12 (4), pp. 229 – 237. DOI: 10.1007/BF00187300.

Lin, J. C. and Rockwell, D., 1995. Evolution of a quasi-steady breaking wave. *Journal of Fluid Mechanics* 302, 29–44. DOI: 10.1017/S0022112095003995.

# Bibliography


Lin, P. and Liu, P. L.-F., 1998. A numerical study of breaking waves in the surf zone. *Journal of Fluid Mechanics* 359, pp. 239 – 264. DOI: 10.1017/S002211209700846X.

Lippmann, T. C. and Holman, R. A., 1989. Quantification of sand bar morphology: A video technique based on wave dissipation. *Journal of Geophysical Research: Oceans* 94 (C1), pp. 995 – 1011. DOI: 10.1029/JC094iC01p00995.

Liu, X. and Duncan, J. H., 2003. The effects of surfactants on spilling breaking waves. *Nature* 421, pp. 520 – 523. DOI: 10.1038/nature01357.

Longo, S., Petti, M., and Losada, I. J., 2002. Turbulence in the swash and surf zones: a review. *Coastal Engineering* 45 (3–4). Surface and Swash Zone Mechanics, pp. 129 – 147. DOI: 10.1016/S0378-3839(02)00031-5.

Longuet-Higgins, M. S., Cartwright, D. E., and Smith, N. D., 1963. Observations of the directional spectrum of sea waves using the motions of a floating buoy. *Ocean Wave Spectra, proceedings of a conference, Easton, Maryland*. National Academy of Sciences. Prentice-Hall, pp. 111–136.

Lubin, P., Vincent, S., Abadie, S., and Caltagirone, J.-P., 2006. Three-dimensional Large Eddy Simulation of air entrainment under plunging breaking waves. *Coastal Engineering* 53 (8), pp. 631 – 655. DOI: 10.1016/j.coastaleng.2006.01.001.

Martins, K., Blenkinsopp, C. E., and Zang, J., 2016. Monitoring Individual Wave Characteristics in the Inner Surf with a 2-Dimensional Laser Scanner (LiDAR). *Journal of Sensors, 2016*, pp. 1 – 11. DOI: 10.1155/2016/7965431.

Martins, K., Bonneton, P., Frappart, F., Detandt, G., Bonneton, N., and Blenkinsopp, C. E., 2017a. High Frequency Field Measurements of an Undular Bore Using a 2D LiDAR Scanner. *Remote Sensing* 9 (5). DOI: 10.3390/rs9050462.

Martins, K., Blenkinsopp, C. E., Power, H. E., Bruder, B., Puleo, J. A., and Bergsma, E. W. J., 2017b. High-resolution monitoring of wave transformation in the surf zone using a LiDAR scanner array. *Coastal Engineering* 128, pp. 37 – 43. DOI: 10.1016/j.coastaleng.2017.07.007.

Martins, K., Blenkinsopp, C. E., Almar, R., and Zang, J., 2017d. The influence of swash-based reflection on surf zone hydrodynamics: a wave-by-wave approach. *Coastal Engineering* 122, pp. 27 – 43. DOI: 10.1016/j.coastaleng.2017.01.006.

Martins, K., Blenkinsopp, C. E., Deigaard, R., and Power, H. E., submitted. Energy dissipation in the inner surf zone: new insights from LiDAR-based roller geometry measurements. *Submitted to Journal of Geophysical Research: Oceans*.

Masselink, G., Ruju, A., Conley, D., Turner, I., Ruessink, G., Matias, A., Thompson, C., Castelle, B., Puleo, J., Citerone, V., and Wolters, G., 2016. Large-scale Barrier Dynamics Experiment II (*BARDEX II*): Experimental design, instrumentation, test program, and data set. *Coastal Engineering* 113, pp. 3 – 18. DOI: 10.1016/j.coastaleng.2015.07.009.

Masselink, G. and Puleo, J. A., 2006. Swash-zone morphodynamics. *Continental Shelf Research* 26 (5). Swash-Zone Processes, pp. 661 – 680. DOI: 10.1016/j.csr.2006.01.015.

Michallet, H., Barthélemy, E., Lammens, A., Marin, G., and Vaudelin, G., 2017. Bed motion under waves: plug and sheet flow observations. *Proceedings of the Conference on Coastal Dynamics, Helsingør, Denmark*.

Miche, A., 1951. Le pouvoir réfléchissant des ouvrages maritimes exposés à l'action de la houle. *Annales des Ponts et Chaussées* 121, pp. 285 – 319.

Miller, R. L., 1986. Role of vortices in surf zone prediction: sedimentation and wave forces. *The Society of Economic Paleontologists and Mineralogists (SEPM), Special Publications* 10, pp. 92 – 114.

Mizuguchi, M., 1984. Swash on a natural beach. *Proceedings of the 19th Conference on Coastal Engineering, Houston, Texas*, pp. 678 – 694.

Nadaoka, K, 1982. Laboratory measurements of velocity field structure in the surf zone by LDV. *Coastal Eng. Japan* 25, pp. 125 – 145.

Nairn, R., Roelvink, J. A., and Southgate, H., 1990. Transition zone width and implications for modeling surfzone hydrodynamics. *Proceedings of the 22nd Conference on Coastal Engineering, Delft, The Netherlands*, pp. 68 – 81.

National Oceanic and Atmospheric Administration (NOAA) Coastal Services Center, 2012. *Lidar 101: An Introduction to Lidar Technology, Data, and Applications*. Revised. Charleston, SC: NOAA Coastal Services Center.

Newman, J. N., 1977. *Marine Hydrodynamics*. Wei Cheng Cultural Enteroprise Company.

O'Hare, T. J. and Davies, A. G., 1993. Sand bar evolution beneath partially-standing waves: laboratory experiments and model simulations. *Continental Shelf Research* 13 (11), pp. 1149 – 1181. DOI: 10.1016/0278-4343(93)90047-2.

Padilla, E. M. and Alsina, J. M., 2017. Transfer and dissipation of energy during wave group propagation on a gentle beach slope. *Journal of Geophysical Research: Oceans* 122 (8), pp. 6773 – 6794. DOI: 10.1002/2017JC012703.

Park, H. S., Sim, J. S., Yoo, J., and Lee, D. Y., 2011. Breaking wave measurement using Terrestrial LIDAR: validation with field experiment on the Mallipo Beach. *Proceedings 11th International Coastal Symposium*. Vol. SI 64. Journal of Coastal Research, pp. 1718–1721.

Peregrine, D. H., 1983. Breaking Waves on Beaches. *Annual Review of Fluid Mechanics* 15 (1), pp. 149–178. DOI: 10.1146/annurev.fl.15.010183.001053.

Peregrine, D. H. and Svendsen, I. A., 1978. Spilling breakers, bores, and hydraulic jumps. *Proceedings of the 16th Conference on Coastal Engineering, Hamburg, Germany*, pp. 540 – 550.

Postacchini, M. and Brocchini, M., 2014. A wave-by-wave analysis for the evaluation of the breaking-wave celerity. *Applied Ocean Research* 46, pp. 15 – 27. DOI: 10.1016/j.apor.2014.01.005.

Power, H. E., Hughes, M. G., Aagaard, T., and Baldock, T. E., 2010. Nearshore wave height variation in unsaturated surf. *Journal of Geophysical Research: Oceans* 115 (C8). DOI: 10.1029/2009JC005758.

Power, H. E. and Baldock, T. E., 2017. Wave height distributions in the surf zone: implications for surf zone modelling. *Proceedings of the Conference on Coastal Dynamics, Helsingør, Denmark*.

Power, H. E., Hughes, M. G., and Baldock, T. E., 2015. A novel method for tracking individual waves in the surf zone. *Coastal Engineering* 98, pp. 26 – 30. DOI: 10.1016/j.coastaleng.2015.01.006.

Power, H. E., Nielsen, P., Hughes, M. G., Aagaard, T., and Baldock, T. E., 2016. Wave Height Distributions in the Surf Zone on Natural Beaches. *Journal of Coastal Research*, pp. 917 – 921. DOI: 10.2112/SI75-184.1.

Pujara, N., Liu, P. L.-F., and Yeh, H. H., 2015. An experimental study of the interaction of two successive solitary waves in the swash: A strongly interacting case and a weakly interacting case. *Coastal Engineering* 105, pp. 66 – 74. DOI: 10.1016/j.coastaleng.2015.07.011.

Puleo, J. A., Holland, K. T., Plant, N. G., Slinn, D. N., and Hanes, D. M., 2003. Fluid acceleration effects on suspended sediment transport in the swash zone. *Journal of Geophysical Research C: Oceans* 108 (11), pp. 14 – 1.

Puleo, J. A. and Butt, T., 2006. The first international workshop on swash-zone processes. *Continental Shelf Research* 26 (5), pp. 556 – 560. DOI: 10.1016/j.csr.2006.01.008.

Puleo, J. A. and Holland, K. T., 2001. Estimating swash zone friction coefficients on a sandy beach. *Coastal Engineering* 43 (1), pp. 25 – 40. DOI: 10.1016/S0378-3839(01)00004-7.

Puleo, J. A., Hutschenreuter, K., Cowan, P., Carey, W., Arford-Granholm, M., and McKenna, K. K., 2016. Delaware surf zone injuries and associated environmental conditions. *Natural Hazards* 81 (2), pp. 845 – 867. DOI: 10.1007/s11069-015-2108-9.

Qiao, H. and Duncan, J. H., 2001. Gentle spilling breakers: crest flow-field evolution. *Journal of Fluid Mechanics* 439, 57–85. DOI: 10.1017/S0022112001004207.

Radon, J., 1917. Über die Bestimmung von Funktionen durch ihre Integralwerte längs gewisser Mannigfaltigkeiten. *Akad. Wiss.* 69, pp. 262 – 277.

Raubenheimer, B., Guza, R. T., and Elgar, S., 1996. Wave transformation across the inner surf zone. *Journal of Geophysical Research: Oceans* 101 (C11), pp. 25589 – 25597.

Reineman, B. D., Lenain, L., Castel, D., and Melville, W. K., 2009. A Portable Airborne Scanning Lidar System for Ocean and Coastal Applications. *Journal of Atmospheric and Oceanic Technology* 26 (12), pp. 2626–2641. DOI: 10.1175/2009JTECHO703.1.

Reniers, A. J.H. M. and Battjes, J. A., 1997. A laboratory study of longshore currents over barred and non-barred beaches. *Coastal Engineering* 30 (1), pp. 1 – 21. DOI: 10.1016/S0378-3839(96)00033-6.

Rosati, J. D., Gingerich, K. J., and Kraus, N. C., 1990. *Superduck surf zone sand transport experiment*. Tech. rep. ADA225690, DTIC Document.

Ruessink, B. G., Miles, J. R., Feddersen, F., Guza, R. T., and Elgar, S., 2001. Modeling the alongshore current on barred beaches. *Journal of Geophysical Research: Oceans* 106 (C10), pp. 22451 – 22463. DOI: 10.1029/2000JC000766.

SICK, 2015. Laser Measurement Sensors of the LMS5xx Product Family - Operating Instructions.

Sakai, T., Mizutani, T., Tanaka, H., and Tada, Y., 1986. Vortex Formation in Plunging Breaker. *Proceedings of the 20th Conference on Coastal Engineering, Taipei, Taiwan*, pp. 711 – 723.

Sallenger, A. H., Howard, P. C., Fletcher, C. H., and Howd, P. A., 1983. A system for measuring bottom profile, waves and currents in the high-energy nearshore environment. *Marine Geology* 51 (1), pp. 63 – 76. DOI: 10.1016/0025-3227(83)90089-0.

Salmon, J. E., Holthuijsen, L. H., Zijlema, M., Vledder, G. P. van, and Pietrzak, J. D., 2015. Scaling depth-induced wave-breaking in two-dimensional spectral wave models. *Ocean Modelling* 87, pp. 30 – 47. DOI: 10.1016/j.ocemod.2014.12.011.

Sánchez-Badorrey, E., Losada, M. A., and Rodero, J., 2008. Sediment transport patterns in front of reflective structures under wind wave-dominated conditions. *Coastal Engineering* 55 (7–8), pp. 685 – 700. DOI: 10.1016/j.coastaleng.2007.11.005.

Schäffer, H. A., Madsen, P. A., and Deigaard, R., 1993. A Boussinesq model for waves breaking in shallow water. *Coastal Engineering* 20 (3–4), pp. 185 – 202. DOI: 10.1016/0378-3839(93)90001-O.

Seiwell, H. R., 1947. Investigation of underwater pressure records and simultaneous sea surface patterns. *Eos, Transactions American Geophysical Union* 28 (5), pp. 722 – 724. DOI: 10.1029/TR028i005p00722.

Sénéchal, N, Bonneton, P, and Dupuis, H, 2002. Field experiment on secondary wave generation on a barred beach and the consequent evolution of energy dissipation on the beach face. *Coastal Engineering* 46 (3), pp. 233 – 247. DOI: 10.1016/S0378-3839(02)00095-9.

Sénéchal, N., 2003. "Etude de la propagation des vagues au-dessus d'une bathymétrie complexe en zone de surf". PhD thesis. École doctorale sciences du vivant, géosciences, sciences de l'environnement, Université de Bordeaux I.

Sénéchal, N., Dupuis, H., Bonneton, P., Howa, H., and Pedreros, R., 2001. Observation of irregular wave transformation in the surf zone over a gently sloping sandy beach on the French Atlantic coastline. *Oceanologica Acta* 24 (6), pp. 545 – 556. DOI: 10.1016/S0399-1784(01)01171-9.

Sénéchal, N., Abadie, S., Gallagher, E., MacMahan, J., Masselink, G., Michallet, H., Reniers, A., Ruessink, G., Russell, P., Sous, D., Turner, I., Ardhuin, F., Bonneton, P., Bujan, S., Capo, S., Certain, R., Pedreros, R., and Garlan, T., 2011. The ECORS-Truc Vert'08 nearshore field experiment: presentation of a three-dimensional morphologic system in a macro-tidal environment during consecutive extreme storm conditions. *Ocean Dynamics* 61 (12), pp. 2073 – 2098. DOI: 10.1007/s10236-011-0472-x.

Seymour, R. and Duane, D., 1978. The nearshore sediment transport study, pp. 1555 – 1562.

Shand, T. D., Bailey, D. G., and Shand, R. D., 2012. Automated Detection of Breaking Wave Height Using an Optical Technique. *Journal of Coastal Research* 28, pp. 671 – 682. DOI: 10.2112/JCOASTRES-D-11-00105.1.

Short, A. D., 1975. Multiple offshore bars and standing waves. *Journal of Geophysical Research* 80 (27), pp. 3838 – 3840. DOI: 10.1029/JC080i027p03838.

Smullin, L. D. and Fiocco, G., 1962. Project Luna See. *Institute of Electrical and Electronics Engineering Proceedings* 50, pp. 1703–1704.

Soudarissanane, S., Lindenbergh, R., Menenti, M., and Teunissen, P., 2009. Incidence Angle Influence on the Quality of Terrestrial Laser Scanning Points. *Proceedings of Laserscanning '09, Paris, France*, pp. 83 – 88.

Sous, D., Petitjean, L., Bouchette, F., Rey, V., Meulé, S., Sabatier, F., and Martins, K., 2016. Field evidence of swash groundwater circulation in the microtidal rousty beach, France. *Advances in Water Resources* 97, pp. 144 –155. DOI: 10.1016/j.advwatres.2016.09.009.

Stive, M. J. F., 1980. Velocity and pressure field of spilling breakers. *Proceedings of the 17th Conference on Coastal Engineering, Sydney, Australia*, pp. 547 – 566.

Stive, M. J. F., 1984. Energy dissipation in waves breaking on gentle slopes. *Coastal Engineering* 8 (2), pp. 99 – 127. DOI: 10.1016/0378-3839(84)90007-3.

Stokes, G. G., 1847. "On the theory of oscillatory waves". *Trans. Camb. Philos. Soc. 8:441–55*. Vol. 1, Appendices and Suppl.

Streicher, M., Hofland, B., and Lindenbergh, R. C., 2013. Laser Ranging For Monitoring Water Waves In The New Deltares Delta Flume. *ISPRS Annals of Photogrammetry, Remote Sensing and Spatial Information Sciences* II-5/W2, pp. 271 – 276. DOI: 10.5194/isprsannals-II-5-W2-271-2013.

Suhayda, J. N., 1974. Standing waves on beaches. *Journal of Geophysical Research* 79 (21), pp. 3065 – 3071. DOI: 10.1029/JC079i021p03065.

Suhayda, J. N. and Pettigrew, N. R., 1977. Observations of wave height and wave celerity in the surf zone. *Journal of Geophysical Research* 82 (9), pp. 1419 – 1424. DOI: 10.1029/JC082i009p01419.

Sun, J., Burns, S. P., Vandemark, D., Donelan, M. A., Mahrt, L., Crawford, T. L., Herbers, T. H. C., Crescenti, G. H., and French, J. R., 2005. Measurement of Directional Wave Spectra Using Aircraft Laser Altimeters. *Journal of Atmospheric and Oceanic Technology* 22 (7), pp. 869–885. DOI: 10.1175/JTECH1729.1.

Svendsen, I. A., 1984a. Mass flux and undertow in a surf zone. *Coastal Engineering* 8 (4), pp. 347 – 365. DOI: 10.1016/0378-3839(84)90030-9.

Svendsen, I. A., 1984b. Wave heights and set-up in a surf zone. *Coastal Engineering* 8 (4), pp. 303 – 329. DOI: 10.1016/0378-3839(84)90028-0.

Svendsen, I. A., 1987. Analysis of surf zone turbulence. *Journal of Geophysical Research: Oceans* 92 (C5), pp. 5115 – 5124. DOI: 10.1029/JC092iC05p05115.

Svendsen, I. A., 2006. *Introduction to Nearshore Hydrodynamics*. Advanced series on ocean engineering. World Scientific.

Svendsen, I. A. and Buhr Hansen, J, 1976. Deformation up to breaking of periodic waves on a beach.

Svendsen, I. A., Madsen, P. A., and Buhr Hansen, J., 1978. Wave characteristics in the surf zone. *Proceedings of the 16th Conference on Coastal Engineering, Hamburg, Germany*, pp. 520 – 539.

Svendsen, I. A., Qin, W., and Ebersole, B. A., 2003. Modelling waves and currents at the LSTF and other laboratory facilities. *Coastal Engineering* 50 (1), pp. 19 – 45. DOI: 10.1016/S0378-3839(03)00077-2.

Tamari, S., Guerrero-Meza, V., Rifad, Y., Bravo-Inclán, L., and Sánchez-Chávez, J. J., 2016. Stage Monitoring in Turbid Reservoirs with an Inclined Terrestrial Near-Infrared Lidar. *Remote Sensing* 8 (12). DOI: 10.3390/rs8120999.

Thornton, E. B. and Guza, R. T., 1982. Energy saturation and phase speeds measured on a natural beach. *Journal of Geophysical Research: Oceans (1978 – 2012)* 87 (C12), pp. 9499 – 9508.

Thornton, E. B. and Guza, R. T., 1983. Transformation of wave height distribution. *Journal of Geophysical Research: Oceans* 88 (C10), pp. 5925 – 5938. DOI: 10.1029/JC088iC10p05925.

Thornton, E. B. and Guza, R. T., 1986. Surf zone longshore currents and random waves: Field data and models. *Journal of Physical Oceanography* 16 (7), pp. 1165 – 1178.

Ting, F. C. K. and Kirby, J. T., 1995. Dynamics of surf-zone turbulence in a strong plunging breaker. *Coastal Engineering* 24 (3), pp. 177 – 204. DOI: 10.1016/0378-3839(94)00036-W.

Ting, F. C. and Kirby, J. T., 1996. Dynamics of surf-zone turbulence in a spilling breaker. *Coastal Engineering* 27 (3), pp. 131 – 160. DOI: 10.1016/0378-3839(95)00037-2.

Tissier, M., Bonneton, P., Almar, R., Castelle, B., Bonneton, N., and Nahon, A., 2011. Field measurements and non-linear prediction of wave celerity in the surf zone. *European Journal of Mechanics - B/Fluids* 30 (6), pp. 635 – 641. DOI: 10.1016/j.euromechflu.2010.11.003.

Tissier, M., Bonneton, P., Michallet, H., and Ruessink, B. G., 2015. Infragravity-wave modulation of short-wave celerity in the surf zone. *Journal of Geophysical Research: Oceans* 120 (10), pp. 6799 – 6814. DOI: 10.1002/2015JC010708.

Tissier, M., Bonneton, P., and Ruessink, G., 2017. Infragravity waves and bore merging. *Proceedings of the Conference on Coastal Dynamics, Helsingør, Denmark*.

Turner, I. L., Russell, P. E., and Butt, T., 2008. Measurement of wave-by-wave bed-levels in the swash zone. *Coastal Engineering* 55 (12), pp. 1237 – 1242. DOI: 10.1016/j.coastaleng.2008.09.009.

Vousdoukas, M. I., Kirupakaramoorthy, T., Oumeraci, H., Torre, M. de la, Wübbold, F., Wagner, B., and Schimmels, S., 2014. The role of combined laser scanning and video techniques in monitoring wave-by-wave swash zone processes. *Coastal Engineering* 83, pp. 150 – 165. DOI: 10.1016/j.coastaleng.2013.10.013.

Vrbancich, J., Lieff, W., and Hacker, J., 2011. Demonstration of Two Portable Scanning LiDAR Systems Flown at Low-Altitude for Investigating Coastal Sea Surface Topography. *Remote Sensing* 3 (9), pp. 1983 – 2001. DOI: 10.3390/rs3091983.

Vries, S. de, Hill, D. F., Schipper, M. A. de, and Stive, M. J. F., 2011. Remote sensing of surf zone waves using stereo imaging. *Coastal Engineering* 58 (3), pp. 239 – 250. DOI: 10.1016/j.coastaleng.2010.10.004.

Walstra, D. J. R., Mocke, G. P., and Smit, F., 1996. Roller contribution as inferred from inverse modelling techniques. *Proceedings of the 25th Conference on Coastal Engineering, Orlando, Florida*, pp. 1205 – 1218.

Wang, Z., Yang, J., and Stern, F., 2016. High-fidelity simulations of bubble, droplet and spray formation in breaking waves. *Journal of Fluid Mechanics* 792, pp. 307 – 327. DOI: 10.1017/jfm.2016.87.

White, F. M., 2003. *Fluid Mechanics*. McGraw-Hill international editions. McGraw-Hill.

Wright, L. D and Short, A. D, 1984. Morphodynamic variability of surf zones and beaches: A synthesis. *Marine Geology* 56 (1), pp. 93 – 118. DOI: 10.1016/0025-3227(84)90008-2.

Wübbold, F, Vousdoukas, M., Hentschel, M, and Wagner, B, 2012. Towards Autonomous Coastal Monitoring using 3D Laser Range Scanners and Camera Vision. *Proceedings of the 33rd Conference on Coastal Engineering, Santander, Spain*.

Yoo, J., Fritz, H. M., Haas, K. A., Work, P. A., and Barnes, C. F., 2011. Depth inversion in the surf zone with inclusion of wave nonlinearity using video-derived celerity. *Journal of Waterway, Port, Coastal, and Ocean Engineering* 137 (2), pp. 95 – 106. DOI: 10.1061/(ASCE)WW.1943-5460.0000068.

Zhang, C., Chen, Y., Zheng, J., and Demirbilek, Z., 2014. Variation of wave roller slope in the surf zone. *Proceedings of the 34th Conference on Coastal Engineering, Seoul, Korea*. DOI: 10.9753/icce.v34.waves.12.

Zhang, C., Zhang, Q., Zheng, J., and Demirbilek, Z., 2017. Parameterization of nearshore wave front slope. *Coastal Engineering* 127, pp. 80 – 87. DOI: http://dx.doi.org/10.1016/j.coastaleng.2017.06.008.

# Appendix A

## Published material not used for the thesis: "High frequency field measurements of an undular bore using a 2D LiDAR scanner"

# Appendix A.



Kévin Martins*, Philippe Bonneton, Frédéric Frappart, Guillaume Detandt, Natalie Bonneton and Chris E. Blenkinsopp, "High frequency field measurements of an undular bore using a 2D LiDAR scanner", Remote Sensing, 2017.
doi: 10.3390/rs9050462

## Abstract

The secondary wave field associated with undular tidal bores (known as whelps) has been barely studied in field conditions: the wave field can be strongly non-hydrostatic, and the turbidity is generally high. In situ measurements based on pressure or acoustic signals can therefore be limited or inadequate. The intermittent nature of this process in field and the complications encountered in the downscaling to laboratory conditions also render its study difficult. Here, we present a new methodology based on LiDAR technology to provide high spatial and temporal resolution measurements of the free surface of an undular tidal bore. A wave-by-wave analysis is performed on the whelps, and comparisons between LiDAR, acoustic and pressure-derived measurements are used to quantify the non-hydrostatic nature of this phenomenon. A correction based on linear wave theory applied on individual wave properties improves the results from the pressure sensor (*RMSE* of 0.19 m against 0.38 m), however, more robust data is obtained from an upwards-looking acoustic sensor despite high turbidity during the passage of the whelps (*RMSE* of 0.05 m). Finally, the LiDAR scanner provides the unique possibility to study the wave geometry: the distribution of measured wave height, period, celerity, steepness and wavelength are presented. It is found that the highest wave from the whelps can be steeper than the bore front, explaining why breaking events are sometimes observed in the secondary wave field of undular tidal bores.

## Declaration concerning the article used for this Chapter:

| | |
|---|---|
| Title | High frequency field measurements of an undular bore using a 2D LiDAR scanner |
| Status | Published and available in Open Access in Remote Sensing (MDPI) |
| Details | Kévin Martins*, Philippe Bonneton, Frédéric Frappart, Guillaume Detandt, Natalie Bonneton and Chris E. Blenkinsopp, "High frequency field measurements of an undular bore using a 2D LiDAR scanner", Remote Sensing, 2017.<br>DOI: 10.3390/rs9050462 |
| Contribution from the authors | K. Martins: Collection/Processing/Analysis of the LiDAR data; Manuscript (60%)<br>P. Bonneton: Design of the experiments; Help with the analysis; Edited drafts of manuscript (15%)<br>G. Detandt: Design; deployment of in situ instruments and assistance with the LiDAR (10%)<br>C. E. Blenkinsopp: Edited drafts of manuscript (10%)<br>N. Bonneton, F. Frappart: Design of the experiments; (5%) |
| Statement | This paper reports on original research I conducted during the period of my Higher Degree by Research candidature. |
| Date and Signature | |

# Appendix A.

## Preamble

The data presented in this Appendix were collected during a field experiment performed on the Garonne River at Podensac, France, in collaboration with the French laboratory EPOC (Talence, France). The main objective was to perform surface elevation measurements of an undular tidal bore with a 2D LiDAR scanner. This natural phenomenon is a highly non-hydrostatic process, meaning that classic deployments of pressure sensor cannot be used to retrieve the surface elevation. In this study, the non-hydrostatic character of the undular tidal bore is quantified.

Although not directly linked to surf zone waves, the secondary wave field (the so-called whelps) that propagates behind the main surge of the tidal bore represents an interesting case for a LiDAR deployment. In the absence of wave breaking, but in a turbid environment, it is unsure how the scanner can perform. If the surface elevation can be measured, valuable spatial information such as complete wave profiles can be obtained from the scanner. The following research objectives/questions were set for the present study:

- Adapt the LiDAR methodology applied in beach and surf zone deployments to study an undular tidal bore and the whelps generated along its propagation
- Make sure that we correctly detect the surface elevation and that there is no signal penetration in the water column, as sometimes observed in the swash zone in the absence of foam
- Study the non-hydrostatic character of the whelps

## A.1 Introduction

For coastal and estuarine applications, the ability to accurately measure the surface elevation of long waves such as tides, tsunamis or infragravity waves is paramount. A commonly used approach is to deploy underwater pressure transducers on the seabed and reconstruct the surface elevation using the hydrostatic assumption. However, with the intensification of non-linear interactions as the wave propagates into shallow water, the wave shape becomes more asymmetrical and the front steepens, potentially leading to the formation of dispersive shocks, also called undular bores (e.g. Vignoli et al., 2003; Madsen et al., 2008; Tissier et al., 2011; Bonneton et al., 2016). The hydrostatic assumption is no longer valid for these highly non-linear processes (Bonneton et al., 2015; Frappart et al., 2016). To monitor undular bores in the field, a new approach to obtain high-frequency direct measurements of the wave surface elevation is required.

The use of LiDAR technology has recently gained much interest for nearshore field studies (e.g. Blenkinsopp et al., 2010; Martins et al., 2016; Brodie et al., 2015). When deployed on beaches, LiDAR scanners use the time of flight of a light beam to directly measure the water surface or beachface evolution at high spatial and temporal resolution. In contrast to other remote sensing tools (e.g. RaDAR, video camera), 2D scanners are capable of accurately measuring surf zone wave geometry. In freshwater conditions where the presence of foam or air bubbles (required to scatter the incident laser) is scarcer, single point LiDAR has application for steady water body monitoring (Tamari and Guerrero-Meza, 2016) as well as for more dynamical systems such as flash floods (Tamari et al., 2016). In laboratory conditions, Martins et al. (2017d) demonstrated the potential of 2D LiDAR to describe the geometry of breaking waves at prototype scale. This study indicated substantial differences between LiDAR and pressure-derived free-surface measurements at the individual wave scale, highlighting the limitations of linear wave theory in highly non-linear conditions.

Despite the short time scale that characterizes their passage, undular bores have very distinctive phases that provide highly varying conditions for detection using a LiDAR scanner. Prior to the bore passage, the river water surface is glassy and steady with no significant roughness or surface bubbles to scatter the incident laser from the LiDAR. Although tidal bores generally generate and propagate in quite turbid environments (Bonneton et al., 2016), there may not always be sufficient particle density at the surface to reflect the infra-red laser. Hence, the laser will often penetrate the water column and be scattered by particles floating at some unknown depth below the surface which can vary with location (Tyndall effect, e.g. Tamari and Guerrero-Meza, 2016). This issue has also been observed in laboratory studies using the same scanner deployed in the present study (LMS511 SiCK commercial scanners, Streicher et al., 2013). Signal penetration was thought to be responsible for the bent edges of the LiDAR scanning profiles obtained for increasing grazing angles (Streicher et al., 2013). Although Streicher et al. (2013) suspected another underlying reason for the observed curved surface elevation (see Appendix), they successfully applied an empirical correction based on an estimation of the distance of penetration. Despite obtaining

a flat surface in the wave flume, they noticed an overestimation of the signal penetration distance, suspecting that the bending could also be associated with another unknown phenomenon. After the passage of the wave, the turbidity significantly increases due to the mixing occurring in the water column (Tessier et al., 2016). With the increased roughness at the water surface and potential presence of air bubbles in case of wave breaking, this changes the ability of the surface to scatter light back to the Lidar.

In this paper, the methodology to obtain 2D profiles of the undular tidal bore with a LiDAR scanner is presented. The field experiment is first described in Section 2; the procedure to obtain the surface elevation at hundreds of points is also presented. Section 3 presents the comparison of the LiDAR measurements at the nadir (directly below the LiDAR) with in situ acoustic and pressure measurements. A particular consideration is given to the non-hydrostatic nature of the tidal bore phenomenon. The LiDAR scanner provides a unique opportunity to study the geometrical shape of the front and secondary waves; this section also aims at presenting the different physical quantities than can be extracted from the LiDAR dataset. Finally, a correction based on linear wave theory at the individual wave scale is attempted on the pressure signal to correct for signal attenuation in the water column.

## A.2 Material and Methods

### A.2.1 Field experiments description

A 4-day experiment was conducted between the 16$^{th}$ and 19$^{th}$ of October 2016 on the Garonne River, at Podensac (see Figure A.1). The Garonne River meets with the Dordogne River to form the Gironde estuary, where the so-called 'mascaret' tidal bore forms (Bonneton et al., 2011). This part of the Bay of Biscay coastline is a macrotidal environment with the tidal range at the field site in the range 5.80 to 6 m over the experiment period. Figure A.2 shows the time-variation of the water depth over the whole experiment period, with the period of primary interest for this paper highlighted. For that particular tide (number 5), the Froude number $F_r$ was estimated to 1.21 (Bonneton et al., 2015).

To measure the time-varying free surface during the passage of the tidal bore, a SICK LMS511 commercial 2D LiDAR scanner was cantilevered over the side of the field site platform (see Figure A.3), extending 1.5 m from the safety railing. The typical height of the scanner above the mean water level prior to the passage of the tidal bore was 8 m. A recent description of the working principle of the LiDAR can be found in Tamari and Guerrero-Meza (2016). A description of the 2D scanner used in the present study is provided in Martins et al. (2016). Data was collected at a sampling rate of 25 Hz, with an angular resolution of 0.1667°. This corresponded to a spatial resolution during passage of the undular bores ranging from 0.024 m at nadir to 0.05 m at the outer edges of the LiDAR scans.

On the same cross-section line as the LiDAR and at a distance of approximately 1.3 m from it, a Nortek Signature 1000 kHz current profiler was deployed together with a pressure transducer (10 Hz, Ocean Sensor Systems). To reconstruct the time-varying surface

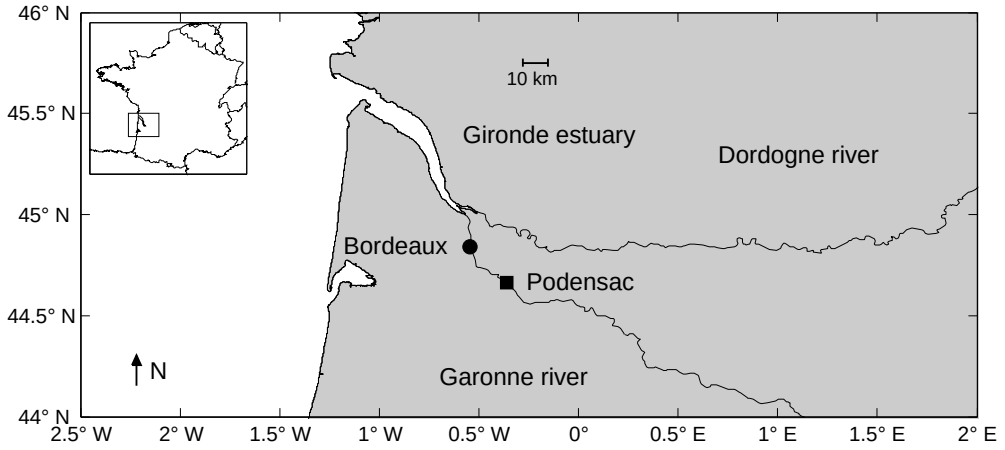


Figure A.1: Location map of the Gironde estuary in the Bay of Biscay. The field site of Podensac is shown as a black square.

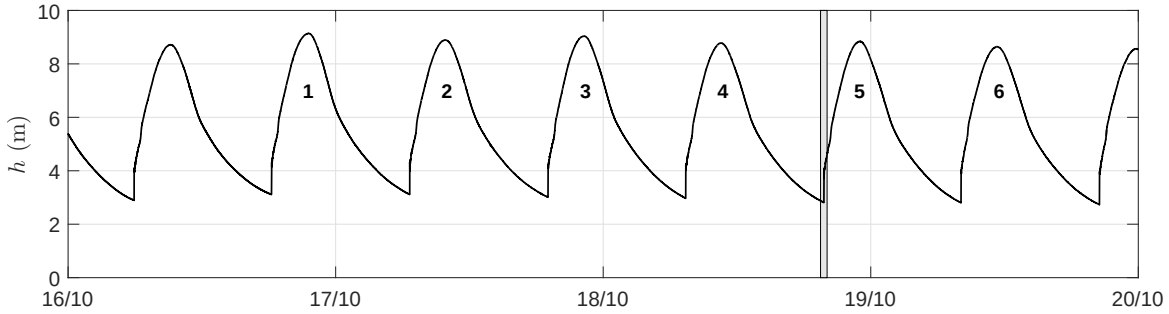


Figure A.2: Water depth evolution over the course of the experiments. The water depth was derived from the pressure measurements assuming hydrostatic pressure (Equation A.1). The present paper uses mainly data from the tide monitored number 5, which is highlighted by the grey region.

elevation from the measured pressure signal, the hydrostatic relation has been used as this provides the opportunity to study the non-hydrostatic nature of the mascaret:

$$h = (p - p_{atm})/\rho g \tag{A.1}$$

where $h$ is the water depth assuming hydrostatic pressure, $p$ the measured pressure, $\rho$ the water density, $g$ gravity and $p_{atm}$ the atmospheric pressure. Additionally, an Optical Backscatter Sensor (0.1 Hz, Campbell) was deployed to monitor the water turbidity at the bed. The Signature 1000 kHz also collects altimeter data using its vertical beam (hereafter referred to as the acoustic sensor, sampled at 8 Hz). Three different methods to detect the water surface location were therefore used and are compared in this paper: direct measurement by laser from the LiDAR, by an acoustic signal from the bottom-mounted Signature 1000 kHz and reconstructed from the pressure measurements at the bottom.

An undular bore is made up of a primary wave, i.e., a mean jump, between two different states of velocity and water depth, on which is superimposed secondary waves known as whelps when referring to a tidal bore. Bonneton et al. (2011, 2015) showed that the tidal bore mean jump is nearly uniform over the river cross section and that its intensity (or its Froude number) is mainly controlled by the local dimensionless tidal range $T_r/D_1$, where $T_r$

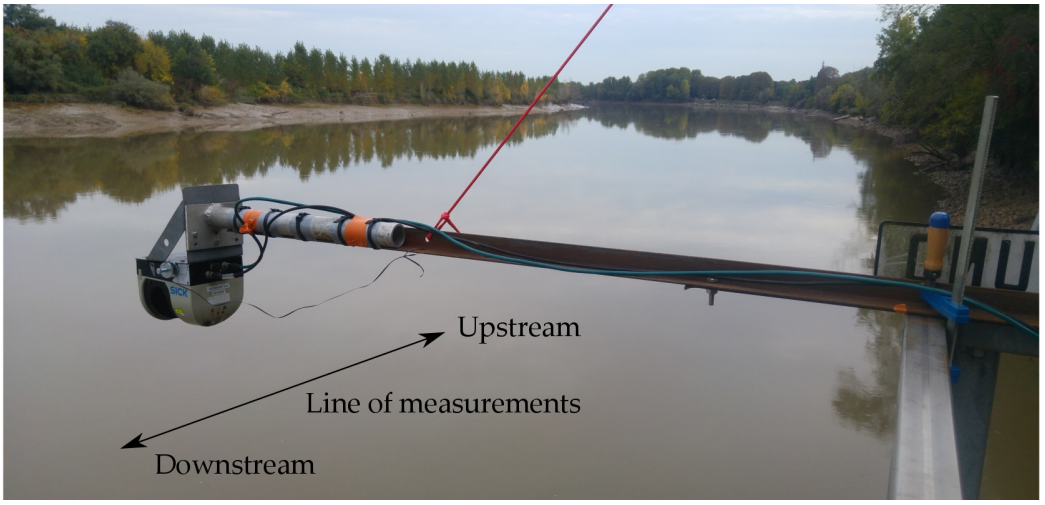


Figure A.3: Photograph of the LiDAR scanner deployment. The scanner was cantilevered over the platform edge, at a distance of approximately 1.5 m. The scanning line was approximately 11.5 m from the river bank at low tide.

is the tidal range and $D_1$ the cross-sectionally averaged water depth. By contrast, a strong variability along the river cross section of the secondary wave field can be observed, with whelp amplitude generally larger at the banks than in the mid-channel (Bonneton et al., 2011, 2015). This variability is due to the interaction between the secondary wave field and the gently sloping alluvial river banks. In the present paper we analyse the non-breaking wave field close to the bank. Despite being relatively close to the river side no breaking was observed below the LiDAR during the experiments.

### A.2.2 Processing of the LiDAR data

To track the tidal bore and its properties, the LiDAR measurements were first rotated to correct for the roll angle introduced at deployment. This was done by matching the data prior to the tidal bore passage to a horizontal free surface. The measurements are then interpolated onto a 0.1 m regular along-stream grid. When carrying out this process it was found that the mean free surface was slightly bent toward the edges of the scanning range, see Appendix. The methodology of Streicher et al. (2013) to correct the bent edges was applied to a wave dataset by Damiani and Valentini (2014), but higher frequency waves seemed to be introduced in the surface elevation timeseries, showing that it might not be appropriate. As similar profile distortion was observed in the present study, some baseline measurements were performed on a solid horizontal surface with the same ranging distance to investigate this phenomenon for a case without the possibility of any signal penetration (see Appendix). The results showed that the LiDAR profile curvature was entirely due to the deformation of the light beam on the surface for high incident angles, rather than signal penetration in the water column.

Based on these results, the free surface prior to the passage of the bore was extracted using the methodology described in the Appendix which uses the distinct peaks in elevation point distribution (corresponding to the 'real' surface and sub-surface). Just after the passage of the tidal bore, no filter was applied to the measurements to correct for curvature

or signal penetration. This is justified by the fact that the tidal bore mixes the water column (Tessier et al., 2016), hence greatly increasing the turbidity and the surface roughness, which allows for more consistent detection of the 'real' free surface. In fact, no rapid fluctuations in the surface timeseries were observed immediately after its passage, see Figure A.11 for illustration. Note that the curvature only induces changes of 0.02 m over a distance of 16 m (1.5% of the first wave height), and does not affect the local wave properties (wave height $H$ and celerity $c$).

## A.3 Results

### A.3.1 Comparison with in situ sensors

The water depth measured by the LiDAR scanner at the nadir was compared with the water depth derived from the pressure and acoustic sensors. Figure A.4a shows the comparison with the pressure sensor and illustrates the non-hydrostatic nature of the tidal bore secondary wave field. The discussion here focuses on tide number 5 (see Figure A.2), which provided the best LiDAR dataset: high tidal coefficient and low humidity, which minimizes signal losses. Indeed, due to the transient nature of the tidal bore and the innovative character of the experiments, the preceding tides were used to optimize the data collection process for tide 5. For instance, the early morning tides did not allow for the collection of usable data, due to strong fog conditions. It is worth noting that the present dataset was obtained without any atmospheric filter in the data collection software (SOPAS Engineering Tool©, SICK AG).

It is observed in Figure A.4a that except for the mean jump of the tidal bore, the signal reconstructed from the pressure using the hydrostatic assumption largely underestimates the wave amplitudes, regardless of their characteristics (wave height or wave length). For this comparison, a Root mean square error ($RMSE$) of 0.1 m is obtained, with a correlation coefficient $r = 0.93$ and scatter index ($SI$) of 0.03. By contrast, the agreement between acoustic-derived water depth and the LiDAR data, which both directly measure the time-varying water surface elevation is very good ($RMSE = 0.05$ m, $r = 0.93$ and $SI = 0.01$), see Figure A.4b. Despite the increasing turbidity levels as the tidal bore propagates, the surface is still accurately detected by the bottom-mounted sensor. A slight overestimation of the water depth measured by the acoustic sensor seems to occur after the second wave group passage. As the two measurements (LiDAR and acoustic) give very similar results far behind the bore front, this is mainly explained by an underestimation of the acoustic wave celerity when the turbidity is at its maximum in the water column, just a few minutes after its passage (Tessier et al., 2016).

To further illustrate the non-hydrostatic nature of the bores, a wave-by-wave analysis was performed on the three datasets: individual waves were extracted by detecting wave crests and surrounding troughs (Martins et al., 2016). The wave height $H$ is defined as the vertical distance between crest and preceding trough while the wave period is defined as the time elapsed between the passages of the two surrounding troughs at the nadir of the LiDAR measurements. Figure A.5 shows the comparison of $H$ and $T$ extracted from

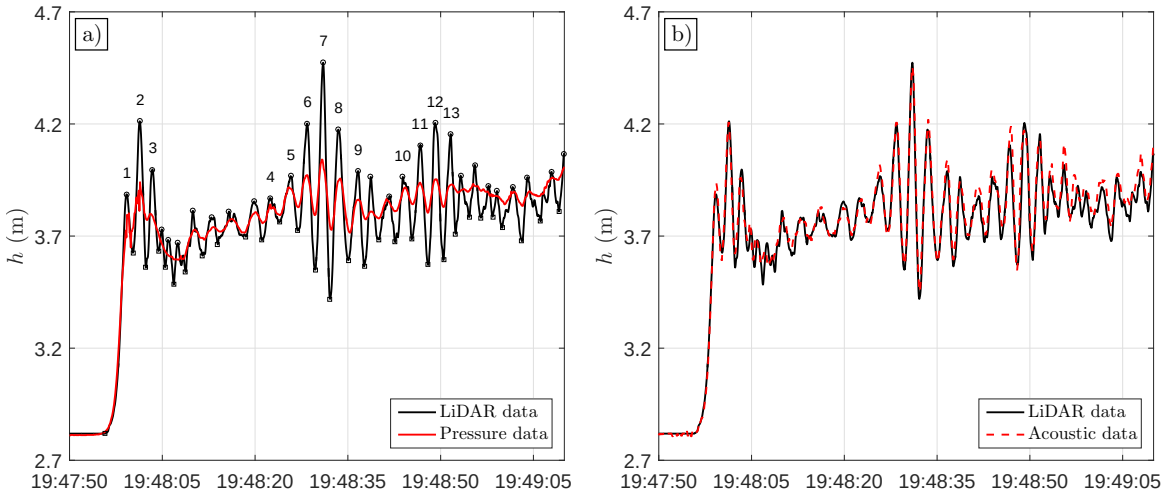


Figure A.4: Comparison of the measured water depths by the pressure, acoustic and LiDAR sensors at the nadir. Panel a) shows the pressure-derived water depth timeseries computed with the hydrostatic assumption (Equation A.1) from pressure data along with the LiDAR data for the tide number 5 (grey shaded region in panel Figure A.3). Panel b) compares the acoustic-derived water depth with the LiDAR data for the same time period.

the three datasets, for the thirteen waves numbered in Figure A.4a. It is observed that differences up to 0.67 m (75% of $H$) exist for the 6th wave between the pressure-derived and LiDAR datasets. Only small discrepancies (error of 8% of $H$) are observed for the primary wave front height. This is thought to be because the first wave front is effectively a surge where the mean water level suddenly increases and so is mostly captured using a hydrostatic assumption, however this approach is unable to capture the more rapid surface fluctuations in the secondary wave field. Better agreement is found for $H$ between the acoustic-derived and LiDAR datasets (*RMSE* of 0.05 m against 0.38 m for the pressure data, see Figure A.5). Similarly, a better fit between acoustic and LiDAR datasets than between pressure-derived and LiDAR is observed for the wave periods. This is mainly explained by the flatter troughs in the hydrostatic signal, which can delay the detection of the minimum, defining the wave trough. The relatively good fit between pressure-derived and LiDAR wave periods suggest that the pressure peaks at the river bottom coincide to those at the free surface.

### A.3.2 Spatial structure of the tidal bore

Individual waves and their properties were tracked using the wave-by-wave approach described in Martins et al. (2017d). The methodology described in Section 3.1 to extract wave crests can be applied at different along stream positions, which enables the tracking of a wave and its properties in time and space. At every position of the 0.1 m regular grid, the wave crests were detected in the surface elevation timeseries using this procedure, allowing geometrical properties such as wave height $H$ and wave period $T$ to be studied in the direction of propagation (along-stream direction). Figure A.6 displays the obtained wave tracks on a timestack of surface elevation profiles measured by the LiDAR. Because the spatial information of the waves is available at the same time as the temporal characteristics,

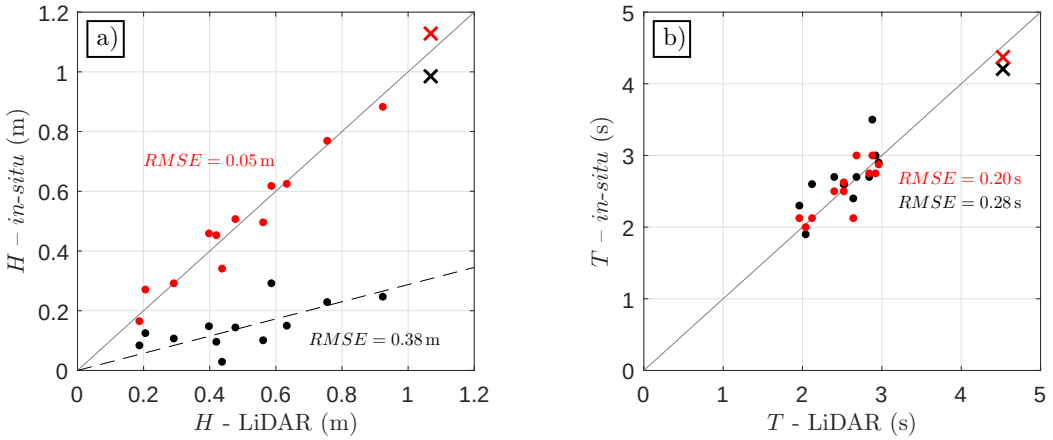


Figure A.5: Comparison of the 13 individual wave properties extracted from the LiDAR (Figure A.3a) with in situ pressure-derived data (black dots) and acoustic sensor data (red dots). The root-mean square errors between the datasets are directly shown in the plots, in the corresponding colour. Panel a) shows the individual wave height $H$. For indication, the linear regression fit forced to pass in (0,0) performed on the secondary waves is shown for the pressure-derived data (slope of 0.28). Panel b) shows in the individual wave period $T$. The bore front properties are shown as a cross. The 1:1 lines are shown as gray line.

Table A.1: Mean ( $\bar{.}$ ) and standard deviation ($\sigma(.)$) values of every tracked individual wave from Figure A.4a. The wavelength $L$ is only estimated for wave crests located in the region $x = -2$ to 2 m, since the wave trough can sometimes be out of the monitored area otherwise.

| Properties | 1 | 2 | 3 | 4 | 5 | 6 | 7 | 8 | 9 | 10 | 11 | 12 | 13 |
|---|---|---|---|---|---|---|---|---|---|---|---|---|---|
| $\bar{c}$ (m/s) | 5.62 | 6.07 | 5.84 | 6.27 | 6.22 | 6.17 | 6.18 | 6.37 | 5.76 | 5.75 | 6.11 | 5.76 | 5.74 |
| $\sigma(c)$ (m/s) | 0.33 | 0.10 | 0.48 | 0.32 | 0.82 | 0.12 | 0.04 | 0.08 | 0.15 | 0.62 | 0.41 | 0.17 | 0.19 |
| $\bar{H}$ (m) | 1.04 | 0.52 | 0.22 | 0.17 | 0.24 | 0.42 | 0.74 | 0.62 | 0.42 | 0.27 | 0.40 | 0.49 | 0.36 |
| $\sigma(H)$ (m) | 0.03 | 0.05 | 0.09 | 0.04 | 0.05 | 0.06 | 0.08 | 0.11 | 0.06 | 0.06 | 0.05 | 0.07 | 0.10 |
| $\bar{T}$ (s) | 2.90 | 2.15 | 2.51 | 2.86 | 2.96 | 2.61 | 2.43 | 3.06 | 2.39 | 2.80 | 2.25 | 2.47 | 2.08 |
| $\sigma(T)$ (s) | 0.24 | 0.03 | 0.47 | 0.03 | 0.04 | 0.03 | 0.04 | 0.07 | 0.07 | 0.29 | 0.18 | 0.05 | 0.06 |
| $\bar{\theta}$ (°) | 6.37 | 5.54 | 2.85 | 1.21 | 1.51 | 3.39 | 7.57 | 5.80 | 3.83 | 2.01 | 4.01 | 3.73 | 3.66 |
| $\sigma(\theta)$ (°) | 0.35 | 0.75 | 1.41 | 0.41 | 0.49 | 0.92 | 1.37 | 1.93 | 1.37 | 1.93 | 0.95 | 0.84 | 1.01 |
| $\bar{L}$ (m) | - | 12.3 | 17.9 | 16.6 | 16.8 | 15.3 | 14.2 | 17.4 | 13.1 | 15.4 | 16.5 | 12.8 | 10.8 |
| $\sigma(L)$ (m) | - | 0.78 | 0.83 | 1.20 | 0.88 | 1.27 | 0.49 | 0.76 | 1.68 | 0.04 | 1.53 | 0.38 | 0.58 |

the wave celerity can also be directly estimated. Table A.1 presents the averaged individual wave properties and the standard deviation for every wave tracked in Figure A.6. An interesting observation lies in the steep front observed in the highest wave of the first group (number 7). In the present conditions, this wave is actually steeper than the bore front, and this may explain why breaking sometimes occurs behind the tidal bore, while the front is not breaking.

Figure A.7 shows the evolving shape of the tidal bore front and the following wave (1 and 2 in Figure A.4a). The tidal front wave is found to steepen just in front of the LiDAR platform (Figure A.6a); this process is accompanied by a slight increase of the wave height (Figure A.7b) and a decrease in local wave celerity (not shown). This is likely to be due to a shoaling effect caused by decreasing water depth under the platform, as measured by depth

soundings obtained around the platform. The second wave is affected by the presence of a scattered wave, probably generated from the first wave either from the platform or from the river banks (reflection), which locally affects both the wave steepness and the wave height. When the crest of the scattered wave interferes with the crest of the second wave, the local wave height is enhanced (see at nadir, Figure A.7b and A.7d) and when the scattered wave trough interferes with the crest, $H$ decreases locally. This appears in the local wave steepness (Figure A.7a) as rapid fluctuations of the order of 2-2.5°. This phenomenon is of the same nature as observed in Martins et al. (2017d), where it was shown that reflected waves caused intra-wave variability of individual wave properties in the surf zone of a prototype-scale laboratory beach. The wave profile evolution displayed in Figure A.7d further illustrates this process of interaction with the steeper, larger wave detected around the nadir. In contrast, the tidal bore front wave shape is more stable (Figure A.7c).

This interaction between scattered waves and whelps is also observable in the individual properties of the secondary waves. Figure A.8 shows the along-stream evolution of the individual wave height from tracked waves number 5, 6 and 7 (Figure A.4a). Since

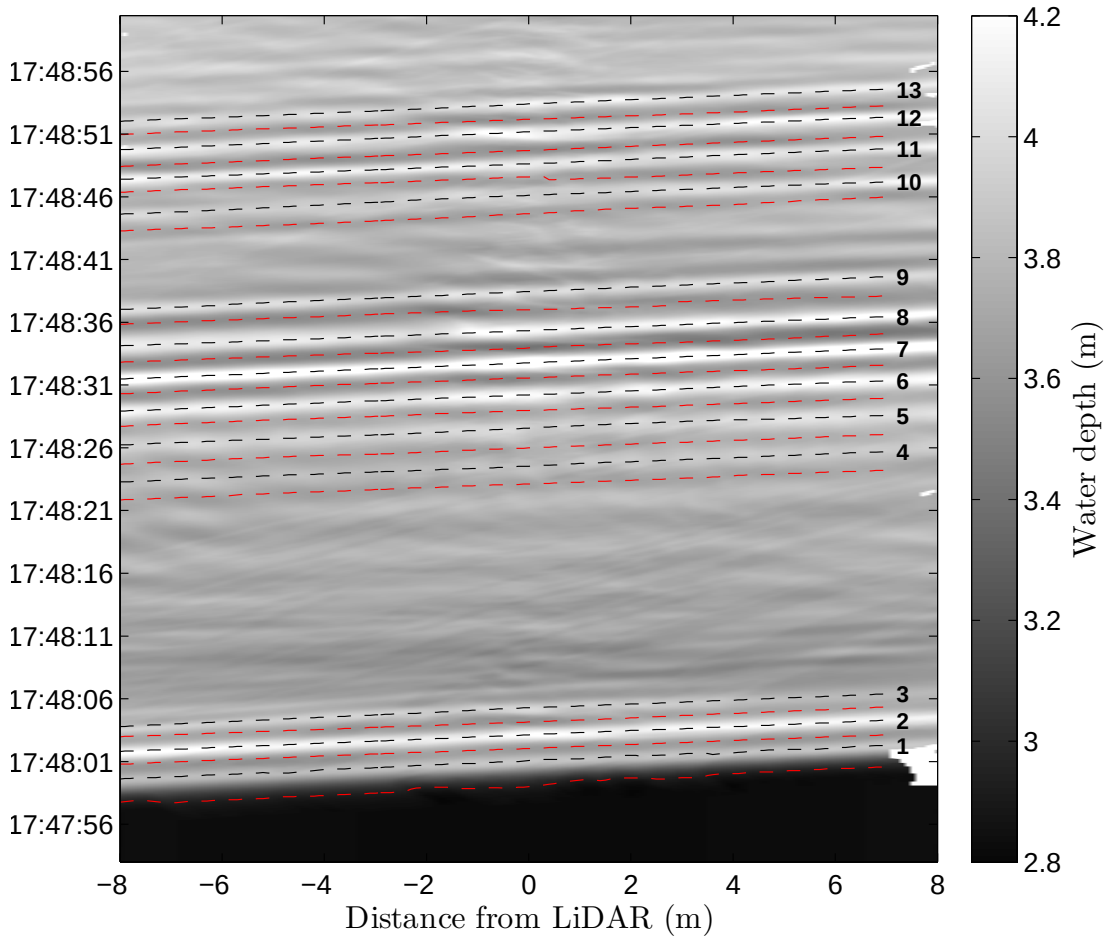


Figure A.6: Timestack of the water depth measured by the LiDAR scanner during the tide number 5 (grey region in Figure A.3). The individual wave crest and trough tracks are shown as black and red dashed lines respectively. The same numbering as in Figure A.4 is shown.

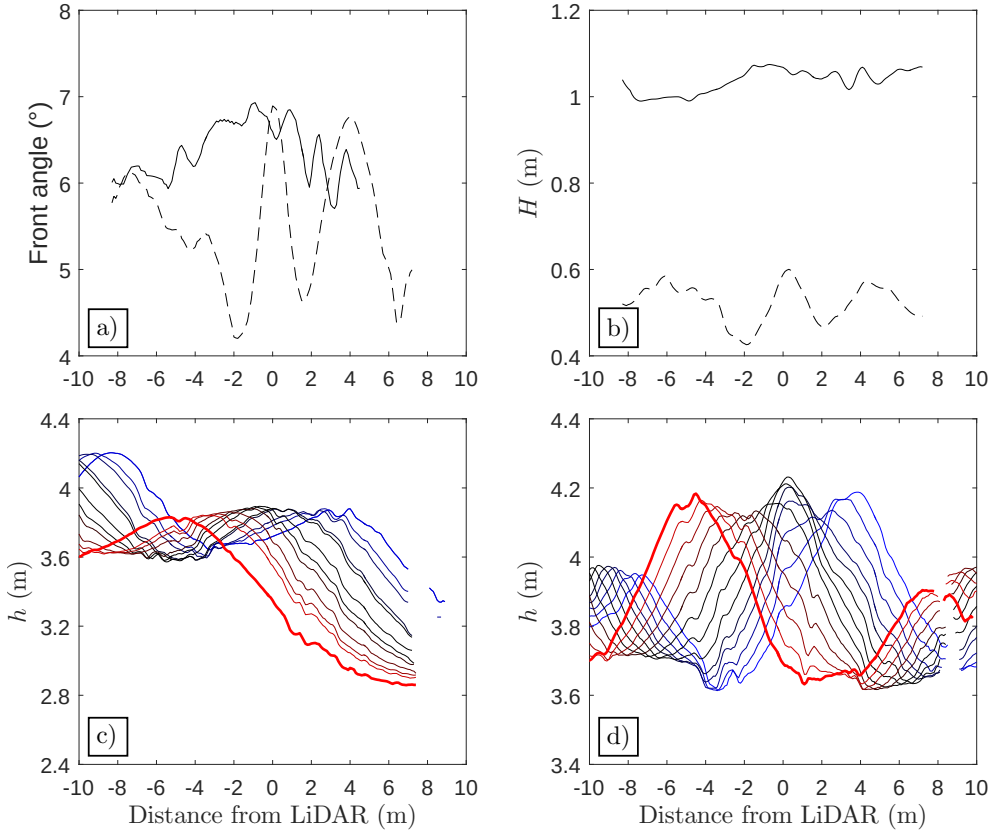


Figure A.7: Spatial evolution of waves number 1 and 2 (see Figure A.4). Panels a) and b) show the wave front angle and height respectively for wave 1 (black continuous line) and wave 2 (black dashed line). Panel c) and d) show the wave propagation of wave 1 and 2 respectively: the wave profile is shown when the crest is detected at 0.7 m intervals. For clarity, each profile is drawn in a different colour: wave profiles are first shown as thick red lines (first profile shown as thick red lines), and evolve towards black at the nadir, and finally blue after having passed under the LiDAR. Note that the tidal bore propagates from left to right (axis positive in the upstream direction).

the waves are increasing in size, the paths of scattered wave crests and troughs are clearly observed. These interactions can also be seen in the timestack of Figure A.6 with local fluctuations of the surface elevation. They have the effect of making the individual wave height and period fluctuate due to the propagation of scattered wave crests and troughs (Table A.1).

## A.4 Discussion

A tidal bore is a highly non-linear wave accompanied by secondary waves that cannot be studied using the assumption of a hydrostatic pressure distribution (Figure A.4a, A.5a). Depth attenuation of the pressure signal is typically corrected in datasets from coastal environments such as the surf zone (see e.g. Bishop and Donelan, 1987). In practice, the correction derived from linear theory is applied to each frequency of the surface elevation Fourier spectrum (denoted by $\widehat{.}$):

$$\widehat{\eta} = K_f \widehat{\eta_{hyd}} \tag{A.2}$$

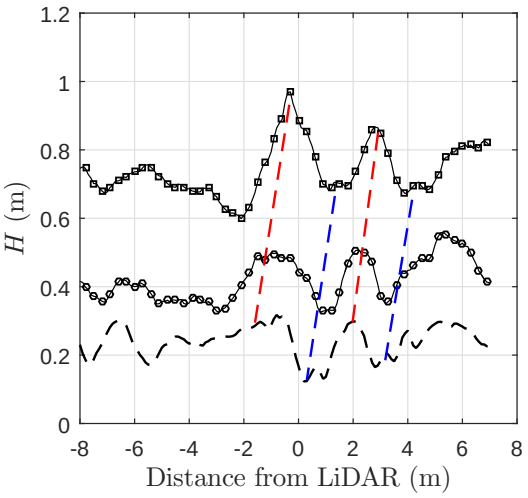


Figure A.8: Along-stream evolution of the individual wave height of wave number 5 (dashed black line), 6 (black line and circles) and 7 (black line and squares); see Figure A.4a for wave numbering. The crest and trough paths of two scattered waves are shown as red and blue dashed lines respectively.

with $\eta_{hyd}$ the surface elevation around a mean derived with the hydrostatic assumption (Equation A.1). $K_f$ represents the transfer function applied for the frequency $f$ and is defined as follows:

$$K_f = \frac{\cosh(kh_0)}{\cosh(kz_{pt})} \tag{A.3}$$

where $z_{pt}$ is the height of the pressure sensor above the bed, $k = 2\pi/L$ the wavenumber associated to the frequency $f$ and $h_0$ the mean water depth. As this relation needs the description of the surface elevation around a mean state, this formulation is not fully adapted to a tidal bore which is characterized by a mean jump. Another approach remains possible and consists of directly correcting the individual wave height $H_{i,hyd}$ from the pressure-derived dataset (Figure A.5a) using the wavenumber $k_i$ estimated from the LiDAR scanner:

$$H_i = K_i H_{i,hyd} \tag{A.4}$$

where $K_i$ is the transfer function for the measured individual wave defined as follows:

$$K_i = \frac{\cosh(k_i h_0)}{\cosh(k_i z_{pt})} \tag{A.5}$$

Equation A.5 requires an estimate of an individual wavelength $L_i$, which can be obtained by evaluating $c_i T_i$. The drawback of this method lies in the non-linearity and unsteadiness of an individual wave: as shown before, $c_i$ can vary over small distances and $T_i$ can be influenced by the presence of scattered waves. When LiDAR data is available, the wavelength can be estimated directly as the whole wave is visible when the crest is around the nadir. Figure A.9a shows the comparison between measured wavelength (distance between two surrounding troughs) and $c_i T_i$. It is observed that $c_i T_i$ generally overestimates the 'instantaneous' wavelength directly estimated from the LiDAR but generally provides a good estimate. The comparison between corrected wave heights $K_i H_{i,hyd}$ and measured

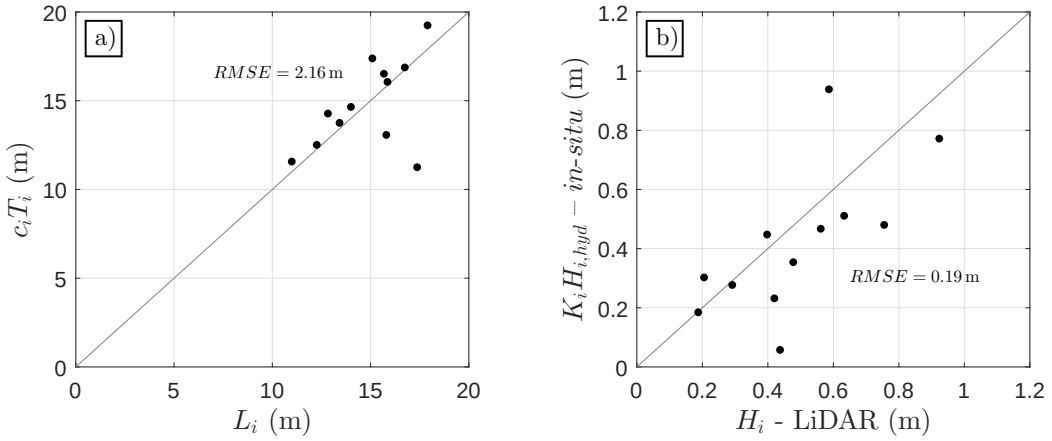


Figure A.9: Wave-by-wave depth attenuation correction of the pressure-derived wave heights. Panel a) shows the estimated individual wavelength $cT$ as a function of the measured wavelength $L$ estimated from the tracking algorithm (Section 4). In panel b), the individual wave heights estimated from pressure measurements and corrected for depth attenuation $K_i H_{i,hyd}$ are shown as a function of the wave height measured by the LiDAR. The 1:1 lines are shown as gray line.

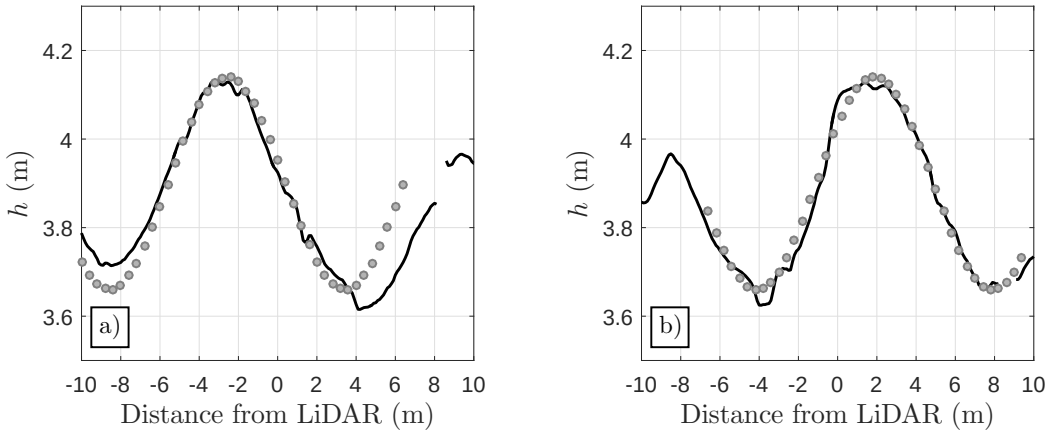


Figure A.10: Wave profile comparison between measurements (black line) and linear wave theory (gray dots) for the wave number 2 (see Figure A.4 or A.6), at two times: a) when the wave crest is located at $x = -3$ m; and b) 0.8 s after.

wave heights by the LiDAR are shown in Figure A.9b. Except for wave number 2 (see Figure A.4a), the depth attenuation based on linear wave theory is able to reconstruct the wave height measured using the LiDAR (*RMSE* of 0.19 m against 0.38 m without correction).

This is an interesting result as it would be expected that non-linear effects could have an impact on the wave geometry, due to the non-linear character of the tidal bore, but also to the interactions with the low-sloping estuarine banks (Bonneton et al., 2015). Chanson (2011) tried to fit wave profiles from linear wave and Boussinesq theory to measurements. Some discrepancies were observed in the wave shape, and especially its asymmetry. Similar comparisons were performed here and an example is displayed in Figure A.10 for the tracked wave number 2. The linear wave profile was constructed using the mean individual wave properties presented in Table A.1. While the comparisons in Figure A.10a exhibit some clear discrepancies, especially in the asymmetric surrounding trough positions, the two profiles match very well at the later stage of the propagation (Figure A.10b). The

primary reason for this is the effect of the interactions discussed earlier (Figure A.6-A.8) between scattered waves and the secondary wave field. We can therefore hypothesize that despite the non-linear character of the tidal bore, the individual waves in the secondary wave field have a general form close to that described by linear wave theory. However, the presence of scattered waves can induce some asymmetry in the crest/trough locations and the wave steepness, inducing potential discrepancies with commonly used wave theory. Additionally, these interactions might in turn trigger some breaking events.

## A.5 Conclusions

A 2D commercial LiDAR scanner has been deployed for the first time to monitor the undular tidal bore of the Garonne River, at high spatial and temporal resolution. The procedure to extract the water level prior to the passage of the bore has been described. This analysis showed that the bent edges of the scanning profiles previously observed with the scanner model for low incident angle are actually due to the displacement of the highest return point, when the light beam goes from a circle to an ellipse for high incident angles, and not to the signal penetration in the water column.

For this Froude number, it was shown that the pressure under the mean jump accompanying the tidal bore is approximately hydrostatic. However, the hydrostatic hypothesis is inadequate to reconstruct the secondary wave field: large differences are observed at the wave-by-wave scale, especially for the wave height ($RMSE$ of 0.38 m over 13 waves). Despite the high levels of turbidity encountered, the acoustic sensor performed extremely well and was able to measure the individual wave characteristics accurately ($RMSE = 0.05$ m). The results show that LiDAR technology can be used to obtain accurate measurements of undular tidal bore geometry, even in the absence of breaking events, which greatly contributes to the advancement of coastal ocean and riverine observing systems (Liu et al., 2015). Here the field deployment focused on the along-stream direction; the analysis highlighted the influence of scattered wave on individual wave properties and profile. However, the possibility of deploying a 2D LiDAR scanning in the cross-section direction seems very promising and could elucidate the variability of the secondary wave field along the cross-section direction.

**Acknowledgments:**

The authors would like to acknowledge the financial assistance provided by CNES through the TOSCA grant GNSS-R Appliqué à l'Environnement Littoral (GRAEL). Kévin Martins was supported by the University of Bath, through a URS scholarship. The assistance of G.s.m in facilitating access to the site platform is greatly appreciated. Finally, the three reviewers are greatly acknowledged for their constructive comments, which helped improving the manuscript.

## Appendix: Accurate detection of steady water surface with a 2D LiDAR Scanner

As the Garonne River is naturally turbid, the scanner beam may be reflected by the 'real' free surface, or by particles in suspension at some depth below the surface (this is referred to as sub-surface hereafter). An example of this is shown at nadir in Figure A.11a prior to the arrival of the bore front at 17:48. The elevation obtained from the LiDAR is observed to jump between two elevations approximately $0.06 - 0.07$ m apart. If it is assumed that the real surface will always lie above the sub-surface, the correct elevation of the flat water surface prior to the passage of the mascaret can be resolved.

At each LiDAR measurement position, the distribution of the measured elevations LiDAR was computed (two examples shown in Figure A.11b-c). Because the measurements typically oscillate between the real and sub-surface; the elevation distribution features two distinct peaks. The correct elevation of the real and sub-surface were estimated by detecting these two peaks. This process was performed at every measurement location and the resulting measured 'flat' real and sub-surfaces are shown in Figure A.11d.

To explain the bent edges of the measured surface profiles (see also in Streicher et al., 2013) the surface of a wall at the same distance range was measured. This represents a 'no-penetration' test, the results of which are also shown in Figure A.11d. It is observed that the real free surface has the same curvature as the wall, which gives confidence to the method to separate the two surfaces. This result also suggests that the penetration of the signal observed with the same LiDAR scanner in previous studies was not the reason for the water surface curvature, as suspected by Streicher et al., 2013. As the incident angle increases, the beam projection becomes an ellipse (see Figure A.12) and we hypothesize that the energy spreads in this increased surface area (Soudarissanane et al., 2009). The scanner then matches the strongest reflected signal to the theoretical position, located at the centre of the ellipse. However, in practice the position of the strongest reflected signal moves away from the beam centre, as illustrated in Figure A.12. This means that the distance measured is shorter than for the assumed measurement location. At high incident angle, this has the effect of introducing curvature into the measured surfaces.

The sub-surface has a slightly different curvature, due to the fact that closer to the nadir, the signal penetrates deeper into the water column since it is stronger for lower incident angle. The penetration extent ranges from 0.07 m around the nadir to 0.05 m at the outer edges of the LiDAR scans. Attempts to correct for the observed profile curvature were not performed for this study as the effect was considered negligible: the changes are small compared to the height of the bore front, and after its passage, the turbidity and surface roughness significantly increase, which ensured that the scanner detected the real surface.

Finally, it is worth noting that the LiDAR scanners provides an output of the return signal strength index (*RSSI*). The *RSSI* was not found to vary significantly between no-penetration/penetrating cases, at a fixed along-stream position. In fact for the present dataset (Tide 5), it was found to linearly increase from the downstream to upstream di-

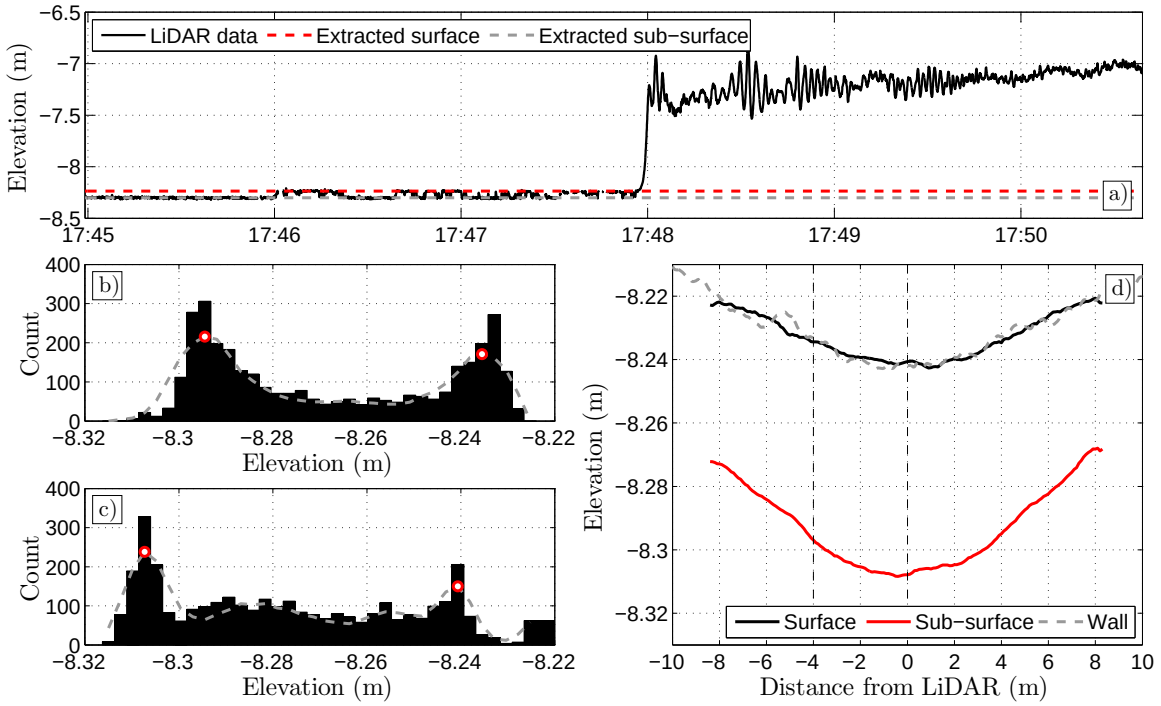


Figure A.11: Illustration of the methodology developed to extract the free surface elevation prior to the bore passage. Panel a) shows the surface elevation timeseries measured by the LiDAR scanner at the Nadir ($x = 0$ m). Panels b) and c) show the distribution of the elevation points measured at $x = -4$ and 0 m respectively. The window-averaged distribution is shown as a dashed grey line. The two peaks, corresponding to the average position of the surface and sub-surface are represented using red circles. Panel d) shows the curved real and sub-surface elevations extracted using the distribution peak methodology. Measurements of a horizontal wall at the same range as measured in the field are also provided. Note that the vertical, $z$ datum is given relative to the LiDAR scanner (and not to the river bed)

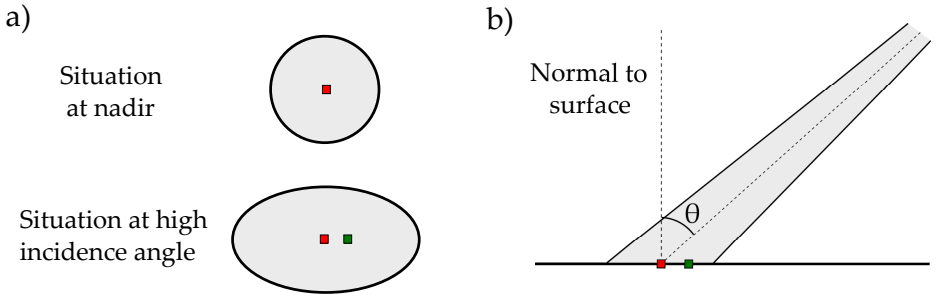


Figure A.12: Schematic of the LiDAR beam spot deformation at high incident angle $\theta$: panel a) shows a view from above the surface measured by the scanner; panel b) shows the lateral view. The red squares represent the centre of the LiDAR beam which is generally assumed to be the measurement location. The green squares represent the actual measurement location. Note that at the nadir, these are the same.

rection; the light conditions (nightfall in this case) are suspected to have influenced this quantity.

## References

Bishop, C. T. and Donelan, M. A., 1987. Measuring waves with pressure transducers. *Coastal Engineering* 11 (4), pp. 309 – 328. DOI: 10.1016/0378-3839(87)90031-7.

Blenkinsopp, C. E., Mole, M. A., Turner, I. L., and Peirson, W. L., 2010. Measurements of the time-varying free-surface profile across the swash zone obtained using an industrial LIDAR. *Coastal Engineering* 57 (11 – 12), pp. 1059 – 1065. DOI: 10.1016/j.coastaleng.2010.07.001.

Bonneton, P., Parisot, J.-P., Bonneton, N., Sottolichio, A., Castelle, B., Marieu, V., and Pochon, N., 2011. Large Amplitude Undular Tidal Bore Propagation in the Garonne River, France. *Proceedings of the Twenty-first (2011) International Offshore and Polar Engineering Conference, Maui, H.I.*

Bonneton, P., Bonneton, N., Parisot, J.-P., and Castelle, B., 2015. Tidal bore dynamics in funnel-shaped estuaries. *Journal of Geophysical Research: Oceans* 120 (2), pp. 923 – 941. DOI: 10.1002/2014JC010267.

Bonneton, P., Filippini, A. G., Arpaia, L., Bonneton, N., and Ricchiuto, M., 2016. Conditions for tidal bore formation in convergent alluvial estuaries. *Estuarine, Coastal and Shelf Science* 172, pp. 121 – 127. DOI: 10.1016/j.ecss.2016.01.019.

Brodie, K. L., Raubenheimer, B., Elgar, S., Slocum, R. K., and McNinch, J. E., 2015. Lidar and Pressure Measurements of Inner-Surfzone Waves and Setup. *Journal of Atmospheric and Oceanic Technology* 32 (10), pp. 1945 – 1959. DOI: 10.1175/JTECH-D-14-00222.1.

Chanson, H., 2011. Undular Tidal Bores: Basic Theory and Free-Surface Characteristics. *Journal of Hydraulic Engineering* 136 (11), pp. 940–944. DOI: 10.1061/(ASCE)HY.1943-7900.0000264.

Damiani, L. and Valentini, N., 2014. Terrestrial Laser Scanner as a measurement instrument for laboratory water waves. *SCORE@ POLIBA 2014*. Cangemi Editore spa: Roma, Italy, pp. 63 – 67.

Frappart, F., Roussel, N., Darrozes, J., Bonneton, P., Bonneton, N., Detandt, G., Perosanz, F., and Loyer, S., 2016. High rate GNSS measurements for detecting non-hydrostatic surface wave. Application to tidal borein the Garonne River. *European Journal of Remote Sensing* 49 (1), pp. 917–932. DOI: 10.5721/EuJRS20164948.

Liu, Y., Kerkering, H., and Weisberg, R. H., 2015. *Coastal Ocean Observing Systems*. Elsevier (Academic Press): London, UK, 2015; 461p.

Madsen, P. A., Fuhrman, D. R., and Schäffer, H. A., 2008. On the solitary wave paradigm for tsunamis. *Journal of Geophysical Research: Oceans* 113 (C12). C12012. DOI: 10.1029/2008JC004932.

Martins, K., Blenkinsopp, C. E., and Zang, J., 2016. Monitoring Individual Wave Characteristics in the Inner Surf with a 2-Dimensional Laser Scanner (LiDAR). *Journal of Sensors, 2016*, pp. 1 – 11. DOI: 10.1155/2016/7965431.

Martins, K., Blenkinsopp, C. E., Almar, R., and Zang, J., 2017d. The influence of swash-based reflection on surf zone hydrodynamics: a wave-by-wave approach. *Coastal Engineering* 122, pp. 27 – 43. DOI: 10.1016/j.coastaleng.2017.01.006.

Soudarissanane, S., Lindenbergh, R., Menenti, M., and Teunissen, P., 2009. Incidence Angle Influence on the Quality of Terrestrial Laser Scanning Points. *Proceedings of Laserscanning '09, Paris, France*, pp. 83 – 88.

Streicher, M., Hofland, B., and Lindenbergh, R. C., 2013. Laser Ranging For Monitoring Water Waves In The New Deltares Delta Flume. *ISPRS Annals of Photogrammetry, Remote Sensing and Spatial Information Sciences* II-5/W2, pp. 271 – 276. DOI: 10.5194/isprsannals-II-5-W2-271-2013.

Tamari, S. and Guerrero-Meza, V., 2016. Flash Flood Monitoring with an Inclined Lidar Installed at a River Bank: Proof of Concept. *Remote Sensing* 8 (10). DOI: 10.3390/rs8100834.

Tamari, S., Guerrero-Meza, V., Rifad, Y., Bravo-Inclán, L., and Sánchez-Chávez, J. J., 2016. Stage Monitoring in Turbid Reservoirs with an Inclined Terrestrial Near-Infrared Lidar. *Remote Sensing* 8 (12). DOI: 10.3390/rs8120999.

Tessier, B., Furgerot, L., and Mouazé, D., 2016. Sedimentary signatures of tidal bores: a brief synthesis. *Geo-Marine Letters*, pp. 1 – 7. DOI: 10.1007/s00367-016-0479-x.

Tissier, M., Bonneton, P., Almar, R., Castelle, B., Bonneton, N., and Nahon, A., 2011. Field measurements and non-linear prediction of wave celerity in the surf zone. *European Journal of Mechanics - B/Fluids* 30 (6), pp. 635 – 641. DOI: 10.1016/j.euromechflu.2010.11.003.

Vignoli, G., Toffolon, M., and Tubino, M., 2003. Non-linear frictional residual effects on tide propagation. *Proceedings of the XXX IAHR Congress, Thessaloniki, Greece*.

# List of publications and presentations

## Journal Publications:

E.W.J. Bergsma* et *al*. Observations and automated detection of bore-collapse using LiDAR measurements at Nha Trang beach, Vietnam. Continental Shelf Research, *under review*.

L.P. Almeida* et *al*. Tide control on the swash dynamics of a steep beach with low-tide terrace. Marine Geology, *under review*.

**K. Martins***, C.E. Blenkinsopp, R. Deigaard, H.E. Power. Energy dissipation in the inner surf zone: new insights from LiDAR-based roller geometry measurements. Journal of Geophysical Research: Oceans, *under review*.

**K. Martins**, C.E. Blenkinsopp*, H.E. Power, B. Bruder, J.A. Puleo and E.W.J. Bergsma. High-resolution monitoring of wave transformation in the surf zone using a LiDAR scanner array. Coastal Engineering **128** (2017) 37-43. DOI: 10.1016/j.coastaleng.2017.07.007.

**K. Martins***, P. Bonneton, F. Frappart, G. Detandt, N. Bonneton and C.E. Blenkinsopp. High frequency field measurements of an undular bore using a 2D LiDAR scanner. Remote Sensing **9** (2017) 462. DOI: 10.3390/rs9050462.

**K. Martins***, C.E. Blenkinsopp, R. Almar and J. Zang. The influence of swash-based reflection on surf zone hydrodynamics: a wave by wave approach. Coastal Engineering **122** (2017) 27-43. DOI: 10.1016/j.coastaleng.2017.01.006.

D. Sous* et *al*. Field evidence of swash groundwater circulation in the microtidal Rousty beach, France. Advances in Water Resources **97** (2016) 144 -155.
DOI: 10.1016/j.advwatres.2016.09.009.

**K. Martins**, C.E. Blenkinsopp* and J. Zang. Monitoring Individual Wave Characteristics in the Inner Surf with a 2-Dimensional Laser Scanner (LiDAR). Journal of Sensors (2016). DOI: 10.1155/2016/7965431.

## Conference Proceedings:

**K. Martins** et *al*. Remote-sensing of wave transformation in the surf zone. Proceedings of Coastal Dynamics, Denmark, 2017.

L.P. Almeida et *al*. Swash zone dynamics of a sandy beach with low tide terrace during variable wave and tide conditions. Journées Nationales de Génie Côtier, Génie Civil, Toulon, 2016 (Paralia eds). DOI: dx.doi.org/10.5150/jngcgc.2016.016.

L.P. Almeida et *al*. Swash dynamics of a sandy beach with low tide terrace Proceedings of Coastal Dynamics, Denmark, 2017.

## Presentations at conferences or seminars:

**K. Martins**, C.E. Blenkinsopp. Wave transformation in the surf zone: new insights from 2D LiDAR scanners. Seminar presentation at LIENSs (Oct. 2017), La Rochelle, France.

**K. Martins**, C.E. Blenkinsopp, H.E. Power, B. Bruder, J.A. Puleo and E.W.J. Bergsma. Monitoring of wave transformation in the surf zone using LiDAR technology. Presentation at YCSEC 2017, Bath, UK.

**K. Martins**, C.E. Blenkinsopp and J. Zang. Individualisation of wave processes in the surf zone. Presentation at YCSEC 2016, Swansea, UK.

**K. Martins** and C.E. Blenkinsopp. Wave monitoring in the surf zone. Presentation at WWEM 2016, Telford, UK.

**K. Martins**, C.E. Blenkinsopp and J. Zang. Use of terrestrial LIDAR for the monitoring of coastal processes. Presentation at LEGOS (November 2015), Toulouse, France.

**K. Martins** et *al*. Field Study of microtidal beach inner-surf and swash zones using 2D LiDAR: Rousty beach, Camargue (France). Poster at YCSEC 2015 (Best Poster Prize), Manchester, UK.

## Awards and scholarships:

**2016:** SWIG Poster prize at the WWEM 2016.

**2016:** Bursary support for the WASH Chile field trip, from Santander Bank.

**2016:** Poster prize at the YCSEC 2015, Manchester.

**2016:** Bursary to attend the YCSEC 2015, from the University of Bath.

**2014-2017:** University Research Services (URS) scholarship from the University of Bath to carry research as a PhD student.